3D-Printed Cell Culture Devices for Engineering Extracellular Microenvironments

Dogan, Asli Aybike

Publication date:
2022

Document Version
Publisher's PDF, also known as Version of record

Aslı Aybike Doğan - Ph.D. thesis

3D printed cell culture devices for engineering extracellular microenvironments

DTU

Technical University of Denmark

organovir
ORGANOIDS FOR VIRUS RESEARCH

3D printed cell culture devices for engineering extracellular microenvironments

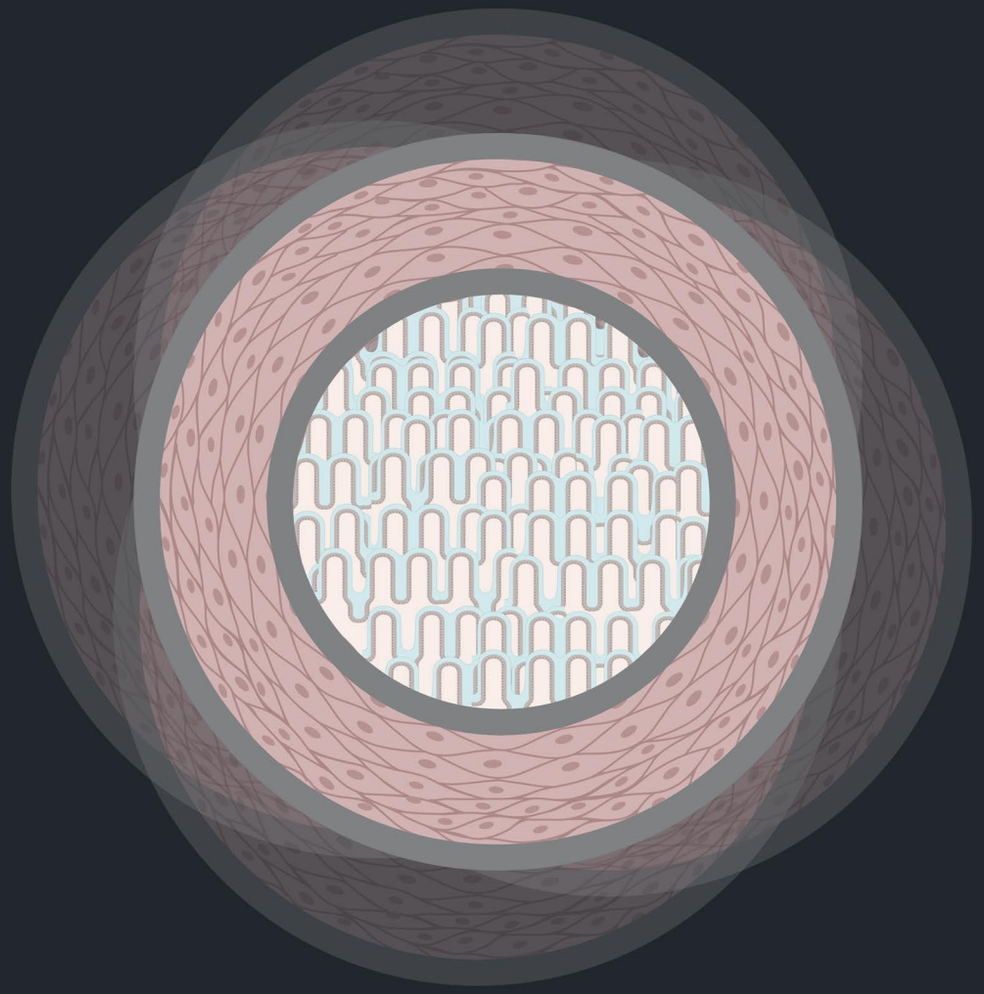

DTU Health Tech
Department of Health Technology

Doctoral Dissertation by
Aslı Aybike Doğan

TECHNICAL UNIVERSITY OF DENMARK
DOCTORAL THESIS

3D-Printed Cell Culture Devices for Engineering Extracellular Microenvironments

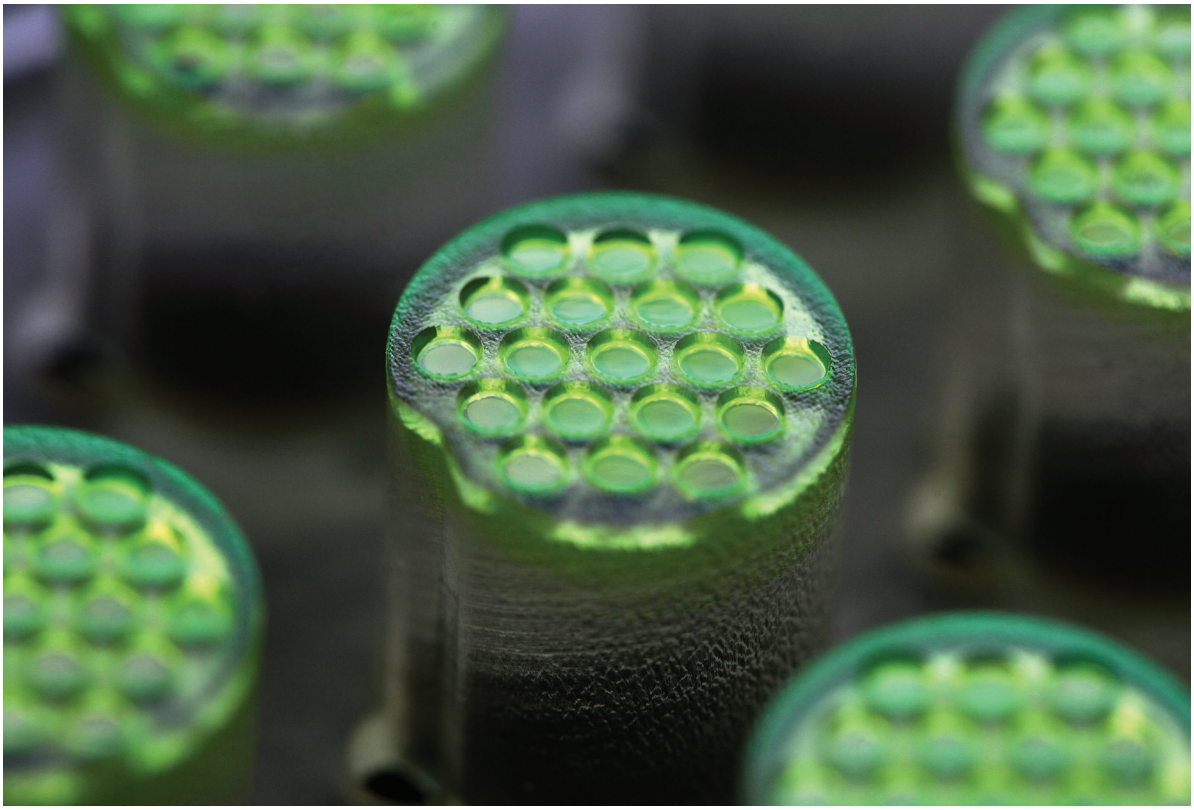

Author:
Aslı Aybike DOĞAN

Supervisors:
Martin Dufva, Associate Professor
Johan Ulrik Lind, Associate Professor

DTU HEALTH TECH | DEPARTMENT OF HEALTH TECHNOLOGY

2022

PREFACE

This doctoral thesis fulfills the requirements for the Ph.D. degree established by the Technical University of Denmark. All work presented here was completed while working as a Ph.D. student in the Fluidic Array Systems and Technology group led by Assoc. Prof. Martin Dufva at the Department of Health Technology (DTU Health Tech) from September 2019 to September 2022. The European Union Horizon 2020 Program under the Excellent Science - Marie Skłodowska-Curie Innovative Training Network and Grant Agreement No. 812673 has funded this project. During my Ph.D. study, Assoc. Prof. Martin Dufva and Assoc. Prof. Johan Ulrik Lind from DTU Health Tech supervised me.

To my endless source of inspiration and motivation,

ATA' M, Mustafa Kemal ATATURK...

"Dünyada her şey için; uygarlık için, hayat için, başarı için en hakiki mürşit ilimdir; fendir."

- Mustafa Kemal ATATÜRK

"Science is the most real guide for civilization, for life, for success in the world."

- Mustafa Kemal ATATÜRK

ACKNOWLEDGEMENT

First, I would like to thank my supervisor, **Martin Dufva**, Associate Professor, for giving me the opportunity to conduct this thesis in the Fluidic Array Systems and Technologies (FAST) group. Through all the ups and downs of this journey during the pandemic, you always kept your optimistic attitude and pushed me to perform at the highest level possible. I am thankful for the opportunity to pursue my own ideas, explore my potential, and grow immensely as an independent researcher. Secondly, I would like to express my sincere gratitude to my co-supervisor, **Johan Ulrik Lind**, for providing valuable insights regarding biomaterials and for trusting and encouraging me when feeling down.

I want to thank **all former and current group members, Arianna, Anna, Salime, Hakan, Alex, Hongxia, and Morten of the FAST group**, for being great colleagues and for their valuable friendship outside of work. Also, I want to thank **my excellent students Andreas, Marina, Isra, Malthe, Marianne, Daina, Simin, Iqra, and Sylvia**, whom I have enjoyed supervising and spending fruitful time within the laboratory. You were a great motivation for me with your enthusiasm, curiosity, and determination despite difficulties during uncertain times of the pandemic. Furthermore, my special thanks go to **Morten**! Your excellent success was the initiation fuel for my project. I am so glad I got to know you before you left. Even though we spent a short period, you became a great friend to me at DTU and outside. And **Ari**! I am glad we had a chance to share our craziness for some time during this journey. xD After our long nights capturing bacteria, I look forward to changing our last moments with propagating succulents! xD

I want to thank the **OrganoVIR family** for collaborations, fruitful discussions, training, and for our great time during our meetings. It was a privilege to work with excellent scientists and try to make a difference in developing tissue models for virology studies during an incredibly challenging time of the pandemic.

Thank you for all my international collaborations during my Ph.D. journey. I want to thank **Dr. My Hedhammar, Savvina Gkouma, Mona Widhe, and Dr. Jean-Luc Bailly**, for fruitful discussions and constructive feedback that was very helpful in understanding the needs of users from different fields. Despite all difficulties of the pandemic, we could manage to initiate a great collaboration to test one of our platforms with SARS-CoV-2! I was lucky to spend at least one month at Virogenetics Laboratory, the Jagiellonian University (JU), Krakow, Poland, under **Prof. Krzysztof Pyrć**. I want to thank Krzysz for letting me into his laboratory and all the members of

the Virogenetics group for making me feel at home in Krakow. Especially thank you, **Emilia**, for being my closest collaborator and friend during our project. I wish you great success in your PhD, I look forward to celebrating our publication and (hopefully) PhDs together!

I would also like to express my deepest gratitude to my collaborators from DTU Health Tech. Dr. **Babak Rezaei, Alex Sánchez Pérez, Dr. Arto Heiskanen, Prof. Jenny Emnéus, and Dr. Murat Serhatlioglu**, thank you all for the tremendous scientific conversations and exciting projects we have initiated. Especially, Arto, special thanks to your addition to our fruitful discussions for being so kind as to drive Hakan and me home after some long nights at the lab. Also, Murat, thank you so much for your help supplying instruments for PIV experiments (you are such a lifesaver!) and, of course, for your valuable friendship and our fruitful conversations.

Many thanks to **the former and current board members of the Scandinavian Society for Biomaterials (SCSB): Prof. Cecilia Persson, Dr. Mats Hulander, Dr. Peter Uppstu, Dr. Jānis Ločs, Prof. Berit Løkensgard Strand, Dr. My Hedhammar, Dr. Gissur Örlygsson, Dr. Hanna Tiainen, Dr. Giuseppe Schiavon, And Dr. Alireza Dolatshahi-Pirouz.** Being a member and student representative on the board has been a privilege. Thank you all for your warm, welcoming, and inspiring attitude. You are admirable in keeping the society like a continually expanding family full of Biomaterials lovers for years.

I want to thank L**otte, Lene, Ole, Helene, Marlene, and Lars** for being available to help and keeping the laboratories organized and functional. Without you, it would be much more challenging to do my experiments. Also, thank you, **Tine, Trine, and all Ph.D. school staff**, for the great help in all administrative processes for ensuring I meet the degree requirements.

I want to thank my colleagues, friends, and family in Denmark, **Sarkhan, Lamia, Selgin, Murat, Seda, Arjen, Sven, Afia, Salman, Milena, Lina, Christopher, Christina, Babak, Mozhdeh, Nayere, Sina, Carmen, Sarvesh, Ralu, Marcos, Alex, Michelle, Morten, Julie, Janko**... Thank you for being amazing friends and such a motivation to keep up with the hard work in stressful moments. I felt blessed to meet you all and loved the time we spent together; I wish we would have many more moments.

I have been blessed with lifetime friends, **Fulya, Ece, Aytul, Ecem, Seyma, Haluika, Mali, Manual, Valeria, Marija, Melanie,** and **Dechen**; inspiring mentors, **Dr. Aylin Sendemir, Prof. Ismet Gurhan-Deliloglu, Prof. Erdal Bedir, Prof. Yannis Missirlis, Prof. Ozlem Yesil-Celiktas;** and my family, **my mom, Hamide and my father, Fehmi and my brother, Aral, my mother-in-law, Lutfiye, my father-in-law, Coskun,** and **my brother-in-law, Gokhan.**

Despite the distance and being often disconnected, you were always with me. I would not have completed this work without your encouragement, understanding, and sympathetic ear, throughout the process. Thank you so much! Love and miss you all!

With loads of love… Hakan, since our master's years, you have been my labmate, my boyfriend, and now in Ph.D., my husband, my collaborator, and finally labmate again! xD You are my partner in crime and love; the closest witness and victim of long days and sleepiness nights…Thank you for providing me with liters of coffee and tones of weight because of your delicious unhealthy food during this journey! xD I feel blessed with your love, immense support, understanding, and patience. Thank you, my love, for always believing in me and being my shoulder to lean on. Without you, the hand-in of this thesis would not have been possible.

Aslı Aybike DOĞAN

ABSTRACT

Barrier tissues such as endothelial and epithelial are one essential passageway of drug delivery to the digestive system to maintain homeostasis in the body. Within the scope of the 3Rs (Replacement, Reduction, and Refinement) principles of animal studies, there is a growing interest in developing physiologically relevant in vitro barrier tissue alternatives. In vitro barrier tissue models are often based on their static cultures on traditional Transwell inserts that provide vertical compartmentalization for transport solutes through co-cultured barrier tissue layers. On the other hand, microphysiological systems (MPS) offer platforms with increased (bio)complexity by combining biomaterials, bioactive components, and mechanical stimuli such as stretching and flow shear stress. This thesis presents scalable (6- to 96-well plate formats), customized, and modular cell culture device prototypes designed, fabricated, and validated considering accessibility, (bio)complexity, and higher throughput. To demonstrate such customization, design considerations, e.g., the number of wells, the number of layers, the wall thickness, and the capillary forces were discussed, and a small design library of 3D-printed inserts and a robust method to functionalize the inserts with hydrogel and synthetic membrane materials were presented **(Paper I)**. Moreover, bidirectional **(Paper II)** and unidirectional **(Paper III)** fluidic approaches were demonstrated to mimic the mechanical microenvironment of epithelial endothelial barrier tissues into dynamic devices. Intestinal epithelium showed heterogenous morphogenesis where 2D monolayers and 3D villi-like structures formed in dynamic conditions. On the other hand, the endothelial cells were actuated and elongated through the flow direction and coupled with 3D differentiated intestinal cells to test crosstalk between barrier tissues. Taken together, these findings show that customized cell culture devices provide modularity that the platforms can be tuned by mechanical stimuli to activate intestinal and endothelial barrier functions with higher throughput.

Keywords: 3D-printed cell culture devices**,** customized hanging inserts, tissue engineering, hydrogels, barrier tissues, mechanical stimuli

ABSTRACT (DANISH)

Inden for rammerne af 3Rs (Replacement, Reduction, og Refinement) principper for dyreforsøg er der en stigende interesse for at udvikle fysiologisk relevante reagensglasmodeller af tarme og blodkar for at studere transport af lægemidler. Reagensglasmodeller er ofte baserede på statiske kulturer på membraner. Disse reagensglasmodeller er simple at bruge og standardiserede men ikke helt relevante. Mikrofysiologiske systemer øger relevansen ved at kombinere biomaterialer, bioaktive komponenter med mekaniske stimuli som efterligner dem i menneske. Denne afhandling præsenterer en metodik at tilpasse indsatser til brønde for celle dyrkning så at de kan skaleres til 6- til 96-brønds pladeformater, kobles sammen med hinanden, og giver korrekt mekaniske stimuli. For at demonstrere denne tilgang designedes et bibliotek af 3D-printede indsatser til forskellige formater **(Paper I)**. En nem og hurtig metode at funktionalisere indsatserne med hydrogel og syntetiske membranmaterialer udvikledes. Herefter udvikledes indsatser til mekaniske stimuli i form af perfusion. Indsatser til tovejs **(Paper II)** og ensrettet **(Paper III)** perfusion brugtes til dyrkning af tarme væv (epitel) og blodkar (endotel). Epitelet i tarme væv under perfusion viste heterogen dannelse af væv in 2D og 3D. Cellerne viste forbedrede egenskaber i 3D sammenligning med 2D. Endotelcellerne, som efterligner blodkar, opviste store morfologiske forandringer og tilpassede sig strømningsretningen. Dyrkning af tarmens epitel og blodkarets endotel i samme indsats viste at tarmens epitel påvirkerede blodkarrets funktion. Tilsammen viser disse resultater, at tilpassede brønde-indsatser giver f.eks. mekaniske stimuli for at aktivere tarm- og endotelbarriere-funktioner uden at gå på kompromis med mængden prøver som kan studeres.

Nøgleord: 3D-printede cellekulturenheder, tilpassede hængende indsatser, vævsteknologi, hydrogeler, barrierevæv, mekaniske stimuli

LIST OF CONTRIBUTIONS

The results presented in this work are part of the following published contributions, also available in Chapters 5-7.

I. **Asli Aybike Dogan**, Martin Dufva, **Customized 3D-printed stackable cell culture inserts tailored with bioactive membranes**, Scientific Reports, 12, 3694 (2022), Doi: 10.1038/s41598-07739-7

II. **Asli Aybike Dogan**, Martin Dufva, **Heterogenous morphogenesis of Caco-2 cells reveals that flow induces 3D growth at high cell densities but is insufficient to induce intestinal cell maturation in 2D**, submitted.

III. **Asli Aybike Dogan**, Martin Dufva, **High throughput shear stress platforms coupling the intestine and blood vessels**, submitted.

List of conference contributions for 2019-2022: The results presented in this work are part of the following contributions, also available in Chapter 8.

I. **Asli Aybike Dogan,** Martin Dufva**, "Evaluation of Biocompatibility on 3D-printed Inserts using Mouse Intestinal Organoids"**. Poster presentation at EUROoCS 2020 (08 - 09 July 2020)

II. **Asli Aybike Dogan** & Emilia Barreto Durán, Krzysztof Pyrć & Martin Dufva**, "3D-printed Bioengineered Platform for Co-culturing Caco-2/Immune Cells to Study SARS-CoV-2 Infection"**. Poster presentation at ScSB 2022 Annual Meeting (13 - 15 June 2022)

III. **Asli Aybike Dogan**, Daina Santapau Arbós, Alexander Jönsson, Hakan Gurbuz, Martin Dufva, **"Perfusion Device for 3D Gastrointestinal Spheroids"**. Poster presentation at TERMIS 2022 EU Chapter (28 June - 01 July 2022)

IV. **Asli Aybike Dogan**, Martin Dufva**, "3D-printed Shear Stress Platform for Endothelial Cell Mechanoinduction"**. Poster presentation at TERMIS 2022 EU Chapter (28 June - 01 July 2022)

V. **Asli Aybike Dogan**, Marina Orenga Sánchez, Martin Dufva**, "Patterning of Photo-crosslinkable Hydrogels to Mimic Intestine Tissue"**. Poster presentation at OrganoVIR Virtual Event 2021 (01 - 02 July 2021)

Other article contributions by the author (not covered in this thesis):

- **Asli Aybike Dogan***, Andreas Willumsen, Anna Kathrine Bach Mortensen, Christian Victor Parigi Dagnæs-Hansen, Morten Leth Jepsen, Salime Bazban-Shotorbani, Nazila Kamaly, Martin Dufva, **FAST Microbioreactor: Customized, 3D-printed, Fluidic Platforms for Tissue Engineering Applications**, in preparation.

- **Asli Aybike Dogan*** and Emilia Barreto Durán, Krzysztof Pyrć and Martin Dufva, **3D-printed Bioengineered Platform for Co-culturing Caco-2/Immune Cells to Study SARS-CoV-2 Infection**, in preparation.

- Arianna Toppi, Louise L. Busk, Hongxia Hu, **Asli A. Dogan***, Alexander Jönsson, Rafael J. Taboryski, and Martin Dufva, **Photolithographic Patterning of FluorAcryl for Biphilic Microwell-Based Digital Bioassays and Selection of Bacteria**, ACS Applied Materials & Interfaces, 13 (37), 43914-43924 (2021), Doi: 10.1021/acsami.1c10096

- John Rizk, Rasmus Agerholm, Alexander Jönsson, **Asli Aybike Dogan***, Martin Dufva, Vasileios Bekiaris, **cIAP1/2 antagonization by SMAC mimetic induces non-canonical NF-κB mediated TH17 cell homotypic interactions and increases their resistance to shear stress**, European Journal of Immunology (EJI) (2021), 51 (8), 2097-2099, Doi: 10.1002/eji.202048983

- Ecem Saygili and **Asli Aybike Dogan-Gurbuz***, Ozlem Yesil-Celiktas and Mohamed S. Draz, **3D bioprinting: A powerful tool to leverage tissue engineering and microbial systems**, Bioprinting (2020), ISSN: 2405-8866, Vol: 18, Page: e00071, Doi: 10.1016/ j.bprint.2019.e00071

- Hakan Gürbüz, **Asli Aybike Dogan***, Babak Rezaei, Janko Kajtez, Alberto Martinez- Serrano, Stephan Sylvest Keller, Martin Dufva, Arto Heiskanen, Jenny Emnéus, **Pyrolyzed embedded 3D-printed scaffolds for stem cell differentiation and electrochemical detection of dopamine exocytosis**, in preparation.

Supervision:

- MSc thesis, **Coupled intestine and blood vessel models for drug discovery**, by Andreas Willumsen, 2020, DTU Health Tech (w/ Assoc. Prof. Martin Dufva)
- MSc thesis, **Perfusion cell system for improved cell functions**, by Isra Parvaze, 2021, DTU Health Tech (w/ Assoc. Prof. Martin Dufva)
- MSc thesis, **Development of a topographical bio-scaffold for improved in vitro intestinal tissue modeling**, by Marina Orenga Sánchez, 2021, DTU Health (w/ Assoc. Prof. Martin Dufva)
- MSc special project course, **Characterization of a 3D printer for hydrogel printing**, by Marina Orenga Sánchez, 2020, DTU Health (w/ Assoc. Prof. Martin Dufva)

CONTENTS

LIST OF ABBREVIATIONS

3D	Three-Dimensional
2D	Two-Dimensional
BBB	Blood-brain-barrier
CAD	Computer-aided design
CBC	Crypt base columnar
CSK	Cytoskeletal
ECM	Extra cellular matrix
ECs	Endothelial cells
FDM	Fused Deposition Modeling
FITC	Fluorescein isothiocyanate
GI	Gastrointestinal
HS	High shear
HTS	High-throughput screening
JAMs	Junctional adhesion molecules
LS	Low shear
LY	Lucifer Yellow
µPIV	Microparticle image velocity
MPS	Microphysiological systems
mTG	Microbial transglutaminase
MUC-2	Mucin-2
OOC	Organ-on-a-chip
PBS	Phosphate-buffered saline
PC	Polycarbonate
PDMS	Polydimethylsiloxane
PE	Polyethylene
PEG	Poly (ethylene glycol)
PET	Polyester

PTFE	Polytetrafluoroethylene
RGD	Arginine-glycine-aspartic acid
SLA	Stereolithography
TE	Tissue engineering
TEER	Transepithelial electrical resistance
TJs	Tight junctions
TNF-α	Tumor necrosis factor-alpha
ZO-1	Zonula occludens-1

“Searching and learning is where the miracle process all begins.”

-Jim Rohn

Chapter 1

INTRODUCTION

1.1 Scope and Motivation

Biological barriers such as endothelial and epithelial are essential for homeostasis in the body. As mentioned earlier, most barrier models rely on traditional culture, and Transwell insert platforms offer vertical compartmentalization for co-culture and transport through barrier tissue applications. On the other hand, microphysiological systems (MPS)[1–3], in particular, “on-chip” or microfluidic devices[4–7], provide more sophisticated approaches by combining heterotypic cell cultures with physiologically relevant dynamic microenvironment conditions where biomaterials can be implemented to mimic ECM with tissue-specific stiffness and topography. Moreover, these tissues can be subjected to mechanical forces such as stretching and flow shear stress as in blood flow in the body.

Although these systems are up-and-coming and growing in the field to be alternative replacements for animal testing based on the principles of the 3Rs (Replacement, Reduction, and Refinement)[8,9], they are still debatable to emulate the complexity of the human body. Moreover, fabricating a platform that could cover all essential parameters of an organ is not trivial. Numerous articles deal with these concerns and mostly rely on microfluidics that would require either complex operational settings or advanced fabrication technologies.

These difficulties create communication barriers between engineers and biologists that cause a significant delay in scientific development. Since in vitro tissue modelling needs multidisciplinary effort and cooperation between biologists, tissue engineers, and clinicians, designed platforms should be more accessible by most laboratories.

In these regards, 3D stackable SLA printed inserts were successfully applied for drug delivery applications in previous work performed by Dr. Morten Leth Jepsen from the Fluidic Array Systems and Technology (FAST) Group of the DTU Health Tech[10]. The FAST group is a multidisciplinary group that has provided innovative technological solutions[10–15] to relevant biological problems for years. The OrganoVIR (Organoids for Virus Research) project (Grant No. 812673, under the European Union's Horizon 2020 research and innovation program under the Marie Skłodowska-Curie grant agreement) has been a continuation of this research line. It was based on a highly multidisciplinary collaboration between biology, virology, biomaterials, and tissue engineering to develop high-throughput screening (HTS) platforms with 3D organoids.

Within the scope of my project in the OrganoVIR and FAST group, three distinct challenges of the 3D-printed insert approach[10] have been identified. First, rescaling inserts were necessary to achieve higher-throughput screening (HTS), dominated by the 96-well plate scale due to its lower reagent usage. Second, the extracellular matrix (ECM)-mimetic hydrogel membrane fabrication method must have been simplified for such minor scales as 96-well plates. Third, membrane thickness was supposed to be thinner than the previously reported hydrogel membranes (1-3 mm) to prevent slow mass transport of oxygen and nutrients[16].

On the other hand, considering the sagging effect of thin membranes (<1-3 mm)[11], which could create inconsistency in model barrier tissues, was supposed to be minimized. It is also essential to prevent any disruptions in paracrine-signaling events toward the membrane that organize cell-cell and cell-matrix interactions[17–21]. Also, designed systems should have been modular and complex enough to be used for mimicking barrier tissues and practical enough with higher throughput. A simplistic approach needed to be taken into consideration to be able to transfer the developed technology to partner laboratories for further scientific evaluations in viral infections and/or different organoid models. In addition to all these challenges, my background and scientific interests in engineering artificial extracellular microenvironments prompted me to design fluidic insert platforms to investigate further cell-matrix and cell-cell interactions and mechanical stimuli on cells.

This thesis work was performed by considering all these motivations and aimed to introduce a scientific and technological perspective by focusing on the development, characterization, and application of 3D-printed cell culture devices. Particularly concentrated on dynamic intestinal and endothelial microenvironments to improve biological functionality in balance with scalability and throughput. Highlighted findings of this thesis work were disseminated *via* scientific publications, manuscripts, and conference contributions listed above.

“Learning is not a destination; it is a continuous process.”

-Kevin Horsley

Chapter 2

BACKGROUND AND THEORY

In this chapter, first of all, epithelial/endothelial barrier tissues and their microenvironment and microarchitecture were described. Then, current tissue-engineered in vitro barrier models, more specifically, dynamic microphysiological systems (MPS) to mimic native tissues, were outlined by giving a theoretical overview of the state the art of flow dynamics and the use of rapid prototyping technologies. Finally, recent advances in biomaterials and fabrication technologies have evolved to fabricate these in vitro cell culture platforms to mimic in vitro.

2.1 Tissue Engineered In Vitro Barrier Models

Tissue engineering (TE) is a broad concept mainly aiming to model native tissues in vitro by integrating biomaterials, cells, and bioactive molecules. Due to the fact that tissue-engineered in vitro models are transitioning between traditional 2D cell culture and in vivo testing during drug development, their popularity in the preclinical testing field has been increasing day by day. The main big aim is to develop physiologically relevant in vitro tissue models and artificial organs for transplantations more reliably and efficiently to replace, reduce and refine (3Rs) animals known as not representative preclinical models for human physiology[22–24]. Moreover, *in vivo* testing is costly, time-consuming, and ethically questionable[22,23]. However, increasing complexity in vitro is not a trivial concept in practice. Therefore, many scientists and engineers make tremendous efforts to develop alternative in vitro tissue models that could be implemented in the drug development pipeline[8,9]. This means the developed platforms should be as simple as possible and balanced by providing efficient (bio)complexity, standardization, automatization, and throughput[8,9] (Figure 2.1-1).

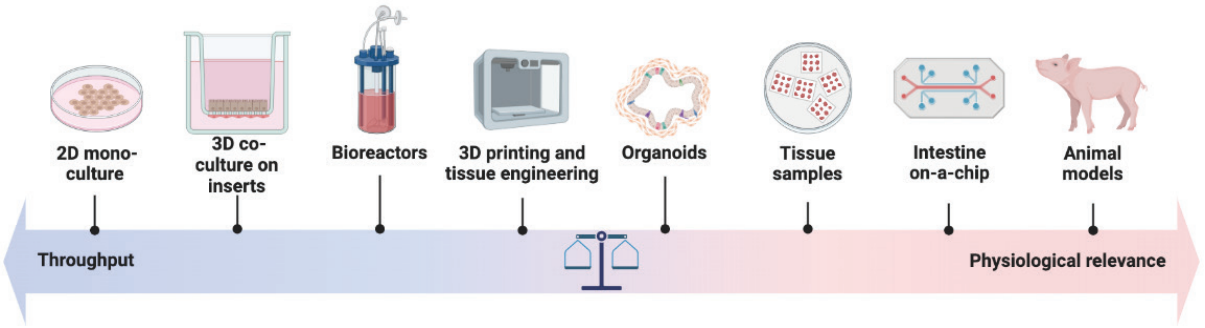

Figure 2.1-1: An overview of example tissue engineering platforms is placed in balance of throughput and complexity level. Adapted from "Intestine Tissue Culture and Engineering Platforms" by BioRender.com (2022). Retrieved from https://app.biorender.com/biorender-templates

When it comes to the increasing complexity of an in vitro platform, microfluidic-based organ-on-a-chip (OCC) or microphysiological systems (MPS) dominate the field due to their excellent mass transfer characteristics. On the other hand, MPSs provide a sophisticated approach by combining heterotypic cell cultures with physiologically relevant dynamic microenvironment conditions where biomaterials can be implemented to mimic ECM with tissue-specific stiffness and topography, and these tissues can be subjected to mechanical forces such as stretching, flow shear stress as in blood flow in the body[2,3]. However, the usability and scalabilities of these systems often fail due to the need for the number of experiments that should be run in parallel. Therefore, conventional cell culture plates and Transwell-type inserts for *in vitro* tissue models have still been the most commonly used[25,26].

2.1.1 Epithelial and endothelial tissues

The most common in vitro application in drug development processes is testing the absorption and bioavailability of drugs by the gastrointestinal (GI) tract. Caco-2 cells, generated from a human colon adenocarcinoma, are one of the most well-known and often used human intestinal epithelial cell lines to study the small intestinal tissue for these purposes. They are well-established in traditional culture methods[27], commonly on standard plastic multi-well plates or

Transwell inserts. However, these methods often lack to mimic the natural biomechanical microenvironment of the gut with physical inputs such as fluid flow, irregular compressive and tensile strains, fluid shear stress, cyclic peristaltic motions, and villus motility patterns[28–31]. The intestinal cytoskeleton senses these physical inputs to initiate the cell signaling process for epithelial differentiation and proliferation. However, the exact mechanisms of these biochemical signals are mostly unknown. Therefore, it is very crucial to develop in vitro gastrointestinal tract models that can recapitulate native intestinal tissues that possess the basic morphogenesis (e.g., villi–crypt structure with regiospecific intestinal cell distribution) and functions (e.g., barrier functions and mucus production) of the natural intestinal epithelium[18,20,32].

Endothelial cells (ECs) are the major cells that act as a monolayer interface between blood vessels and the underlying tissue. They create a barrier together with epithelial cells that regulate diffusion and selective permeability[33] controlled by biochemical cues in the cell microenvironment such as cell-cell communications (i.e., direct contact, autocrine, and paracrine communications), ECM involving basement membrane, interstitial matrix components, and cell-ECM interaction through membrane receptor proteins as well as physical cues such as flow-induced shear stress (Figure 2.1-2)[34].

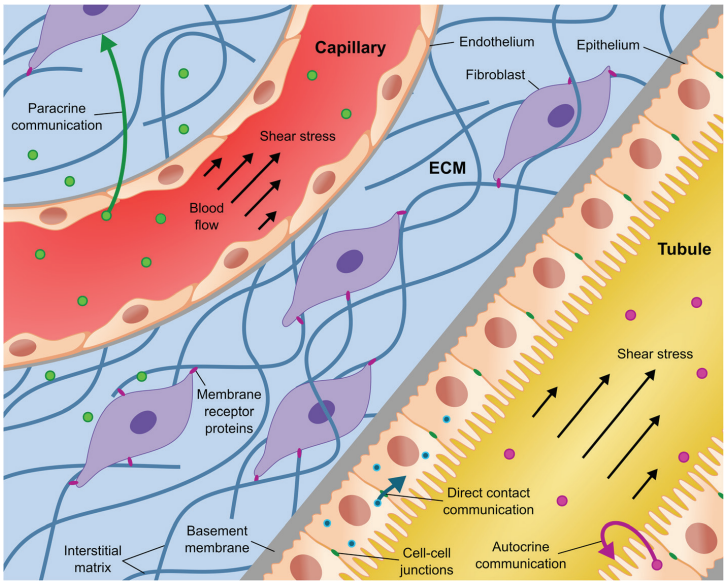

Figure 2.1-2: Illustration of an epithelial tubule and an endothelial capillary embedded within an ECM and physical and biochemical cues in the cell microenvironment. Figure adapted with permission from [34].

The extracellular stimuli and mediators by these cascades of signaling mechanisms, such as direct contact, endocrine, paracrine, and autocrine signaling[34], involve the crosstalk between the permeability of endothelial barriers by paracellular and transcellular pathways[34,35]. These main possible routes for solutes to cross the epithelial and endothelial barriers are **1) the transcellular pathway** in which ions and molecules pass through the cell membrane passively by a driving force such as a concentration gradient, an electrical potential difference, a hydrostatic pressure, or an osmotic gradient; **2) the paracellular pathway** where solutes cross between cells. Moreover, cells also have an active transport by a transcellular mechanism involving transmembrane proteins (Figure 2.1-3)[35].

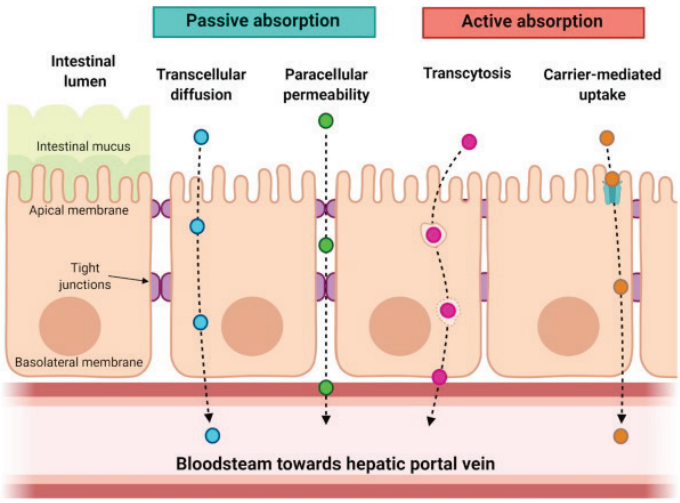

Figure 2.1-3: Schematic drawing of main transport routes between epithelial and endothelial barriers. Figure adapted with permission from [35].

In epithelial and endothelial barrier tissues, intercellular junctions (Figure 2.1-4); gap (e.g., connexins), adherens (e.g., E-cadherins), and tight (Junctional adhesion molecules (JAMs), Occludins, Claudins) junctions, play an essential role in regulating the permeability in the paracellular pathway. These proteins, especially tight junctions (TJs), are responsible for transporting substances to maintain and control the fluid composition between distinct tissue compartments [36].

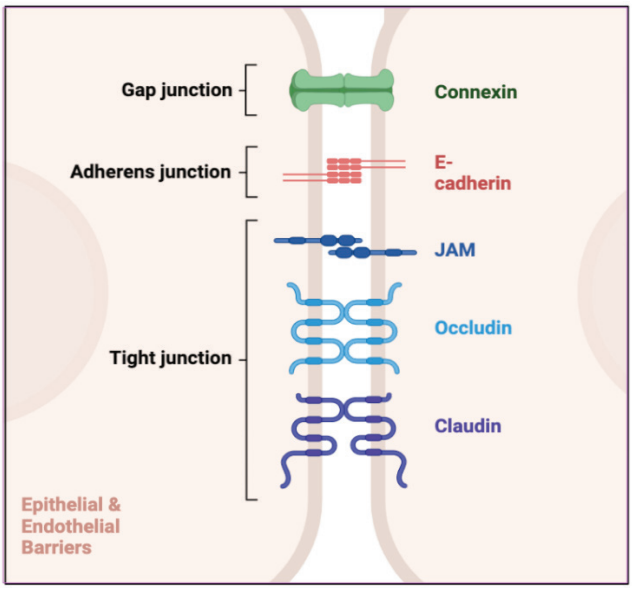

Figure 2.1-4: Schematic drawing of intercellular junction proteins of epithelial and endothelial cells. Adapted from "Cell Junction Types" by BioRender.com (2022). Retrieved from https://app.biorender.com/biorender-templates

2.1.2 Physiology of intestinal epithelial tissues

The small intestine, a part of the gastrointestinal tract, has main functions such as propelling, blending, digestion, absorption, and elimination of elements such as food and liquid. There are central parts of the small intestine starting from the stomach by connecting the jejunum, duodenum, and ileum, respectively. All parts of the small intestine have villi (villus) structure, increasing the endothelial layer's surface area into the lumen (Figure 2.1-5)[37]. These villi structures are surrounded by multiple crypts that have crypt base columnar (CBC) cells that are involved in protecting and nurturing stem cells by lineage-committed progenitor cells in the transit amplifying zone as well as acting as intestinal stem cells by generating new cells that differentiate and migrate upwards towards the villus tip when they get mature. This process continues by cells undergoing apoptosis close to the villus tip and is rapidly replaced by advancing cells[37].

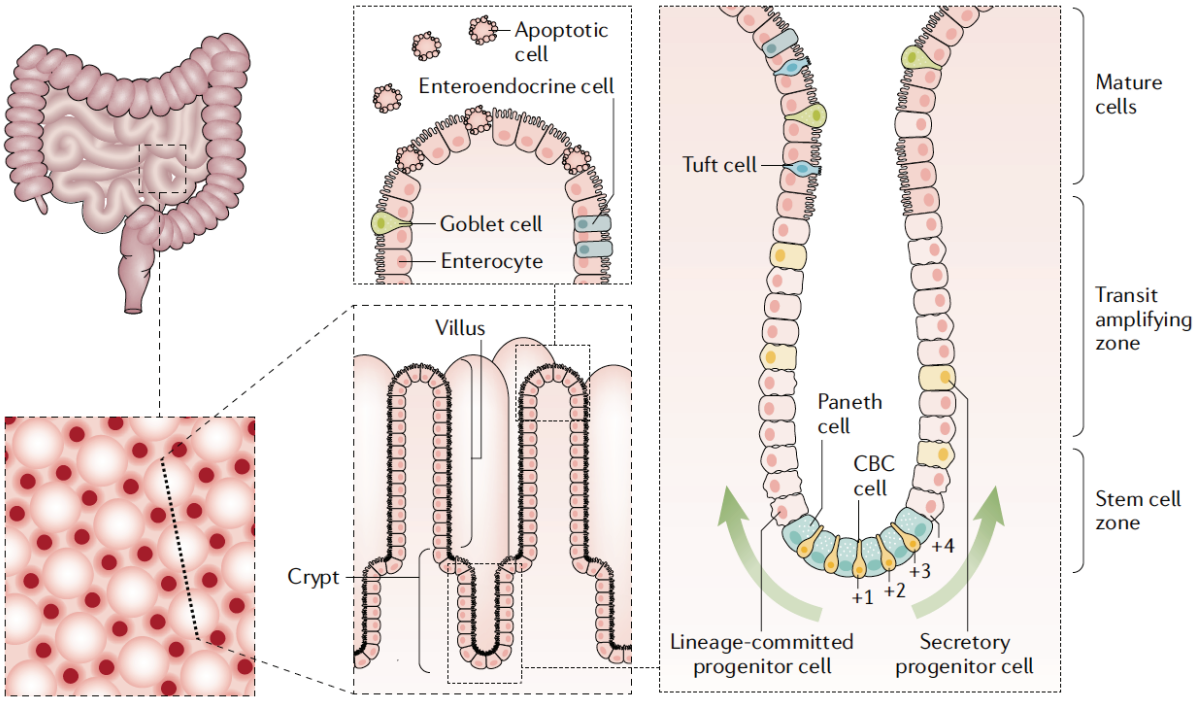

Figure 2.1-5: Schematic drawings of the intestinal structure, cell types, and cycles play a role in forming Crypts and villi structures in the epithelium. Figure adapted with permission from[37].

Epithelial cells are polarized as they connect to the extracellular matrix (ECM) from the basolateral side, separating from the apical side. Enterocytes with microvilli increase the surface area further by absorbing nutrients from the lumen. Apart from enterocytes, the primary roles of the other four cells present in villi:

- Goblet cells for mucin secretion.
- Paneth cells for immunity and mucus.
- Enteroendocrine cells for hormonal production and microfold cells to cover the lymphatic nodes in lamina propria[37].

2.1.3 Physiology of endothelial tissues

Blood vessels connect tissues and organs by conducting the blood throughout the body. Vascular endothelium, the innermost layer of blood vessels, is highly specialized and composed of a cell monolayer that is in contact with blood flow. This layer acts as

a barrier that mediates the exchange of water, solutes, and cells through paracellular or transcellular pathways between the vessel and the bloodstream[38,39]. The basal membrane surrounding the endothelium includes the main essential extracellular matrix (ECM) components, like collagen IV and laminin, that give flexibility and perfusion for substances to exchange. The number and thickness of blood vessel layers vary depending on the physiological conditions (Figure 2.1-6). Capillaries are the thinnest endothelium (in 9 μm diameter) with a cell monolayer surrounded by pericytes for quick and effective oxygen and nutrient diffusion. On the other hand, arteries in different thicknesses depending on where they are subjected and have the ability to hold high blood pressure. In contrast, veins with thin walls (in 0.6-16 mm diameter) could easily deform and only maintain low blood pressure[39].

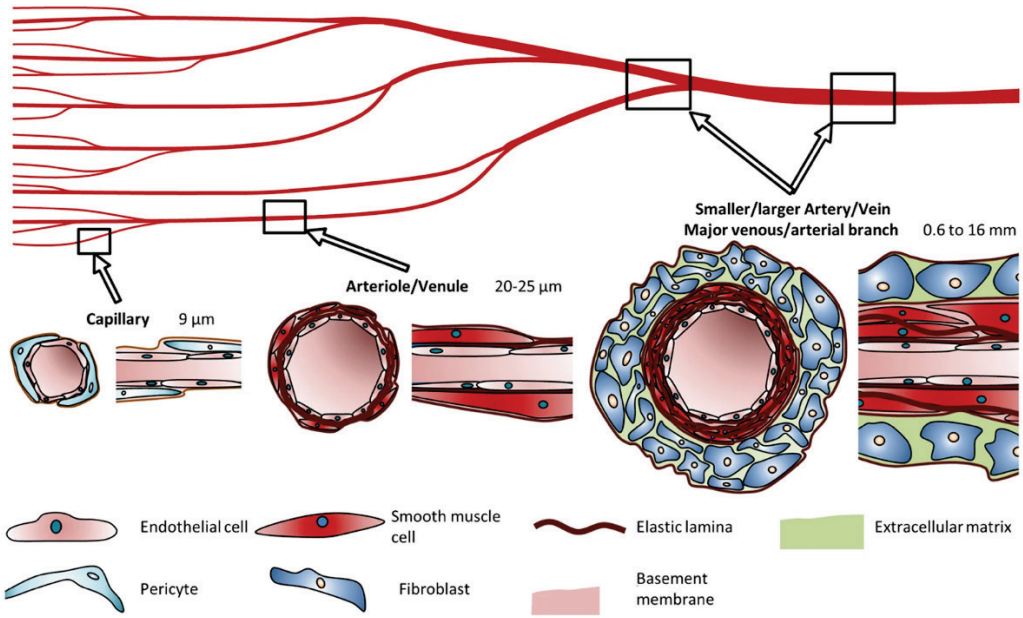

Figure 2.1-6: Illustration of blood vessels; capillary, artery, and vein, and their cell types; endothelial cells, pericytes, smooth muscle cells, and fibroblast. Figure adapted with permission from [39].

2.1.4 Extracellular matrix (ECM)

The extracellular matrix (ECM) is a three-dimensional support structure surrounding cells within organs and plays an essential role in tissue homeostasis by dynamically remodeling itself. It mainly consists of water, proteins, and polysaccharides produced by cells and regulates many crucial cellular functions such as proliferation, migration, differentiation, and cell fate[40,41]. In Cell-ECM interaction, mechanosensitive transmembrane receptor proteins (e.g., integrins) are mediators that act as a bidirectional channel in transferring biochemical signals between the ECM and the cytoskeleton (Figure 2.1-7). These proteins also have an essential role in activating intracellular signaling pathways affecting cell migration, differentiation, and gene expression [40].

The ECM consists of many molecules, such as collagens, proteoglycans, glycoproteins, and cell adhesion (Figure 2.1-7). Depending on localization and composition, ECM has two main components: **1) the basement membrane**, a sheet-like layer that separates epithelia from connective tissue and mainly consists of collagen IV and laminins; and **2) the interstitial matrix**, which forms a porous scaffold for surrounding cells and mainly composed of collagen I and fibronectin. Collagen is the major fibrous protein with a triple-helical structure in the mammalian extracellular matrix (ECM), acts as a ligand for many receptors such as integrin, and provides scaffolding support for cells[41]. It regulates the formation and maintenance of mechanical properties in tissues.

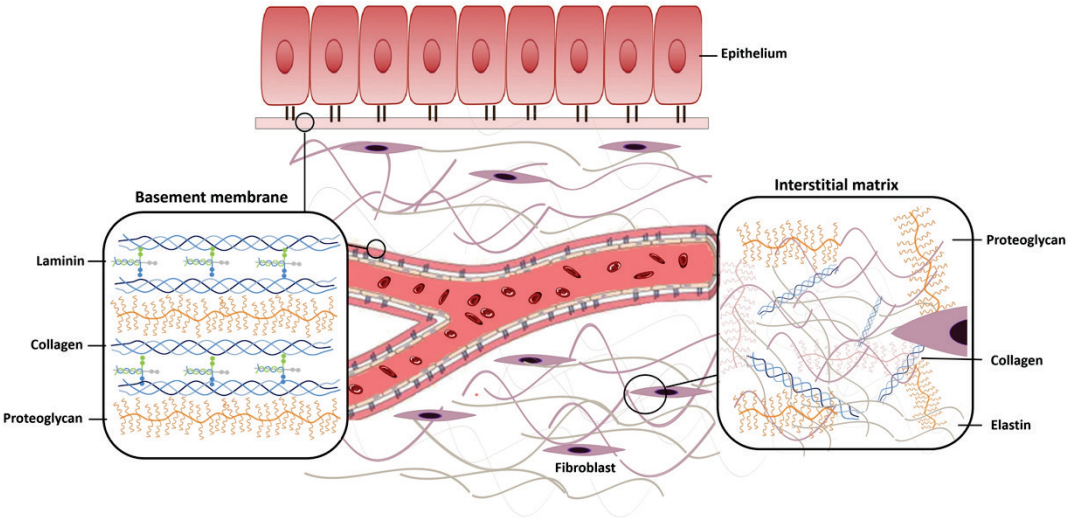

Figure 2.1-7: Illustration of the basement membrane (Laminin, Collagen, and Proteoglycans) and interstitial matrix (Elastin, Collagen, and Proteoglycans) proteins of extracellular matrix between epithelium and endothelium. Figure adapted with permission from [40].

2.2 Mechanotransduction

Mechanotransduction is the phenomenon that describes the biophysical or mechanical stimulation of cells via intracellular or biochemical signaling in healthy microenvironments *in vivo*[42,43]. The combinations of stimuli and, in particular, physical factors such as mechanical forces, substrate stiffness, the topography of the adhesion surface, and fluid flow play essential roles in guiding cell differentiation and proliferation [42,44].

Various mechanical stimuli have a crucial impact on developing the intestinal epithelium model since epithelial cells have the ability to sense biochemical and biomechanical cues coming from their microenvironments such as flow, 3D architectures (villi or crypt topography), and motility (stretching, cyclic peristaltic distension, and contraction) (Figure 2.2-1) [42].

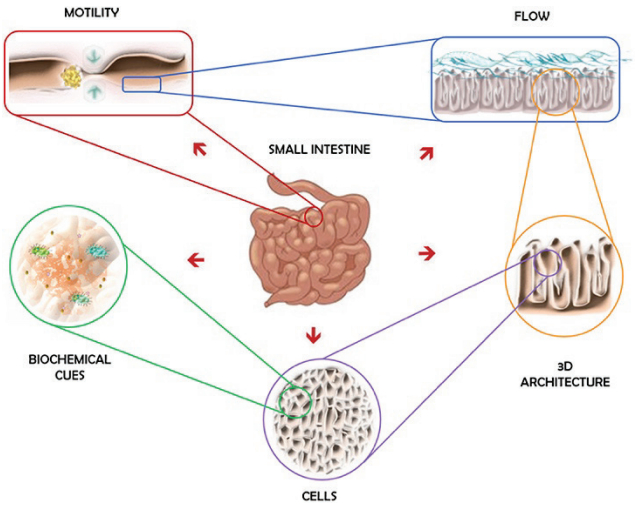

Figure 2.2-1: Key elements of the intestinal microenvironment. Figure adapted with permission from 42.

Likewise, various mechanical stimuli also play essential roles in the interactions of endothelial cells (ECs) (Figure 2.2-2) with their microenvironments[45]. These mechanical stimuli on ECs consist of various biophysical cues categorized as contact and fluid-derived stresses. The contact stresses affect the basal surface of ECs passively due to substrate topography, curvature, and stiffness. On the other hand, fluid-derived stresses, such as compressive and transmural pressure and the circumferential/axial tensile stresses, are mainly caused by blood flow that causes active shear stress on the apical surface of ECs due to blood viscosity. These stresses occur in different dynamic and time scales depending on the location of the vasculature and across organs [39,45,46].

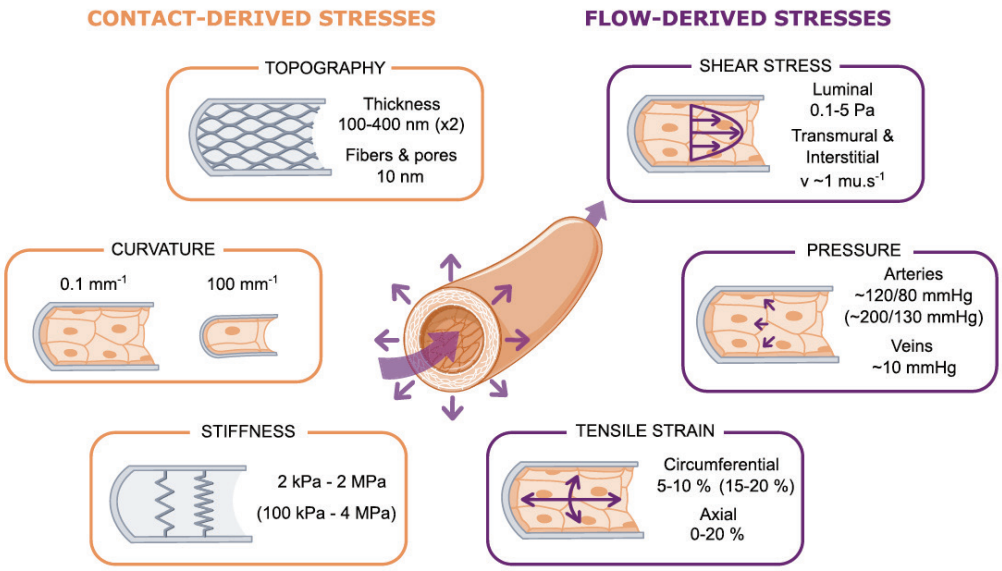

Figure 2.2-2: Illustration of different biomechanical cues experienced by Endothelial cells (ECs) within blood vessels from the substrate (orange, left panels) or from the blood flow (purple, right panels). Physiological (or pathological in parentheses) values are given per type of biomechanical cue. Figure adapted with permission from [47].

2.2.1 Stiffness of cell growth matrices

Cells respond to the stiffness of their extracellular microenvironment by changing their morphologies, motilities, and even their proliferation or differentiation states[48–53]. When the cell growth matrices are stiff, most cells (e.g., tumorigenic cells) increase their spreading and stiffness, decreasing their volume and proliferating more. On the other hand, some cells (e.g., stem cells) respond to the stiff growth matrices oppositely due to their ligand-specific response through their dependence on adhesion receptors and actin-binding proteins. Since their response is ligand-specific, they differentiate best on the growth matrices with closer stiffness to the target tissue[48]. Therefore, stiffness is one of the essential parameters when choosing the correct cell growth matrices to design tissue-engineered in vitro models.

A rheometer is an instrument to measure rheological properties such as viscosity or shear moduli of a material. It has two separated plates where the liquid material is filled to

apply shear stress by rotating the plates until the sample deforms. The first law of thermodynamics suggests that an increase in the applied shear stress into the Newtonian liquid sample (e.g., water) will cause an increase in the temperature. Thus, the liquid sample gets deformed easier. On the other hand, if the material obtains minimal deformation with a substantial temperature increase, the material is called "gel-like" liquid, non-Newtonian fluids (e.g., Gelatin, Collagen, Matrigel). Based on these definitions, hydrogel-made cell growth matrices are characterized to evaluate physical features such as stiffness and topography of the ECM-like substrates that affect cells through integrin-based adhesion complexes[54]. The "stiffness" indicates if the material is "soft" or "hard" in other words, "bent" or "stretched" by the ratio of an applied force to the elongation in the direction of the force (SI units of N/m) depending on the material's dimensions and described as Young's modulus (or Elastic Modulus) that is the bulk deformability of an elastic material as the ratio of stress to strain (SI units of Pa)[55].

2.2.2 ECM-mimetic hydrogel membranes

Numerous natural, synthetic, and hybrid hydrogels such as Poly (ethylene glycol) (PEG)[56], silk[57], Matrigel[58], decellularized tissues[59], and gelatin[55,60–63], provide efficient cell growth matrices with high-water absorption capacity[64] due to their permeable and porous structures and often transparency that is important for microscopy. To use a hydrogel as a cell growth matrix, hydrogels are crosslinked by various mechanisms such as chemical[65], anionic[66], self-assembly[67], and enzymatic[68]. They are fabricated by multiple techniques such as molding[69,70], 3D bioprinting[71,72], or film/ membrane formation[55,60].

2.2.2.1 Gelatin

Gelatin is a natural protein obtained by hydrolytic degradation of collagen, the most common extracellular matrix (ECM) protein in the body[73,74]. It is a polymer obtained from different sources such as pig skin, fish skin, bovine hide, cattle bones, and,

more interestingly, human skin[75]. It has leading amino acid chains of glycine-X-Y sequences, where X usually proline and Y hydroxyproline in different amounts depending on the source of species[76]. In particular, gelatin contains arginine-glycine-aspartic acid (RGD) peptide sequences, essential for cell adhesion, proliferation, and differentiation[76,77] (Figure 2.2-3). Together with the amino acid composition, the molecular weight distribution has a necessary impact on the physical, structural, and mechanical properties of gelatin —low-molecular-weight fragments of gelatin cause weaker and more deformable biomaterials[76].

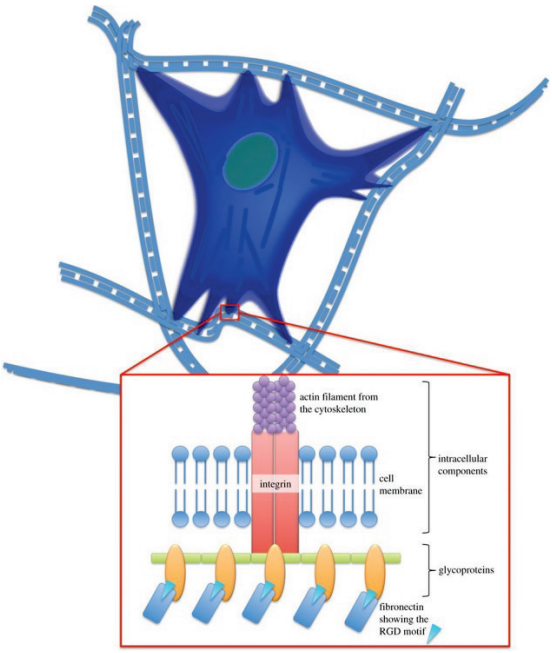

Figure 2.2-3: Illustration of cell-ECM interactions between the RGD motif of the cell adhesive fibrillar matrix and integrin-mediated actin cytoskeleton of cells. Figure adapted with permission from [77].

Gelatins display several advantages as a biomaterial, such as complete reabsorb ability in vivo and crosslinking capacity. They are named by the pre-treatment conditions based on alkaline (pH 12-13) or acidic (pH 1-2) extraction, as Gelatin type-A (the isoelectric point (IP) ≈ 5) obtained at acidic conditions; Gelatin type-B (IP ≈ 9) at alkaline conditions. Gelatin type-B has a lower viscosity and enhanced biocompatibility due to its negative charge under physiological pH compared to gelatin type-A[74,76].

Gelatin is a non-Newtonian, viscoelastic fluid that is liquid at above 37 ºC, whereas it crosslinks reversibly as transparent gels at below this temperature[78,79]. Therefore, it must be crosslinked with an irreversible technique to be used as a cell growth matrix. Microbial transglutaminase (mTG) was used to form a thermally stable hydrogel from gelatin by catalyzing the covalent bond formation between lysine and glutamine[80]. This enzyme is commonly used in food manufacturing processes approved for human consumption by the U.S. Food and Drug Administration[81]. The high activity level of mTG over a wide range of temperatures (~50% at 37 °C, max. at 50 °C) and pH values (~90% between 5 and 8) make the enzyme amenable to a wide variety of gel formation. Yung et al. proposed a dual crosslinking scheme of more resistant hydrogel formation against proteolysis[82] (Figure 2.2-4). The double crosslinking method consists of thermal cooling before the mTG crosslinking. Thermal cooling stimulates the self-organization of gelatin into a tight network of polypeptides through hydrogen bonding. Thus, more potential junction points occur to create a denser hydrogel.

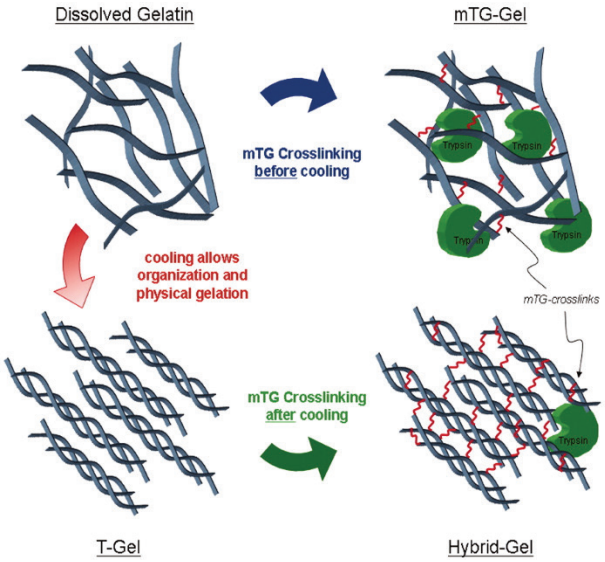

Figure 2.2-4: Scheme of hydrogel formation single and dual crosslinking method: Hybrid-Gels indicate gels made by dual crosslinking; thermal cooling before the mTG crosslinking, whereas T-Gel indicates gels made by single crosslinking method, only mTG crosslinking. Figure adapted with permission from [82].

2.2.3 Fluid flow-induced shear stress

Fluid flow-induced shear stress is one of the most studied forces on endothelial and epithelial tissue models. It has been reported that shear stress, caused by peristalsis and interstitial fluid movement in the gastrointestinal tract system, results in biochemical responses on intestinal tissues such as mucus secretion and villi formation[18,20,32]. On the other hand, blood flow causes fluid shear stress, in other words, the tangential frictional force per unit area on the endothelium. Since the blood is a complex non-Newtonian fluid, it exhibits shear-thinning behavior at sufficiently low shear rates (below ~100 s^{-1}) [46]. Therefore, non-Newtonian blood strongly affects endothelial cells (ECs), which can sense minor variations in the direction, magnitude, and regularity of blood flow-induced shear stress and respond to the mechanical stimuli by adaptations and modifications in their number, morphology, and orientation[83]. As reported by many researchers, ECs respond to physiological shear stress (arteries: 10-20 dyn/cm^2; arterial branches: 30-100 dyn/cm^2; veins: 1-6 dyn/cm^2) phenotypically by cytoskeletal elongation, junctional relocation, and cellular orientation parallel to the flow direction and functionally by inducing their mechanotransduction and maturation[46,84–86].

Depending on the flow regime, shear stress regulates essential functions of ECs, such as angiogenesis and vessel remodeling (Figure 2.2-5). Undisturbed flow zones (Reynolds number (Re)<2000) create laminar shear stress that affects the elongation of ECs and alignment of their actin filaments in the direction of blood flow both in vivo[87] and in vitro conditions.

In contrast, disturbed flow zones (Re>2000) cause more cuboidal (round), therefore, shortened actin filaments and randomly oriented cells[46]. Functionally, it is reported that steady unidirectional flow promotes an anti-inflammatory and antithrombotic phenotype of

ECs with reduced cell apoptosis and proliferation46. In contrast, the pulsatile or oscillatory disturbed flow has an adverse effect by increased inflammatory response[84]. On the other hand, flow direction plays a vital role in specific EC functions. For example, luminal flow creates shear stress on the apical surface of ECs. In contrast, transmural flow-based shear stress is exerted on the cell-cell junctions by increasing filopodial protrusions and vascular sprouting. Interstitial flow originated from the transmural flow stem from the porous substrate, simulating a 3D network formation, tubular alignment in the flow direction, and elongated endothelial sprouting against the flow direction[46].

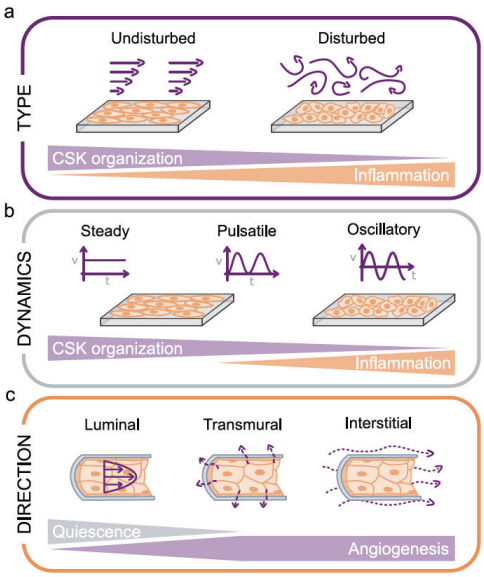

Figure 2.2-5: Illustration of flow-induced shear stress generated by flow in different types, dynamics, and directions experienced by endothelial cells (ECs). a) Cytoskeletal (CSK) organization and the inflammatory effects of undisturbed or disturbed flow. b) CSK organization and the inflammatory effects of steady, pulsatile, or oscillatory flow. c) Quiescence and/or angiogenesis effects of flow in the luminal direction (parallel to cells, on the apical side), transmural (across the endothelium, on cell-cell junctions), or interstitial (in the vessel wall or parenchymal tissue, on the basal side). Figure adapted with permission from [47].

2.3 Devices for Dynamic Epithelial and Endothelial Tissue Engineering

Different dynamic shear stress platforms have been shown to study biomechanical induction of tissues, such as the cone and plate and parallel plate flow chamber

systems[88–91], rotating vessels[92], an oscillating orbital shaker[19,93–95], and rocking "see-saw" platforms[4,7,96–102]. Recent advances in microphysiological systems (MPS) (Figure 2.3-1) provide a variety of setups such as individual, single tissue, or multiple connected MPSs[103]. Since these devices are modular, they can be integrated with various cell/tissue types, ECM-mimetic biomaterials, membranes, and physiological cues such as shear stress, pH, and signaling factors[103]. In particular, microfluidic and "on-chip" technologies incorporate dynamic flow shear stress, precise flow control, and continuously refreshed culture medium[104–109]. However, these devices are more abundantly associated with using multiple pumps/tubing and connections, making them labor-intensive and prone to errors such as bubble formation, clogging, and fluid leakage[110–112]. Therefore, numerous passive microfluidic pumping or pumpless fluidic platforms[4–7] have been studied to overcome these challenges. These platforms are based on various mechanisms such as evaporation, gravity, surface tension, osmosis, capillary flow, and thermo-viscous expansion[4,113–117]. In particular, the gravity-induced flow has been more widely explored due to its ease and/or inexpensiveness on multi-well plates[96,98,118–120] and/or microfluidic devices to model tissues such as bone[88,121], skin[100], blood-brain-barrier (BBB)[122], intestine[99,123].

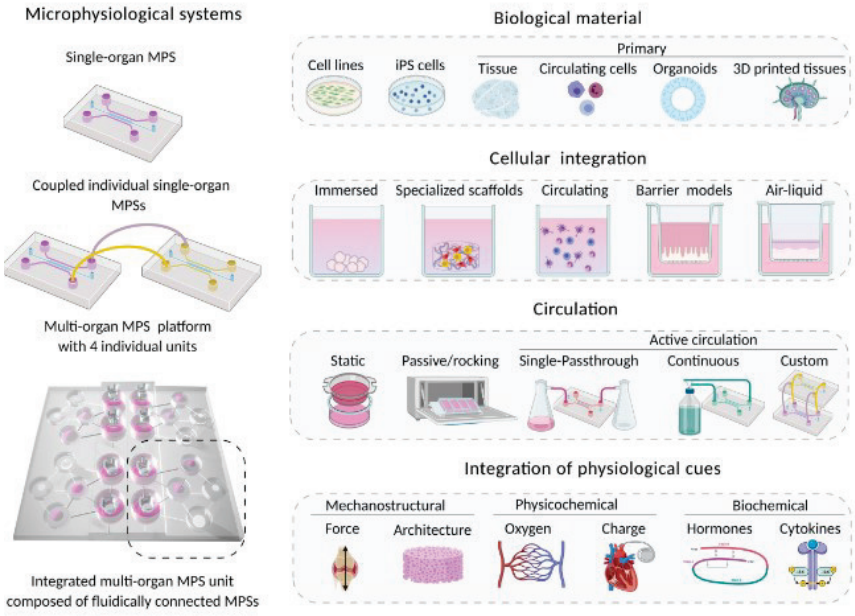

Figure 2.3-1: Microphysiological systems (MSPs) and their integral components [103].

However, while these gravity-driven alternative microfluidic-based platforms[101,102,124–127] could be used for high-throughput applications, they cannot be accessed by many research laboratories due to their expensiveness. Moreover, their fabrications require intensive expertise and advanced technical infrastructure. Therefore, most in vitro barrier tissue models such as the intestinal wall, the skin, vasculature, and the blood-brain barrier[103,128] still rely on scalable cell culture inserts commercially called Transwell inserts, developed by Dr. Stephen Boyden in the 1960s[129]. These inserts are standardized with synthetic, permeable membranes such as Polyethylene (PE), Polyester (PET), polycarbonate (PC), and polytetrafluoroethylene (PTFE) that cells are grown on and allow free access to both apical and basolateral compartments for loading and ejecting the medium. However, even though Transwell inserts provide robustness and simplicity, they do not provide complex and dynamic tissue microenvironments as in vivo. Synthetic membrane materials have many advantages, such as reproducible fabrication due to relatively controlled manufacturing conditions. They can be selected by defining

pore size, density, or hydrophilicity/hydrophobicity properties[130]. However, plastic membranes with high stiffnesses (e.g., PE membrane: ~180 MPa[131]) are not representative of the native extracellular matrix (ECM), and its physiological stiffness (e.g., endothelial cells: 5-20 kPa[47]; intestinal epithelial cells: 1-40 kPa[42,50,132]), which is known as critical in inducing essential metabolic functions of cells and determining the differentiation fate of cells[133–136]. Moreover, except for some examples[105,106,137,138] integrated with perfusion systems, Transwell inserts often either are complex to work/ fabricate or lack combination fluidic with ECM-mimetic cell culture substrates interconnect tissues on hanging inserts to achieve functionality, complexity, and throughput. Therefore, there is a tremendous need to develop alternative platforms based on cell culture inserts integrated with ECM-mimetic biomaterials and perfusion systems to improve the functionalities of in vitro models.

2.3.1 Fabrication of cell culture devices

Choosing necessary tools and methods is always a trade-off for designers and engineers due to the need to balance quality and time[139]. Since each device and method have its strengths and weaknesses during the product development process, it has been shown that there is a spectrum from high fidelity/slow fabrication/low flexibility to low fidelity/rapid fabrication/high flexibility (Figure 2.3-2). Therefore, prototyping is the most critical stage within the product development process with four distinct purposes Learning (Proof-of-Concept), Communication (Proof-of-Product), Integration (Proof-of-Process), and Milestones (Proof-of-Production)[140]. In research laboratories, researchers mainly focus on “Proof-of-Concept” prototyping, whereas each distinct prototyping is used in the industrial setting during the product development process (Figure 2.3-2).

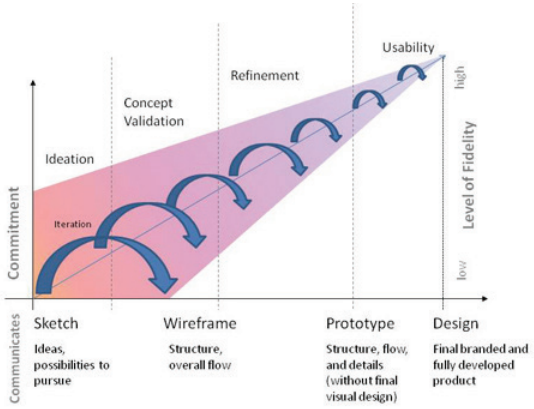

Figure 2.3-2: Product development process. [141]

3D printing provides rapid prototyping for limited-size devices whereas low-volume production. Therefore, 3D printing is often used as a cost-effective alternative in experimenting with innovative designs during prototyping to reduce development time and lower tooling costs. FDM (Fused Deposition Modeling) 3D printing is a layer-by-layer additive manufacturing technique widely used to create insert prototypes using solid thermoplastic materials[142–145]. However, it has drawbacks such as low resolution and low adherence between printed layers; therefore, it lacks reproducibility of insert prototypes[146]. Since it offers better resolution, less time-consuming post-processing, and higher volume production, PolyJet 3D printing is a growing interest in producing cell culture devices [147,148]. However, even though they can be an advantageous alternative, this advanced technology requires more labor for its maintenance, and it became unnecessarily costly for proof-of-concept prototyping [149]. Therefore, due to its high-resolution feature[150], user-friendliness, and affordability, stereolithography (SLA)-based 3D printing is well suited for prototyping cell culture devices, particularly cell culture inserts. In SLA printers, biocompatible class IIa, a photo-curable resin such as Dental LT and Biomed Clear[151] from Formlabs crosslinked by light; thus, the printed devices are suitable for cell culture applications[128,150,152,153]. The light source or screen layer-by-layer projects sliced

computer-aided design (CAD) models with a spatially controlled photo-curable resin polymerization with a specific depth and the layer thickness set by the incremental upwards movement (Figure 2.3-3)[154].

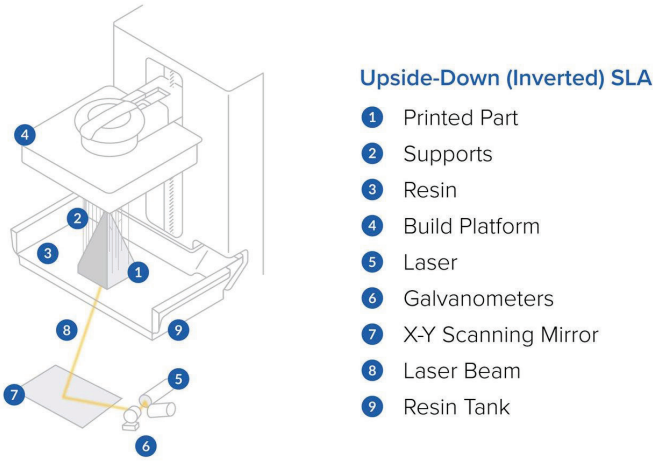

Figure 2.3-3: A graphical representation of the basic mechanics of inverted stereolithography (SLA) printer.[155]

"Science may be described as the art of systematic oversimplification."

-Karl Popper

Chapter 3

SUMMARY OF RESULTS

This chapter presents a summary of results and key contributions based on three scientific papers (**Paper I: Chapter 5, Paper II: Chapter 6, Paper III: Chapter 7**) and posters (**Chapter 8**). In the presented works, 3D SLA printing was used as a convenient and relatively easy fabrication platform that many research laboratories could access. In light of the "**customization of cell culture devices for the biological application of interest"** scope of the PhD thesis, several 3D-printed custom insert prototypes (Figure 3.1-1) were designed, fabricated, and validated for different cell culture applications as proofs of concept. Since the fabrication method is known as a rapid prototyping technique with a higher margin of error in precision, the usability of fabricated inserts was questioned.

3.1 Designs of Cell Culture Devices

Together with design considerations, different applications were applied for biological validation as proof of concepts. Presented devices were categorized as below:

- **Co-culture applications:** STACKs (Paper I), Close-Contact (CC-inserts) (Poster II), and Orbital-insert (O-insert) (Paper III and Poster IV) approaches.
- **High-throughput screening (HTS) applications:** Scalable well plate formats (Paper I and Poster I); e.g., 96-well and 48-well stackable inserts (Paper I)
- **Dynamic Operational Mode:** Rocker-insert (R-insert) (Paper II), Orbital-insert (O-insert)(Paper III), Perfusion device for scaffold-free spheroid culture (Poster III)
- **Customized membranes/bottoms:** Synthetic (PET, PTFE, and PDMS) & Gelatin hydrogel

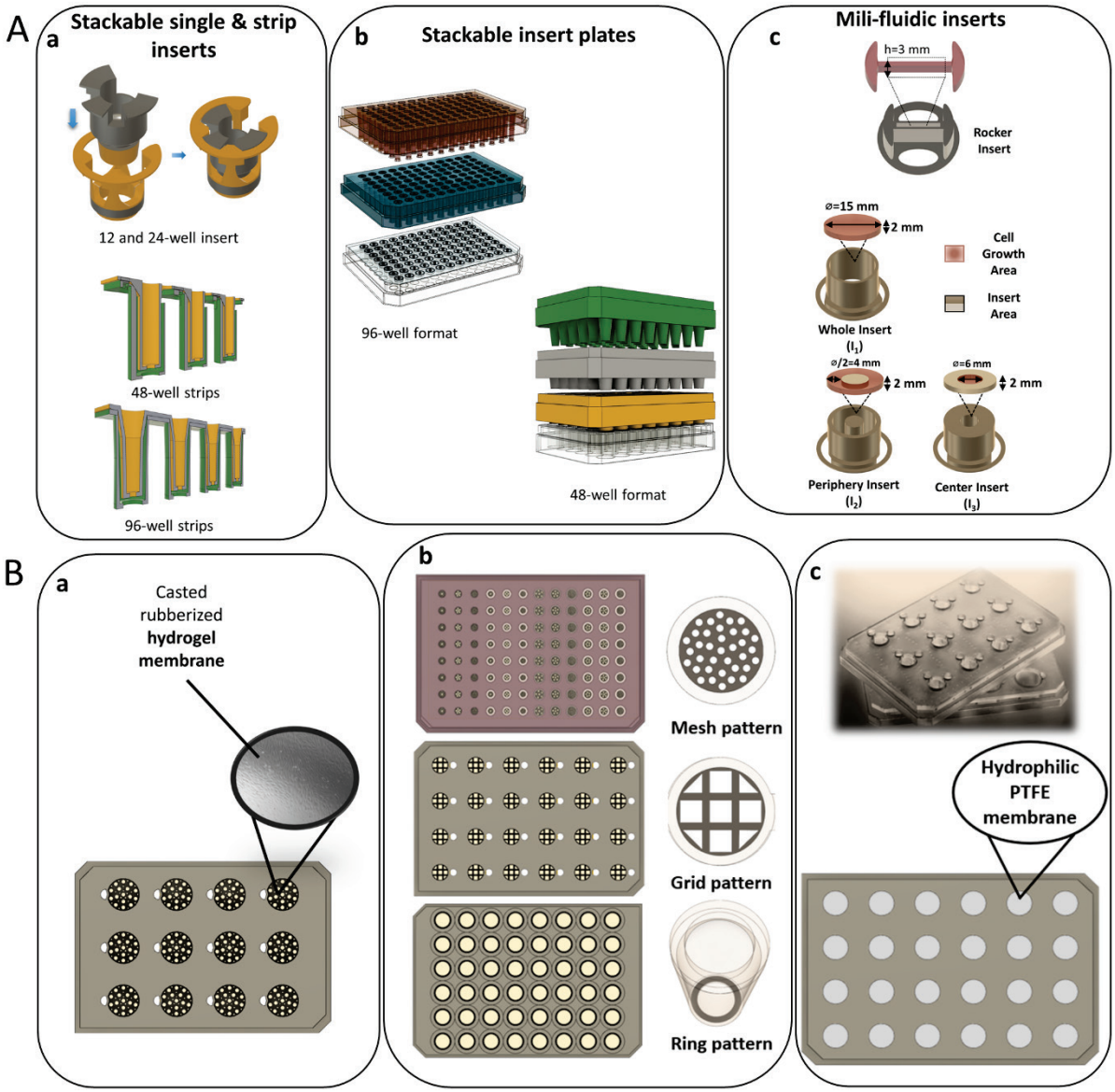

Figure 3.1-1: Representative 3D CAD insert design library. **A: a)** Stackable singlets and strips; close-contact inserts (upper panel), 48- and 96-well plates format strip inserts (lower panel). **b)** Stackable HTS inserts in 48- and 96-well plate formats. **c)** Fluidic inserts; rocker actuated inserts (R-insert), orbital shaker actuated inserts (O-inserts) **B: a)** Gelatin membrane functionalized well plate insert bottoms. HUVECs are seeded on 15% (w/v) Gelatin membrane. **b)** Rectangular mesh/grid patterns on the bottom of insert plates with 96-, 48-, 24-, and 12- well plate formats **c)** hydrophilic PTFE membrane pinned 24-well insert plate. Adapted from Paper I, II and III, Poster II.

3.1.1 Membrane pinning techniques for functionalization of inserts

Apart from insert design and fabrication considerations, the functionalization of insert/device bottoms with synthetic and natural biomaterials was also evaluated. For barrier tissue applications, materials that can be potential porous membranes were the primary criteria. Therefore, different membrane pinning techniques were introduced and performed based on the membrane materials that could also be customized depending on the application, as listed below.

- **Dip-casting (Paper I-II-III and Poster IV):** In this study, since the first aim was to microscale stackable inserts, the tool-free dip-casting technique was developed and validated with better applicability. First, external conditions such as temperature and crosslinking methods were controlled. Then, gelatin content was modified by increasing concentration within the physiological stiffness conditions for barrier tissues to have better consistency during the dip-casting process. Second, hydrogel membrane features were characterized. And finally, relatively consistent, thin (approximately 500 µm) gelatin membranes (Chapter 5: Paper I) were successfully pinned to the insert bottom with a ring-shaped aperture. Later, the optimized dip-casting technique was implemented for the following projects performed in dynamic operational mode by achieving the creation of 50-150 µm thick gelatin membranes that will be discussed in detail below (Chapter 6: Paper II and Chapter 7: Paper III).

- **Gluing (Paper I and Poster I):** This method was introduced to assemble rigid, microporous, hydrophilic PTFE membranes (MilliporeSigma, Merck KGaA, Darmstadt, DE) to the 3D-printed insert bottoms by gluing with the insert printing resin (Dental LT, Formlabs, USA)(Paper I).

- **Ring-pinning (Poster II):** Since gluing was not possible with PET membrane (ipCELLCULTURE membranes, it4ip SA, BE), a “ring” apparatus was designed by getting inspiration from a commercialized insert design called “CellCrown” (Scaffdex, Tampere, FI) to assemble the membrane to the insert bottom.

3.2 Paper I (Chapter 5)

In this study, a CAD design library of inserts was introduced to emphasize the scalability and modularity of cell culture devices from applications to fabrication methodologies. Design considerations were discussed based on dimensional boundary conditions of conventional plastic well plates. More specifically, 1) the wall thicknesses, 2) the wall-to-wall distance, and 3) the number of stack layers was discussed in the respective well format to provide a guideline to scale the stackable insert fabricated with Dental LT (Formlabs, USA) SLA printing resin. The well-plate format inserts were introduced for high-throughput, and strip- and singlet-type inserts were presented in different scales (12- to 96-well formats) for convenience of lower-throughput research applications. Stackable inserts in the 48-well format were defined as a minimum scale for potential automatization and high-throughput screening (HTS) applications.

Experiments for biological validations were performed to investigate 1) biocompatibility/ applicability of inserts and membrane materials on mouse intestinal organoid cultures and 2) intestinal barrier function with model cell line, Caco-2. A preliminary study with mouse intestinal organoids was conducted to evaluate the biocompatibility of inserts printed with Dental LT resin and pinned with different membrane materials. As the control condition, a generic dome culture protocol was used on the well plate. Filter (PTFE) and gelatin membrane pinned inserts were used as holders for domes to have 3D access to medium transport. On the 1st day, the organoids on PTFE and gelatin membranes

had larger surface areas with very few tiny clusters. In comparison, culture in wells displayed organoids with smaller surface areas and many small clusters (Figure 3.1-2). Taken together, the results suggested that Dental LT resin is biocompatible with complex processes like organoid formation.

In the second application, Caco-2 cells were successfully cultured on 10%, 15%, and 20% gelatin membrane pinned inserts in 96-well format for three weeks to create intestinal barrier models. Barrier functions were assessed by Lucifer Yellow transport assay by monitoring permeability rates of cells for 3 weeks.

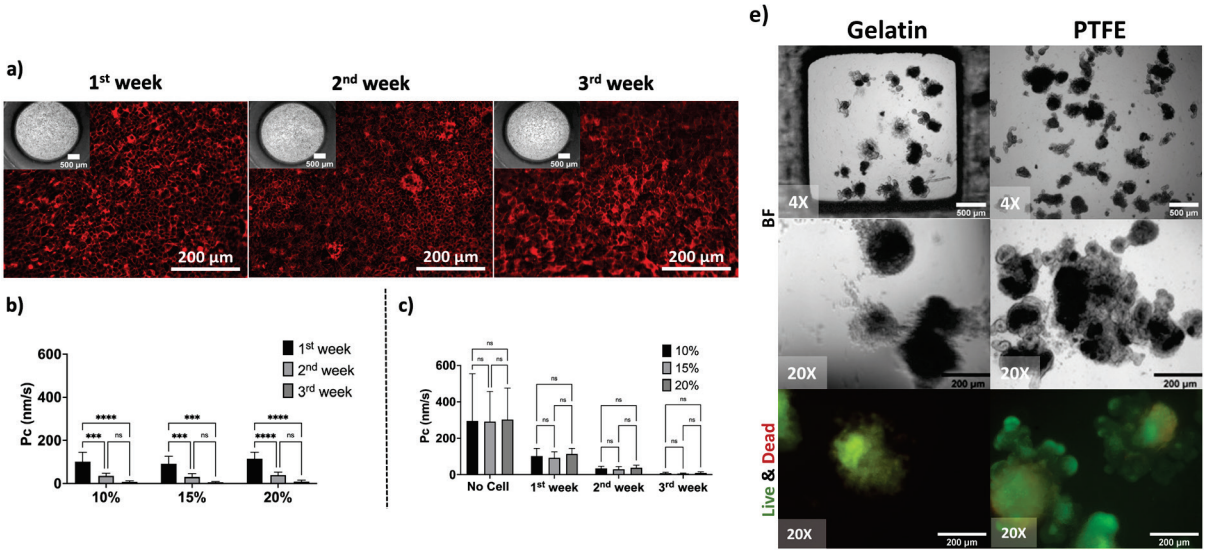

Figure 3.2-1: Biological validation of 3D-printed inserts. **a)** Growth of Caco-2 cells on the 15% (w/v) gelatin membrane pinned 3D-printed 96-well inserts over three weeks. Insert apertures at the bottom are shown in the upper panels of fluorescence images (the magnification: 4x; scale bars: 500 µm), and the F-actin (red) stain of the cells on the hydrogel membranes (scale bars: 200 µm; the magnification: 20x). **b)** Permeability coefficient (mean + SD) of lucifer yellow across Caco-2 cells on the 10%, 15%, 20% (w/v) gelatin membrane pinned inserts ($n \geq 3$), and **c)** comparison of Pc values of empty hydrogel and 10%, 15%, 20% membrane pinned inserts ($n \geq 5$). Error bars indicate mean S.D. statistical significance: ns = $P > 0.05$, ***$P < 0.001$, ****$P < 0.0001$. **e)** Representative light and fluorescence microscopy images of mouse intestinal organoids in Matrigel dome on hydrophilic PTFE and Gelatin membranes. Images ($n = 3$) were taken during their culture for 7 days in the insert plate wells with a light microscope (scalebar: 500 µm for 4x magnification; scalebar: 200 µm for the 20x magnification). Adapted from Paper I and Poster I.

Up until now, presented inserts were fabricated with Dental LT resin. However, for the rest of the studies, Biomed Clear resin was used as a primary printing material due to its potential for better precision in printing, autoclavability, and convenient transportation of inserts to our international collaborators. However, the fabrication setup was not changed to provide a similar workflow during the fabrication and post-processing of inserts. Regarding biological applications, no adverse results have been observed regarding biocompatibility with used cell lines or operational processes during experiments. Therefore, both materials are still suggested to fabricate insert prototypes for specific applications covered in this thesis.

3.2.1 3D-printed Bioengineered Platform for Co-culturing Caco-2/Immune Cells to Study SARS-CoV-2 Infection

The first example of the insert design oriented using Biomed Clear resin was meant for a co-culture application to study the coronavirus-2 (SARS-CoV-2) (Chapter 8 - Poster II). After the SARS-CoV-2 pandemic (COVID-19), many scientists tried to understand and find how to tackle this unfortunate situation we experience all over the world. In most reports, SARS-CoV-2 was mainly characterized by an infection of the airways and the lung. However, Lamers et al. (2020)[156] showed that SARS-CoV-2 also infected intestinal organoids. Moreover, Lehman et al. (2021)[157] recently reported that immune cells ($CD8^+$ T cells) were activated after the post-infection of intestinal epithelial cells. In light of this information, we initiated a collaborative project with our colleagues (Prof. Krzysztof Pyrć and Emilia Barreto Duran) from Virogenetics Laboratory, Jagiellonian University, Krakow, Poland, to investigate the intestinal barrier and immune cells crosstalk in the presence of SARS-CoV-2 in a novel in vitro model that could be an alternative platform to study the biology of coronaviruses and effects of antivirals in the future.

In this regard, the close-contact insert (CC-insert) was designed, and the co-culture protocol was developed to further evaluate the crosstalk phenomenon where macrophage migration through intestinal barrier tissue was expected upon SARS-CoV-2 infection. For efficient cell migration, the stacking approach and ring-type insert bottom were implemented to fix tissue layers and prevent any tissue damage and interruption in the crosstalk process during the maintenance of co-culture (Fig 3.2-2). The soft, gel-like 3D network with 3% (w/v) Gelatin was used as a macrophage carrier from the bottom to the upper insert layer. Moreover, the height between insert layers was designed as “0” to minimize the distance that might happen due to the printing dimension tolerance. As mentioned earlier, the ring-pinning approach was implemented for the close-contact insert design due to the need for using a custom-made commercialized polyester (PET) membrane (8 µm; ipCELLCULTURE™ Track-etched, It4ip, BE) that was chosen to be more suitable for the cell migration application and immunostaining sample preparations. Moreover, it was also convenient for autoclavability, accessible storage, and transportation to our collaborator’s laboratory in Poland to perform experiments on the crosstalk between intestinal barrier tissue and macrophage network after viral infections.

The preliminary results showed that SARS-CoV-2 infected intestinal barrier tissue apically, and macrophages were activated after 48h post-infection by the virus. Thus, they migrated through intestinal barrier tissue and were infected by viruses similar to intestinal barrier monolayers (Fig 3.2-2-B). The developed model was successfully implemented to create a suitable microenvironment for co-culturing intestinal barrier tissue and macrophages to study viral infections. Further application experiments of the developed co-culture protocol are ongoing by my colleague, Emilia Barreto Durán.

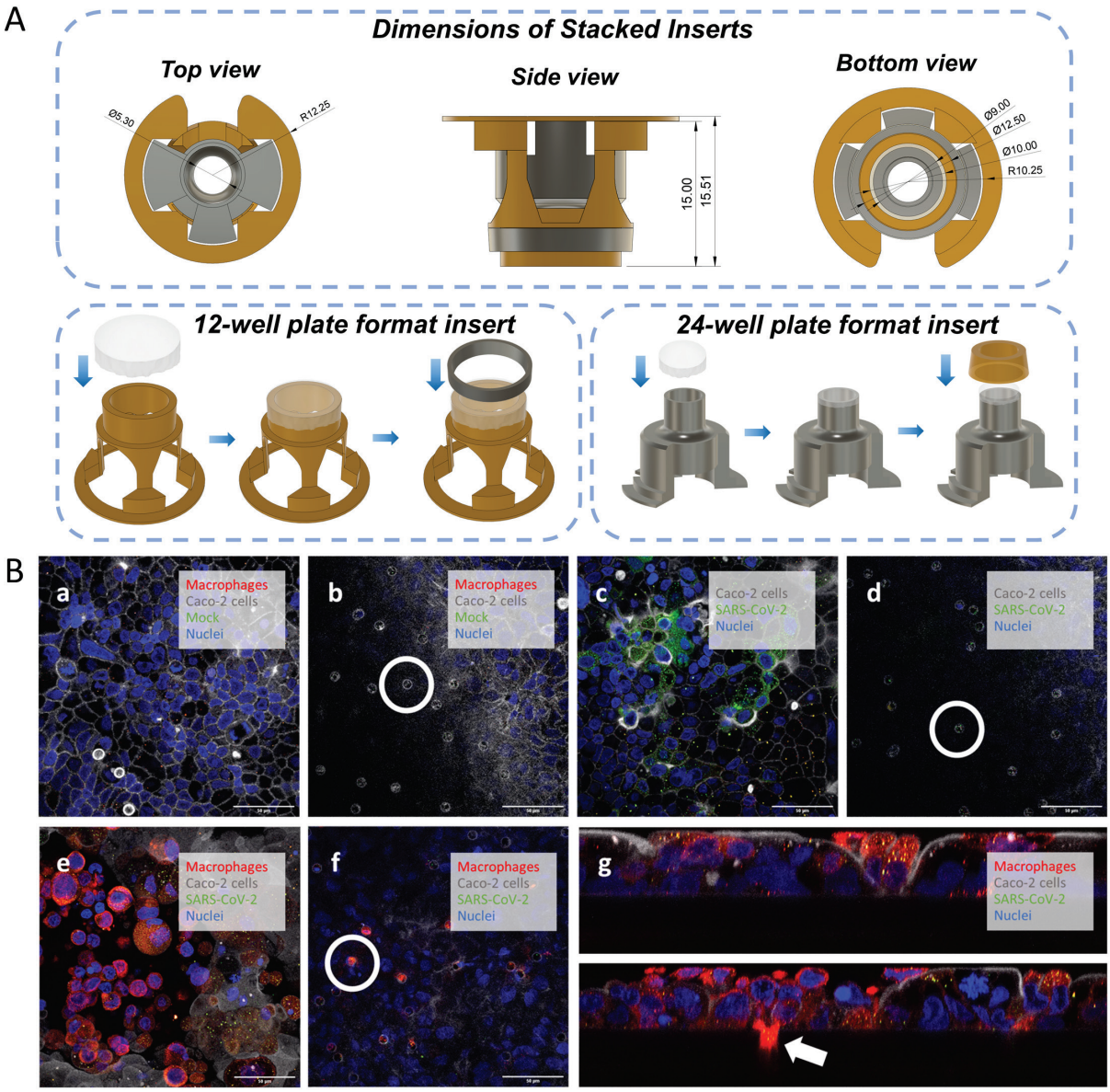

Figure 3.2-2: (A) Design and fabrication overview of stackable close contact inserts. **(B)** Representative immunostaining images of 3D stacked co-culture platform. Micrographs demonstrating the apical **(a, c, e)** and basolateral **(b, d, f)** compartments of co-cultured the intestinal epithelium on porous PET membrane and activated macrophages after SARS-CoV-2 post-infection. **g-top and bottom panels** visualize a co-culture cross-section. **White:** F-actin (phalloidin)-stained intestinal apical border, **Red:** CD68-stained macrophages, **Green:** SARS-CoV-2 nucleocapsid proteins, and **Blue:** DAPI-stained nuclei (scale bars, 50 µm). **White circles:** 8 µm PET membrane pores, and **White arrow:** a migrated macrophage to the infected intestinal tissue through the membrane pore. Adapted from Poster II.

Apart from the static culture inserts, dynamic insert designs were also introduced both in bidirectional (by rocker) and unidirectional (by orbital shaker) flow operations to provide more complexity to in vitro intestinal and endothelial barrier tissues as still keeping throughput functionality for potential HTS applications.

3.3 Paper II (Chapter 6)

In Paper II, the customized and modular Rocker-inserts (R-inserts) were introduced as an open-top, rectangular chamber (Figure 3.3-1-A). The gelatin membranes were cast at the channel bottom, as mentioned above. A 2D see-saw rocking rocker is used to actuate oscillatory flow by periodic recirculation of the cell growth medium by tilting the R-insert. Caco-2 cells were used as a model for intestinal cell lines to evaluate the effects of bidirectional flow perfusion on intestinal morphogenesis (Figure 3.3-1B-C). Channel dimensions and the medium height were defined based on physiological shear stress in the intestine to be in a range of 0.02-5 dyn/cm^2 [107,158,159] at 7-degree tilting angle (Figure 3.3-1). Later, membrane thickness analysis and microparticle image velocity (μPIV) measurements were performed (Figure 3.3-1D) to verify theoretical calculations (Paper II). Both results showed that the flow regime is laminar and provided physiological shear stress of the intestine as in 1-1.3 dyn/cm^2.

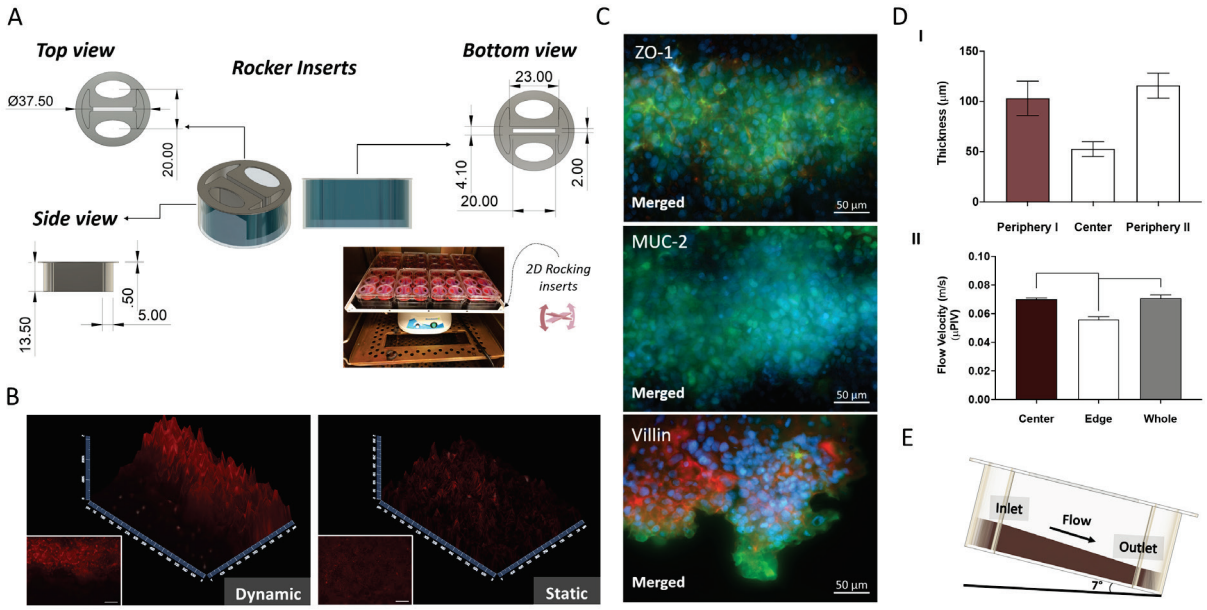

Figure 3.3-1: **(A)** Design dimension overview of rocker actuated 3D-printed insert (R-insert) **(B)** Representative 2.5D F-actin fluorescence intensity plot of Caco-2 cells under static and dynamic conditions. **(C)** Representative immunostaining images of 3D cellular structures under dynamic condition. **Green:** ZO-1, MUC-2, Villin; **Red:** F-actin; **Blue:** Nuclei expression. **(D)** Regional comparison plots of thickness (µm) **(I)** and flow velocity (m/s) **(II)** at 7-degree tilting angle. **(E)** Representative image of the R-insert at 7-degree tilting angle. Adapted from Paper II.

To investigate the intestinal barrier function of Caco-2 cells, TEER measurements were performed in different initial cell densities (50-100k/cm2). Interestingly, the highest density condition (100k/cm2) showed heterogenous morphology with both 2D cell monolayers and 3D cellular structures under dynamic flow conditions but not static conditions. Therefore, intestinal barrier function and other functional properties such as villi formation and differentiation to mucus-secreting cells of these 3D structures were further investigated. The results show the increase in the barrier function by flow confirmed with increased TEER values, tight junction marker (ZO-1) expressions, and decreased molecular (0.44 kDa lucifer yellow (LY)) transport. Furthermore, 3D cellular structures showed higher expression of MUC-2, F-actin, and Villin than 2D cell monolayers both under static and dynamic conditions. Each immunostaining image was analyzed to define

the flow (Figure 3.3-1-B-C). Taken together, the R-insert with 75-150 µm thin hydrogel membranes (Figure 3.3-1-D) provided a simplistic approach and accessible platform for any research laboratory to investigate the effects of both flow and initial cell seeding density on the 3D morphogenesis of Caco-2 cells.

3.3.1 Rocker-actuated perfusion device for intestinal spheroid culture

For another alternative application (Chapter VIII - Poster III), R-insert was modified to be a rocker-actuated perfusion device for intestinal spheroid cultures as a part of an internal collaboration with my colleagues from the FAST group. Instead of hydrogel membrane casting, we functionalized the bottom of R-insert with microwells (Figure 3.3-2). Microwell bottom was made with non-adhesive PDMS (Polydimethylsiloxane), silicone-based organic polymer fabricated using a 3D-printed mold successfully (Figure 3.3-2-top panel). Microwells were designed to be modular in size and composition in different diameters to control and compare spheroid size and circularity during their incubation under dynamic flow conditions by rocking. The tilting angle of the rocker unit was set to be 7 degrees to keep the flow shear stress in the physiological range (1 dyn/cm^2), as mentioned above. The 3D-printed perfusion device enabled a sufficient mass exchange of the growth medium supplemented with ECM molecules based on Matrigel. Adequate medium circulation provided increased viability compared to static conditions; likewise, spheroids' circularity was improved (Figure 3.3-2-right panel). Taken together, the preliminary results were promising to use the novel perfusion device for scaffold-free spheroid culture applications, particularly for Caco-2 spheroids, to investigate further their barrier/ transport functions and potential changes in cell phenotypes.

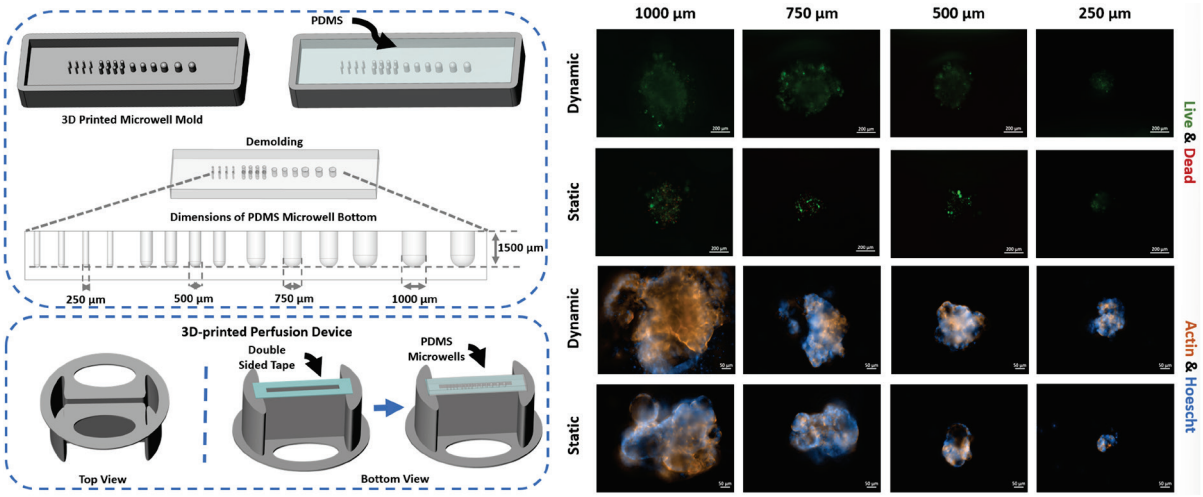

Figure 3.3-2: **Left:** Design and fabrication overview of **(top)** PDMS (Polydimethylsiloxane) demolded hemisphere-type microwells **(bottom)** pinned rocker-actuated 3D-printed perfusion device**. Right:** Representative fluorescence images of Caco-2 spheroids in 250 µm - 1000 µm diameter sized microwells under static (no flow) and dynamic flow conditions. **Top-right panels:** Viability of spheroids by Live & Dead staining. Green: Calcein AM (live cells); Red: Ethidium Homodimer-1 (dead cells). **Bottom right-panels:** F-Actin (cytoskeleton; orange) and Hoechst (nuclei; blue) stained Caco-2 spheroids. Magnifications and scale bars: 10x, 200 µm (Live & Dead); 20x, 50 µm (F-actin & Hoechst). Adapted from Poster III.

3.4 Paper III (Chapter 7)

In Paper III, another dynamic insert was introduced using an orbital shaker to study the effects of unidirectional flow on endothelial cells (ECs) and later their co-culture with intestinal epithelium. The 3D-printed dynamic inserts (O-inserts) were designed to separate compartments with different shear profiles (Figure 3.4-1) and functionalized in the insert bottom apertures with gelatin membrane using the dip-casting technique, as mentioned above, with a minor modification. Due to relatively big apertures and no ring shape support to limit filled gel to the aperture, inserts were slid over the gelatin solution instead of pressing on a surface after dip-casting (Paper III). Three insert bottom zones were defined based on (1) applicability of the dip-casting method for hydrogel membrane pinning, (2) sufficient wall-to-wall medium flow, and (3) separating shear gradient zones as the ‘center’

and ‘periphery’ for defining uniform shear stress areas and possible co-culture applications (Figure 3.4-1-b). The main focus of this study was to actuate the alignment of the endothelial cell by the unidirectional laminar flow-induced shear stress. Therefore, the periphery region was chosen to place ECs. Later, the central area was defined as the intestinal compartment for co-culture. Two orbital shakers with different orbit diameters were used to generate high (HS) and low (LS) shear stress with operatable speeds (Ø=10 mm at 160 rpm and Ø=2 mm at 250 rpm) to culture intestinal epithelial and endothelial cells since both cells have different physiological shear needs. The flow regime was calculated as laminar ($96 \leq Re \leq 600$), and the defined stresses were HS: 20.7 dyn/cm^2 (CI-huVECs) and LS: 0.3 dyn/cm^2 (Caco-2 cells). ECs alignment was observed after 48h HS exposure, and alignment orientation was characterized by vector analysis based on actin fiber orientations compared to the flow direction. The periphery region showed the most uniform alignment, whereas the central part showed spontaneous orientation and cobblestone morphologies of ECs (Paper III – Poster IV). Next, the effects of physiological shear stress on barrier integrities of ECs were investigated with and without 50 ng/mL of Tumor necrosis factor-alpha (TNF-α) as a barrier disturbance agent for 12h (Figure 3.4-1-c). TEER measurements were performed to define the barrier integrities of TNF-α treated and non-treated ECs under static and dynamic conditions. As expected, the results showed that TEER values decreased after TNF-α treatment over time, and dynamic conditions provided higher barrier integrity by ECs. These results were correlated with molecular transport analyses and supported by gap size and nuclei counting studies that showed ECs have more resistance to TNF-α under dynamic conditions than static conditions.

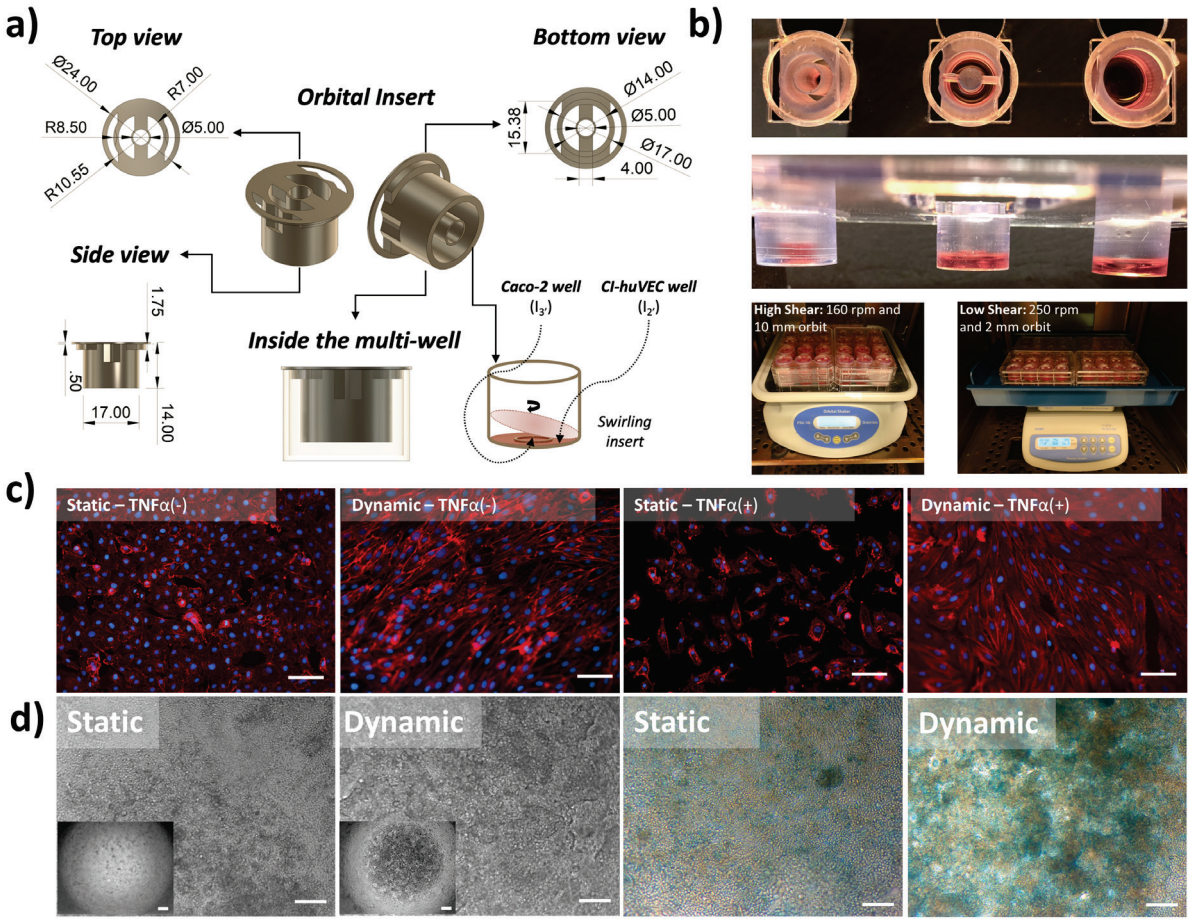

Figure 3.4-1: Orbital shaker actuated insert (O-insert) designs for mono- and co-culture of cells. **a)** Dimensions of dual compartmentalized co-culture inserts in mm. **b)** top (upper panel) and side (below panel) views of gelatin membrane assembled compartmentalized inserts. Red liquid represents medium (about 2 mm high in the compartment) while the membrane is not stained. **c)** F-actin (red) and nuclei (blue)-stained CI-huVECs after the TNF-α and high shear stress (20.7 dyn/cm^2) shear exposure. **d)** Light microscopy images of Caco-2 cells after low shear stress (0.3 dyn/cm^2) induction; **Control:** static (Magnifications: 4x and 10x; Scale bars: 100 µm). Adapted from Paper III.

On the other hand, Caco-2 cells exposed to LS showed 3D villi-like structures similar to the previous study with rocker-actuated inserts. The functionality of intestinal tissue was confirmed with improved barrier function based on TEER (4-fold) and molecular transport analysis and Alcian blue staining, which indicates mucus formation after 6-day incubation (Figure 3.4-1-d). Furthermore, crosstalk between intestinal and endothelial tissues was investigated based on 0.44 kDa LY and 4 kDa-FITC-Dex molecular transport between tissues.

ECs showed a reduced barrier function in the presence of intestinal cells, whereas Caco-2 cells' barrier function was not affected by co-culture conditions significantly.

Taken together, an alternative fluidic platform was introduced based on insert walls to compartmentalize shear zones for both vertical and horizontal co-culture. The platform was designed in the 12-well plate format to increase throughput to activate barrier cell functions. Similar to the rocker platform, a generic orbital shaker was used and characterized to emphasize the accessibility and simplicity of the approach in any research laboratory.

"Developing a balance between logic and imagination. After all, imagination without logic is daydreaming, and logic without imagination is boring."

-Leonardo da Vinci

Chapter 4

DISCUSSION

This chapter presents essential highlights of presented cell culture devices compared to conventional peers and the design considerations for developing these devices to model tissue platforms in a more functional and reproducible manner.

4.1 Design and Fabrication Considerations for Cell Culture Devices

Regarding the fabrication of HTS inserts, the first step was to design a stackable insert in 96-well plate format to increase throughput and also make it fit standard plastic well plates. However, it was found that even though two stacks were printable, they would not be possible to use due to physical limitations of standard well plates, used printing material, and tolerances of the Formlabs' SLA printer (around ± 0.2% (lower limit: ± 0.1 mm)[149]. The solution would be to customize a well plate. Still, it would increase the cost and complexity of the fabrication and not fit the aim to make inserts and also fabrication techniques accessible to many research laboratories. Therefore, these inserts were kept as single-layer HTS inserts in strips and well plate formats as an alternative to their peers in the market[160,161]. And instead of a 96-well format, 2-layer stackable 48-well inserts prototypes were introduced as minimum size limitations to overcome the limitations discussed above, which offered a novel alternative to the field as being suitable for automatized HTS applications.

Furthermore, inserts were functionalized with ECM-mimetic hydrogel membranes to increase bioactivity, unlike Transwell inserts with rigid plastic membranes.

To do so, the dip-casting method was developed and introduced as the HT membrane formation technique due to its simple mechanism. This technique offered significant advantages such as simplicity and applicability with other hydrogels. However, the way of the procedure manual and external conditions needed to be controlled as much as be. External conditions such as temperature, immersion, and withdrawal time were controlled; however, maintaining the immersion rate would only be possible with an automatized system. On the other hand, since the dip-casting method relies on hydrogel-insert surface interaction, the insert bottom surface was tried to be optimized to increase the consistency of membranes. In order to do this, the insert bottom was designed as a ring structure with a defined wall thickness (approximately 500 µm) as observed as the most stable achieved with printing conditions. The wall thickness below 500 µm would be much better to reduce membrane thickness, thus improving mass transport efficiency. However, it would need a change in fabrication method and/or printing material. As a part of the optimization process, bottom apertures were also tested. Apertures bigger than 4 mm in diameter cause a sagging or balloon effect[162] that can be a feature for some applications, for example, in vitro airway models[163] or a bug, as it might cause an adverse effect on barrier cultures[26]. In this study, both cases could be touched on by limiting the aperture diameters in HTS inserts in 96-48 well format inserts and dynamic inserts where the bottom could not be defined to prevent any flow disturbance. On the other hand, it might cause a sagging effect due to the non-uniform thickness (center: 50-75 µm, edge: 100-150 µm). Uniform membrane formation would be much preferable to limit variations in dynamic inserts. Still, a change in the membrane material and formation technique or the insert fabrication method might need to be made. Within the limited source during the project, since cells would only localize to apertures via the dip-casting approach, multiple apertures in the bottom would be the solution to create a more extensive surface area of inserts. However, potential effects of mass transport limits caused by molecule and surface interactions of insert material should be considered in these designs.

Taken together, customization in both inserts and membranes was achieved thanks to affordable, accessible, and straightforward techniques; 3D SLA printing and dip-casting. Moreover, alternative membrane pinning techniques, gluing and ring-pinning apparatus, were also introduced in the case of plastic membranes preferred by keeping novel insert functions such as stackable, close-contact, lateral co-culture inserts in both dynamic and static operational modes that are not provided by commercialized inserts. Since increased (bio)complexity was also one of the essential aims of this thesis work, a dynamic blood flow microenvironment was integrated into the design of cell culture devices. Flow is generated using simple instruments such as rockers and orbital shakers that can be accessed in many research laboratories. Many scientists previously explored these platforms to actuate biological functions on epithelial and intestinal cells[27,164–167]. However, they were used with traditional cell cultures with/without considering flow dynamics or commercialized Transwell inserts without characterizing the overall dynamic platform.

As the first attempt, bidirectional flow-based perfusion devices (Paper II and Poster III) were designed to potentially create the peristaltic-like movement of liquid to mimic the motility of the intestine. For generating bidirectional flow, a 2D see-saw rocker was used in a customized 3D-printed insert with an open-top rectangular channel. Tilting angle and frequency settings of the rocker unit are defined to achieve physiologically relevant parameters of small intestinal tissues such as peristalsis[30,31,168,169] and flow shear stress 0.02-5 dyn/cm2[107,158,159]. Open-top fluidic is a growing concept in the literature due to its operational easiness without physical complexities such as bubble formation and capillary effect[110,111,170]. The system was designed to be open based on these motivations. It combined orbital shaker and rocker actuated well plate approaches[96,119,120,171–175] with inserts by providing the "exact" static control compared to most microfluidic-based organ-on-chip devices where Transwell inserts are used as "static" controls due to their microscale content would cause evaporation under static conditions. Also, the platform is compatible with

standard techniques and instruments used with Transwells, for example, STX3/ chopstick electrodes (for EVOM2), to measure trans-endothelial/epithelial electrical resistance (TEER) for barrier integrity evaluations[33,176–178]. Taken together, it was shown that the simplistic dynamic inserts approach increased (bio)complexity while keeping the throughput in multiple ways.

4.2 Biological Considerations

4.2.1 Membrane selection should also be customized

Regarding biological evaluations of devices, there have been some interesting findings. The 3D-printed inserts functionalized with hydrophilic PTFE and gelatin membranes were tested with the mouse intestinal organoids. The results showed that the hydrophilic PTFE membrane provided better viability than the gelatin membrane and control condition on multi-well plates[179]. It was an indication for biocompatibility of inserts; however, incompatibility of gelatin membranes with the mouse intestinal organoids. It would be most likely due to better mass transport towards the basolateral side of the membrane, as confirmed by the 10-fold thinner PTFE membrane showing 10-fold quicker molecular transport (Paper I).

4.2.2 3D morphogenesis might not be related to flow shear

Another interesting result was obtained from evaluating bidirectional flow on Caco-2 intestinal cells. 3D-printed inserts functionalized with Gelatin membranes were optimized on Caco-2 cells, in agreement with reported findings in the literature[128,180,181] (Paper I). Therefore, the same gelatin membrane conditions were used to investigate the effects of dynamic conditions with initial cell density. Since there was no consensus about the initial Caco-2 cell density which varies from 50.000 (50k) cells/cm^2-500k/cm^2 [167,182–185], the minimum density was defined as 50k/cm^2; the intermediate density was 80k/cm^2 as was the previous optimized condition (Paper I) and 100k/cm2 as the maximum intensity condition.

Higher than 100k/cm^2 conditions were not investigated as reported might cause multilayer cellular growth and inconsistency on barrier tissues under static conditions[27,186–188]. Each density condition showed increased barrier integrities based on increased TEER values under dynamic conditions, as would have been expected. However, the 50k/cm^2 group showed the highest integrity. It might most likely be due to the cells proliferating more due to the longer time spent in the culture to reach confluency before the flow exposure. Thus, it might induce maturation toward the enterocytes due to contact inhibition[186,189,190]. On the other hand, 100k/cm^2 showed heterogenous morphogenesis under dynamic conditions where 2D cell monolayers (thin epithelium) and 3D villi-like cellular structures (10-fold thicker epithelium) exist together (Figure 3.3-1).

Since this result was exciting, this condition was further investigated by characterizing regiospecific expressions of tight junction marker (ZO-1), Villin (villi; epithelium brush border), and MUC-2 (mucus-secreting cells). ZO-1 was expressed in all cultures as an indication of barrier integrity[12,20,28,191–194], whereas dynamic culture had an improved barrier function in agreement with TEER and LY transport analyses. On the other hand, the results were similar for both Villin and MUC-2, as reported[19,20,191]. Taken together, each result showed consistency in increased expression of each marker in 3D cellular structures that were seen in dynamic conditions compared to 2D monolayers seen in both static and dynamic conditions. However, 3D areas were not always in a similar orientation. They were either compact or patchier in the central axis of the channel, even in two different wells from the same experiment (Paper III). Since inconsistent differentiation behaviors of Caco-2 cells due to high initial density is reported[184], it could be related to it. However, static culture did not show this characteristic. Therefore, this phenomenon was related to stochastic uneven seeding during cell culture applications. Since there was no consensus about the behavior of Caco-2 cells in both static[27,195] and dynamic culture and no precise comparison/analysis of distinct regiospecific morphogenesis/differentiation between 2D and 3D regions, speculating on this phenomenon became very challenging but intellectually stimulating.

A widely accepted view was that shear stress results in 3D villi-like structures[32,191,192,196,197]. But there are also views that basolateral feeding and removal of paracrine factors such as Wnt antagonists, specifically Dickkopf-1 (DKK-1), affect the 3D maturation[17–20]. Therefore, platform-specific characteristics were taken as a focus to explain this phenomenon. As already discussed, the membrane showed non-uniform thickness where the center is thinner than the edge of the channel, where regional mass transport difference is expected. On the other hand, obtained regional flow velocity values also agreed with thickness results. Therefore, the regional difference in basolateral feeding and shear stress would together be involved in regiospecific morphogenesis. Since this phenomenon happened just in the high-density group, the initial density likely also has an essential role in this process. Taken together, all these results provided by a simplistic custom device approved that there is a considerable need for evaluating Caco-2 cells' differentiation and maturation mechanisms at the single cell level due to the high heterogeneity of the culture, which is one of the challenges in the standardization of in vitro models for drug developments. Since Caco-2 cells are commonly used, established cell lines for drug development pipelines, the characterization of cells at a single level should be noted as a challenge that needs to be tackled in future studies.

4.2.3 Physiological shear stress improved endothelial barrier function

As the second attempt to investigate a unidirectional flow on both endothelial and epithelial cells, another 3D-printed custom insert (O-inserts) was designed for the orbital shaker actuated flow shear stress. First, the mechanosensitive feature of ECs to shear stress[171,173,198,199] was used to

define the most uniform shear stress areas in the insert by using orientation vector analysis (Paper III). Then, barrier integrities of ECs were characterized under physiological shear stress. After confirming the increased barrier integrity values in the dynamic group, TNF-α was applied as a disruptive barrier agent to evaluate further the protective effect of laminar shear stress. The results showed that the applied TNF-α conditions prevented the protective effect of physiological shear stress; however, cells were swollen by shear as an indication of counteracting to TNF-α treatment. It would be related to LDL uptake, one of the well-known atheroprotection mechanisms, reduced by TNF-α [200,201].

4.2.4 Crosstalk between barriers

After characterizing EC culture conditions and the insert design parameters, the platform was implemented as a co-culture platform by culturing intestinal barrier cells (Caco-2) in the central region. Since physiological shear needs and maturation times of ECs and Caco-2 cells were different, first Caco-2 cells were differentiated in the central area under low shear stress (LSS: 0.3 dyn/cm^2) conditions. Cells showed higher barrier integrity, 3D morphogenesis, and increased mucus production under physiological shear stress conditions. It agreed with reports[202] in the literature and the previous study performed using rocker (Paper II). Once cells were differentiated, ECs were seeded in the periphery by actuating alignment for 48h. During the actuation of ECs under HSS, the barrier function of Caco-2 cells was kept their barrier function. However, barrier integrities of ECs reduced in the presence of Caco-2 cells in the culture. The exact mechanism could not be clarified, whereas the medium incompatibility was neglected due to the enormous volume differences between compartments. Obtained results showed that the O-insert provided sufficient shear stress to activate intestinal and epithelial cell functions. However, indeed, crosstalk between both cells is supposed to be further investigated in future studies.

4.3 Future perspectives and recommendations

Apart from future perspectives based on biological evaluations mentioned above, some further device developments could be done. Since the overall platform prototypes were designed to be modular, scalable, and customized, more improvements can always be made. In this study, the prototypes were produced using Formlabs' 3D SLA printer (Form 3B) and photo-curable printing resins (Biomed Clear and Dental LT) due to their biocompatibility, user-friendliness, and proven quality by experience in the group. Since research (proof-of-concept), prototyping was the main intention, and tolerance might happen due to printing being within the acceptable range for presented applications. Under these circumstances, any other fabrication method was not needed to be explored when producing inserts. However, the fabrication setup can be modified with alternative technologies to reduce costs or improve printing quality. In particular, Biomed Clear, due to its autoclavability, is suggested to fabricate insert prototypes for specific applications covered in this thesis.

Nevertheless, it should be noted that chosen methodology is sufficient for a research project for a limited time. For long-term projects and possible higher volume productions, other technologies such as PolyJet 3D Printing[149] for complex insert designs or plastic forming methods (e.g., injection molding and thermo-forming)[203,204] for simpler insert designs can be explored by considering the dependency the fabrication material supplier. Moreover, intestinal and epithelial tissues were used as validation subjects for designed 3D-printed platforms. However, other barrier tissues, such as the lung, skin, and blood-brain barrier (BBB), can be implemented into the model with application-specific modifications in the platform design.

Highlighted recommendations on insert design approaches:

- **Stackable close-contact inserts** can be modified with other membrane materials and used for any crosstalk, cell migration assays, and (micro)vascularization applications 205.

- **Dynamic Operational Mode:** Rocker (R-inserts) and Orbital shaker (O-insert) actuated inserts can be rescaled as Circle Ripple inserts (CR-inserts).
    - R-insert in 6-well format can be converted to stackable inserts in case higher shear stress is needed. A potential application would be with endothelial cells (ECs); however, it should be noted that the bidirectional fluidic model would be more suitable to model "diseased" endothelial tissue due to the mechanosensitive nature of ECs[5,206]. Moreover, 12-well format R-inserts were not investigated due to the need for a bigger basolateral container and longer channel distance for perfused spheroid applications. However, apical flow shear stress can be further explored on a smaller scale for higher throughput.
    - In contrast, the CR-inserts can be scaled to a 6-well plate format to increase uniform shear stress zones for expanded co-culture applications.

When zooming into the designed devices, the closest mechanical and biochemical effects come from the membrane material, the artificial ECM substrate for cells. Since each tissue and organ have its own microenvironment, providing a customized extracellular matrix (ECM) would be the first step. In this thesis, customization of membrane materials was slightly discussed. However, there is still a huge opportunity to improve biomaterial selection, properties, and biofabrication methods.

Current studies mostly use Matrigel, a mouse tumor extracellular matrix protein mixture, as a gold standard, and it is a nearly universal material due to its rich content of bioactive ECM components [207]. However, it is overly expensive for long-term usage and needs a significant scale due to its production complexities. Moreover, it may show batch-to-batch variations due to the animal-based content[208]. Therefore, Collagen is a growing trend in tissue engineering, particularly in organoid studies, as a more innocent alternative from an ethical point of view even though it is still animal-based[209]. However, it still does not represent ECM fully. Moreover, it is still relatively expensive due to its small batches and more challenging to work for membrane production. Specifically, as mentioned before, the dip-casting technique is already dependent on too many external conditions that are difficult to control to increase consistency. Therefore, the preference in this study is to have similar properties as Collagen but with more affordable and practical options.

Since Gelatin has similar bioactivity to Collagen, it was used as the primary biomaterial in this study. However, it should be noted that Gelatin cannot be a universal material for all applications due to its limited bioactivity and physical properties. Especially, it might be insufficient during the differentiation process of stem cells and organoids, and ECM is needed to be remodeled. Therefore, there is a need for alternative biomaterials and/or membrane fabrication techniques that could mimic ECM more accurately. For example, peptide-based hydrogels are a growing trend due to their more controllable synthetic content with custom bioactive motives[208]. These novel materials show promising results with stem cells but are also costly alternatives and must be optimized for each cell and application. Alternatively, there are some hybrid approaches where the backbone can be selected from an accessible hydrogel, and modifications can be done to improve bioactivity via chemical mechanisms such as click chemistry, enzymatic ligation, and affinity

binding[210]. For example, surface modification of the Gelatin-based membranes would be the next improvement step. To do it, synthetic peptides would be used with a linker peptide sequence that could be immobilized on the membrane surface via the enzymatic crosslinking mechanism described in the literature[211].

Furthermore, as mentioned above, the topography of the cell culture substrate is one of the mechanical stimuli on barrier cells. The topography would be achieved using various techniques such as soft lithography, photolithography, and hot embossing[212]. Photolithography techniques such as the traditional optical lithography (photomask-based) technique or 3D printing (e.g., stereolithography (SLA) and digital light processing (DLP) printers[150]). 3D printing (digital photomask-) based-photolithography, is the most popular techniques due to achieving desired resolution and structural dimensions via photo-patterning of photo-crosslinkable hydrogels.

It can be argued that materials are limited, and these technologies/materials might be expensive and/or labor-intensive. With a high development rate of printing technologies, it is expected that these technologies will be more affordable, accessible, and compatible to work with under aseptic conditions. Until then, the transitional optical lithography technique can be suggested since accessibility to technologies was one of the motivations of this thesis study. In particular, the optical lithography technique can be implemented in the customized insert approach to photo-patterned membranes and scaffolds (Figure 4.3-1) as microwells to form spheroids (Figure 4.3-1a-b), villi-like topography (Figure 4.3-1d-f) or microgroove structures to form for elongating cells such as neurons, muscles, and vascular cells[212].

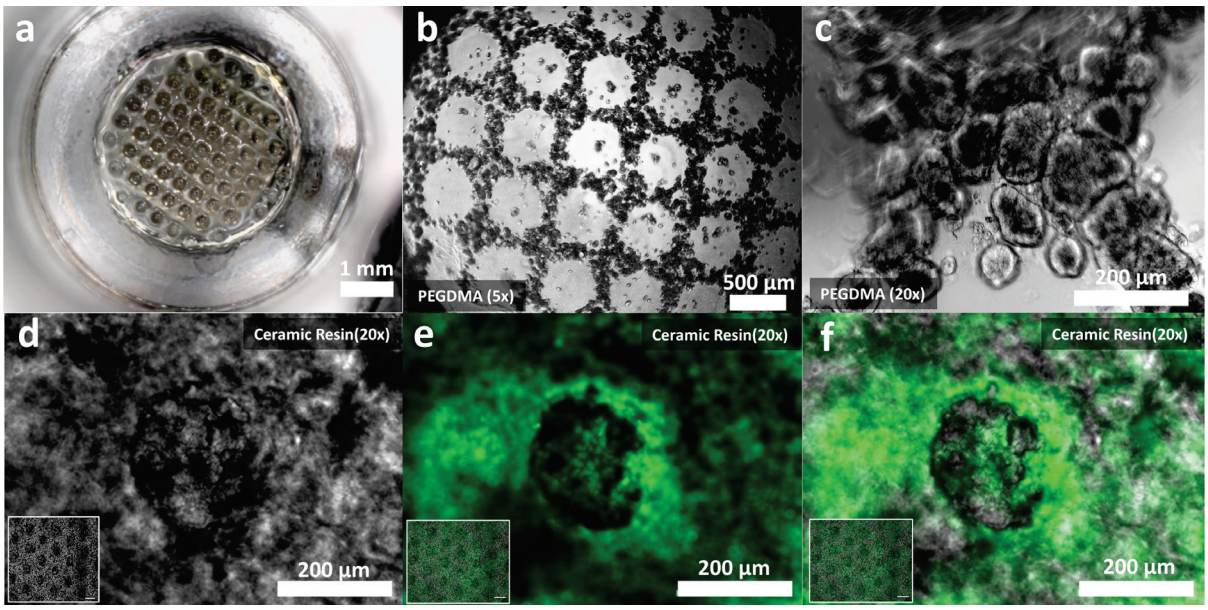

Figure 4.3-1: Photopatterning application examples from preliminary studies. a) Representative image of photopatterned Polyethylene glycol dimethacrylate (PEGDMA) hydrogel membrane in 3D-printed cell culture inserts through a mask. b) Caco-2 spheroids on microwell-like patterned PEGDMA (Zeiss AxioVision, Magnification: 5x, Scalebar: 500 µm), c) Caco-2 spheroids on microwell-like patterned PEGDMA (Zeiss AxioVision, Magnification: 20x, Scalebar: 200 µm). Figures were adapted from Marina Orenga Sánchez's Master's thesis. d-f) Brightfield (d), fluorescence (e) and merged (f) images of Acridine Orange (live cell staining) stained Caco-2 cells on villi-like patterned ceramic scaffolds (300 µm height pillars, 10 pillars/mm^2) (Magnifications: 5x and 20x; Scale bars: 100 µm and 200 µm; Zeiss AxioVision) on day 21. Ceramic scaffolds were provided by Dr Babak Rezaei from DTU Nanolab.

4.4 Conclusion

In conclusion, the work presented in this thesis showed promising methods and designs for fabricating tissue-engineered static and dynamic insert-based platforms. Platforms were mainly used to mimic endothelial and epithelial barrier extracellular matrix (ECM) microenvironments as proofs-of-concept, and ECM-mimetic hydrogel membrane material characterizations were performed. Furthermore, mechano-induced functionalities of both endothelial and epithelial tissues were characterized by biological evaluations. The most important findings of each paper are listed below.

Paper I

3D-printed inserts were presented with a small library of inserts as a solid alternative to commercialized inserts limited to customization. Design considerations were challenged within the physical limits of 3D printing, capillary effects, and liquid handling. Furthermore, membrane material selection was discussed, and the dip-casting technique was offered as a straightforward method to form 500 µm thin hydrogel membranes. Biocompatibility of 3D-printed insert pinned with synthetic and hydrogel members was validated on mouse intestinal organoids and intestinal barrier models with model cell line (Caco-2 cells).

Paper II

2D see-saw rocker actuated custom hanging insert (R-insert) provided physiological shear stress induced by the bidirectional flow on Caco-2 cells. Dynamic flow generated the regiospecific expressions of F-actin, MUC-2, and Villin markers compared under static and dynamic flow conditions. Moreover, flow improved intestinal barrier function, confirmed by increased ZO-1 expression and TEER values and decreased lucifer yellow permeability.

Paper III

Orbital shaker actuated compartmentalized inserts provided a gradient of laminar flow and shear stress zones. The periphery region was characterized as the most uniform shear stress area where endothelial cells were actuated and elongated through the flow direction. The central region was offered as an optional application of dual lateral compartmentalized inserts for co-culturing. The 12 -well plate inserts provided an effective shear stress platform to activate intestinal and endothelial barrier functions with higher throughput.

"Every science begins as philosophy and ends as art."

- Will Durant

Chapter 5

PAPER I

Customized 3D-printed stackable cell culture inserts tailored with bioactive membranes

Asli Aybike Dogan, Martin Dufva

Scientific Reports (2022)

scientific reports

Check for updates

OPEN

Customized 3D-printed stackable cell culture inserts tailored with bioactive membranes

Asli Aybike Dogan & Martin Dufva✉

There is a high demand in various fields to develop complex cell cultures. Apart from titer plates, Transwell inserts are the most popular device because they are commercially available, easy to use, and versatile. While Transwell inserts are standardized, there are potential gains to customize inserts in terms of the number of layers, height between the layers and the size and composition of the bioactive membrane. To demonstrate such customization, we present a small library of 3D-printed inserts and a robust method to functionalize the inserts with hydrogel and synthetic membrane materials. The library consists of 24- to 96-well sized inserts as whole plates, strips, and singlets. The density of cultures (the number of wells per plate) and the number of layers was decided by the wall thickness, the capillary forces between the layers and the ability to support fluid operations. The highest density for a two-layer culture was 48-well plate format because the corresponding 96-well format could not support fluidic operations. The bottom apertures were functionalized with hydrogels using a new high-throughput dip-casting technique. This yielded well-defined hydrogel membranes in the apertures with a thickness of about 500 µm and a %CV (coefficient of variance) of < 10%. Consistent intestine barrier was formed on the gelatin over 3-weeks period. Furthermore, mouse intestinal organoid development was compared on hydrogel and synthetic filters glued to the bottom of the 3D-printed inserts. Condensation was most pronounced in inserts with filters followed by the gelatin membrane and the control, which were organoids cultured at the bottom of a titer plate well. This showed that the bottom of an insert should be chosen based on the application. All the inserts were fabricated using an easy-to-use stereolithography (SLA) printer commonly used for dentistry and surgical applications. Therefore, on demand printing of the customized inserts is realistic in many laboratory settings.

In vitro tissue/organ modelling is an increasingly popular field for tissue engineering and drug development. For instance, organ systems have been employed to model pharmacokinetics and dynamics[1–4], first-pass metabolism[5], and uteritis colitis[6]. The field has been dominated by microfluidics chips due to their excellent mass transfer characteristics. However, microfluidics chips are often challenging to use and not easily scalable in terms of the number of experiments that can run in parallel. Transwell-type of inserts for in vitro organ models have therefore been explored[5,7].

Transwell hanging inserts have been extensively used to recreate single barrier tissues like the intestine, skin, and blood–brain-barrier. They are also used to interconnect tissues by co-culturing multiple cell lines or creating 3D tissue such as organoid cultures with hydrogels[8–10]. These inserts are standardized with permeable supports with microporous synthetic membranes[11] such as polycarbonate (PC), polyester (PET), polytetrafluoroethylene (PTFE). The pore sizes range from 0.4 to 8 µm, the thickness is between 10 and 30 µm, and the porosity is 10–15%. The drawbacks of commercial Transwell inserts are the lack of flexibility to choose the material and size of the bioactive cell culture area. Another limitation is that Transwell inserts provide only one layer.

Custom-made, three-layer 3D-printed insert plates for interconnecting different tissues in the 12-well format have recently been demonstrated[5]. In contrast to the relatively complex and expensive fabrication process of culture devices such as injection molding[12], 3D printing is superior due to its flexibility to create customized inserts rapidly and cost-efficiently for low-volume, lab-scale production. Hanging inserts are relatively large that are well within the bounds of the performance of even low-cost 3D printers. The low-cost extrusion-based filament printers could potentially be used to manufacture inserts. However, even though polymers such as native polylactic acids (PLA) are biocompatible[13], printing smaller features like holes with this technique is challenging

Department of Health Technology, Technical University of Denmark, 2800 Kgs. Lyngby, Denmark. ✉email: dufva@dtu.dk

because the resolution is in several hundreds of µm. It is also unclear if the insert walls are completely sealed with filament printing which is necessary to block liquid or the electrical current when analyzing the cell barriers. The SLA and projection printers (e.g., digital light processing (DLP) printers) have better resolution and provide liquid-proof prints[14]. In these printers, light is utilized to crosslink a photo-curable resin that is biocompatible for cell culture applications[14,15]. Some resins such as Dental LT from Formlabs conform to biocompatibility class IIa because the prints are intended for dentistry. Even though dental resins are biocompatible, they do not support cell attachment[5]. This property allows for defining the bioactive area with a filter or a hydrogel to resize and shape the cell culture area according to experimental needs.

Hydrogel scaffolds have high-water absorption capacity due to their permeable/porous structures. They are widely used as ECM-mimetic biomaterials and are shaped by film/membrane formation[5,16], molding[17,18], or 3D bioprinting[19,20]. Hydrogels as a membrane (here, we define all membranes as the material closing the bottom of an insert) make it possible to utilize soft growth matrices instead of the rigid filter membranes used in Transwell inserts. Cells sense the stiffness of their growth matrices[21,22], and the intrinsic biodegradability of hydrogels is considered a crucial feature during tissue regeneration[23]. Various natural, synthetic, and hybrid biomaterials such as Poly (ethylene glycol) (PEG)[24], silk[25], Matrigel[8], decellularized tissues[26], and gelatin[5,16,27–29] have been explored in the literature. An advantage of hydrogels is that they are often transparent, which is not always the case for filters. Transparency is a major feature for microscopy.

From our previous work[5], we have identified three district challenges addressed here. Firstly, the 12-well plates are not suitable for high-throughput screening (HTS), where the 96-well plate format dominates due to its lower reagent usage. Secondly, the method for functionalizing the insert with a hydrogel membrane must be simplified if 96-well plates are used. Thirdly, the previous hydrogels were 1–3 mm thick, resulting in slow mass transport through the membrane. Hydrogels have been casted to obtain defined thicknesses which requires a custom-made apparatus[5]. Scaling this approach to 96-well will be difficult because it requires exchangeable surfaces that repel gelatin, such as parafilm[5] or pristine PDMS.

To address these challenges, a dip-casting method to form hydrogel membranes was developed and validated. The procedure reliably created 500 µm thin gelatin membranes. We also challenged the 3D printing technology to scale the 12-well inserts to 24-, 48- and 96-well plate formats as strips, singlets, and multiple stacked layers, to investigate physical or mechanical limitations of stacking. We also described a method to assemble synthetic filters to the insert bottom. We investigated the biocompatibility of 3D-printed custom inserts on mouse intestinal organoids and epithelium barriers.

Results

Physical limits of stacked inserts. 24- to 96-well inserts were designed as full plates, strips, and singlets (Fig. 1 and Supplementary Fig. S1). The design followed the previous described modular vertical stacking of cell culture inserts where insert slide into each other[5]. We considered the wall thickness, the wall-to-wall distance, and the number of layers that could be stacked in the respective well format. The distance between the bottoms of the respective insert layers was not optimized but kept to 500–750 µm. Generally, the insert closest to the bottom of the well was 1–2 mm from the bottom of the well to enable microscopy using a long working distance objective without moving the inserts stacks from the plate. The 24-well format had access ports for medium sampling and TEER measurements without disturbing the cultures (Fig. 1b). Due to space restraints, access ports were not included in the 48- or 96-well formats.

As the wall of each insert layer fills in the well, it is limited how many layers a specific well size can hold. We focused on 2-layer stacks for 96- and 48-well plate formats (Fig. 1a) to investigate how small stackable inserts could be and yet be functional. We aimed to minimize design dimensions to be able to stack multiple layers by limiting capillary effects and bubble formations due to trapped air during the stacking of the layers. The wall thickness of each printed insert was 545 µm ± 34 µm (mean ± SD; n = 36) with ± 80 µm tolerance to the design dimension (500 µm). 250 µm thin walls were not rigid, and inserts got damaged during stacking (data not shown). The distance between the two walls in the respective stacked insert was 757 µm ± 22 µm (mean ± SD; n = 6; with ± 30 µm tolerance to the design dimension: 750 µm). Smaller wall distances made stacking insert layers difficult, especially regarding entrapment of bubbles and capillary effects. Thus, each insert layer occupies about 2.5 mm in diameter (2*750 + 2*500 µm) plus the inner diameter, which limits the number of layers in a well. Both 48- and 96-well plate sizes could hold two stacked inserts, but the topmost insert in the 96-well plates was as narrow as a well in 384-well plates ($Ø_{inner}$ = 2 mm, Fig. 1c). Such narrow wells are easy to operate manually when the tip of the pipette is hitting the insert bottom before ejecting the liquid. This mode of operation is not possible because that would destroy cell layers or the hydrogel membranes. Therefore, the 96-well format could not hold two layers. The bottom-most insert in the 96-well formats was by contrast 5 mm in diameter, which we consider to be a minimum usable inner diameter.

The bottom of the insert had one large hole, an array (Fig. 1b) or a pattern of smaller holes (Supplementary Fig. S2). One large hole was used for gluing or adhering rigid polymeric filter membranes to the insert (Supplementary Fig. S1).

Functionalization of the inserts with filter membranes. Hydrophilic PTFE membranes were used to modify the bottom of the inserts with a microporous filter membrane. The PTFE membrane was glued using the Dental LT resin to 3D-printed 96-, 48- and 24-well plate inserts with one large aperture in the bottom. Initial trials included applying a thin layer of uncured Dental LT to the rim of the bottom. However, we often observed that the resin absorbed into the filter, which resulted in blockage after UV crosslinking (Supplementary Fig. S1a-top left panel). This was especially troublesome for small formats such as 96-wells. An improved gluing process was developed where the resin was applied to the sides of the 3D-printed insert (Supplementary Fig. S1b). The

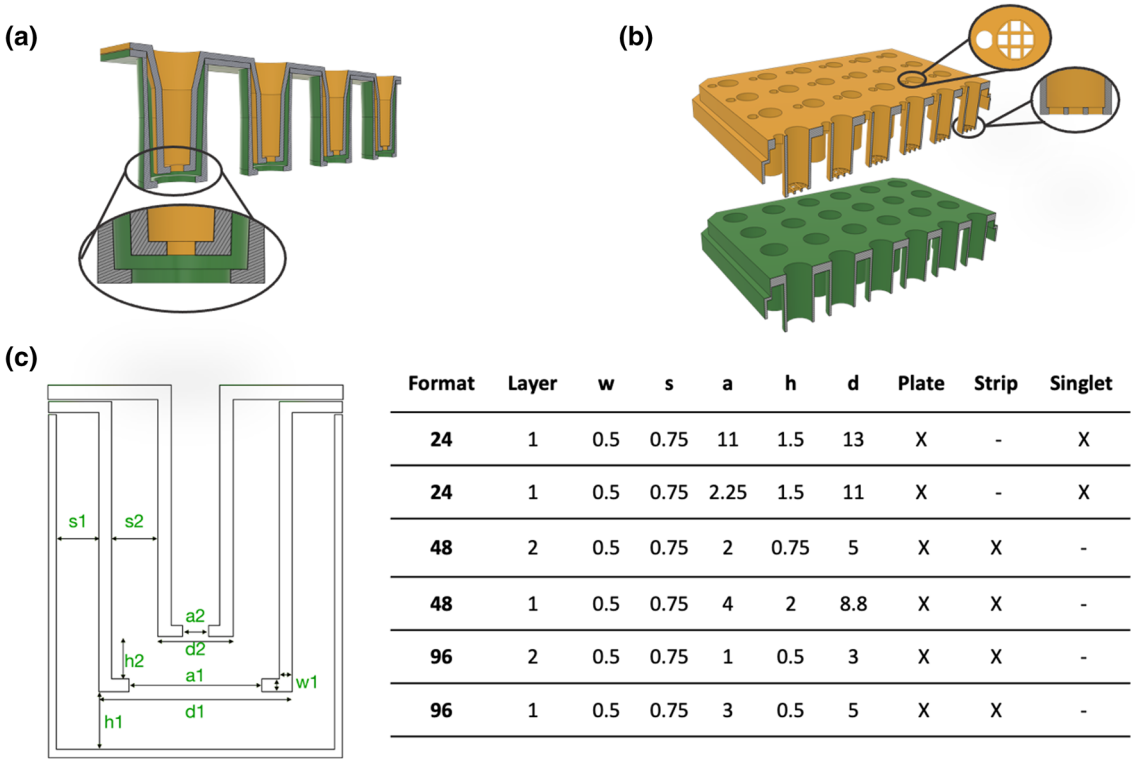

Format	Layer	w	s	a	h	d	Plate	Strip	Singlet
24	1	0.5	0.75	11	1.5	13	X	-	X
24	1	0.5	0.75	2.25	1.5	11	X	-	X
48	2	0.5	0.75	2	0.75	5	X	X	-
48	1	0.5	0.75	4	2	8.8	X	X	-
96	2	0.5	0.75	1	0.5	3	X	X	-
96	1	0.5	0.75	3	0.5	5	X	X	-

Figure 1. Representative illustrations of 3D-printed inserts. (**a**) Stacked (layering) insert approach. (**b**) 24-Well format insert plates. (**c**) Dimensions of introduced 3D-printed inserts and representative examples of singlet, strip, and plate format inserts in the online library (*w* width, *s* distance between layer walls, *a* aperture, *h* height from the well/insert below, *d* diameter; all dimensions in mm.)

PTFE membrane was placed on the bottom and secured with a ring slipped over the bottom of the insert. The ring was pressing the filter towards the sides of the insert. The excess resin was absorbed in the filters on the sides of the inserts rather than the bottom, which minimized the blockage of the filter in the aperture (Supplementary Fig. S1a-top right panel). The PTFE membrane could not be removed without destroying it (data not shown), which indicated a tight seal.

Functionalization of the inserts with hydrogel membranes. A quick and scalable hydrogel functionalization method was developed and characterized based on a tool-free casting procedure[16]. The viscosity was controlled by keeping gelatin (without mTG) at 37 °C. The device was dipped a few mm into the gelatin solution, and the immersion time was standardized to 5 s. The devices were subsequently gently removed (Supplementary Fig. S3). Excess gels solution was removed by sliding the bottom of the insert against a warm sterile petri dish. The procedure ensured that only the apertures were filled with the hydrogels (Fig. 2). This functionalization method was also compatible with agarose and soy-based hydrogels (data not shown).

Irreversible crosslinking was achieved using a two-step protocol. Firstly, the gelatin membranes were reversibly physically crosslinked by reducing the temperature to 4 °C. The gelatin membranes were subsequently irreversibly chemically crosslinked by adding a solution of mTG[29]. The formed membranes could be used immediately, stored in a refrigerator, or even dried and stored at room temperature for later use. A dried membrane rehydrates quickly and supports cell cultures (e.g., Caco-2, data not shown).

The range of gelatin concentrations that could be used in the process was investigated. 2.5% and 5% gelatin solutions did not give consistent results, and damaged membranes were often observed after the dip-casting and crosslinking procedures. 10% w/v (10%), 15% w/v (15%), 20% w/v (20%) gelatin concentrations resulted in 25–30% failures which was acceptable. Functionalizing apertures larger than 4 mm typically increased the failure rate. We estimated the respective compositions' elasticity and stiffness by analyzing rheology at 37 °C. The calculated shear/complex modulus ($G^* = \sim 2.48, \sim 3.12, \sim 3.81$) and Young's modulus ($E = \sim 7.44, \sim 9.36,$ and ~ 11.44 kPa) for 10, 15 and 20% gelatin respectively (Fig. 3a).

The transport characteristics of hydrogels (10%, 15%, 20%) were compared with hydrophilic PTFE membrane (Fig. 3b) using a standard curve of fluorescein salt as a reference (Supplementary Fig. S4-right panel). As mass transport is a function of gel thickness, these results also indirectly measure the consistency of the formed membranes. Each hydrogel membrane had no significant difference in the mass transport of Fluorescein salt dye, while they were significantly slower than the hydrophilic PTFE membrane ($P < 0.0001$). The %CV (coefficient of variance) was 16% (PTFE), 6.7% (10%), 6% (15%), 13% (20%), showing that the variance of the mass transport through dip-cast membranes was low.

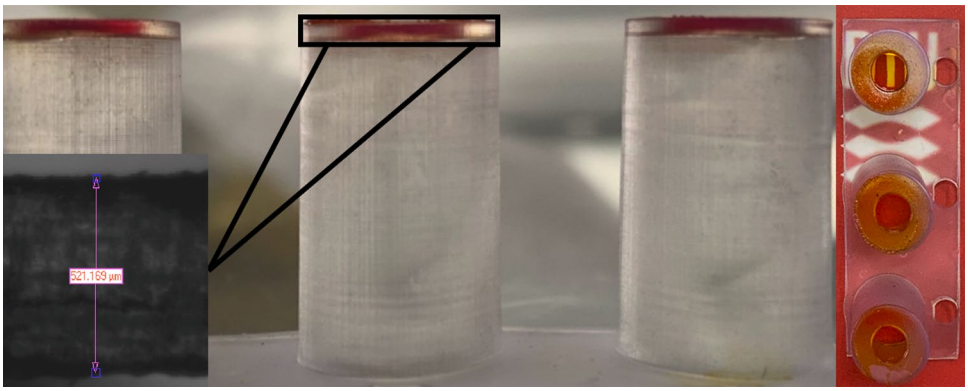

Figure 2. 3D-printed Gelatin-inserts (Ø: d = 8.8 mm; a = 4 mm); dip-cast with red food dye colored gelatin membrane. *Left* The thickness of the 3D-printed material at the bottom, 521 µm) was measured with a 6.5-fold zoom lens USB 3 camera of contact angle device (Dataphysics, Germany). *Right* Transparency of a dry gelatin membrane.

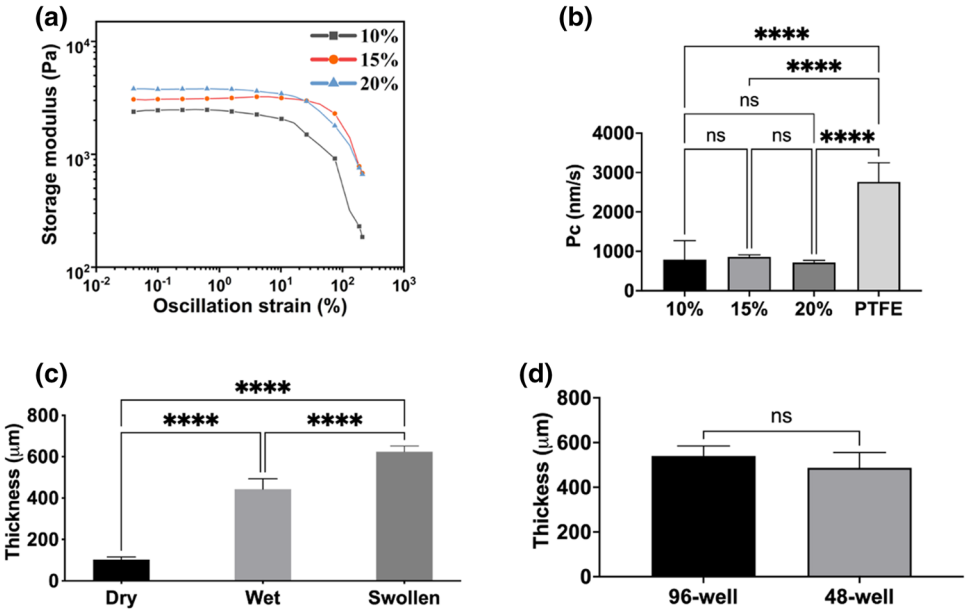

Figure 3. Determination of mechanical properties of 10% w/v (10%), 15% w/v (15%), 20% w/v (20%) gelatin membranes. (**a**) Analysis of storage and loss modulus of each membrane under applied oscillatory compression. (**b**) Comparison of 20 µM Fluorescein sodium salt dye transport through each membrane assembled to 96-well plate format 3D-printed strip insert wells (10–20%: n = 4; PTFE: n = 7). Insert well aperture surface area for transport is 0.05 cm^2. (**c**) Determination of thickness changes of 15% (w/v) Gelatin membranes assembled to 48-well format (Ø: d = 8.8 mm; a = 4 mm); wet (n = 5), swollen (n = 5), and dry (n = 5). (**d**) Thicknesses measurement of 15% (w/v) gelatin membranes (n = 5) via fluorescence intensity analysis. Error bars indicate mean ± SD. Statistical significance: ns = P > 0.05, ****P < 0.0001.

The thicknesses of membranes were measured using two different methods. 48-well insert (Ø: d = 8.8 mm, a = 4 mm) was chosen as it allowed for using a micrometer screw to measure the membrane thickness in dry, wet, and swollen status. The thicknesses for casted and crosslinked hydrogel membranes were 440 ± 50 µm (mean ± SD). The thicknesses for membranes swollen in PBS for 1 h at 37 °C were 620 ± 27 µm (mean ± SD). The thicknesses for membranes dehydrated overnight at room temperature were 103 ± 12.5 µm (mean ± SD). Gelatin membranes swelled approximately 6 times from the dry phase (Fig. 3c). As the second method for measuring the thickness, 1 µg/mL Fluorescein sodium salt was added to the gelatin solution. Fluorescence membranes were dip-casted, and the fluorescence intensity was measured using a microscope. The thickness in µm was obtained using a standard curve of fluorescence labelled hydrogels with known heights (from 150 to 900 µm) (Supplementary Fig. S4-left panel). No significant differences were found between the thicknesses of membranes of 96-well

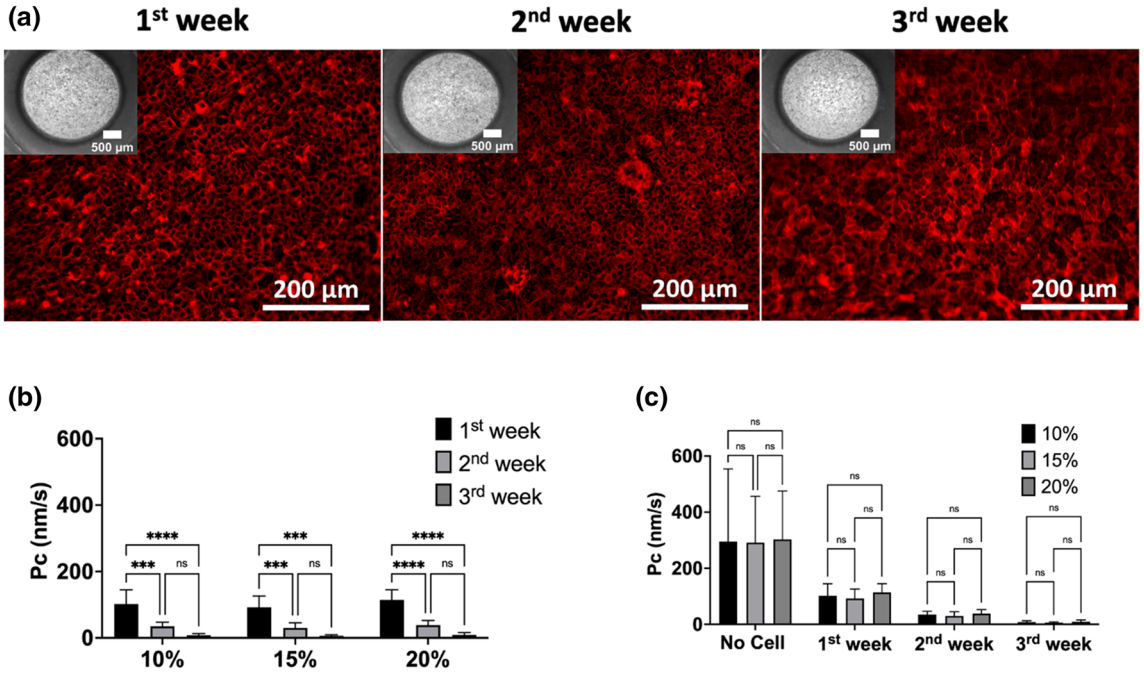

Figure 4. Biological validation of 96-well inserts. (**a**) Growth of Caco-2 cells on the 15% (w/v) gelatin membranes over three weeks. The 10% and 20% cultures had identical morphologies, so only the 15% cultures are displayed. Insert apertures at the bottom are shown at upper panels of fluorescence images (the magnification: 4x; scale bars: 500 µm), and the F-actin (red) stain of the cells on the hydrogel membranes (scale bars: 200 µm; the magnification was 20x). (**b**) Permeability coefficient (mean + SD) of lucifer yellow across Caco-2 cells on the 10%, 15%, 20% (w/v) gelatin membrane assembled inserts ($n \geq 3$) and (**c**) comparison of Pc values of empty hydrogel, 10%, 15%, 20% membrane assembled inserts ($n \geq 5$). Error bars indicate mean S.D. statistical significance: ns = $P > 0.05$, ****$P < 0.001$, ****$P < 0.0001$.

inserts 540 ± 44 µm, and 48-well inserts 487 ± 68 µm (mean ± SD, $p = 0.4244$) (Fig. 3d). These results confirmed the results obtained with the micrometer screw method. (Fig. 3c).

All gelatin concentrations had similar mechanical properties, thickness, and transport properties. However, the different concentrations functioned differently in the dip-casting process where 10% (w/v) gelatin solution had lower viscosity but formed more fragile membranes. In comparison, 20% (w/v) gelatin had higher viscosity which made the dip-casting step more difficult. 15% (w/v) gelatin membrane composition was, therefore, a good compromise.

Biological validation of the dipping approach using transport studies. The dip-casting process was tested for sustaining long-term cell growth using 96-well inserts (Ø: a = 3 mm). Caco-2 cells were cultured and differentiated on the 10%, 15%, 20% gelatin membranes for three weeks to create intestinal barrier models. Caco-2 cells displayed cobblestone morphologies on all membrane conditions (Fig. 4a). Caco-2 cells were confluent in week 1 and kept their stability on the membranes during the 3-week incubation (Fig. 4a). F-actin (phalloidin staining) was expressed at the cell–cell border and is an indicator for tight interactions of cells[30] (Fig. 4a). There was no apparent difference in morphology of cells grown on the respective hydrogels with the different gelatin concentrations (Supplementary Fig. S5).

TEER using chopstick electrodes could not be performed due to lack of space (see above) in the 48- and 96- well inserts. Instead, lucifer yellow (LY) transport was performed to assess barrier function as the permeability rates (Pc) correlate with barrier function[5,31,32]. Using an LY standard curve (Supplementary Fig. S6), transport rates were estimated to be on average 4.1 ± 2.5, 1.5 ± 3.4, 0.5 ± 1.0 nm/s, respectively (mean ± SD) in week 3 (Fig. 4b). By contrast, a gel without cells showed transport rates of 261 ± 113, 260 ± 74, 270 ± 79 nm/s, respectively, over the three different hydrogels (mean ± SD, Fig. 4c). It is considered that Pc ≤ 12 nm/s describes a well-established intestinal barrier function of Caco-2 cells[5,31,32].

Biocompatibility of the inserts for mouse intestinal organoid culture. The biocompatibility of the inserts was studied by culturing mouse intestinal organoids in 3D Matrigel dome culture on the well plate (control), hanging insert plates with filter (PTFE) and gelatin membranes, respectively (Fig. 5). Despite the same initial cell density and Matrigel contents, the culture behaved differently from each other. The organoids on filters and gelatin showed larger aggregates with very few smaller clusters at day one, while culture in wells displayed smaller organoids and many smaller clusters (Fig. 5). The organoids are surrounded by single cells on gelatin but not on the other culture conditions.

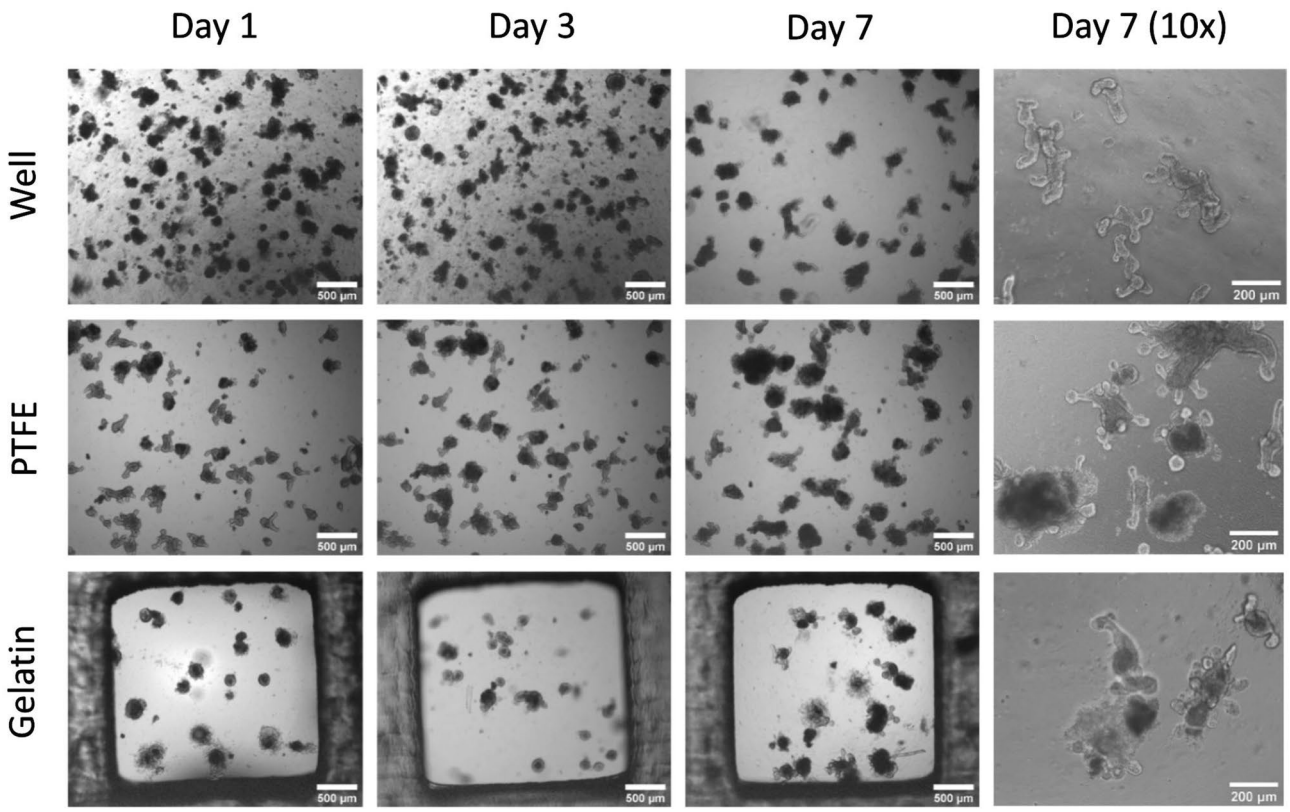

Figure 5. Representative light microscopy images of mouse intestinal organoids in Matrigel dome on hydrophilic PTFE filters and Gelatin membrane. Images (n = 3) were taken during their culture for 7 days in the insert plate wells with a light microscope (scalebar 500 µm for 4 × magnification; scalebar: 200 µm for the 10 × magnification.

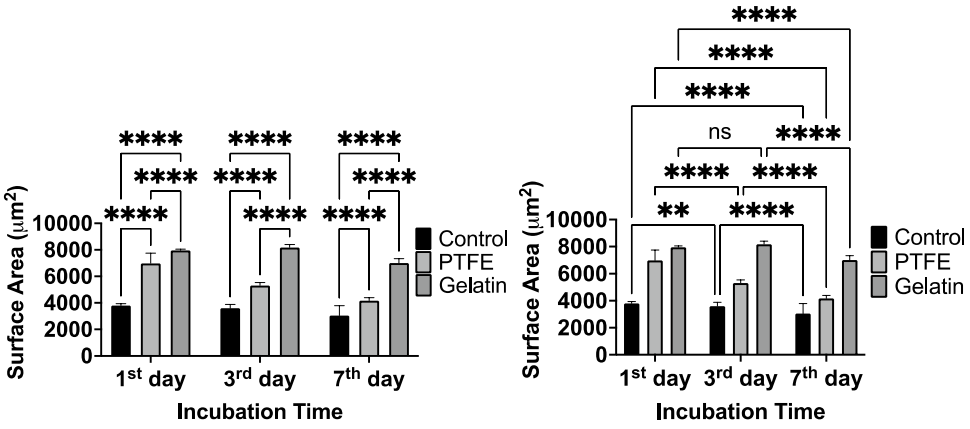

Figure 6. The surface area of organoids during 7 days of culture. *Left* Comparison of size changes of organoids depending on the surface substrate. *Right* Comparison of size changes of organoids during the incubation time. Error bars indicate mean S.D. statistical significance: ns = P > 0.05, **P < 0.01, ****P < 0.0001.

On day 3, the well cultures still had many smaller clusters while organoids began to get compact on the filter but not on gelatin. During the 7-day incubation period, surface areas of organoids were significantly reduced (20% for control, 40% for filter insert, 12% for gelatin inserts) (Fig. 6-Right). The condensation of organoids initiates villus morphogenesis is essential for the maturation of intestinal tissue[33]. Organoids on the gelatin membrane showed approximately two times higher surface area than culture on the filter membrane (Fig. 6-Left) after 7 days. Both insert groups showed a significantly larger surface area of organoids (filter-insert: 4170 µm^2; gelatin-insert: 7000 µm^2) compared to the control group (3000 µm^2) after 7-day incubation. Nevertheless, differentiation and maturation indicators such as extruding cells into the central lumen structure, multiple buds, and multi-crypt structures were observed in all conditions (Fig. 5). On day 10, Live & Dead staining was performed, and it showed

only a few dead cells in the buds in filter-insert groups (Supplementary Fig. S7). By contrast, more cell death and dispersion were observed in the gelatin-insert group. In conclusion, filter-inserts provided a more suitable microenvironment than gelatin-inserts or the well for 3D-cultured mouse intestinal organoids.

Taken together, the Dental LT material is biocompatible for a range of cells lines and processes. The results suggest that Dental LT is biocompatible and compatible with complex processes like organoid formation, which is more demanding than the maturation of a Caco-2 layer which previously has been described[5].

Discussion

Here, we present a small library of inserts that challenge the physical limits of 3D printing, capillary effects, and liquid handling. While 96-well plate format was achievable, only one layer could be used due to the difficulties of liquid handling. 48-well plates could, by contrast, host two usable layers of inserts. The dip-casting method was robust and yielded hydrogel membranes in the range of around 500 µm thicknesses, which correlated with the wall thickness of the 3D-printed insert. The dip-casting process resulted in < 10% variance in thickness. The biocompatibility was tested with mouse intestinal organoids. Organoids formed better on filters than at the bottom of a titer plate well or inserts functionalized with gelatin hydrogels. This indicates that the bottom of the insert should be chosen to match the requirements of the specific experiments.

The membrane-forming method was based on the dip-casting procedure (Supplementary Fig. S3), a simple, quick, and low-cost technique that relies on a range of physical and chemical parameters. Casting between two well-defined molds is less dependent on such parameters but requires a complex apparatus and non-sticky molds. During the dip-casting procedure, the gelatin liquid film is formed due to the adhesion of the gelatin liquid to the rim of the 3D-printed material. The surface tension and other physical properties such as adhesion and cohesive forces[34] contribute to filling the holes. Although there is a significant failure rate (25–30%), the inserts that were successfully functionalized had very consistent properties of the gelatin membrane in terms of transport (Fig. 3) and thicknesses (Fig. 3c,d) and support for intestine barriers (Fig. 4). However, the process is dependent on many parameters, and just a few have been addressed here. Parameters such as immersion time/depth, withdrawal speed, removal of excess gelatin, number of dip-casting cycles, density/viscosity of the hydrogels, evaporation/crosslinking conditions of the solution and material characteristics of the insert may influence the membrane formation. Mixing mTG solution with gelatin creates a time-dependent increase of the viscocity[5,16]. To avoid that, we modified the protocol to control the viscosity. The dip-casting was done at 37 °C, a temperature in which pure gelatin keeps the viscosity for a long time. After the thermal setting of the gelatin at 4 °C, it was subsequently irreversibly crosslinked by adding a solution of mTG. The incubation with mTG was at 37 °C, which would melt the gelatin again. The small volume of mTG solution on top of the cold gelatin membrane likely initiated irreversible crosslinking of the gelatin, especially at the membrane surface, suppressing the dissolution of the gelatin in the mTG solution. Pressing and dragging the inserts toward a sterile, warm petri dish were used after dipping to remove excess gelatin, which would increase the variance of the obtained thickness. However, this process created failures with low-dense (≤ 5% w/v) gelatin solutions or large apertures, suggesting that the soluble gel needs to have a certain viscosity to support the process. Therefore, smaller apertures in the insert bottom were designed to protect the gel from physical strains of the casting process (Supplementary Fig. S2).

The mouse intestinal organoids performed better on filters than gelatin and the wells (Fig. 5). This observation correlated with mass transfer to and away from the culture (Fig. 3b). Presumably, the cultures are fed best through the filter, followed by the gelatin and the bottom of the well. The latter is used in dome culture approaches[35]. The result with intestinal organoids showed that a filter sometimes is preferable. However, a filter does not have any self-adhesive properties and therefore needs to be glued or thermally sealed. Gluing with Dental LT was possible but was not trivial as it was quite easy for the filter to absorb the resin. This resulted in clogging of the pores upon UV crosslinking (Supplementary Fig. S1a-bottom panel). The absorption was minimized by applying the resin on the sides of the insert (Supplementary Fig. S1b). This manual process is, however, cumbersome. A photomask defining the gluing areas followed by a rinse to remove the monomers could be used as an alternative. A similar approach was followed in the reported work by Tan et al.[36] to pattern PTFE membrane via thiol-ene to fabricate an organ-on-a-chip model. Nevertheless, this approach is only suitable for hydrophilic and porous membranes that could absorb photo-crosslinkable glues. Some plastic membranes could attach using heat-based methods[37,38]. However, heat would not be used to assemble membranes due to the thermoset properties of photo-crosslinkable resins[39] such as Dental LT.

SLA or DLP 3D printers have much higher resolution than needed for these inserts. The only problematic parameter is the high aspects ratio combined with relatively thin walls of the insert. Here we used 500 µm walls, but thinner walls would make it possible to fit more layers into a given well size (Fig. 1). However, that will challenge the structural integrity of the inserts unless other materials than the brittle Dental LT can be employed. The most significant issue with fitting many layers of inserts is the capillary effects between the walls and bubble capture. Empirically, we have found that 750 µm distance to be acceptable using the given materials and mediums. A more hydrophobic material would decrease the capillary effects and allow for more layers in each well size. However, this will likely increase the difficulties for liquid handling to avoid e.g., bubbles being trapped in smaller diameter wells. From the organ modelling point of view, many layers may not be needed. For instance, to model the path from the intestine to the brain would require three layers: one for the intestine/blood barrier, one for the liver and one for the blood–brain barrier where the brain model is located at the bottom of the well. Three layers could fit using the current design in 24- to 48-well plates, but with material improvements suppressing capillary effects, a 96-well plate could be utilized (Fig. 1).

Distributed fabrications of customized inserts allow for any adjustment such as the distance between the layers, the number of layers and the material and sizes of the bioactive area in the bottom of each insert. For distributed fabrication to be widespread, it must be cost-efficient and accessible. Many easy-to-use 3D printers

can be hosted in any bio-lab as these printers are intended for custom dentistry applications. The costs of 3D SLA and DLP printers vary a lot depending on one vendor to another ($2000–3000)[40]. Low-cost printers < $1000 are available in the market, but they are still not convincingly tested in biocompatibility of printing resins for cell culture applications. Especially, dental resin formulations such as Dental LT resin from Formlabs are biocompatible but still need to be tested for individual cellular experiments. Moreover, alternative resin formulations and post-processing methods[14] could be explored for biocompatibilities of 3D-printed inserts for customization purposes. A commercial 12-well Transwell inserts cost 8€/ insert (Supplementary Table S1). By contrast, the material cost of an insert 3D-printed with Dental LT resin is about 7 times less despite the costs of the biocompatible resin (Supplementary Table S1). Post-processing takes approximately 30 min of hands-on time for a full plate of inserts, making the price for distributed fabrication competitive.

The bottom defines how the cells will react. As apparent, the Dental LT resin is biocompatible but not bioactive, and cells do not grow directly on it without surface coating with bioactive motives[5,41,42] (Fig. 4). Bioactive and bio-passive patterning can be achieved by controlling these cell adhesion areas. The dip-casting procedure can produce cm^2 large hydrogel films[16]. However, these hydrogels are flexible, which can negatively affect barrier function[5]. Therefore, many smaller apertures (0.5–4 mm in diameter) were tested here. However, the geometry can be designed freely (Supplementary Fig. S2). While not crucial for the barrier function explored, the shape of the cell culture area can align, for instance, muscle cells[27].

To conclude, we showed that 3D-printed inserts are a solid alternative to commercialized inserts that cannot provide the freedom to customize inserts and provide layers of the inserts. It opens the door for any scientists to design their own culture ware more imaginatively and tailored to the experiment. We also reported that dip-casting could offer a straightforward method to create hydrogel membranes, and control experimental conditions would improve the standardization of the method and membrane fabrication efficiency.

Methods

Fabrication of 3D-printed inserts. 3D-printed inserts with different formats and dimensions (Fig. 1c) were designed for tissue-culture-treated (TCT) well plates (Nunc, Thermo Fisher, Slangerup, DK) using Fusion 360 (Autodesk, California, USA) and exported as .STL format files. The print files were processed by adding external supports (with 0.5 density and 0.4 mm touchpoint size and mini rafts with 0.5 mm thickness) and converted to .FORM files in PreForm (v.3.11.0, Formlabs, Somerville, Massachusetts, USA) before printing by a Form 3B 3D printer (Formlabs). Inserts were printed in Dental LT v1 resin (Formlabs) with a layer thickness of 0.1 mm. After printing, inserts were washed in the isopropyl alcohol (IPA) tank (Formlabs) and the support structures were cut off. All prints were subsequently cleaned twice in fresh IPA for 1 h, respectively. After washing, inserts were air-dried and post-cured in the Form Cure UV-oven (Formlabs) for 2 h at 60 °C. After the post-curing step, inserts were submerged in sterile water with a 30 mL resin to 1 L water ratio for a day. Once the prints were air dry, a further 15 min UV exposed for each side for sterilization was performed using Asiga Flash UV Curing Chamber (New South Wales, AUS) under the laminar flow biosafety level 2 (BSL-2) cabinet.

Assembling synthetic and hydrogel membrane. Hydrophilic Polytetrafluoroethylene (PTFE) membrane (BioPore Membrane Filter, with a pore size of 0.4 µm, Millipore®, Sigma-Aldrich, Missouri, USA) was assembled on the bottom of the 3D-printed insert and referred to as Filter inserts). Dental LT was applied to the insert walls and punched out PTFE membrane discs was affixed. Afterwards, the membrane was fixed towards the wall of inserts using a printed cylindrical ring that also stretched the filter. It was post-cured in a Form Cure UV-oven (Formlabs) for 20 min at 60 °C. Sequential IPA washing steps and UV post-curing were conducted as described above.

The gelatin (48723, Sigma-Aldrich) was mixed with 5 mL phosphate-buffered saline (PBS) (D8537, Sigma, St Louis, USA) and heated to 37 °C. The solution was adjusted to pH 7 by titrating with a 10 M NaOH. For a 5 mL 10% solution, approximately 3.7 µL of 10 NaOH was added. For 5 mL 15% and 20% gelatin solutions, the corresponding values were 5.7 and 7.7 µL. Chloroform was added (0.5% v/v) to sterilize the solution. These standardized volumes made it possible to mix all components and place the tubes a in a 37 °C water bath until the gelatin was fully dissolved to obtain a sterile working solution with the correct pH. Once dissolved, gelatin solutions were poured to a pre-heated sterile petri dish (Nunc, Thermo Fisher Scientific, USA) on the homemade hot plate (Supplementary Fig. S3) set at 50 °C under the laminar flow biosafety cabinet. Note, the LAF bench requires an exhaust into free air as the chloroform will evaporate quickly. Sterile 3D-printed inserts without PTFE membrane were immersed in the gelatin solution for 5 s until the bottom was covered with hydrogel liquid. The inserts were fully withdrawn and pressed on a sterile pre-warmed petri dish lid on the homemade Peltier unit at 50 °C to form a thin hydrogel membrane by removing the extra hydrogel liquid. After dip-casting the membranes, inserts were placed to the cell culture plate and placed at 4 °C for at least 20 min to thermally (reversible) crosslink the gelatin. In the meantime, 15 U/mL microbial Transglutaminase (mTG) solution was prepared by mixing mTG (1002, 100 U/g, ACTIVA® TI, Ajinomoto Food Ingredients LLC, Illinois, USA) with PBS. The mTG solution was vortexed until the mTG powder was fully dissolved and filtered through a 0.45 µm sterile syringe filter (Avantor, VWR, USA). After the reversible crosslinking of the gelatin membranes, the mTG solution was added to wells with the amount to cover insert well surfaces (for 96-well: 50 µL; for 48-well: 100 µL; for 24-well: 200 µL). The plates were placed in an incubator at 37 °C for 1 h to crosslink membranes irreversibly. After crosslinking, the sterile hydrogel membranes were washed in PBS for 10 min three times. All inserts with gelatin membrane (Gelatin-inserts) were either used for cell culture experiments directly or stored in the fridge for max. 2 weeks or dried overnight in the incubator and stored at room temperature for maximum 1 month prior to use.

Mass transport through membranes. The permeability of 96-well strip inserts was tested by mass transport studies of Fluorescein sodium salt (F6377, Sigma-Aldrich). Inserts were placed in a 96-well plate and, 225 µL of pre-heated (to 37 °C) PBS was added to the basolateral side, and 75 µL of 50 µM Fluorescein sodium salt was added to the apical side in each insert. The transport study was performed at 37 °C with 100 rounds per minute (rpm) shaking under dark conditions for 2 h. After the incubation, samples of 50 µL were transferred to a 96-well plate to analyze their Relative Fluorescence Units (RFU) emission at an excitation wavelength of 460 nm and emission wavelength of 515 nm (Spark® multimode microplate reader, TECAN, Männedorf, CH). A standard curve was obtained by evaluating RFU of fluorescein sodium salt in different concentrations from 50 µM to 0 µM, and RFU data was collected and analyzed using GraphPad Prism (version 9.0.0 for macOS, GraphPad Software, La Jolla California USA, www.graphpad.com).

Mechanical testing of hydrogel membranes. Gelatin hydrogel discs were prepared using the sandwich casting method. Two polymethyl methacrylate (PMMA) slides with a thickness of 3 mm were coated with 5% (w/v) PVA (Polyvinyl alcohol)–EtOH (ethanol) solution used as a mold released agent and air-dried. Afterwards, two 1 mm thick-PMMA slides were glued on two pairs of 3 mm-thick PMMA slides (base) with PVA solution. 500 µL gelatin solution was cast on one of the base slides, and the other base slide was closed on top of the other pair. Then, gelatin discs with 1 mm thickness were crosslinked in the fridge at 4 °C. After crosslinking, the gelatin discs were carefully removed by flushing mTG solution between the base slides and incubated in mTG loaded petri dish for 1 h in the incubator at 37 °C. Irreversibly crosslinked gelatin discs were washed with PBS twice and stored in a closed petri dish with PBS to avoid dehydration. Rheological properties were characterized using a rheometer (TA Instruments, DHR 20, New Castle, Delaware, USA) equipped with a 20 mm diameter cylinder with parallel plate geometry and a gap of 1 mm. Tests in gelatin discs were performed at 37 °C. Manufactured samples were loaded on the lower Peltier plate of the rheometer and trimmed to adjust the shape to the upper parallel plate geometry. First, a frequency sweep test was performed from 200 rad/s to 1 rad/s at the strain of 0.01% to calibrate the instrument. Then, the amplitude/strain sweep test was performed from 0.2 to 200% at 1 rad/s, and the results were used to evaluate material properties. Finally, time sweep up to 1000 s (about 16 and a half minutes), at 5% strain and 1 rad/s to ensure that the material was stable in the estimated time. Stiffness and elasticity of the developed hydrogels were assessed from shear modulus, and Young's modulus of each disc was obtained as previously described[16]. The shear modulus or complex modulus (G^*) was calculated by:

$$G^* = \sqrt{G'^2 + G''^2} \tag{1}$$

where, G' is the storage modulus, and G" is the loss modulus.

Then, Young's modulus (E) was obtained as:

$$E = 2G^*(1 + \mu) \tag{2}$$

where, µ is the Poisson's ratio, assumed to be 0.5 as the hydrogels are considered incompressible materials.

Thickness measurement of hydrogel membranes. For measurement of gelatin membrane thickness, fluorescence intensity analysis was performed. Fluorescent gelatin was prepared by mixing 15% (w/v) gelatin powder in 1 µg/mL Fluorescein sodium salt (F6377, Sigma-Aldrich)—PBS solution. First, 6 liquid coupled slides were created by using the similar sandwich method described before to form the standard curve of fluorescence intensity of different heights provided by stacking coverslips (150 µm thick) onto a 1 mm thick glass microscope slide (base) and 500 µL fluorescence gelatin was pipetted onto the base slide and covered with the other pair of the base slide. Inserts (96- and 48-well format strips) were fabricated as described above and placed onto a base slide (Avantor, VWR, USA). Gelatin membranes were imaged with Zeiss™ AxioObserver Z1 epifluorescence microscope (Carl Zeiss MicroImaging GmbH, Gottingen, Germany). All images (n = 5) were obtained at an emission wavelength range of 495 nm to 517 nm by a LED (Light-emitting Diode) laser with filter set 38 HE (Carl Zeiss MicroImaging GmbH) and within 150–900 µm thickness range. All the .TIF files were processed with Zeiss Zen Blue 3.4 Lite Digital Imaging Software (version 3.4.91.00000, Carl Zeiss Microscopy GmbH) to correlate membrane height according to fluorescence intensity.

Swelling ratio of hydrogel membranes. For determination of thickness change of hydrogel membranes, 15% (w/v) Gelatin membranes were assembled to 48-well format Gelatin-inserts as mentioned above. Membranes were punched with 3 mm diameter biopsy skin punch (Acu-Punch®, Acuderm Inc., USA)) as freshly crosslinked (wet, n = 5), and swollen (n = 5) in PBS for 1 h at 37 °C to mimic equilibrate status of membranes and dehydrated overnight at room temperature (dry, n = 5). The thickness of punched membrane discs was measured by using a micrometer screw (Mitutoyo, JP) and the swelling ratio (SF_v) was calculated by deriving the equation below[43] (diameter was taken constant due to the dry, wet, and swollen membranes were taken out of the inserts using the puncher:

$$SF_v = \frac{\pi r_f^2 h_f}{\pi r_0^2 h_0} = \frac{(d_t/2)^2 h_f}{(d_0/2)^2 h_0} = \frac{\cancel{d_t^2} h_f}{\cancel{d_0^2} h_0} = \frac{h_f}{h_0} \tag{3}$$

where, r_f is the final radius (µm), h_f is the final height (µm), r_0 is the initial radius (µm), h_0 is the initial height (µm), d_f is the final diameter (µm), d_0 is the initial diameter (µm).

Cell types and culture conditions. Human epithelial colon carcinoma cells (Caco-2, passage 55–65, 09042001, European Collection of Authenticated Cell Cultures (ECACC), Salisbury, UK) were cultured in T-75 cell culture flasks (Sarstedt, Nümbrecht, Germany) in High-glucose Dulbecco's DMEM medium (Sigma-Aldrich) with 10% (v/v) fetal bovine serum (FBS, Hyclone™, CA), 1% (v/v) non-essential amino acids (NEAA, Gibco, Fisher Scientific, Slangerup, Denmark), and penicillin (100 U/mL)-streptomycin (100 µg/mL) (P/S, Sigma-Aldrich). The Caco-2 cells were seeded on hydrogel membranes at a density of 80,000 cells/cm^2 and incubated for 3 weeks before analyses. Human umbilical vein endothelial cells (HUVEC, passage 5–9, Cell Applications Inc., California, USA) were cultured in endothelial culture growth medium (ECGM, Cell Applications) with 10% (v/v) FBS and 1% (v/v) P/S. The HUVEC cell cultures were seeded on gelatin micro-membranes and Matrigel-coated PTFE membranes at a density of 100,000 cells/cm^2 and incubated for up to 1 week before analyzes. Cells were split with trypsin-ethylenediaminetetraacetic acid (EDTA) for 3–5 min upon ~ 90% confluency. After use, the gelatin membranes could be dissolved using trypsin–EDTA to reuse the 3D-printed parts. Mouse intestinal organoids were cultured according to the protocol from StemCell Technologies (Cambridge, UK). Intestinal crypts were thawed, centrifugated and re-suspended in Matrigel (Corning, New York, USA) and transferred into 24-well PTFE membrane assembled insert plates. After polymerization, IntestiCult mouse organoid growth medium (StemCell Technologies) supplemented with 1% (v/v) P/S was overlaid on the gel in each well. All cell lines and organoids were maintained in an incubator (37 °C, 100% Humidity, 5% CO_2) with the culture medium replaced every 2 days.

F-actin, nuclei, live/dead stains. For F-actin (Alexa Fluor™ 594 Phalloidin, Invitrogen) and Hoechst 33342 (nuclei, Invitrogen™, Thermo Fisher) staining, samples were washed for 15 min in PBS followed by fixation in 2% (v/v) PFA in PBS for 2 min and fixation in 4% (v/v) PFA in PBS for 13 min at room temperature. PFA was aspirated from the samples and washed three times in PBS. Then, the samples were incubated with the stain (5 µL phalloidin and 1 µg/mL Hoechst 33342 in PBS diluted in 200 µL PBS with 1% (v/v) bovine serum albumin (BSA, Sigma)) for 20 min at room temperature. The samples were washed three times in PBS and left in PBS.

For live/dead staining (LIVE/DEAD™ Viability/Cytotoxicity Kit, L3224, Invitrogen™, Thermo Fisher) was used. Samples were washed three times in PBS and stained in 500 µL of a solution with Ethidium homodimer-1 (8 nM, EthD-1) and Calcein AM (4 mM) for 1 h at room temperature. The samples were washed in PBS two times and then kept in PBS to keep the hydrogel growth-matrices moisturized.

Microscopy imaging. Phase-contrast bright-field micrographs were obtained using a Zeiss Primovert microscope (Carl Zeiss MicroImaging GmbH, Gottingen, Germany) with the following objective: Plan-Achromat 4x/0.10 while staining images were acquired with Zeiss™ AxioObserver Z1 epifluorescence microscope (Carl Zeiss MicroImaging GmbH) with the following objectives: EC Epiplan-NEOFLUAR 5x/0.16 Ph1 M27: EC Epiplan-NEOFLUAR 10x/0.3 Ph1, LD Epiplan-NEOFLUAR 20x/0.4 Korr M27. The obtained images were fitted with scale bars and were processed in Zeiss Zen Blue 3.4 Lite Digital Imaging Software (v. 3.4.91.00000, Carl Zeiss Microscopy GmbH) and ImageJ/Fiji[44]. Surface area analysis of organoids were performed using the macro; OrgM[45] on the ImageJ/Fiji.

Transport of lucifer yellow. Single inserts were placed in a 96-well plate and 225 µL (well compartment) of pre-heated (to 37 °C)) HBSS transport buffer (HBSS (1x), Sodium bicarbonate (0.0375% w/v), HEPES (10 mM), BSA (0.05% w/v, pH 7.4) was added to the basolateral side and 75 µL of 60 µM lucifer yellow was added to the apical side in each insert. The transport study was performed at 37 °C with 100 rounds per minute (rpm) shaking under dark conditions for 2 h for Caco-2 cells. After the transport experiment, the 100 µL samples (from 1st insert and the well compartments), 50 µL samples (from 2nd insert compartment) and 50 µL HBSS transport buffer were transferred to a 96-well plate to analyze their Relative Fluorescence Units (RFU) emission at an excitation wavelength of 428 nm and measuring emission at 536 nm. The permeability coefficients (Pc, nm/s) were calculated by the equation:

$$Pc = (V_r \times C_f)/(C_i \times A \times t) \quad (4)$$

where, Pc is the permeability coefficient (nm/s), V_r is the receiver volume in mL, A is the membrane growth area in cm^2, C_i is the initial apical concentration (µM), C_f is the final receiver concentration (µM), t is the assay time in seconds.

Statistical analysis. The data are presented as the sample sizes (n), means, standard deviations (SDs). Calculations were done using Microsoft Excel (Version 2016, Microsoft Office, Seattle, Washington) and data were analyzed using GraphPad Prism (version 9.0.0 for macOS, GraphPad Software, La Jolla California USA, www.graphpad.com). Saphiro–Wilk for normality testing of multiple comparisons. Data was analyzed by ordinary one-way ANOVA or 2way ANOVA ($\alpha = 0.05$) with post-hoc Tukey's multiple comparison tests for equality of means among groups in membrane characterization, lucifer yellow transport of stacked co-culture and biocompatibility of organoids experiments. P-values were obtained using Bartlett's corrections and determined significant differences when p-value < 0.05. F-test for Welch's t-test was performed to compare variances of membrane thicknesses. The significant differences are highlighted with symbols on figures.

Data availability

STL files of 3D-printed designs are available from the authors upon request. A list of links to repository will be hosting the respective. STL is provided below: https://www.thingiverse.com/asliaybikedogan/collections/customized-3d-printed-inserts.

Received: 17 December 2021; Accepted: 16 February 2022
Published online: 07 March 2022

References

1. Sung, J. H., Kam, C. & Shuler, M. L. A microfluidic device for a pharmacokinetic-pharmacodynamic (PK-PD) model on a chip. *Lab Chip* **10**, 446–455 (2010).
2. Shinha, K., Nihei, W., Ono, T., Nakazato, R. & Kimura, H. A pharmacokinetic-pharmacodynamic model based on multi-organ-on-a-chip for drug-drug interaction studies. *Biomicrofluidics* **14**, 044108 (2020).
3. Abaci, H. E. & Shuler, M. L. Human-on-a-chip design strategies and principles for physiologically based pharmacokinetics/pharmacodynamics modeling. *Integr. Biol.* **7**, 383–391 (2015).
4. Edington, C. D. *et al.* Interconnected microphysiological systems for quantitative biology and pharmacology studies. *Sci. Rep.* **8**, 1–18 (2018).
5. Leth Jepsen, M. *et al.* 3D printed stackable titer plate inserts supporting three interconnected tissue models for drug transport studies. *Adv. Biosyst.* **4**, 1900289 (2020).
6. Trapecar, M. *et al.* Gut-liver physiomimetics reveal paradoxical modulation of IBD-related inflammation by short-chain fatty acids. *Cell Syst.* **10**, 223-239.e9 (2020).
7. Shafran, Y. *et al.* Co-culture hydrogel micro-chamber array-based plate for anti-tumor drug development at single-element resolution. *Toxicol. Vitro* **71**, 105067 (2021).
8. Altay, G. *et al.* Self-organized intestinal epithelial monolayers in crypt and villus-like domains show effective barrier function. *Sci. Rep.* **9**, 1–14 (2019).
9. García-Rodríguez, I., Sridhar, A., Pajkrt, D. & Wolthers, K. C. Put some guts into it: Intestinal organoid models to study viral infection. *Viruses* **12**, 1288 (2020).
10. Youhanna, S. & Lauschke, V. M. The past, present and future of intestinal in vitro cell systems for drug absorption studies. *J. Pharm. Sci.* **110**, 50–65 (2021).
11. Corning. Transwell_Permeable Supports. *Instructions for Use* https://www.corning.com/catalog/cls/documents/protocols/Transwell_InstructionManual.pdf.
12. Hod Lipson, M. K. Fabricated: The New World of 3D Printing. *Google Books*.
13. Mohanty, S. *et al.* Fabrication of scalable and structured tissue engineering scaffolds using water dissolvable sacrificial 3D printed moulds. *Mater. Sci. Eng., C* **55**, 569–578 (2015).
14. Skliutas, E. *et al.* A bio-based resin for a multi-scale optical 3D printing. *Sci. Rep.* **10**, 1–9 (2020).
15. Grigaleviciute, G., Baltriukiene, D., Bukelskiene, V. & Malinauskas, M. Biocompatibility evaluation and enhancement of elastomeric coatings made using table-top optical 3D printer. *Coatings* **10**, 254 (2020).
16. Jepsen, M. L., Nielsen, L. H., Boisen, A., Almdal, K. & Dufva, M. Characterization of thin gelatin hydrogel membranes with balloon properties for dynamic tissue engineering. *Biopolymers* **110**, e23241 (2019).
17. Akther, F., Little, P., Li, Z., Nguyen, N. T. & Ta, H. T. Hydrogels as artificial matrices for cell seeding in microfluidic devices. *RSC Adv.* **10**, 43682–43703 (2020).
18. Sung, J. H., Yu, J., Luo, D., Shuler, M. L. & March, J. C. Microscale 3-D hydrogel scaffold for biomimetic gastrointestinal (GI) tract model. *Lab Chip* **11**, 389–392 (2011).
19. Benjamin, A. D. *et al.* Light-based 3D printing of hydrogels with high-resolution channels. *Biomed. Phys. Eng. Express* **5**, 025035 (2019).
20. Taebnia, N. *et al.* Dual-material 3D-printed intestinal model devices with integrated villi-like scaffolds. *ACS Appl. Mater. Interfaces* **13**, 58434–58446 (2021).
21. Onfroy-Roy, L., Hamel, D., Foncy, J., Malaquin, L. & Ferrand, A. Extracellular matrix mechanical properties and regulation of the intestinal stem cells: When mechanics control fate. *Cells* **9**, 2629 (2020).
22. Handorf, A. M., Zhou, Y., Halanski, M. A. & Li, W. J. Tissue stiffness dictates development, homeostasis, and disease progression. *Organogenesis* **11**, 1–15 (2015).
23. Xia, T., Liu, W. & Yang, L. A review of gradient stiffness hydrogels used in tissue engineering and regenerative medicine. *J. Biomed. Mater. Res. A* **105**, 1799–1812 (2017).
24. Cruz-Acuña, R. *et al.* PEG-4MAL hydrogels for human organoid generation, culture, and in vivo delivery. *Nat. Protoc.* **13**, 2102–2119 (2018).
25. Gustafsson, L. *et al.* Recombinant spider silk forms tough and elastic nanomembranes that are protein-permeable and support cell attachment and growth. *Adv. Funct. Mater.* **30**, 2002982 (2020).
26. Rozmus, E. *A Novel 3D PDAC Model System Developed with the Use of Decellularized Matrix Scaffolds* (2019).
27. Jensen, J. H. *et al.* Large-scale spontaneous self-organization and maturation of skeletal muscle tissues on ultra-compliant gelatin hydrogel substrates. *Sci. Rep.* **10**, 1–10 (2020).
28. Pimentel, C. R. *et al.* Three-dimensional fabrication of thick and densely populated soft constructs with complex and actively perfused channel network. *Acta Biomater.* **65**, 174–184 (2018).
29. Yung, C. W. *et al.* Transglutaminase crosslinked gelatin as a tissue engineering scaffold. *J. Biomed. Mater. Res. A* **83**, 1039–1046 (2007).
30. Li, B. R. *et al.* In vitro and in vivo approaches to determine intestinal epithelial cell permeability. *J. Vis. Exp.* https://doi.org/10.3791/57032 (2018).
31. Patient, J. D. *et al.* Nanofibrous scaffolds support a 3D in vitro permeability model of the human intestinal epithelium. *Front. Pharmacol.* **10**, 456 (2019).
32. Ghaffarian, R. & Muro, S. Models and methods to evaluate transport of drug delivery systems across cellular barriers. *J. Vis. Exp.* https://doi.org/10.3791/50638 (2013).
33. Kwon, O., Han, T. S. & Son, M. Y. Intestinal morphogenesis in development, regeneration, and disease: The potential utility of intestinal organoids for studying compartmentalization of the crypt-villus structure. *Front. Cell Dev. Biol.* **8**, 1192 (2020).
34. Schonhorn, H. Wetting phenomena pertaining to adhesion. *Prog. Surf. Membr. Sci.* **5**, 121–137 (1972).
35. Shin, W. *et al.* Spatiotemporal gradient and instability of Wnt induce heterogeneous growth and differentiation of human intestinal organoids. *iScience* **23**, 101372 (2020).
36. Tan, H.-Y.H.-Y. *et al.* A multi-chamber microfluidic intestinal barrier model using Caco-2 cells for drug transport studies. *PLoS ONE* **13**, e0197101 (2018).
37. Scott, S. M. & Ali, Z. Fabrication methods for microfluidic devices: An overview. *Micromachines* **12**, 319 (2021).
38. Heat Sealing. In *Handbook of Plastics Joining* 121–126 (Elsevier, 2009). https://doi.org/10.1016/B978-0-8155-1581-4.50014-7.

39. Wang, B., Zhang, Z., Pei, Z., Qiu, J. & Wang, S. Current progress on the 3D printing of thermosets. *Sci. Rep* **11**, 1–11. https://doi.org/10.1007/s42114-020-00183-z/Published (2021).
40. *Best Resin 3D Printers in 2021—SLA, DLP, LCD*. https://www.aniwaa.com/buyers-guide/3d-printers/the-best-resin-3d-printer-sla-and-dlp/.
41. Koroleva, A. *et al.* In vitro development of human iPSC-derived functional neuronal networks on laser-fabricated 3D scaffolds. *ACS Appl. Mater. Interfaces* **13**, 7839–7853 (2021).
42. Moreno-Rivas, O., Hernández-Velázquez, D., Piazza, V. & Marquez, S. Rapid prototyping of microfluidic devices by SL 3D printing and their biocompatibility study for cell culturing. *Mater. Today* **13**, 436–445 (2018).
43. Sievers, J. *et al.* Determination of hydrogel swelling factors by two established and a novel non-contact continuous method. *J. Appl. Polym. Sci.* **138**, 50326 (2021).
44. Schindelin, J. *et al.* Fiji: An open-source platform for biological-image analysis. *Nat. Methods* **9**, 676–682 (2012).
45. Cai, E. & Thomas, R. A. *OrgM A Jython Macro for Automated Measurements Organoid Size (Diameter and Area) and Shape (Roundess and Circularity) from Brightfield Images*. https://github.com/neuroeddu/OrgM (2019).

Acknowledgements

This project has received funding from the European Union's Horizon 2020 research and innovation program under the Marie Skłodowska-Curie grant agreement No. 812673 and was conducted within the Organoids for Virus Research (OrganoVIR) network. A.A.D. and M.D. would like to thank Dr. Hakan Gurbuz from Technical University of Denmark to supply the homemade Peltier unit.

Author contributions

A.A.D.: Project administration, Conceptualization, Data curation, Formal analysis, Investigation, Methodology, Validation, Visualization, Writing—original draft, review, editing. M.D.: Project administration, Conceptualization, Resources, Supervision, Writing—review & editing.

Competing interests

The authors declare no competing interests.

Additional information

Supplementary Information The online version contains supplementary material available at https://doi.org/10.1038/s41598-022-07739-7.

Correspondence and requests for materials should be addressed to M.D.

Reprints and permissions information is available at www.nature.com/reprints.

Publisher's note Springer Nature remains neutral with regard to jurisdictional claims in published maps and institutional affiliations.

Customized 3D-printed stackable cell culture inserts tailored with bioactive membranes

Asli Aybike Dogan[1], Martin Dufva[1,*]
[1]Dept. of Health Technology, Technical University of Denmark, 2800 Kgs. Lyngby, Denmark.
*dufva@dtu.dk

Supporting Information

Table S1. The source, printing time and cost of materials for fabricating inserts comparing the cost of commercialized peers.

Material/insert type	Amount per unit	Material amount	Printing time (h)	Total Cost (€)	Source of materials
Dental LT	-	1 L	-	482.79*	https://formlabs.com/store/dental-lt-clear-resin/
Millipore PTFE	-	1 Roll	-	1360*	https://www.sigmaaldrich.com/DK/en/product/mm/bgcm00010
Gelatin	-	500 g	-	96.10*	https://www.sigmaaldrich.com/DK/en/product/sial/48723?context=product
IPA	-	1 L	-	5.42*	https://uk.vwr.com/store/product/732526/2-propanol-99-8-hipersolv-chromanorm-for-hplc
96-well plate format 4-well strips stack 1st layer	42	~ 17.74 mL	~ 3	10.47**	-
96-well plate format 4-well strips 2nd layer	42	~ 22.59 mL	~ 3	12.82**	-
96-well insert plate	1	~ 65 mL	~ 4	33.60**	
48-well plate format 3-well strips 1st layer	24	~ 34.62 mL	~ 3	18.63**	-
48-well plate format 3-well strips 2nd layer	24	~ 24.23 mL	~ 3	13.61**	-
24-well plate insert (For PTFE membrane)	1	~ 56.20 mL	~ 4	29.05**	-
24-well plate insert (For Gelatin membrane)	1	~ 55.51 mL	~ 4	26.80**	-

* Price is acquired from the 2021 price list of the company.
** Price calculation based on the used volume of resin, IPA, gelatin, and PTFE membrane for all amount of per unit.

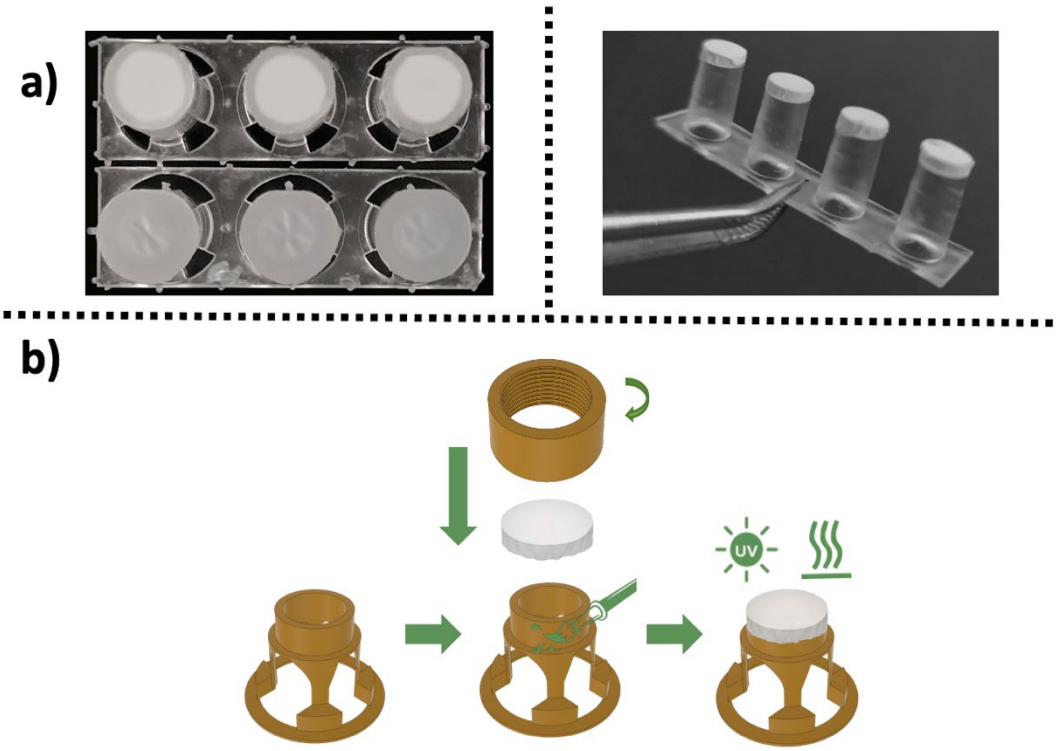

Figure S1. **a)** ***Left:*** 48-well format strip inserts glued from off-set of apertures (***top:*** partially clogged PTFE membrane; ***bottom:*** Clogged PTFE membrane (***white area:*** view of dry hydrophilic PTFE membrane; ***shaded area:*** view of wet/glued hydrophilic PTFE membrane). ***Right:*** 96-well format strip insert glued from side walls of wells). **b)** Illustration of hydrophilic PTFE membrane glued with Dental LT resin to the 3D-printed inserts.

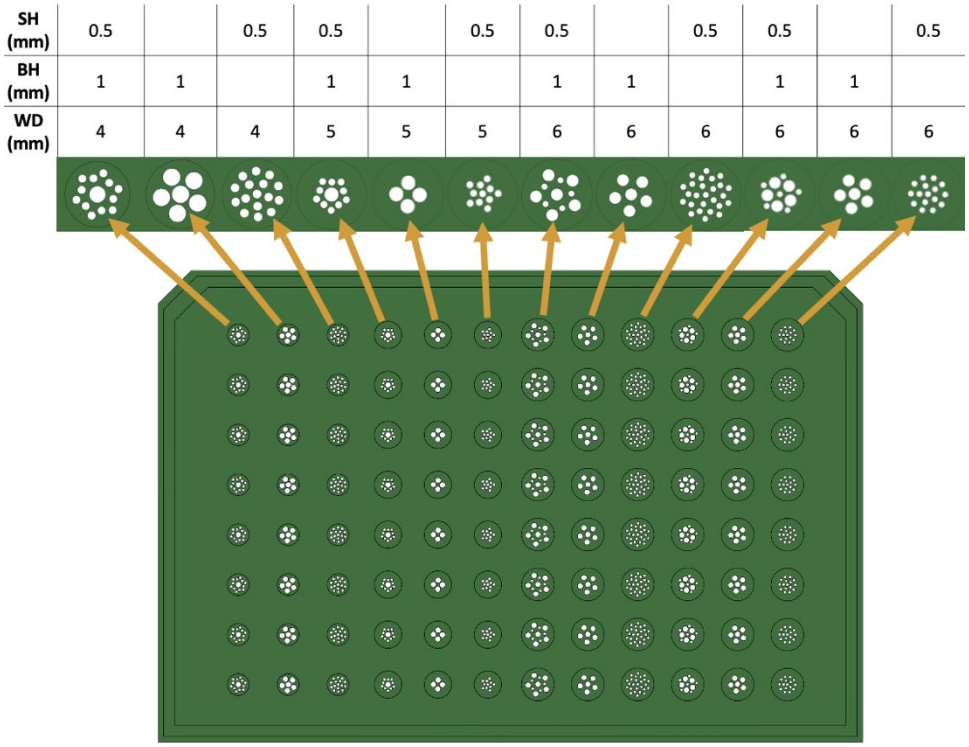

Figure S2. Illustration of 96-well format insert plate with different aperture patterns. *SH:* Small holes (Ø=0.5 mm), *BH:* Big holes (Ø=1 mm), *WD:* Well diameter (Ø=4-6 mm).

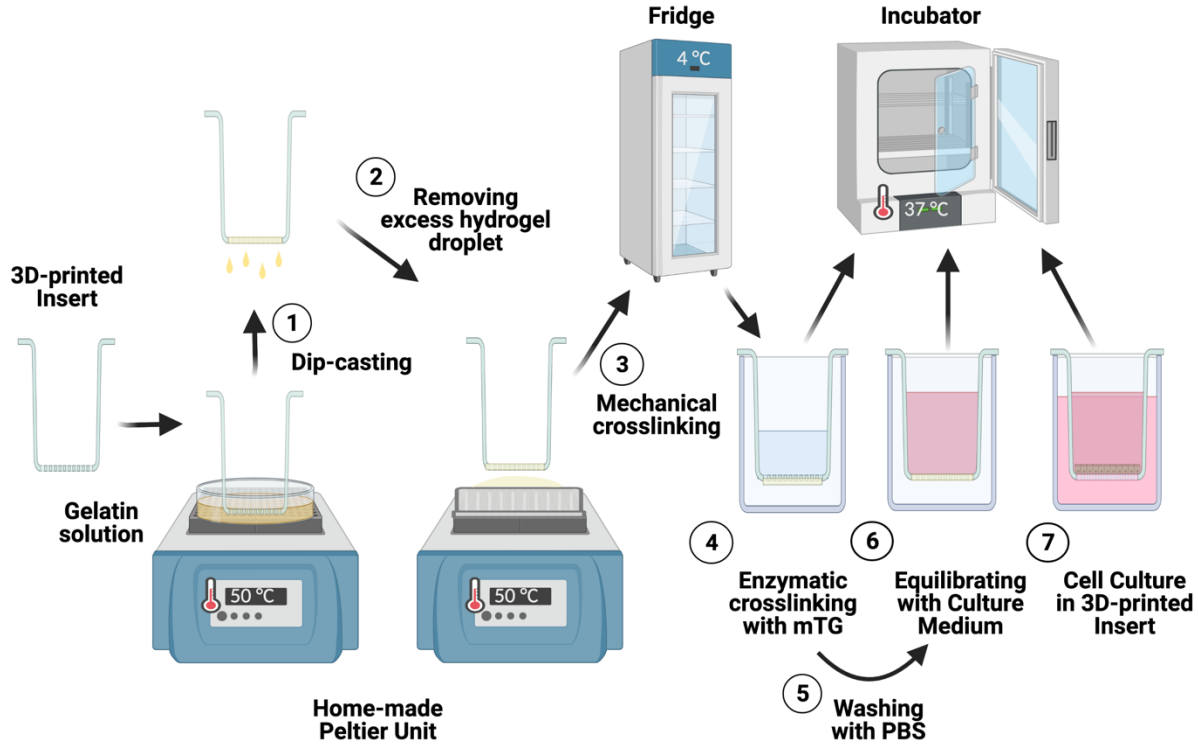

Figure S3. Illustrative outline of **1-2)** the dip-casting method were performed at approx. 37 °C using a home-made Peltier unit at 50 °C for Gelatin hydrogel membrane assembling to the 3D-printed inserts platforms. **3)** Gelatin membranes were mechanically crosslinked at 4 °C for at least 20 mins. Then, **4)** enzymatically crosslinked at 37 °C for 1 h. **5-7)** Membranes were washed and equilibrating with culture media before cell culture experiments. *Created with BioRender.com*

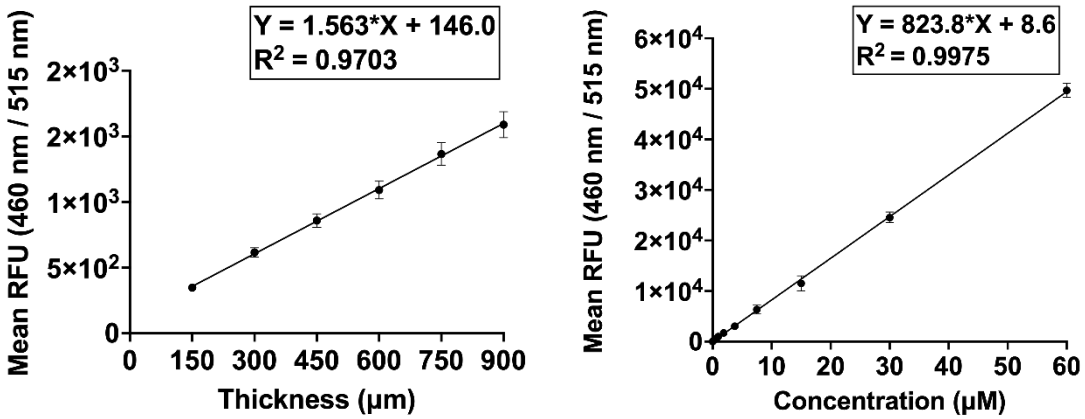

Figure S4. ***Left:*** Standard curve of fluorescein intensity for Gelatin membrane thickness measurement. ***Right:*** Standard curve of Fluorescein (0-60 µM) for Gelatin membrane permeability evaluation.

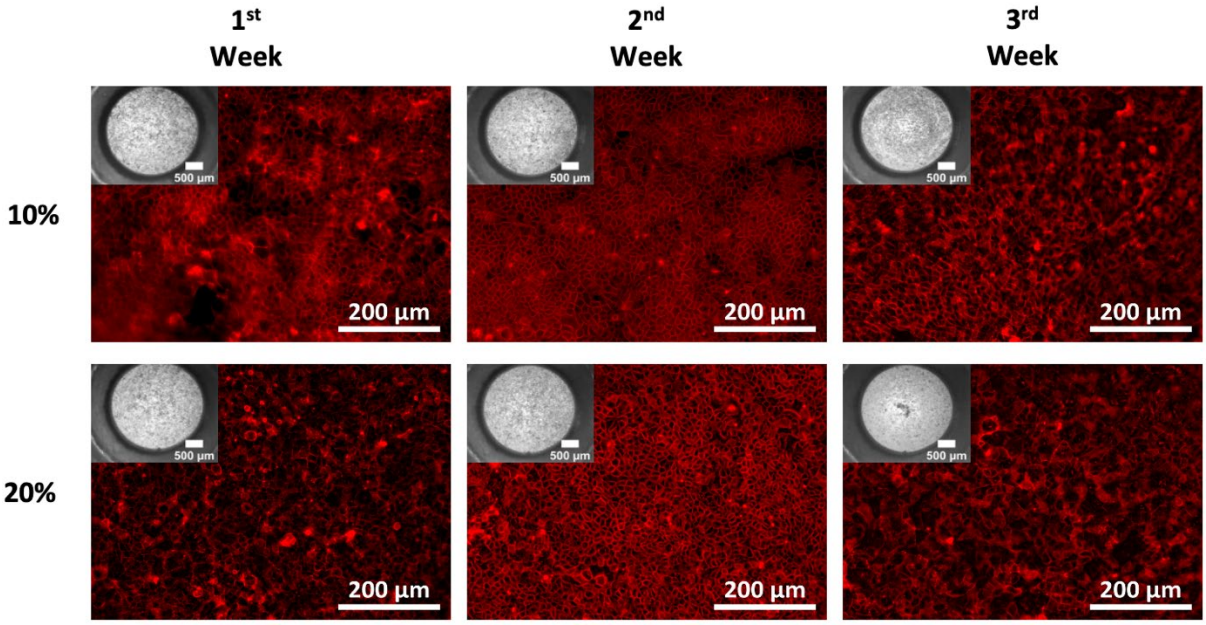

Figure S5. Biological validation of 96-well inserts. **a)** Growth of Caco-2 cells on the 10% and 20% (w/v) gelatin membranes over three weeks. Insert apertures at the bottom are shown at upper panels of fluorescence images (the magnification: 4x; scale bars: 500 µm), and the F-actin (red) stain of the cells on the hydrogel membranes (scale bars: 200 µm; the magnification was 20x).

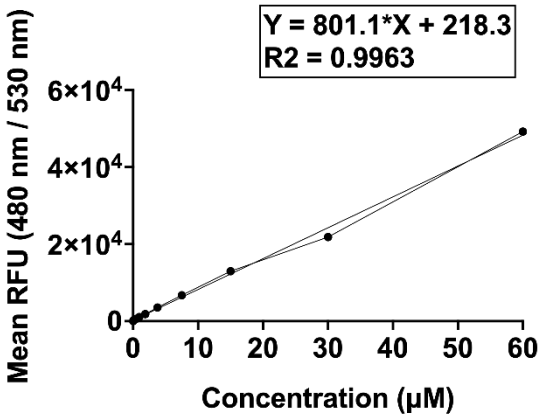

Figure S6. Standard curve of Lucifer Yellow (0-60 µM) for calculation of permeability coefficient to evaluate barrier functions of Caco-2 cells.

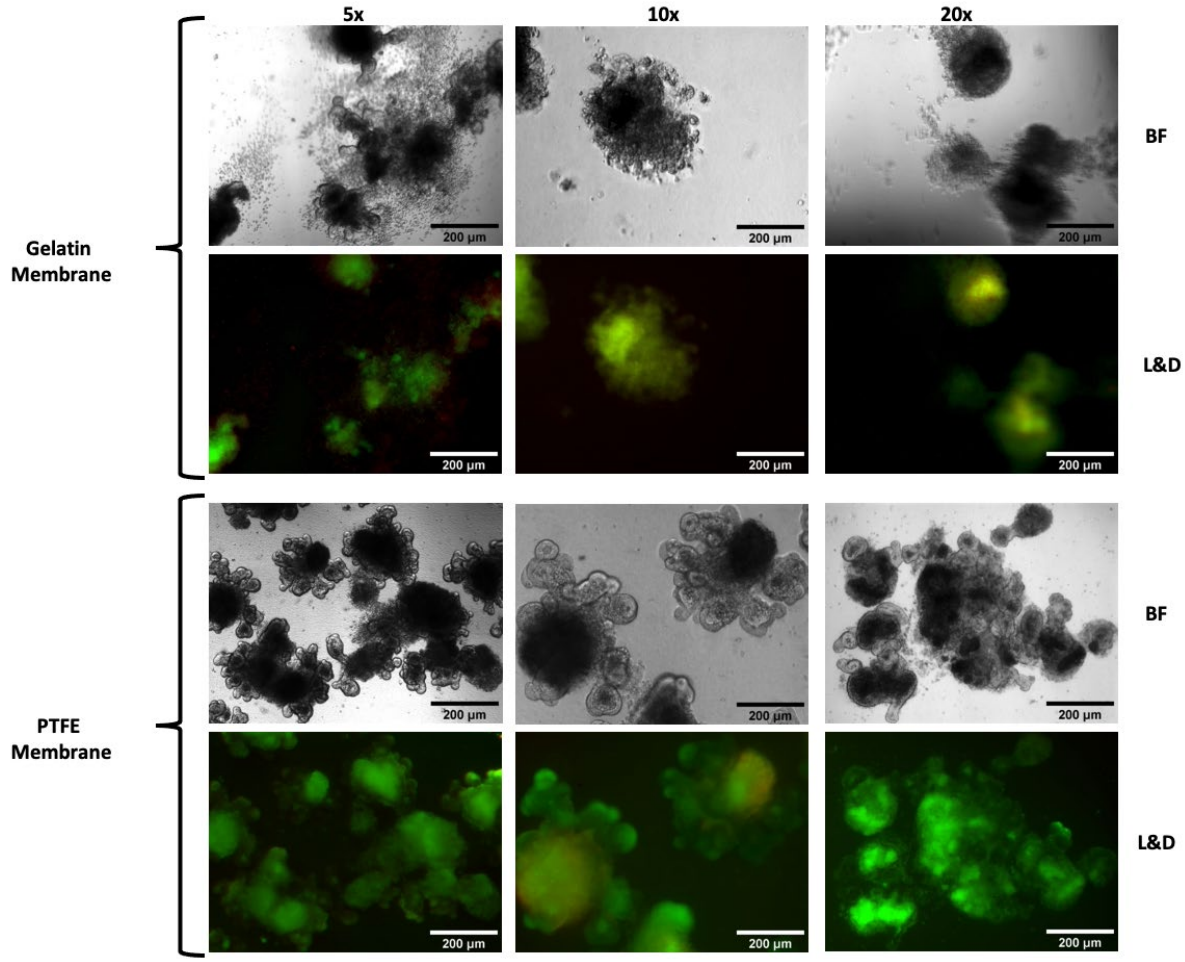

Figure S7. Brightfield (BF) and Live & Dead (L&D) staining photos of mouse intestinal organoids on day 10. Organoids in 24-well format square grid patterned Gelatin- and filter-insert plates. Scalebar: 200 µm, the magnification: 5x-10x-20x)

Chapter 6

PAPER II

Heterogenous morphogenesis of Caco-2 cells reveals that flow induces 3D growth at high cell densities but is insufficient to induce intestinal cell maturation in 2D

Asli Aybike Dogan, Martin Dufva

Submitted (2022)

Heterogenous morphogenesis of Caco-2 cells reveals that flow induces 3D growth at high cell densities but is not sufficient to induce intestinal cell maturation in 2D

*Asli Aybike Dogan, and Martin Dufva**

Department of Health Technology, Technical University of Denmark, 2800, Kgs. Lyngby, Denmark
*E-mail: dufva@dtu.dk

Abstract

Caco-2 cell monolayers are widely used in vitro models for intestinal epithelial barriers. Depending on the seeding density or perfusion, they can grow in 2D monolayers or 3D structures associated with improved cell functions. Here, we introduce a customized hanging insert as a perfusion device using a rocker unit to provide a dynamic flow microenvironment for Caco-2 monolayers. The results show that both flow and cell seeding density in combination are necessary for the 3D morphogenesis of Caco-2 cells. Flow increases columnar cells in 2D cell monolayers. This correlates with increased TEER, reduced lucifer yellow permeability, and increases in tight junction marker (ZO-1) expression. The barrier function of 2D layers could be tuned with the flow in low-density cultures. 2D static and 2D dynamic cell monolayers have similar morphology and heterogeneity in the expression of mucin-2 (MUC-2) and Villin markers. By contrast, 3D cellular structures had higher expression of MUC-2, ZO-1, F-actin, and Villin than the static and dynamic 2D cell monolayers. The result supports a model where flow induces 3D intestinal morphogenesis while the 3D cellular structures induce the expressions of key markers for intestinal differentiation.

Keywords: microphysiological systems, tissue engineering, 3D printing, intestinal barriers, intestinal morphogenesis, see-saw rocking, perfusion

1. Introduction

In vivo preclinical models to study physiological tissues often fail to mimic drug-tissue interactions [1,2]. Therefore, it is crucial to develop in vitro models of, for instance, the intestine wall that possesses the basic morphogenesis (e.g., crypt-villi structure with regiospecific intestinal cell distribution) and functions (e.g., barrier functions and mucus production) of the natural intestinal epithelium [3–5]. Organoids and *in vivo* cell migration models have demonstrated that the intestine villi are formed by a stem cell proliferation in the crypt, and daughter cells gradually mature as they are pushed up to the villi tip [6–10]. This differentiation also happens in static cultures. Hence mechanoactivation such as fluidic shear stress is not necessary for differentiation, but it could still enhance cell functions, especially at the villi tip. In intestinal mechanobiology, the intestinal cytoskeleton senses physical inputs such as irregular compressive/tensile strains, flow-induced shear stress, cyclic peristaltic motions, and villus motility patterns [11–14]. The cytoskeleton converts them into biochemical signals for epithelial differentiation and proliferation. However, the exact mechanisms of these biochemical signals are still unknown.

Fluid flow-induced shear stress is one of the most studied forces on intestinal tissue models. Dynamic incubation, caused by peristalsis and interstitial fluid movement in the gastrointestinal system, results in biochemical responses such as mucus secretion and villi-like structures [3–5]. These findings suggest that enhanced functions of cells seem to be linked to 3D morphogenesis induced by flow shear stress. However, recent research reports suggest that the basolateral flow induces 3D “villi” like structures on-chip [4,5] or on Transwell inserts where the basolateral side is under the dynamic flow condition [4,15] or where the Transwell was incubated in static condition with a very large basolateral medium volume [5]. These findings strongly suggest that shear stress is not the mechanism that drives 3D morphogenesis but basolateral feeding or removal of waste/paracrine factors and Wnt antagonists, such as Dickkopf-1 (DKK-1), which is one of the suppressors for the proliferation and morphogenesis of the intestinal epithelium [16], is. Another result where very low and exclusively apical shear stress (0.007-0.03 dyn/cm^2) was investigated suggested that apical side shear stress could induce weak 3D morphogenesis and weak induction of a variety of key parameters for intestine function [17]. In contradiction, exclusive apical flow did not lead to significant 3D morphogenesis [5], pointing out that shear stress is not necessarily essential. None of these

articles could answer if apical shear stress induces key biomarkers expression in Caco-2 cells in a 2D monolayer configuration.

Controlling flow during culture can be done in many ways, each with strengths and weaknesses. Various devices use different flow generating mechanisms, such as the cone and plate and parallel plate flow chamber systems [18–21], rotating vessels [22], an oscillating orbital shaker [15,23–25], and rocking "see-saw" platforms [26–34] have been used for biomechanical induction of tissues. In particular, microfluidic devices have been developed for precise flow control and continuously refreshed culture medium [35–40]. However, microfluidic culture devices are associated with using multiple pumps/tubing and connections, making them labor-intensive and prone to errors such as bubble formation, clogging, and fluid leakage [41–43].

Various passive microfluidic pumping or pumpless fluidic platforms [28,32,44,45] have been described to overcome these challenges by using different mechanisms such as evaporation, gravity, surface tension, osmosis, capillary flow, and thermo-viscous expansion [32,46–50]. Due to their ease and/or inexpensiveness features, gravity-induced flow has been more widely explored. One of the well-known microfluidic-based examples is Mimetas' 3-lane OrganoPlate perfusion platform [51–54] for gravity-driven flow platform. In Mimetas' system, Trietsch et al. (2017) formed a confluent tube of intestinal cells by culturing Caco-2 cells on an ECM gel [51].

Due to their robustness and simplicity, most in vitro intestinal cell culture models used for drug screening still rely on Transwell inserts [55–57]. However, Transwell inserts do not provide complex and dynamic intestinal cell microenvironments like in vivo. Therefore, many have been working on alternative platforms to integrate flow systems into Transwell inserts using pumps [58–60] and, recently, orbital shakers [61].

With these motivations, we have developed a novel 3D-printed insert platform (R-insert) with an open-top channel that enables gravity-induced, bi-directional flow. We replaced the Transwell filter with extracellular matrix (ECM)-mimetic hydrogel membranes using a dip-casting [62] approach. It allowed investigations of key biomarker expressions in 2D cell monolayers and 3D cellular structures under apical and basolateral flow conditions.

2. Materials and Methods

2.1. Design and fabrication of R-inserts with bioactive membranes

The rocker-actuated type, 3D-printed inserts (R-inserts) were designed in Fusion 360 (Autodesk, California, USA) as in 6-well plate formats (See the detailed dimensions in Figure 1a). Biomed Clear resin (Formlabs, USA) was used to fabricate the R-inserts due to its biocompatibility and autoclavability [63]. The pre-processing of print files (.STL), printing conditions on Form 3B stereolithography (SLA) 3D printer (Formlabs, USA), and post-processing of inserts were conducted following the same protocol mentioned in the previous article [62]. To functionalize the insert bottom, 15% (w/v) Gelatin membranes were cast into 3D-printed R-inserts following the dip-casting protocol [62] under sterile conditions. Membrane-assembled R-inserts were either used for experiments or stored at 4 °C for a maximum of two weeks.

The open-top channel configuration was chosen due to its ease of use for homogeneous cell seeding, avoiding bubble formation, and avoiding capillary effect caused by hydrostatic pressure that often occurs in microfluidic cell culture systems [41,42,64]. Two apertures (Figure 1a) were added to the design to ensure easy medium loading/ejection and measuring trans-endothelial/epithelial electrical resistance (TEER) by commonly used STX3/chopstick electrodes (for EVOM2) [60,65–67].

2.2. Membrane thickness measurement

1:1000 diluted 1.1 μm red fluorescent dyed polystyrene beads (1% g/cm^3 solids; #R0100, Fluoro-Max, Thermo Fisher, USA) were mixed with gelatin solution, and the solution was dip-casted to fabricate gelatin membranes as mentioned above. Thickness measurements of gelatin membranes (n=3) were performed by a Zeiss™ AxioObserver Z1 epifluorescence microscope (Carl Zeiss MicroImaging GmbH, Gottingen, Germany) at an emission wavelength range of 542 nm to 612 nm by a Light-emitting Diode laser (LED) with the 38-HE filter set (Carl Zeiss MicroImaging GmbH). 40x magnification (LD Epiplan-NEOFLUAR 40x/0.6 Korr) was used to visualize the micrometer-sized beads to define focal points and the z height. The z heights of the lowest and highest bead in focus were recorded, and the difference between z heights was used to measure the thickness.

2.3. Cell culture

Caco-2 cells (the human colon adenocarcinoma epithelial cells, passage 60-65, 09042001, European Collection of Authenticated Cell Cultures (ECACC), Salisbury, UK) were cultured in the complete epithelial growth medium (Dulbecco′s Modified Eagle′s Medium (DMEM) with High-glucose; Sigma-Aldrich) with 10% (v/v) fetal bovine serum (FBS, Hyclone, CA), 1% (v/v) NEAA (non-essential amino acids; Gibco, Fisher Scientific, Slangerup, Denmark), and 1% (v/v) P/S (penicillin (100 U/mL)-streptomycin (100 μg/mL); Sigma-Aldrich) in T-75 cell culture flasks (Starstedt, Nümbrecht, Germany). Cell subculturing was performed with trypsin-ethylenediaminetetraacetic acid (EDTA) for 3-5 min upon ~ 90 % confluency, and cells were cultured in an incubator at 37 °C, 100% Humidity, 5% CO_2 by changing the complete growth medium every two days.

2.4. Application of shear stress

Caco-2 cells were seeded on 15% gelatin membranes of R-inserts at a density of 5×10^4, 8×10^4, and 1×10^5 cells/cm^2 in 490 μL growth medium and incubated on a 6-well plate (tissue-culture-treated, Nunc, Thermo Fisher, Slangerup, DK) filled 4 mL of the growth medium in the basolateral side until reaching confluency. The confluent Caco-2 cells were cultured for 9 more days under static (control) or dynamic (the 2D Rocker) conditions, respectively, in an incubator at 37 °C and 5 % CO_2. The growth medium in the apical side of the R-inserts was refreshed every two days. 6-well plates containing the 3D-printed R-inserts were placed on the 2D Rocker platform (BenchRocker 2D, Benchmark Scientific Inc., USA) and placed in the incubator (Figure 1c). The tilting angle of the platform was set to ±7° using a digital inclinometer (Laserliner, DE) and a rotation frequency set to 16 rpm using a digital tachograph (laser-aided speedometer; Biltema, Sweden) for culturing of Caco-2 cells under physiological shear stress conditions (Movie S1 and Movie S2). The medium was treated as incompressible, and the hydrodynamic fluidic resistance (R) was only considered from the connecting open-top channel-like chamber; the resistance of reservoirs was neglected. Since no similar study has to our knowledge, examined in the literature, characterizations of the R-insert platform were done by adapting equations collected from microfluidic-based studies using rocker

platforms in a similar manner [32]. The volumetric flow rate (Q), the hydrostatic pressure differences (ΔP), and the resistance (R) were calculated as below:

$$\mathbf{Q} = \mathbf{\Delta P}/\mathbf{R} = (\boldsymbol{\rho} \times \mathbf{g} \times \mathbf{\Delta h})/\boldsymbol{R} \quad (1)$$

$$\mathbf{\Delta h} = \mathbf{\Delta}\boldsymbol{h_r} + (\boldsymbol{h_{v1}} - \boldsymbol{h_{v2}}) \quad (2)$$

$$\mathbf{\Delta}\boldsymbol{h_r} = \mathbf{L} \times \mathbf{sin}(\boldsymbol{\theta}) \quad (3)$$

$$\mathbf{R} = (\mathbf{12} \times \mu \times \mathbf{L})/(\boldsymbol{w} \times \boldsymbol{h^3} \times (\mathbf{1} - \mathbf{0.63} \times \boldsymbol{h}/\boldsymbol{w}) \quad (4)$$

where, **h** is the level of the cell growth medium in the reservoirs at the steady state (m), $\mathbf{\Delta h_r}$ is the height difference generated from the tilting of the insert (m), $\mathbf{(h_{v1}\text{-}h_{v2})}$ is the difference in the medium levels in the reservoirs at the tilting angle (*assumption based on Movie S2:* $\mathbf{h_{v1}}$=h=3 mm; h_{v2}=2 mm). To verify whether the flow was laminar, the Reynolds number (Re) was estimated as follows:

$$\mathbf{Re} = (\boldsymbol{\rho} \times \mathbf{L} \times \mathbf{Q}/\mathbf{A})/\mu \quad (5)$$

The gravity-driven average flow-induced shear stress ($\boldsymbol{\tau_{avg}}$; dyn/cm^2) was estimated as follows:

$$\boldsymbol{\tau_{avg}} = ((\mathbf{6} \times \mu \times \boldsymbol{Q})/(\boldsymbol{w} \times \boldsymbol{h^2})) \times \mathbf{10} \quad (6)$$

Finally, pressure difference (Δp; N/m^2 (Pa)) and meniscus radius (r; m) was calculated as follows:

$$\mathbf{\Delta p} = (\boldsymbol{h_{vmax}} + \boldsymbol{L} \times \mathbf{sin}(\boldsymbol{\theta_{max}})) \quad (7)$$

$$\boldsymbol{r} = (\mathbf{2} \times \boldsymbol{\gamma})/\mathbf{\Delta p} \quad (8)$$

where $\mathbf{h_{vmax}}$ (=h+ (h_{v1}-h_{v2})) is the height of the medium in the reservoirs at the maximum tilting angle (m), **ρ** is the culture medium density (1007 kg/m^3), **g** is the gravity constant (9.81), **L** is the distance between inlet and outlet of the channel in m, **w** is the width of the channel (m), **h** is the culture medium level in the channel (m), **θ** is the tilting angle of the rocker, **μ** is the

dynamic viscosity of the culture medium at 37 °C (0.93×10^{-3} kg/m.s) [68], and $\boldsymbol{\gamma}$ is the surface tension of the medium (0.07 N/m) [32].

2.5. Microparticle image velocimetry (μPIV)

Microparticle image velocimetry (μPIV) was applied to determine the spatial profile of flow velocity at the region of interest (ROI) in the rectangular channel-like cell culture chamber. For the flow analysis, an R-insert was analyzed in the whole cell culture area (total mean velocity), edge (mean velocity), and center (mean velocity) spots of the chamber (Figure 2 and Table S1) (n=3). The average flow rate in each spot was calculated. 55 μm polyamide microparticles (LaVision, DE) were used in a concentration of %0.1 g microparticles/mL prepared in PBS. A volume of 491 μL particle solution was filled into the insert well. A high-speed CMOS camera (Basler acA1300-200uc USB 3.0, DE) with a Fixed Focal Length (16 mm) Lens (C Series; Edmund Optics, New Jersey, USA) was used to track the movement of the microparticles. The exposure time was selected at 500 μs per single image; the frame rate was defined depending on the ROI size (up to 677 fps) at 800x242 pixels resolution. The displacement of the microparticles took up to 6.46 s and was processed using the open-source MATLAB toolbox PIVlab (version 2.57) [69]. Further, volumetric flow rate, Reynolds number, and shear stress calculations were done based on the theoretical equations.

2.6. Barrier integrities of Caco-2 monolayers

EVOM2 volt-ohm meter (World Precision Instruments. Sarasota, USA) was used to measure Transepithelial and endothelial electrical resistance (TEER) values of epithelial monolayers by placing Ag/AgCI chopstick electrode pair (STX3, World Precision Instruments, USA) at the luminal and abluminal compartments. Resistance values (in ohms) were determined by subtracting gelatin-membranes without cell monolayers from the values of the membranes with Caco-2 cultures (n≥3). Standard TEER values in ohms×cm^2 (Ω×cm^2) were calculated according to this formula:

$$\boldsymbol{TEER(\Omega \times cm^2) = ((R_T(\Omega) - R_B(\Omega)) \times A\ (cm^2)} \tag{9}$$

where R_T is the total resistance across cellular monolayer on the membrane, R_B is the blank resistance of membrane without cells, and A is the surface area of the membrane (0.4 cm^2).

2.7. Molecular transport of Caco-2 monolayers

Permeability coefficient (P_c) of 0.44 kDa lucifer yellow (LY; Sigma-Aldrich, USA) was measured as follows; the basolateral compartment of the well was filled with 4 mL of Hanks' Balanced Salt Solution (HBSS; Thermo Fisher, USA) including Sodium bicarbonate (0.0375 % w/v), HEPES (10 mM), 0.05% w/v BSA (bovine serum albumin; pH 7.4) was added to, and the apical side was filled with 60 µM (500 µL) LY. The transport was performed at 37 °C with 16 rounds per minute (rpm) rocking under dark conditions for 2h. After 2h-transport of LY, 100 µL samples from each compartment (n≥3) were transferred to a 96-well plate to measure the Relative Fluorescence Units (RFU) by a plate reader (Spark multimode microplate reader, TECAN, Männedorf, CH). RFU readouts with excitation and emission (Ex/Em) wavelengths of LY (428 nm / 536 nm) were collected, and the concentration of LY in each sample was determined from standard curves (Figure S1). The permeability coefficients (Pc, nm/s) were calculated by derived equations from [62]:

$$\boldsymbol{P_c = ((V_r \times C_f)/(C_i \times A \times t))} \tag{10}$$

where, Pc is the permeability coefficient (nm/s), Vr is the receiver volume in mL, C_f is the final receiver concentration (µM), C_i is the initial apical concentration (µM), A is the membrane growth area in cm^2, and t is the assay time in seconds.

2.8. Fixation of cells

After 15 min washing of samples with PBS, they were fixed in 2 % (v/v) PFA in PBS for 2 min and 4 % (v/v) PFA in PBS for 13 min at room temperature. PFA was removed from the samples, and samples were washed in PBS (3X).

2.9. F-actin and Nuclei stains

The immunostained samples were incubated with the F-actin (1:100; Alexa Fluor Plus 555 Phalloidin, #A30106, Invitrogen, Thermo Fisher, USA) and 1 µg/mL Hoechst 33342 (nuclei, #62249, Invitrogen, Thermo Fisher, USA) stains together with secondary antibody as mentioned before. F-actin was added to the staining solution simultaneously with the secondary

antibody, whereas Hoechst was added to the solution at the last 30 mins to prevent overstaining. After the excess secondary antibody and F-actin/Hoechst stains were washed away, samples were left in PBS before imaging.

2.10. Immunostaining

The fixed cells were permeabilized with 0.1% (v/v) Triton X-100 for 5 mins, blocked with 0.1% (v/v) Triton X-100 + 3% (w/v) BSA for 1h at room temperature (RT). Cells were then incubated with tight junction marker, zonula occluden-1 (ZO-1) antibody (1:50; #33-9100, Invitrogen, Thermo Fisher, USA) in 0.1% (w/v) BSA-PBS overnight at 4 °C; Villin polyclonal antibody (1:100; #PA5-29078, Invitrogen, Thermo Fisher, USA), mucin-2 (MUC-2) antibody (1:100; #33-9100, Invitrogen, Thermo Fisher, USA) in 0.1% (w/v) BSA-PBS for 3h at RT; followed by PBS washing to remove excess primary antibodies and incubated with Alexa Fluor Plus 488-labelled Donkey anti-Mouse antibody (1:2000; #A32766, Invitrogen, Thermo Fisher, USA) for ZO-1 and MUC-2; Alexa Fluor Plus 488-labelled Goat anti-Rabbit antibody (1:2000; #A32731, Invitrogen, Thermo Fisher, USA) for Villin in 0.1% (w/v) BSA-PBS for 1h at RT.

2.11. Microscopy imaging and image processing

Bright-field images were taken using a Zeiss Primovert microscope (Carl Zeiss MicroImaging GmbH, Gottingen, DE) with the following objective: Plan-Achromat 4x/0.10 and Plan-Achromat 10x/0.3, whereas staining images were acquired with Zeiss AxioObserver Z1 epifluorescence microscope (Carl Zeiss MicroImaging GmbH) with the following objectives: LD Epiplan-NEOFLUAR 20x/0.4 Korr M27, LD Plan-NEOFLUAR 40x/0.6 Korr M27. Fluorescence intensity values were obtained from 2D cell monolayers (static and dynamic) and 3D areas (dynamic) by spontaneously selected spots in the whole images using ZEN Lite 3.2 image processing software (Carl Zeiss MicroImaging GmbH) and defined by discarding background values where no intensity observed ($n \geq 8$) as shown in Figure S2. Analyses were plotted by GraphPad Prism (version 9.0.0 for macOS, GraphPad Software, La Jolla California USA, “www.graphpad.com”) software.

2.12. Statistical analysis

The data are presented as the sample size (n), Mean ± Standard Deviation (SD). Calculations were done using Microsoft Excel (Version 2016, Microsoft Office, Seattle, Washington). Different groups were compared for equality of means by using Welch's one-way for fluorescence intensity, epithelial layer thickness, µPIV, and LY permeability analyses; and two-way variance analyses (ANOVA) for TEER measurement analysis, with Tukey's post-hoc analysis (GraphPad Prism; version 9.0.0 for macOS, GraphPad Software, La Jolla California USA, "www.graphpad.com"). P-values were obtained and determined to be significantly different when the p-value<0.05.

3. Results and Discussion

3.1. Flow characteristics of 3D-printed inserts actuating by rocking

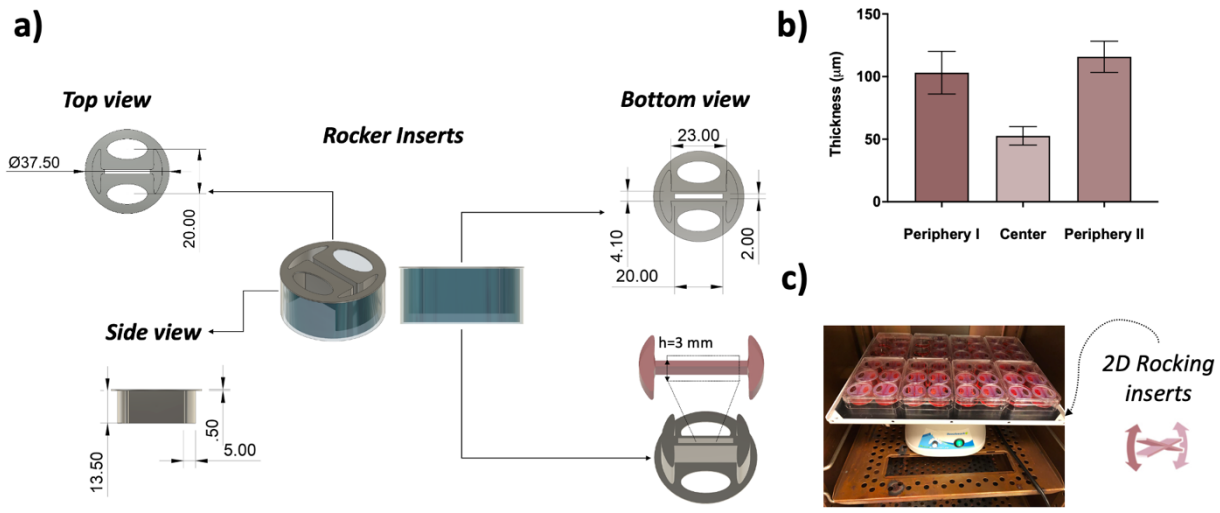

Figure 1. *Device design considerations and characterization.* ***a)*** *Insert design and dimensions.* ***b)*** *Thickness of the dip-cast Gelatin membrane at horizontal (I) and vertical (II) periphery and center regions.* ***c)*** *Representative photo of rocking insert platform allowing scale-up in the incubator.*

The 3D-printed rocker-actuated type of insert (R-insert) was constructed to have a relatively wide cell culture area as defined by a gelatin membrane using the dip casting technique [62] (Figure 1a). The gelatin membranes were thicker at the edges where they pinned to the walls compared to the center of the membrane suggesting a concave form. These gels typically swell 1.5 times when immersed in PBS (Phosphate-buffered saline) buffer, so during cultures, the membrane will be thicker [62]. It is possible that the gelatin membrane is flexible as it is only about 75 µm thin in the middle and 150 µm at the edges when swelled (Figure 1b). We commented that the soft, thin gels with the Young modulus of ~9.36 kPa [62] might cause sagging. However, we could not experimentally confirm this phenomenon, mainly due to

difficulties recording the gel membrane sag during rocking. The Reynolds number (Re) in the channel was calculated to be 1213, and thus the flow is expected to be laminar (Re<2000). Laminar flow was also verified with microparticle image velocity (μPIV) measurement (Figure 2, Movie S3) with calculated Re=1256-1484 (edge-center) and Re=1502 (whole). According to theoretical calculations considering the dimensions and applied angle, the flow velocity was 0.056 m/s; the volumetric flow rate was 336 μL/s, whereas flow-induced shear stress was 1 dyn/cm^2. On the other hand, the μPIV measured the (whole) mean flow velocity as 0.071±0.002 m/s (Mean±SD) (Figure 2c), which gives Q = 426±9.2 μL/s (Mean±SD) during tilting. The calculated shear stress based on the (whole) μPIV measurements was 1.3 dyn/cm^2. The speed of the rocker platform was set to be 16 rpm (calculated as ≈ 0.27 Hz) for this study and fits the frequency of small bowel peristalsis in vivo [13,14,70,71].

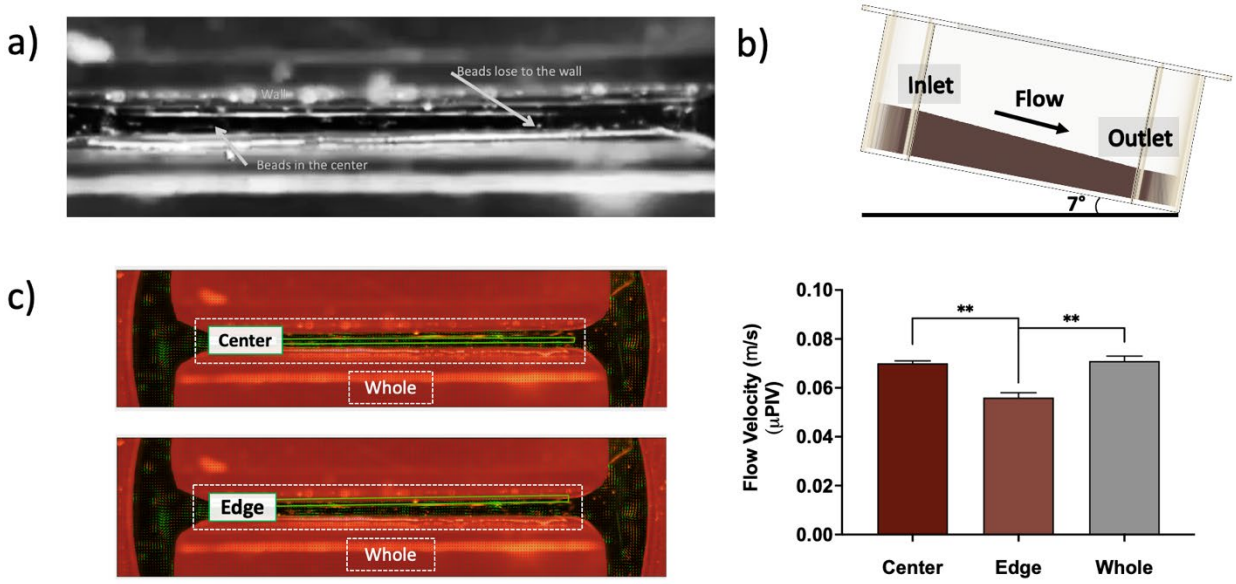

Figure 2. a) *μPIV measurement regions defined by locations of beads of* ***b)*** *rectangular channel-like chamber at 7 degree tilting angle.* ***c)*** *Mean flow velocities (m/s) at center, edge and whole regions were compared. Error bars indicate mean ± SD (n=3). Statistical significance: **P < 0.01.*

3.2. Effects of the cell seeding density and flow on morphogenesis

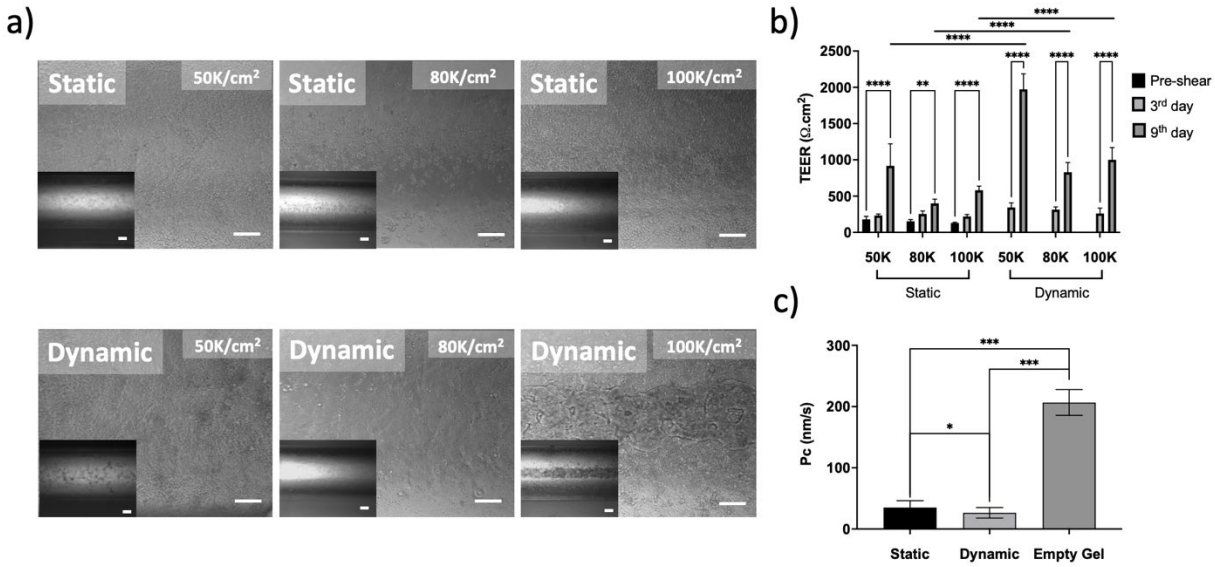

Figure 3. *Representative brightfield images of Caco-2 cells (initial cell densities: 50k-100k/cm²) under dynamic conditions.* ***Magnification:*** *4x-10x;* ***Scale bars:*** *100-200 µm, respectively.* ***b)*** *TEER values of confluent Caco-2 cells (initial cell densities: 50k-100k/cm2) under static and dynamic conditions for 9 more days.* ***c)*** *Lucifer yellow permeability coefficients (Pc (nm/s)) of confluent Caco-2 cells (initial cell density:100k/cm²) after 9-day under static and dynamic conditions. Error bars indicate mean ± SD (n≥3). Statistical significance: *P < 0.1, **P < 0.01, ***P < 0.001, ****P < 0.0001.*

50.000-500.000 cells/cm^2 seeding density has been used in Transwell inserts [72–76]. Higher density leads to a shorter incubation period but multilayer growth in static cultures [77–80]. To investigate different cell seeding densities during flow, the cell density varied from 50.000 (50k) cells/cm^2 to 100k/cm^2. Only the highest plating cell density under dynamic incubation showed 3D villi-like structures along the flow direction of the channel (Figure 3a - lower right panel). The 3D cellular regions were either centered in the middle (Figure 3a) or spread out in patches (Figure S3). The 3D villi-like structures were not observed closer to the channel walls. Such distinct regional zones of 2D cell monolayers and 3D cellular structures in the same culture have not been reported previously.

The TEER values were highest using 50k/cm^2 seeding density in static and dynamic conditions (Figure 3b and Table S2). The TEER value was 2-3 times higher at the 50k/cm^2 cell density in dynamic conditions compared to corresponding static conditions. 100k/cm^2 cell seeding density resulted in half the TEER compared to 50k/cm^2 cell density values in static and dynamic incubations. To verify TEER measurement results (Figure 3b and Table S2), the paracellular transport of LY from apical to basolateral compartments of intestinal epithelium for 100k/cm^2 cultures was evaluated (Figure 3c and Table S3). Permeability coefficients (Pc) of the shear stress-induced (dynamic) group showed slower permeability compared to the static

(no shear stress) group (Figure 3c and Table S3) by being correlated with the higher TEER under dynamic incubation (Figure 3b and Table S2).

It should be noted that the 50k/cm^2 groups proliferate for a longer time compared to the 100k/cm^2 group before the onset of shear stress, which may explain the difference in 2D cell monolayers and 3D cellular structures and the ability to create a barrier. Hence the endpoint after the more prolonged proliferation phase might be a contact inhibited 2D cell monolayers that mature to most highly specialized enterocytes [78,81,82] rather than forming 3D cellular structures with other properties. Interestingly, 2D cell monolayers could be achieved during dynamic culturing by changing the cell density, even slightly, as 80k/cm^2 but not 100k/ cm^2 only gives 2D monolayers (Figure 3a). Others have used 150k/cm^2 cell density [5] to obtain 3D morphogenesis under the dynamic flow condition. Low shear stress and plating at 200k/cm^2 resulted in 2D cell monolayers with some indications of higher cells with increasing shear stress [17]. However, the last report did not use a perfused basolateral side [17] which would inhibit strong 3D morphogenesis [5]. Seeding at high cell densities of >100k/cm^2 in static cultures gives inconsistent multilayer cellular structures [76,80]. By contrast, the data supports that there is a clear link between flow and formation of 3D morphology at higher seeding densities (Figure 3a) which supports the previous report [5].

Why the 3D cellular structures with 100k/cm^2 cell density occur in the middle of the channel in some cases but not at the sides of the channel is unclear. One possibility is that cells, especially during cell seeding, are collected in the center because the gel layer is concave and might even sag to make a shallow trench (see above). If that does not happen, a patchier morphology might be achieved (Figure S3) caused by stochastic uneven seeding. Reevaluation in other fluidics platforms for such regional 3D cellular structures is recommended as this suggests a heterogenous cell layer (see also below). Other possibilities are that cells are exposed to a different amount of shear stress. However, the 3D structure is relatively thin, and the flow rate in the center is about 418 µL/min, while closer to the wall, it is 335 µL/min making this less likely (Figure 2). The third possibility is feeding or waste or paracrine factor removal, where the diffusion from the basolateral side is quicker because the gel is thinner in the center than closer to the wall. It has been reported that diffusing the medium to a large basolateral reservoir provides minimal maintenance of the Wnt antagonists that affect the 3D morphogenesis of Caco-2 cells positively [4,5]. Wnt agonist would be diffused out from the

basolateral side up to four times slower at the edge compared to the center, as the minimal distance in the center was measured to be half as thin as at the edges (Figure 1).

3.3 Epithelial thicknesses

We measured the thickness of 2D cell monolayers and 3D cellular structures in static and dynamic cultures using F-actin staining (Figure 4a). The cell layer height was measured to be 16±1.7 µm and 23.6±4.2 µm under static conditions and in the 2D cell monolayers of the dynamic cell cultures, respectively (Figure 4b). This result suggests that shear stress in apparent 2D configurations increases the height of the cells. The 3D part was measured to be three-four times higher, suggesting multiple cell layers. 2.5D intensity plots also support the formation of 2D cell monolayers and 3D cellular structures (Figure 4a). Similar villi-like 3D morphogenesis was reported in the literature for culture under the flow condition [83–87]. The F-actin stain was slightly higher in dynamic 2D cell monolayers than in static 2D monolayers, whereas the 3D cellular structures showed about 10-fold higher expression of F-actin (Figure 4c).

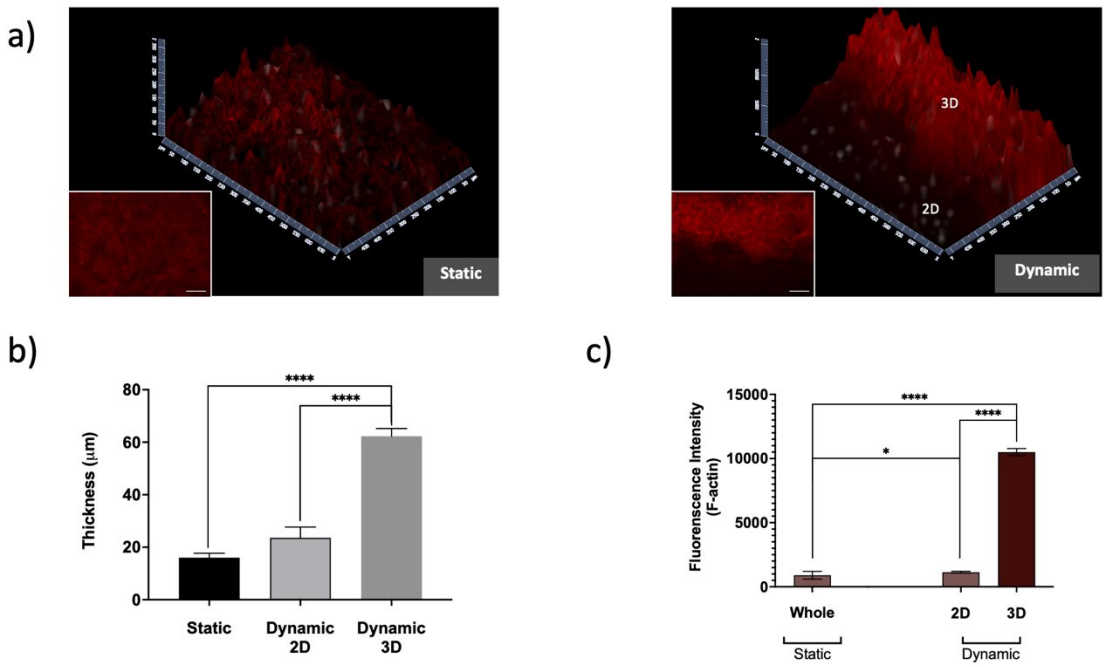

Figure 4. a) *Representative 2.5D fluorescence intensity plots of F-actin-stained cells under Static and Dynamic conditions (2D cell monolayers and 3D cellular structures).* ***b)*** *epithelium thickness (µm) estimation defined by Z-stack thickness (n=3).* ***c)*** *Mean fluorescence intensity plot of F-actin obtained from 2D and 3D areas at static and dynamic conditions (n=12). Error bars indicate mean ± SD. Statistical significance: *P < 0.1, ****P < 0.0001.*

3.4. Differential expression of F-actin and ZO-1 in 2D cell monolayers and 3D

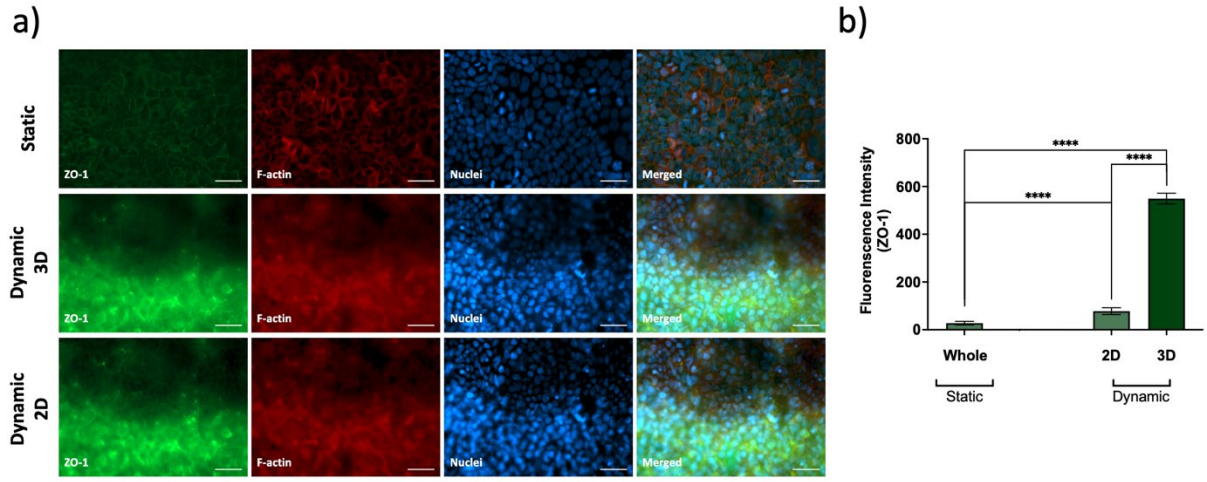

Figure 5. a) *Representative immunofluorescence staining images under Static and Dynamic conditions (2D cell monolayers and 3D cellular structures).* ***Green:*** *ZO-1 (tight junction);* ***Red:*** *F-actin (cytoskeleton);* ***Blue:*** *Hoechst (nuclei).* ***Magnification:*** *40x;* ***Scale bars:*** *50 µm (**See 20x photos in Figure S4**).* ***b)*** *Mean fluorescence intensity plot of ZO-1 obtained from 2D and 3D areas at static and dynamic conditions. Error bars indicate mean ± SD (n≥8). Statistical significance: ****P < 0.0001.*

Having a regional cellular organization in 2D monolayers and 3D structures in the dynamic condition in the same chamber allowed for separating effects of flow and 3D cellular formation on the maturation of the cells. Therefore, localized expression of differentiation markers was investigated at 100k/cm^2 seeding density. Immunocytochemistry (ICC) staining for F-actin (cytoskeleton as a reference), Hoechst (nuclei), and ZO-1 (tight junction) was assessed after 9 days of post-shear stress for 100k/cm^2 cultures. The F-actin staining showed a typical cobblestone morphology in the static and 2D monolayer parts of the dynamic cultures. By contrast, the 3D structures showed clear signs of crypt-villi formations according to F-actin staining. ZO-1 showed clear cell boundary expression in static cultures in agreement with the literature for static cultures and Transwells [4,11,83,85–88]. The 3D region showed fewer clear cell borders, most likely due to difficulties finding a single focal plane (Figure 5a). The ZO-1 signal in the 3D part was seven times higher than in the corresponding 2D monolayer area under dynamic conditions. 2D monolayer areas under the dynamic conditions had three times higher signals than 2D monolayers under the static conditions (Figure 5b and Table S4). The results suggest that ZO-1 was induced by shear stress while it was highly upregulated in the 3D structure under the flow condition. However, cells under shear stress were higher (Figure 5b and Table S4). Therefore, larger areas forming tight junctions in higher cells can explain a part of the increase in the ZO-1 expression. The height and ZO-1 expression increase correlate with the increase in TEER and decrease in LY permeability values of culture under shear stress (Figure 3b-c and Table S2-S3).

3.5. Villin expression is linked to 3D structures

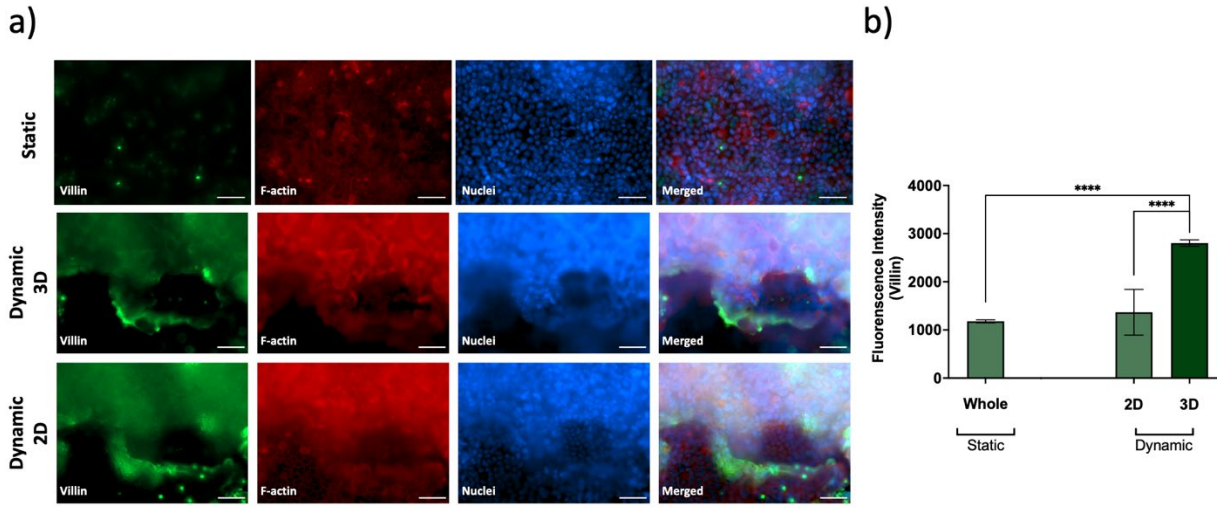

Figure 6. a) *Representative immunofluorescence staining images under Static and Dynamic conditions (2D cell monolayers and 3D cellular structures).* ***Green:*** *Villin (villus);* ***Red:*** *F-actin (cytoskeleton);* ***Blue:*** *Hoechst (nuclei).* ***Magnification:*** *40x;* ***Scale bars:*** *50 µm (**See 20x photos in Figure S5**).* ***b)*** *Mean fluorescence intensity plot of Villin obtained from 2D and 3D areas at static and dynamic conditions. Error bars indicate mean ± SD (n≥8). Statistical significance: ****P < 0.0001; all other combinations are non-significant (ns=p>0.05).*

One of the differentiation indications of the intestinal epithelium is the regiospecific higher expression of Villin, an actin-binding protein in the brush borders of the epithelium [4,15,88]. Cells were stained for the F-actin and Villin to explore differences in the 3D and 2D monolayer areas. Villin staining showed that Villin was highly expressed in the 3D parts, while the 2D monolayer areas showed lower staining irrespective of flow (Figure 6b and Table S4). The Villi staining was nearly homogeneous in 3D (challenging to assess clear cell borders), while 2D cell monolayers in flow or static had a mixture of Villin positive and negative cells. Flow is, therefore, not affecting Villin expression in 2D cell monolayers.

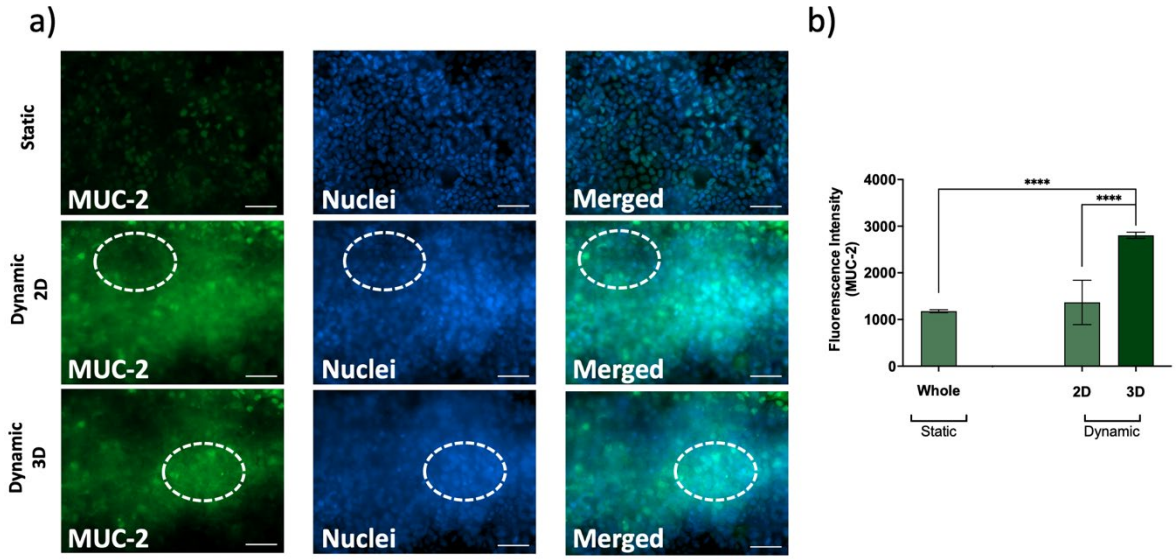

Figure 7. a) *Representative immunofluorescence staining images under Static and Dynamic conditions (White circles indicate 2D cell monolayers and 3D cellular structures).* ***Green:*** *MUC-2 (mucus secreting (goblet) cells);* ***Blue:*** *Hoechst (nuclei).* ***Magnification:*** *40x;* ***Scale bars:*** *50 µm* ***(See 20x photos in Figure S6)****.* ***b)*** *Mean fluorescence intensity plot of MUC-2 obtained from 2D and 3D areas at static and dynamic conditions. Error bars indicate mean ± SD (n≥8). Statistical significance: ****P < 0.0001; all other combinations are non-significant (ns=p>0.05).*

3.6. MUC-2 Expression in 2D cell monolayers and 3D

Next, we wanted to investigate the Mucin-2 (MUC-2) expression as a marker for goblet-like functions in 2D cell monolayers and 3D with and without flow. Compared to Villin, MUC-2 expression varied much more in the 3D area and had regions of high expression and low expression (compare circles). We observe a 2.4-fold higher MUC-2 expression in the 3D areas compared to 2D cell monolayer areas (Figure 7b and Table S4). As observed above, flow did not enhance MUC-2 expression in 2D cell monolayers. Similar to Villin, there are MUC-2 positive and negative cells in the 2D monolayer areas, irrespective of the flow.

Flow provides two primary cues to cells: shear stress and increased feeding or washout of secreted paracrine factors. It is widely accepted that shear stress, induced in fluidic channels, results in 3D growth and improved maturation [3,17,86,88,89]. However, here we have 2D cell monolayers and 3D in the same culture, meaning that the effects of flow or shear stress could be evaluated directly with the different areas serving as internal controls. MUC-2, Villin, and, to some extent, ZO-1 had similar expression in 2D dynamic compared to 2D static cell monolayers while being apparently higher in 3D (Figure 5-7). As the MUC-2, Villin and ZO-1 are lower expressed in 2D cell monolayers; it suggests that 2D monolayers have crypt-like phenotypes, while the increase in MUC-2 and Villin suggests villi-like phenotypes.

Furthermore, the height measurements suggested that cells in the 2D monolayer areas in the dynamic cultures were 1.4 times higher than corresponding cells in static cultures (Figure 4b). This result suggests that cells become more columnar in dynamic conditions, which might induce cell expression such as ZO-1. Taken together, the data suggest a model where flow improves cell maturation to make cells more elongated, but that only affects ZO-1 expression and the tightness of the layer. Flow also induces 3D cellular structures, possibly by removing DKK-1 from the basolateral side [4,5,15,16], and 3D cellular structures are driving the maturation, as illustrated by MUC-2 and Villin.

4. Conclusion

A hanging 6-well insert for rocker type of actuation (R-insert) was constructed and used to induce shear stress on Caco-2 cells. Clear regional 3D morphogenesis was observed in high-density cultures and not low-density cultures. The expression pattern of F-actin, MUC-2, and Villin indicated the flow-induced expression of these markers in the 3D cellular structures compared to 2D cell monolayers. Villin and MUC-2 had heterogeneous expression in 2D cell monolayers irrespective of the flow. ZO-1 expression was by flow in the 2D cell monolayers correlated with increased epithelium height, increased TEER values, and decreased permeability. The results show that flow is necessary to induce 3D cellular structures but insufficient to induce maturation in 2D monolayers.

Supporting Information

Supporting Information is available from the Wiley Online Library or the authors.

Author Contributions

A.A.D.: Project administration, Conceptualization, Data curation, Formal analysis, Investigation, Methodology, Validation, Visualization, Writing—original draft, review, editing. M.D.: Project administration, Conceptualization, Resources, Supervision, Writing—review & editing.

Conflicts of interest

There are no conflicts to declare.

Acknowledgment

Financial support was provided by the European Union's Horizon 2020 research and innovation program under the Marie Skłodowska-Curie grant agreement No. 812673 and was conducted within the Organoids for Virus Research (OrganoVIR) network. A.A.D. and M.D. would like to thank Dr. Murat Serhatlioglu and Dr. Hakan Gurbuz from the Technical University of Denmark for their valuable helps in providing the homemade PIV unit.

References

[1] G.B. Hatton, V. Yadav, A.W. Basit, H.A. Merchant, Animal Farm: Considerations in Animal Gastrointestinal Physiology and Relevance to Drug Delivery in Humans, J Pharm Sci. 104 (2015) 2747–2776. https://doi.org/10.1002/jps.24365.

[2] T.T. Kararli, Comparison of the gastrointestinal anatomy, physiology, and biochemistry of humans and commonly used laboratory animals, Biopharm Drug Dispos. 16 (1995) 351–380. https://doi.org/10.1002/bdd.2510160502.

[3] M. Lindner, A. Laporte, S. Block, L. Elomaa, M. Weinhart, Physiological shear stress enhances differentiation, mucus-formation and structural 3d organization of intestinal epithelial cells in vitro, Cells. 10 (2021). https://doi.org/10.3390/cells10082062.

[4] W. Shin, H.J. Kim, 3D in vitro morphogenesis of human intestinal epithelium in a gut-on-a-chip or a hybrid chip with a cell culture insert, Nat Protoc. 17 (2022) 910–939. https://doi.org/10.1038/s41596-021-00674-3.

[5] W. Shin, C.D. Hinojosa, D.E. Ingber, H.J. Kim, Human Intestinal Morphogenesis Controlled by Transepithelial Morphogen Gradient and Flow-Dependent Physical Cues in a Microengineered Gut-on-a-Chip, IScience. 15 (2019) 391–406. https://doi.org/10.1016/J.ISCI.2019.04.037.

[6] H. Clevers, The Intestinal Crypt, A Prototype Stem Cell Compartment, Cell. 154 (2013) 274–284. https://doi.org/10.1016/j.cell.2013.07.004.

[7] V. Bonis, C. Rossell, H. Gehart, The Intestinal Epithelium – Fluid Fate and Rigid Structure From Crypt Bottom to Villus Tip, Front Cell Dev Biol. 9 (2021) 1222. https://doi.org/10.3389/FCELL.2021.661931/XML/NLM.

[8] O. Kwon, T.S. Han, M.Y. Son, Intestinal Morphogenesis in Development, Regeneration, and Disease: The Potential Utility of Intestinal Organoids for Studying Compartmentalization of the Crypt-Villus Structure, Front Cell Dev Biol. 8 (2020) 1192. https://doi.org/10.3389/FCELL.2020.593969/XML/NLM.

[9] A. Parker, O.J. Maclaren, A.G. Fletcher, D. Muraro, P.A. Kreuzaler, H.M. Byrne, P.K. Maini, A.J.M. Watson, C. Pin, Cell proliferation within small intestinal crypts is the principal driving force for cell migration on villi, FASEB Journal. 31 (2017) 636–649. https://doi.org/10.1096/FJ.201601002/-/DC1.

[10] H. Gehart, H. Clevers, Tales from the crypt: new insights into intestinal stem cells, Nat Rev Gastroenterol Hepatol. 16 (2019) 19–34. https://doi.org/10.1038/s41575-018-0081-y.

[11] S.A. Hewes, R.L. Wilson, M.K. Estes, N.F. Shroyer, S.E. Blutt, K.J. Grande-Allen, In Vitro Models of the Small Intestine: Engineering Challenges and Engineering Solutions, Tissue Eng Part B Rev. 26 (2020) 313–326. https://doi.org/10.1089/ten.teb.2019.0334.

[12] C.L. Thompson, S. Fu, M.M. Knight, S.D. Thorpe, Mechanical Stimulation: A Crucial Element of Organ-on-Chip Models, Front Bioeng Biotechnol. 8 (2020). https://doi.org/10.3389/fbioe.2020.602646.

[13] C.P. Gayer, M.D. Basson, The effects of mechanical forces on intestinal physiology and pathology, Cell Signal. 21 (2009) 1237–1244. https://doi.org/10.1016/j.cellsig.2009.02.011.

[14] M. Balcells, M. Fernández Suárez, M. Vázquez, E.R. Edelman, Cells in fluidic environments are sensitive to flow frequency, J Cell Physiol. 204 (2005) 329–335. https://doi.org/10.1002/jcp.20281.

[15] H.B. Chong, J. Youn, W. Shin, H.J. Kim, D.S. Kim, Multiplex recreation of human intestinal morphogenesis on a multi-well insert platform by basolateral convective flow, Lab Chip. 21 (2021) 3316–3327. https://doi.org/10.1039/d1lc00404b.

[16] S. Koch, C.T. Capaldo, S. Samarin, P. Nava, I. Neumaier, A. Skerra, D.B. Sacks, C.A. Parkos, A. Nusrat, Dkk-1 inhibits intestinal epithelial cell migration by attenuating directional polarization of leading edge cells, Mol Biol Cell. 20 (2009) 4816–4825. https://doi.org/https://doi.org/10.1091/mbc.e09-05-0415.

[17] L.C. Delon, Z. Guo, A. Oszmiana, C.C. Chien, R. Gibson, C. Prestidge, B. Thierry, A systematic investigation of the effect of the fluid shear stress on Caco-2 cells towards the optimization of epithelial organ-on-chip models, Biomaterials. 225 (2019). https://doi.org/10.1016/j.biomaterials.2019.119521.

[18] C.R. Jacobs, C.E. Yellowley, B.R. Davis, Z. Zhou, J.M. Cimbala, H.J. Donahue, Differential effect of steady versus oscillating flow on bone cells, n.d.

[19] M. Franzoni, I. Cattaneo, B. Ene-Iordache, A. Oldani, P. Righettini, A. Remuzzi, Design of a cone-and-plate device for controlled realistic shear stress stimulation on endothelial cell monolayers, Cytotechnology. 68 (2016) 1885–1896. https://doi.org/10.1007/s10616-015-9941-2.

[20] A.M. Malek, R. Ahlquist, G.H. Gibbons, V.J. Dzau, S. Izumo, A cone-plate apparatus for the in vitro biochemical and molecular analysis of the effect of shear stress on adherent cells, Kluwer Academic Publishers, 1995.

[21] L.T. Breen, P.E. McHugh, B.A. McCormack, G. Muir, N.J. Quinlan, K.B. Heraty, B.P. Murphy, Development of a novel bioreactor to apply shear stress and tensile strain simultaneously to cell monolayers, in: Review of Scientific Instruments, 2006. https://doi.org/10.1063/1.2356857.

[22] D.D. Deligianni, N. Katsala, S. Ladas, D. Sotiropoulou, J. Amedee, Y.F. Missirlis, Effect of surface roughness of the titanium alloy Ti–6Al–4V on human bone marrow cell response and on protein adsorption, Biomaterials. 22 (2001) 1241–1251.

[23] C.M. Warboys, M. Ghim, P.D. Weinberg, Understanding mechanobiology in cultured endothelium: A review of the orbital shaker method, Atherosclerosis. 285 (2019) 170–177.

[24] C.M. Warboys, D.R. Overby, P.D. Weinberg, Dendritic cells lower the permeability of endothelial monolayers, in: Cell Mol Bioeng, 2012: pp. 184–193.

[25] C.M. Warboys, R.E. Berson, G.E. Mann, J.D. Pearson, P.D. Weinberg, P.D. Weinberg, Acute and chronic exposure to shear stress have opposite effects on endothelial permeability to macromolecules, Am J Physiol Heart Circ Physiol. 298 (2010) 1850–1856. www.ajpheart.org.

[26] S. Puwanun, R.M. Delaine-Smith, H.E. Colley, J.M. Yates, S. MacNeil, G.C. Reilly, A simple rocker-induced mechanical stimulus upregulates mineralization by human

osteoprogenitor cells in fibrous scaffolds, J Tissue Eng Regen Med. 12 (2018) 370–381. https://doi.org/10.1002/term.2462.

[27] B. Srinivasan, J. Hickman, M. Shuler, Simulation of Gravity-Driven Flow Through a Microfluidic Device on a Rocker Platform, n.d.

[28] Z. Chen, S. He, J. Zilberberg, W. Lee, Pumpless platform for high-throughput dynamic multicellular culture and chemosensitivity evaluation, in: Transactions of the Annual Meeting of the Society for Biomaterials and the Annual International Biomaterials Symposium, Society for Biomaterials, 2019: p. 705. https://doi.org/10.1039/C8LC00872H.

[29] R.P. Tucker, P. Henningsson, S.L. Franklin, D. Chen, Y. Ventikos, R.J. Bomphrey, M.S. Thompson, See-saw rocking: An in vitro model for mechanotransduction research, J R Soc Interface. 11 (2014). https://doi.org/10.1098/rsif.2014.0330.

[30] P.G. Miller, M.L. Shuler, Design and Demonstration of a Pumpless 14 Compartment Microphysiological System, Biotechnol. Bioeng. 113 (2016) 2213–2227. https://doi.org/10.1002/bit.25989/abstract.

[31] H.E. Abaci, K. Gledhill, Z. Guo, A.M. Christiano, M.L. Shuler, Pumpless microfluidic platform for drug testing on human skin equivalents, Lab Chip. 15 (2015) 882–888. https://doi.org/10.1039/c4lc00999a.

[32] Z. Chen, J. Zilberberg, W. Lee, Pumpless microfluidic device with open top cell culture under oscillatory shear stress, Biomed Microdevices. 22 (2020). https://doi.org/10.1007/s10544-020-00515-2.

[33] M.B. Esch, H. Ueno, D.R. Applegate, M.L. Shuler, Modular, pumpless body-on-a-chip platform for the co-culture of GI tract epithelium and 3D primary liver tissue, Lab Chip. 16 (2016) 2719–2729. https://doi.org/10.1039/c6lc00461j.

[34] H.J. Chen, P. Miller, M.L. Shuler, A pumpless body-on-a-chip model using a primary culture of human intestinal cells and a 3D culture of liver cells, Lab Chip. 18 (2018) 2036–2046. https://doi.org/10.1039/c8lc00111a.

[35] T. Hasenberg, S. Mühleder, A. Dotzler, S. Bauer, K. Labuda, W. Holnthoner, H. Redl, R. Lauster, U. Marx, Emulating human microcapillaries in a multi-organ-chip platform, J Biotechnol. 216 (2015) 1–10. https://doi.org/10.1016/j.jbiotec.2015.09.038.

[36] I. Maschmeyer, A.K. Lorenz, K. Schimek, T. Hasenberg, A.P. Ramme, J. Hübner, M. Lindner, C. Drewell, S. Bauer, A. Thomas, N.S. Sambo, F. Sonntag, R. Lauster, U. Marx, A four-organ-chip for interconnected long-term co-culture of human intestine, liver, skin and kidney equivalents, Lab Chip. 15 (2015) 2688–2699. https://doi.org/10.1039/c5lc00392j.

[37] I. Sergachev, A. Rusanov, E. Trushkin, D. Sakharov, U. Marx, A. Tonevitsky, Fluorescent optical fiber sensors for cell viability monitoring, Analyst. 138 (2013) 4066–4069. https://doi.org/10.1039/c3an00248a.

[38] H.Y. Tan, S. Trier, U.L. Rahbek, M. Dufva, J.P. Kutter, T.L. Andresen, A multi-chamber microfluidic intestinal barrier model using Caco-2 cells for drug transport studies, PLoS One. 13 (2018). https://doi.org/10.1371/journal.pone.0197101.

[39] H.J. Kim, D.E. Ingber, Gut-on-a-Chip microenvironment induces human intestinal cells to undergo villus differentiation, Integrative Biology (United Kingdom). 5 (2013) 1130–1140. https://doi.org/10.1039/c3ib40126j.

[40] M. Nikolaev, O. Mitrofanova, N. Broguiere, S. Geraldo, D. Dutta, Y. Tabata, B. Elci, N. Brandenberg, I. Kolotuev, N. Gjorevski, H. Clevers, M.P. Lutolf, Homeostatic mini-

intestines through scaffold-guided organoid morphogenesis, Nature. 585 (2020) 574–578. https://doi.org/10.1038/s41586-020-2724-8.

[41] C.M. Leung, P. de Haan, K. Ronaldson-Bouchard, G.A. Kim, J. Ko, H.S. Rho, Z. Chen, P. Habibovic, N.L. Jeon, S. Takayama, M.L. Shuler, G. Vunjak-Novakovic, O. Frey, E. Verpoorte, Y.C. Toh, A guide to the organ-on-a-chip, Nature Reviews Methods Primers. 2 (2022). https://doi.org/10.1038/s43586-022-00118-6.

[42] A.E. Danku, E.H. Dulf, C. Braicu, A. Jurj, I. Berindan-Neagoe, Organ-On-A-Chip: A Survey of Technical Results and Problems, Front Bioeng Biotechnol. 10 (2022). https://doi.org/10.3389/fbioe.2022.840674.

[43] A.D. Castiaux, D.M. Spence, R.S. Martin, Review of 3D cell culture with analysis in microfluidic systems, Analytical Methods. 11 (2019) 4220–4232. https://doi.org/10.1039/c9ay01328h.

[44] Y.I. Wang, M.L. Shuler, UniChip enables long-term recirculating unidirectional perfusion with gravity-driven flow for microphysiological systems, Lab Chip. 18 (2018) 2563–2574. https://doi.org/10.1039/c8lc00394g.

[45] A.C. Ailiani, T. Neuberger, J.G. Brasseur, G. Banco, Y. Wang, N.B. Smith, A.G. Webb, Quantitative analysis of peristaltic and segmental motion in vivo in the rat small intestine using dynamic MRI, Magn Reson Med. 62 (2009) 116–126. https://doi.org/10.1002/mrm.21982.

[46] Y. Xing, M. Nourmohammadzadeh, J.E.M. Elias, M. Chan, Z. Chen, J.J. McGarrigle, J. Oberholzer, Y. Wang, A pumpless microfluidic device driven by surface tension for pancreatic islet analysis, Biomed Microdevices. 18 (2016). https://doi.org/10.1007/s10544-016-0109-4.

[47] E. Berthier, A.M. Dostie, U.N. Lee, J. Berthier, A.B. Theberge, Open Microfluidic Capillary Systems, Anal Chem. 91 (2019) 8739–8750. https://doi.org/10.1021/acs.analchem.9b01429.

[48] Q. Zhang, S. Feng, L. Lin, S. Mao, J.M. Lin, Emerging open microfluidics for cell manipulation, Chem Soc Rev. 50 (2021) 5333–5348. https://doi.org/10.1039/d0cs01516d.

[49] J.N. Tan, T. Alan, A. Neild, Stability of flowing open fluidic channels, AIP Adv. 3 (2013). https://doi.org/10.1063/1.4792940.

[50] N.M. Oliveira, S. Vilabril, M.B. Oliveira, R.L. Reis, J.F. Mano, Recent advances on open fluidic systems for biomedical applications: A review, Materials Science and Engineering C. 97 (2019) 851–863. https://doi.org/10.1016/j.msec.2018.12.040.

[51] S.J. Trietsch, E. Naumovska, D. Kurek, M.C. Setyawati, M.K. Vormann, K.J. Wilschut, H. L. Lanz, A. Nicolas, C.P. Ng, J. Joore, S. Kustermann, A. Roth, T. Hankemeier, A. Moisan, P. Vulto, Membrane-free culture and real-time barrier integrity assessment of perfused intestinal epithelium tubes, Nat Commun. 8 (2017). https://doi.org/10.1038/s41467-017-00259-3.

[52] A. Nicolas, F. Schavemaker, K. Kosim, D. Kurek, M. Haarmans, M. Bulst, K. Lee, S. Wegner, T. Hankemeier, J. Joore, K. Domansky, H.L. Lanz, P. Vulto, S.J. Trietsch, High throughput transepithelial electrical resistance (TEER) measurements on perfused membrane-free epithelia, Lab Chip. 21 (2021) 1676–1685. https://doi.org/10.1039/d0lc00770f.

[53] C. Beaurivage, E. Naumovska, Y.X. Chang, E.D. Elstak, A. Nicolas, H. Wouters, G. van Moolenbroek, H.L. Lanz, S.J. Trietsch, J. Joore, P. Vulto, R.A.J. Janssen, K.S. Erdmann, J. Stallen, D. Kurek, Development of a gut-on-a-chip model for high throughput disease

modeling and drug discovery, Int J Mol Sci. 20 (2019). https://doi.org/10.3390/ijms20225661.

[54] C. Beaurivage, E. Naumovska, Y.X. Chang, E.D. Elstak, A. Nicolas, H. Wouters, G. van Moolenbroek, H.L. Lanz, S.J. Trietsch, J. Joore, P. Vulto, R.A.J. Janssen, K.S. Erdmann, J. Stallen, D. Kurek, Development of a gut-on-a-chip model for high throughput disease modeling and drug discovery, Int J Mol Sci. 20 (2019). https://doi.org/10.3390/ijms20225661.

[55] L. Dreyer, C. Smith, S.M. Deane, L.M.T. Dicks, A.D. van Staden, Migration of Bacteriocins Across Gastrointestinal Epithelial and Vascular Endothelial Cells, as Determined Using In Vitro Simulations, Sci Rep. 9 (2019). https://doi.org/10.1038/s41598-019-47843-9.

[56] Y. Bian, Y. Dong, J. Sun, M. Sun, Q. Hou, Y. Lai, B. Zhang, Protective Effect of Kaempferol on LPS-Induced Inflammation and Barrier Dysfunction in a Coculture Model of Intestinal Epithelial Cells and Intestinal Microvascular Endothelial Cells, J Agric Food Chem. 68 (2020) 160–167. https://doi.org/10.1021/acs.jafc.9b06294.

[57] B.S. Boyden, The chemotactic effect of mixtures of antibody and antigen on polymorphonuclear leucocytes, J Exp Med. 115 (1962) 453–466.

[58] W. Shin, H.J. Kim, 3D in vitro morphogenesis of human intestinal epithelium in a gut-on-a-chip or a hybrid chip with a cell culture insert, Nat Protoc. 17 (2022) 910–939. https://doi.org/10.1038/s41596-021-00674-3.

[59] S.M. Jung, S. Kim, In vitro Models of the Small Intestine for Studying Intestinal Diseases, Front Microbiol. 12 (2022). https://doi.org/10.3389/fmicb.2021.767038.

[60] A. Nicolas, F. Schavemaker, K. Kosim, D. Kurek, M. Haarmans, M. Bulst, K. Lee, S. Wegner, T. Hankemeier, J. Joore, K. Domansky, H.L. Lanz, P. Vulto, S.J. Trietsch, High throughput transepithelial electrical resistance (TEER) measurements on perfused membrane-free epithelia, Lab Chip. 21 (2021) 1676–1685. https://doi.org/10.1039/d0lc00770f.

[61] H.B. Chong, J. Youn, W. Shin, H.J. Kim, D.S. Kim, Multiplex recreation of human intestinal morphogenesis on a multi-well insert platform by basolateral convective flow, Lab Chip. 21 (2021) 3316–3327. https://doi.org/10.1039/d1lc00404b.

[62] A.A. Dogan, M. Dufva, Customized 3D-printed stackable cell culture inserts tailored with bioactive membranes, Scientific Reports 2022 12:1. 12 (2022) 1–12. https://doi.org/10.1038/s41598-022-07739-7.

[63] Formlabs, BIOMED CLEAR MATERIAL, 2020. https://formlabs.com/store/materials/biomed-clear-resin/ (accessed July 24, 2022).

[64] A. Wnorowski, H. Yang, J.C. Wu, Progress, obstacles, and limitations in the use of stem cells in organ-on-a-chip models, Adv Drug Deliv Rev. 140 (2019) 3–11. https://doi.org/10.1016/j.addr.2018.06.001.

[65] J. Hickman, Transepithelial/endothelial Electrical Resistance (TEER) theory and applications for microfluidic body-on-a-chip devices, J Rare Dis Res Treat. 1 (2016) 46–52. https://doi.org/10.29245/2572-9411/2016/3.1026.

[66] Y.B. Arlk, M.W. van der Helm, M. Odijk, L.I. Segerink, R. Passier, A. van den Berg, A.D. van der Meer, Barriers-on-chips: Measurement of barrier function of tissues in organs-on-chips, Biomicrofluidics. 12 (2018) 42218. https://doi.org/10.1063/1.5023041.

[67] B. Srinivasan, A.R. Kolli, M.B. Esch, H.E. Abaci, M.L. Shuler, J.J. Hickman, TEER Measurement Techniques for In Vitro Barrier Model Systems, J Lab Autom. 20 (2015) 107–126.

[68] C. Poon, Measuring the density and viscosity of culture media for optimized computational fluid dynamics analysis of in vitro devices, J Mech Behav Biomed Mater. 126 (2022) 105024. https://doi.org/10.1016/j.jmbbm.2021.105024.

[69] W. Thielicke, E.J. Stamhuis, PIVlab – Towards User-friendly, Affordable and Accurate Digital Particle Image Velocimetry in MATLAB, J Open Res Softw. 2 (2014). https://doi.org/10.5334/jors.bl.

[70] R. Kant Avvari, Biomechanics of the Small Intestinal Contractions, in: X. Qi, S. Koruth (Eds.), Digestive System - Recent Advances, IntechOpen, 2019. https://doi.org/10.5772/intechopen.86539.

[71] C.S. de Jonge, A.M.J. Sprengers, K.L. van Rijn, A.J. Nederveen, J. Stoker, Assessment of fasted and fed gastrointestinal contraction frequencies in healthy subjects using continuously tagged MRI, Neurogastroenterology and Motility. 32 (2020). https://doi.org/10.1111/nmo.13747.

[72] S. Tavelin, J. Gråsjö, J. Taipalensuu, G. Ocklind, P. Artursson, Epithelial Cell Culture Protocols, Humana Press, 2002.

[73] T. Lea, Caco-2 Cell Line, in: C. Kleiveland, L. Tor, P. Cotter, I. López-Expósito, A. Mackie, T. Requena, D. Swiatecka, H. Wichers (Eds.), The Impact of Food Bioactives on Health In Vitro and Ex Vivo Models, Springer, 2015: pp. 103–111.

[74] M. Natoli, B.D. Leoni, I. D'Agnano, M. D'Onofrio, R. Brandi, I. Arisi, F. Zucco, A. Felsani, Cell growing density affects the structural and functional properties of Caco-2 differentiated monolayer, J Cell Physiol. 226 (2011) 1531–1543. https://doi.org/10.1002/jcp.22487.

[75] S. v. Nikulin, A.A. Poloznikov, D.A. Sakharov, A method for rapid generation of model intestinal barriers in vitro, Bulletin of Russian State Medical University. (2020) 97–103. https://doi.org/10.24075/BRSMU.2020.077.

[76] Y. Cai, C. Xu, P. Chen, J. Hu, R. Hu, M. Huang, H. Bi, Development, validation, and application of a novel 7-day Caco-2 cell culture system, J Pharmacol Toxicol Methods. 70 (2014) 175–181. https://doi.org/10.1016/j.vascn.2014.07.001.

[77] Y. Sambuy, I. de Angelis, G. Ranaldi, M.L. Scarino, A. Stammati, F. Zucco, The Caco-2 cell line as a model of the intestinal barrier: in£uence of cell and culture-related factors on Caco-2 cell functional characteristics, Springer, 2005.

[78] Y. Cai, C. Xu, P. Chen, J. Hu, R. Hu, M. Huang, H. Bi, Development, validation, and application of a novel 7-day Caco-2 cell culture system, J Pharmacol Toxicol Methods. 70 (2014) 175–181. https://doi.org/10.1016/j.vascn.2014.07.001.

[79] J. Costa, A. Ahluwalia, Advances and Current Challenges in Intestinal in vitro Model Engineering: A Digest, Front Bioeng Biotechnol. 7 (2019). https://doi.org/10.3389/fbioe.2019.00144.

[80] I. Behrens, T. Kissel, Do cell culture conditions influence the carrier-mediated transport of peptides in Caco-2 cell monolayers?, European Journal of Pharmaceutical Sciences. 19 (2003) 433–442. https://doi.org/10.1016/S0928-0987(03)00146-5.

[81] D.P. Chopra, A.A. Dombkowski, P.M. Stemmer, G.C. Parker, Intestinal Epithelial Cells In Vitro, Stem Cells Dev. 19 (2010) 131. https://doi.org/10.1089/SCD.2009.0109.

[82] Q.-M. Ding, T.C. Ko, B.M. Evers, Caco-2 intestinal cell differentiation is associated with G_1 arrest and suppression of CDK2 and CDK4, American Journal of Physiology-Cell

Physiology. 275 (1998) C1193–C1200. https://doi.org/10.1152/ajpcell.1998.275.5.C1193.

[83] W. Shin, H.J. Kim, Intestinal barrier dysfunction orchestrates the onset of inflammatory host-microbiome cross-talk in a human gut inflammation-on-a-chip, Proc Natl Acad Sci U S A. 115 (2018) E10539–E10547. https://doi.org/10.1073/pnas.1810819115.

[84] J. Creff, L. Malaquin, A. Besson, In vitro models of intestinal epithelium: Toward bioengineered systems, J Tissue Eng. 12 (2021). https://doi.org/10.1177/2041731420985202.

[85] H.Y. Tan, S. Trier, U.L. Rahbek, M. Dufva, J.P. Kutter, T.L. Andresen, A multi-chamber microfluidic intestinal barrier model using Caco-2 cells for drug transport studies, PLoS One. 13 (2018). https://doi.org/10.1371/journal.pone.0197101.

[86] H.J. Kim, D. Huh, G. Hamilton, D.E. Ingber, Human gut-on-a-chip inhabited by microbial flora that experiences intestinal peristalsis-like motions and flow, Lab Chip. 12 (2012) 2165–2174. https://doi.org/10.1039/c2lc40074j.

[87] Rapid prototyping of a multilayer microphysiological system for primary human intestinal epithelial culture, (n.d.). https://doi.org/10.1101/400721.

[88] H.J. Kim, D.E. Ingber, Gut-on-a-Chip microenvironment induces human intestinal cells to undergo villus differentiation, Integrative Biology (United Kingdom). 5 (2013) 1130–1140. https://doi.org/10.1039/c3ib40126j.

[89] C.A.M. Fois, A. Schindeler, P. Valtchev, F. Dehghani, Dynamic flow and shear stress as key parameters for intestinal cells morphology and polarization in an organ-on-a-chip model, Biomed Microdevices. 23 (2021). https://doi.org/10.1007/s10544-021-00591-y.

SUPPLEMENTARY INFORMATION

Heterogenous morphogenesis of Caco-2 cells reveals that flow induces 3D growth at high cell densities but is not sufficient to induce intestinal cell maturation in 2D

*Asli Aybike Dogan, and Martin Dufva**

Department of Health Technology, Technical University of Denmark, 2800, Kgs. Lyngby, Denmark *E-mail: dufva@dtu.dk

MOVIES

Movie S1. R-inserts on the rocker, motion of liquid in the channel.

Movie S2. R-inserts on the rocker, motion of liquid in the reservoir.

Movie S3. µPIV flow vector map.

FIGURES

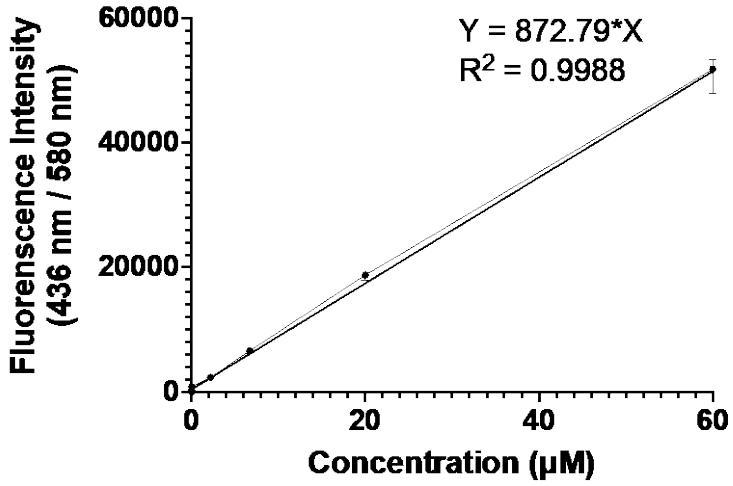

Figure S1. Standard curve of Lucifer Yellow (0-60 µM) for calculation of permeability coefficient to evaluate barrier functions of Caco-2 cells.

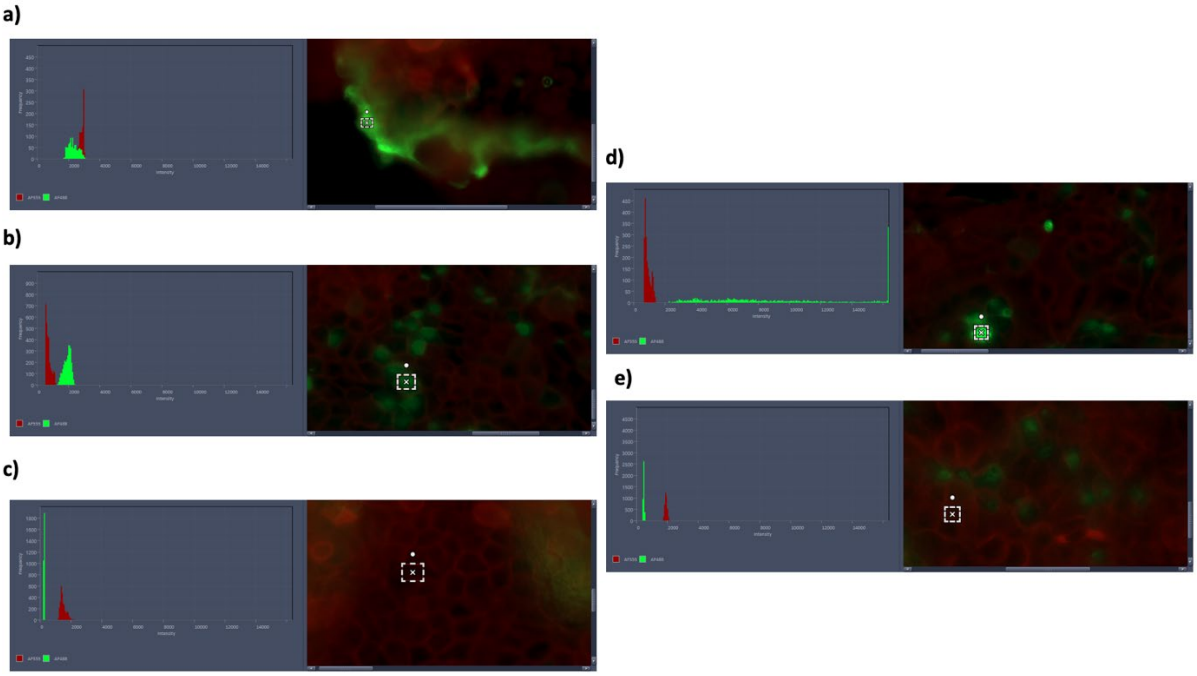

Figure S2. Representative images of fluorescence intensity analysis using ZEN Lite 3.2 image processing software (Carl Zeiss MicroImaging GmbH). Images from Villin intensity analysis were used as examples for each marker fluorescence intensity analysis. **a) Dynamic 3D:** measured as max intensity expressed, **b) Dynamic 2D:** measured as max intensity expressed by single cells, **c) Dynamic 2D Background (Empty Side):** used for discarding from both 2D and 3D intensities, **d) Static:** measured as max intensity expressed by single cells **e) Static Background (Empty Side).**

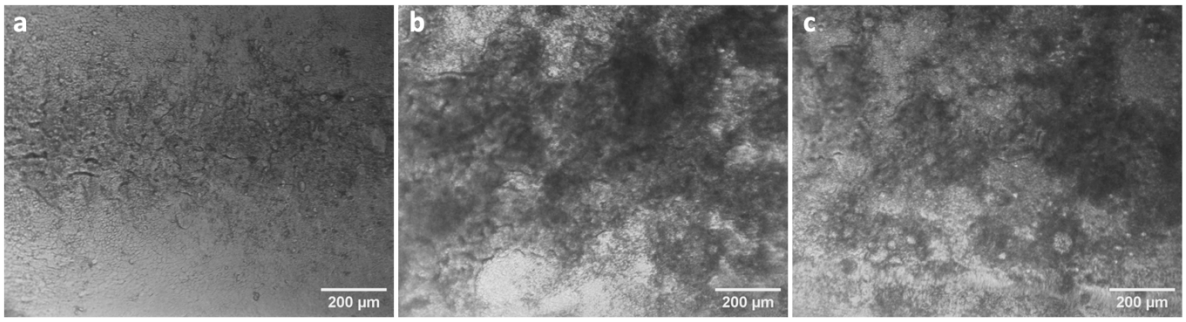

Figure S3. Representative brightfield images of 3D formations of Caco-2 cells (initial cell density: 100k/cm^2) under dynamic conditions. Images were taken from two independent experiments and wells from the same experiment. **a)** Caco-2 cells under dynamic conditions from 1st experiment (passage number: 60). **b)** 1st example of Caco-2 cells (passage number: 62) under dynamic conditions (photo is from 2nd experiment). **c)** 2nd example of Caco-2 cells (passage number: 62) under dynamic conditions (photo is from 2nd experiment). **Magnification:** 10x; **Scale bars:** 200 µm

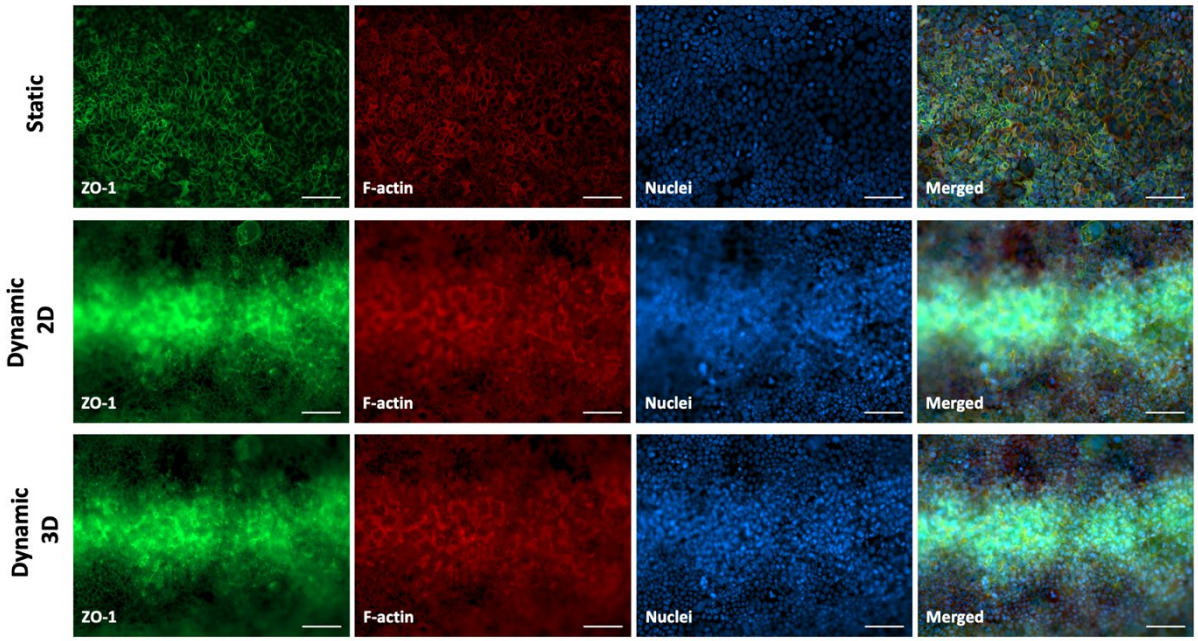

Figure S4. Representative immunofluorescence staining images under Static and Dynamic conditions (2D and 3D). **Green:** ZO-1 (tight junction); **Red:** F-actin (cytoskeleton); **Blue:** Hoechst (nuclei). **Magnification:** 20x; **Scale bars:** 100 µm

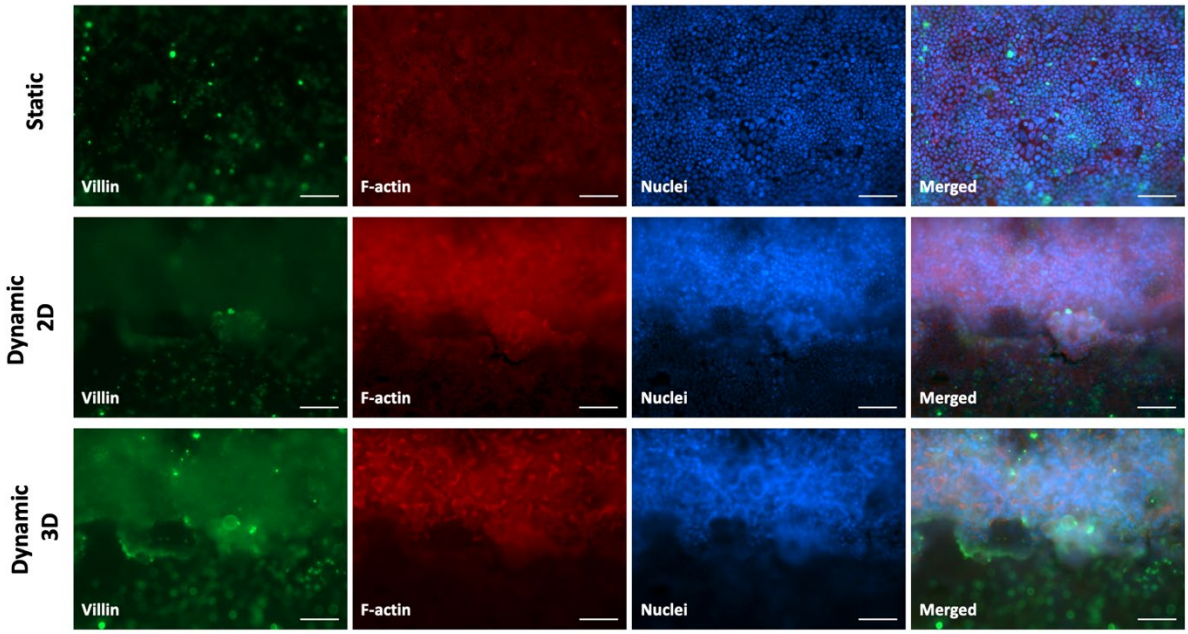

Figure S5. Representative immunofluorescence staining images under Static and Dynamic conditions (2D and 3D). **Green:** Villin (villus); **Red:** F-actin (cytoskeleton); **Blue:** Hoechst (nuclei). **Magnification:** 20x; **Scale bars:** 100 µm

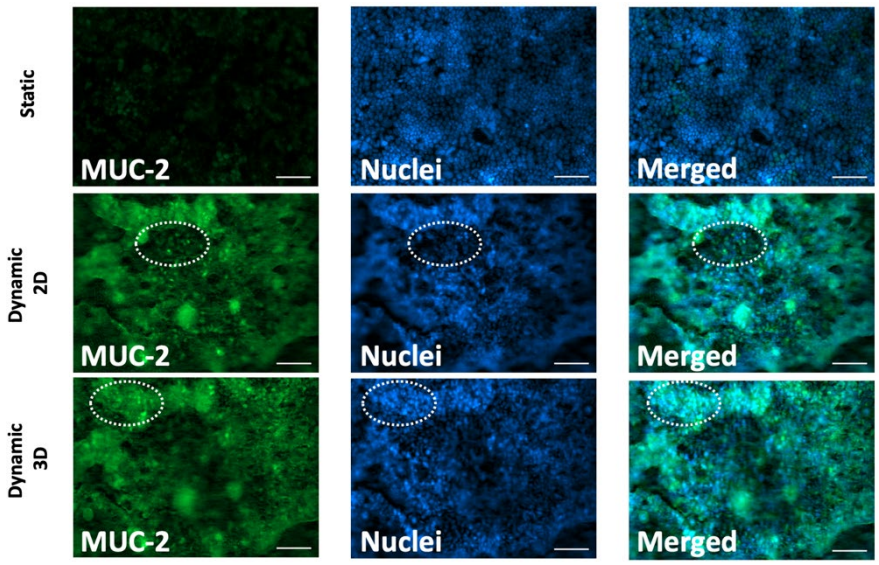

Figure S6. Representative immunofluorescence staining images under Static and Dynamic conditions (White circles indicate 2D and 3D areas). **Green:** MUC-2 (mucus secreting (goblet) cells); **Blue:** Hoechst (nuclei). **Magnification:** 20x; **Scale bars:** 100 µm

TABLES

Table S1. Flow Characteristics Based on Theoretical and µPIV calculations (Tilting angle: 7°)

		V (m/s)	Q (µL/s)	τ (dyn/cm^2)	Reynolds Number (Re)
Theoretical Calculations		0.056	336.05	1.0	1213
µPIV *(Mean±SD)*	**Center**	0.070 ± 0.001	418.36 ± 6.93	1.3	1510
	Edge	0.056 ± 0.002	335.06 ± 13.57	1.0	1209
	Whole	0.071 ± 0.002	426.73 ± 9.22	1.3	1540

Table S2. TEER values of Caco-2 monolayers (Ω×cm^2; n≥3)

TEER *(Mean±SD)*	**Pre-shear**	**Dynamic 3rd day**	**Dynamic 9th day**
50k cells/cm^2	447±105	580±55	2293±760
80k cells/cm^2	381±64	636±102	1049±171
100k cells/cm^2	324±24	548±70	1451±146
50k cells/cm^2		858±160	4930±533
80k cells/cm^2		785±93	2071±336

100k cells/cm^2		653±184	2499±422

Table S3. Permeability Coefficients (Pc; nm/s) of Caco-2 under static and dynamic conditions for 0.44 kDa Lucifer Yellow (LY) transport (n≥3)

LY	**Static**	**Dynamic**	**Empty Gel**
Pc (nm/s) *(Mean±SD)*	35.11±11.13	26.51±8.58	206.66±21.08

Table S4. Mean Fluorescence Intensity Values of Villin, MUC-2 and ZO-1

		2D	**3D**
Villin Intensity (a.u.) *(Mean±SD)*	**Dynamic**	1366.62 ± 474.82	2804.21 ± 67.16
	Static	1178.73 ± 31.53	
MUC-2 Intensity (a.u.) *(Mean±SD)*	**Dynamic**	115.61 ± 23.69	327.07 ± 22.37
	Static	121.79 ± 19.71	
ZO-1 Intensity (a.u.) *(Mean±SD)*	**Dynamic**	77.57 ± 14.31	549.26 ± 22.88
	Static	27.580 ± 7.532	
F-actin Intensity (a.u.) *(Mean±SD)*	**Dynamic**	1130.10 ± 70.77	10500.15 ± 275.64
	Static	897.07 ± 300.28	

Chapter 7

PAPER III

High throughput shear stress platforms coupling the intestine and blood vessels

Asli Aybike Dogan, Martin Dufva

Submitted (2022)

High throughput shear stress platforms coupling the intestine and blood vessels

Asli Aybike Dogan[a], Martin Dufva*[a]

Induction of shear often requires microfluidics that are complex. Here, we designed 3D-printed cell culture inserts containing shear stress zones when actuated with an orbital shaker. The cells' growth matrix was made of gelatin with a thickness of 50 - 100 µm, and inserts were functionalized with this thin hydrogel using a simple dip-casting procedure. The inserts were suitable to grow and activate endothelial (CI-huVECs) and intestinal epithelial (Caco-2) cells. The highest laminar shear stress zone had a calculated shear of 20.7 dyn/cm^2. The endothelial CI-huVECs cultured in dynamic conditions showed alignment following the flow direction, whereas the intestinal Caco-2 epithelium created a three-dimensional (3D) villus-like structure and mucus. Furthermore, shear stress could, to some extent, reverse endothelial gap formation induced by Tumor Necrosis Factor-α (TNF-α). Co-culturing required a two-step process due to different maturation times and shear needs of endothelial and epithelial cells. Caco-2 cells were first matured under low shear stress (LSS: 0.3 dyn/cm^2) in the center zone of a co-culture insert. Secondly, CI-huVECs were plated in the periphery zone and were matured under high shear stress (HSS) for two days. The Caco-2 layer seems to affect the endothelial integrity negatively. It was possible to follow fluorescent tracers from the apical side of the epithelium to the luminal side of the endothelium. Taken together, the presented inserts significantly improved the possibilities of orbital shaking to create shear and to co-culture different cell types while still being compatible with the standard well plates.

Introduction

Endothelial cells (EndoC) line the blood vessels and act as a monolayer interface between blood vessels and the underlying tissue. Endothelial cells, together with epithelial cells (EpiC), form a barrier that regulates diffusion and selective permeability[1] in the intestine, lung and kidney. The coupled epithelial and endothelial barrier permeabilities have mainly been studied *in vivo* for assessing drug delivery[2–4]. However, *in vivo* testing is costly, time-consuming, ethically questionable, and cannot always predict the outcomes of clinical trials[5,6]. Better *in vitro* models mimicking human physiology is therefore in high demand.

Apart from traditional 2D *in vitro* cellular models, 3D microphysiological systems[7–9] are developed to study drug transport across these barriers. These systems mainly focus on mono- and co-cultured cells in microfluidic chip systems by incorporating dynamic fluid flow[10–15]. They aim to achieve complex biochemical (e.g., extracellular matrix (ECM) coatings and/or hydrogel substrates[16,17] or biophysical (e.g., perfusion[18–22], stretching[23,24]) functionalities to mimic the corresponding conditions *in vivo*. Microfluidics platforms based on pumps are expensive, complex and time-consuming to use, which affects the throughput. Even though gravity-driven pumpless multiplexed chip alternatives[25–29] could be used for high-throughput applications, these systems are expensive to produce. Furthermore, most rely on bi-directional flow, which is reported to be less suitable for the function of endothelial barrier tissues[30].

Due to the complexities and limitations of chip systems, most preclinical barrier models used for drug screening still rely on the scalable commercial culture platform called Transwell inserts[31,32] that Dr. Stephen Boyden developed in 1960s[33]. In this robust platform, cells are grown on permeable membranes that allow open access to both apical and basolateral compartments. Thus, drug absorption can easily be evaluated by monitoring the concentrations of test drugs through the barrier tissue (such as the intestinal wall, the skin, vasculature, and the blood-brain barrier)[34,35]. Even though it is a practical platform, their porous membrane, which is the substrate for cells, lacks physiological relevance. As often reported in the literature, tissues grown in/on ECM-mimetic substrates have demonstrated a better ability to recapitulate tissue histogenesis and many biological functions, including drug metabolism and stem cell fate[9,36–38]. Both endothelium and epithelium are affected by shear forces which are not usually existing when using Transwell plates. Therefore, integrating perfusion systems

[a] *Department of Health Technology, Technical University of Denmark, 2800 Kgs. Lyngby, Denmark.*

* Corresponding author. (Email: dufva@dtu.dk)

into Transwell inserts was reported as an alternative strategy to achieve this functionality[11,12,39,40]. However, most of these systems also require complex multiple pumps/tubes, which might compromise the mentioned advantages of the Transwell system.

To overcome these complexities, orbital shakers have been used to mimic healthy and disease endothelial tissue models in dishes[41–48], which would be an easy-to-implement and scalable method to provide shear to barrier cells. Commercial Transwell insert cultures actuated with an orbital shaker suppressed proliferation of Caco-2 cells and induced differentiation to secrete mucus[49]. With these motivations, we aimed to provide shear functionality to 3D-printed customized inserts with dip-cast hydrogel membranes[50]. Here, we introduce circular rings to separate high shear stress (HSS) and low shear stress (LSS) zones within an insert for the co-culture of barrier endothelium and epithelium on hydrogels suitable for drug transport studies.

Materials and methods

Design and fabrication of the O-inserts with hydrogel membranes

Compartmentalized 3D-printed orbital inserts (O-insert; for mono- and co-culture) were designed to fit 12-well plates (tissue-culture-treated, Nunc, Thermo Fisher, Slangerup, DK) using Fusion 360 (Autodesk, California, USA). The detailed dimensions are described in Figure 1. The 3D-printed inserts were fabricated from biocompatible and autoclavable Biomed Clear resin[51] on Form 3B SLA printer (both from Formlabs, USA) using 100 µM layer thicknesses. The pre-processing of print files (.STL), fabrication and post-processing of inserts were conducted by following the same protocol mentioned in the previous article [50]. Gelatin membranes (15%) were cast into sterile 3D-printed O-inserts following a modified dip-casting protocol[50] in a laminar flow biosafety cabinet. Inserts were not pressed to a surface after dipping into the gelatin solution to remove excess liquid. Instead, inserts were slid over the gelatin solution surface to fill the apertures (Figure S1). Functionalized inserts were either used for cell culture experiments directly or stored in the fridge for a maximum of two weeks.

Membrane Thickness Measurement

To measure gelatin membrane thickness, 1.1 µm red fluorescent dyed polystyrene beads (1% g/cm^3 solids; #R0100, Fluoro-Max, Thermo Fisher, USA) were used. 1:1000 diluted fluorescent beads were mixed with gelatin solution, and membranes were fabricated by dip-casting technique as mentioned above. Thickness measurements of gelatin membranes (n≥3) in each compartment were done with a Zeiss™ AxioObserver Z1 epifluorescence microscope (Carl Zeiss MicroImaging GmbH, Gottingen, Germany) at an emission wavelength range of 542 nm to 612 nm by a LED (Light-emitting Diode) laser with filter set 38 HE (Carl Zeiss MicroImaging GmbH) and with 40x magnification (LD Epiplan-NEOFLUAR 40x/0.6 Korr). The beads were used as focus points, and the z height was recorded for the lowest and highest bead in focus. The difference was used as a measurement of height.

Cell culture

The human colon adenocarcinoma epithelial cells (Caco-2, passage 60-65, 09042001, European Collection of Authenticated Cell Cultures (ECACC), Salisbury, UK) were cultured in T-75 cell culture flasks (Starstedt, Nümbrecht, Germany) with the complete epithelial growth medium (Epi-GM; High-glucose Dulbecco's DMEM medium (Sigma-Aldrich) with 10 % (v/v) fetal bovine serum (FBS, Hyclone, CA), 1% (v/v) non-essential amino acids (NEAA, Gibco, Fisher Scientific, Slangerup, Denmark), and penicillin (100 U/mL)-streptomycin (100 µg/mL) (P/S, Sigma-Aldrich)). The human umbilical vein endothelial cells (CI-huVEC, passage 11-16, #INS-CI-1002, InSCREENeX GmbH, DE) were cultured in 0.5% (w/v) Gelatin (diluted from 2% (w/v) Gelatin solution, #INS-SU-1015, InSCREENeX GmbH, DE) coated T-75 cell culture flasks with the complete endothelial growth medium (Endo-GM, #INS-ME-1011, InSCREENeX GmbH, DE) with and 1 % (v/v) P/S. Each cell line above was split with trypsin-ethylenediaminetetraacetic acid (EDTA) for 3-5 min upon ~90 % confluency and maintained in an incubator (37 °C, 100 % Humidity, 5 % CO_2) with the culture medium replaced every two days.

Application of shear stress

CI-huVEC cells were seeded on hydrogel membranes of the whole (I_1), periphery (I_2), and center (I_3) compartmentalized inserts at a density of 2×10^5 cells/cm^2 in (I_1: 352 µL; I_2: 252µL; I_3: 60 µL) EndoGM and incubated on a 12-well plate filled with 1 mL of the EndoGM in the basolateral side for 24h. The confluent CI-huVEC cells were further cultured under static (control) and dynamic (the orbital shaker) conditions for 48h in a humidified incubator at 37 °C and 5 % CO_2.

The Caco-2 cells were seeded on hydrogel membranes of the center compartment (I_3) of inserts at a density of 10^5 cells/cm^2 in 100 µL of EpiGM and incubated on a 12 -well plate filled 1 mL of the EpiGM in the basolateral side until the Caco-2 cells formed a confluent monolayer. The confluent Caco-2 cells were further cultured under static (control) conditions for 8 days and gradual dynamic (the orbital shaker) conditions (LSS condition until day 6; the HSS condition for 2 days) in a humidified incubator at 37 °C and 5 % CO_2. The EpiGM in the apical side of the well inserts was exchanged with fresh EpiGM every two days.

For co-cultivation, a functional Caco-2 layer was formed, including exposure to LSS, see above, before plating the CI-huVEC cells as described above. 1 mL EndoGM was used in the basolateral side (well) in co-cultures after the CI-huVEC cells were introduced.

12-well plates containing the 3D-printed inserts were placed on the platform of orbital shakers (PSU-10i, Biosan, LV or

Thermomixer, Eppendorf, DE) housed in the incubator (Figure S2). The orbit of the platform was circular with a radius of 1 mm and a rotation rate set to 250 rpm for mono-culturing of Caco-2 cells, whereas with a radius of 5 mm and a rotation rate set to 160 rpm for mono and co-culturing of CI-huVEC cells; this movement induced a swirling motion of the medium over the cells. The shear stress ($\boldsymbol{\tau_{max}}$) within the cell cult ure well estimated as follows:

$$\boldsymbol{\tau_{max} = a\sqrt{\eta\rho(2\pi f)^3}}$$

(1)

where a is the orbital radius of the shaker (0.1 and 0.5 cm), ρ is the density of the culture medium (0.9973 g/mL), η is the dynamic viscosity of the medium (0.0101 poise), f is the orbital speed (rotational frequency; rotation/sec), and υ is the kinematic viscosity (1.012×10^{-6} m^2/s)[52]. To determine whether the flow was laminar or turbulent, the Reynolds number (Re) was estimated as follows:

$$\boldsymbol{Re = (f\rho d^2)/\eta}$$

(2)

where d is the inner diameter of the insert.

Stimulation with TNF-α

Tumor Necrosis Factor-α (TNF-α), 50 ng/mL solution was added to the medium in each apical and basolateral side of the insert after static (no shear) and dynamic (shear) conditions for 48h and TNF- α exposure were performed under the same respective condition for another 12h.

Electrical resistance across CI-HUVEC and Caco-2 monolayers

Transepithelial and endothelial electrical resistance (TEER) values were measured with an EVOM2 volt-ohm meter (World Precision Instruments. Sarasota, FL) using an Ag/AgCI chopstick electrode pair (STX3, World Precision Instruments, USA) by placing the electrode sticks in the apical and basolateral compartment. Resistance values (in ohms) from gelatin-membranes were subtracted from the values for membranes holding CI-HUVEC and Caco-2 cultures to determine the resistance across the cell monolayers. Standard TEER values in ohms-cm^2 ($\Omega.cm^2$) were calculated according to this formula:

$$\boldsymbol{TEER(\Omega.\, cm^2) = ((R_T(\Omega) - R_B(\Omega)) \times A\ (cm^2)}$$

(3)

where R_T is the total resistance across cellular monolayer on the membrane, R_B is the blank resistance of membrane only (without cells), and A is the surface areas of the membranes (I_2: 1.26 cm^2; I_3: 0.3 cm^2).

Measurement of epithelial and endothelial monolayer permeability

Permeability assays were performed with 0.44 kDa lucifer yellow (LY; Sigma-Aldrich, USA) and the mixture of two fluorescent labelled dextran tracers (4 kDa fluorescein isothiocyanate (FITC)-dye and 70 kDa Rhodamine B (RhB) dye (Sigma-Aldrich, USA)). 1 mL of pre-heated (to 37 °C) HBSS buffer (HBSS (1X), Sodium bicarbonate (0.0375 % w/v), HEPES (10 mM), BSA (0.05 % w/v, pH 7.4) was added to the basolateral side, and 60 µM lucifer yellow; 1 mg/mL FITC-Dex and Rhodamine B-dextran (RhB-Dex) were added to the apical side in each insert compartment in HBSS buffer (I_2: 252 µL; I_3: 100 µL). The transport was performed at 37 °C with 100 rounds per minute (rpm) shaking under dark conditions for 2h. 50 µL samples from each compartment were mixed with 50 µL HBSS transport buffer and transferred to a 96-well plate. The Relative Fluorescence Units (RFU) were measured with a plate reader (Spark multimode microplate reader, TECAN, Männedorf, CH) with excitation and emission (Ex/Em) wavelengths of LY (428/536) FITC (490/522) and RhB (540/580). The concentration of LY and fluorescent labelled dextran tracers in each sample was determined from standard curves (Figure S3). The permeability coefficients (Pc, nm/s) were calculated by derived equations from[50]:

$$\boldsymbol{P_c = ((V_r \times C_f)/(C_i \times A \times t))}$$

(4)

where, P_c is the permeability coefficient (nm/s), V_r is the receiver volume in mL, A is the membrane growth area in cm^2, C_i is the initial apical concentration (µM), and C_f is the final receiver concentration (µM), t is the assay time in seconds.

F-actin and Nuclei Stains and Immunostaining

Samples were washed for 15 min in PBS, followed by fixation in 2 % (v/v) PFA in PBS for 2 min and fixation in 4 % (v/v) PFA in PBS for 13 min at room temperature. PFA was aspirated from the samples and washed three times in PBS. For F-actin (Alexa Fluor Plus 555 Phalloidin, #A30106, Invitrogen, Thermo Fisher, USA) and Hoechst 33342 (nuclei, #62249, Invitrogen, Thermo Fisher, USA) staining, the samples were incubated with the stain (5 µL phalloidin and 1 µg/mL Hoechst 33342 in PBS diluted in 200 µL PBS with 1 % (v/v) bovine serum albumin (BSA, Sigma-Aldrich, USA) for 20 min at room temperature. Prior to imaging, the samples were washed three times in PBS and left in PBS.

Alcian Blue Staining

Alcian blue was used to detect acidic mucous substances. After fixation of the cell (mentioned above), 1% Alcian Blue solution (in 3% acetic acid; #B8438, Sigma, USA) was added to central wells and

incubated for 20 mins at room temperature (RT). The samples were washed (4x) with PBS and examined under a light microscope.

Microscopy Imaging and Image Processing

Bright-field micrographs were taken using a Zeiss Primovert microscope (Carl Zeiss MicroImaging GmbH, Gottingen, DE) with the following objective: Plan-Achromat 4x/0.10, whereas staining images were acquired with Zeiss AxioObserver Z1 epifluorescence microscope (Carl Zeiss MicroImaging GmbH) with the following objectives: LD Epiplan-NEOFLUAR 20x/0.4 Korr M27. The obtained images were fitted with scale bars and nuclei counting analysis and image processing were done in Zeiss Zen Blue 3.4 Lite Digital Imaging Software (v. 3.4.91.00000, Carl Zeiss Microscopy GmbH). Vector analyses of aligned actin fibers (using the macro OrientationJ plugin[53]) were performed with an 80x80 pixel^2 local window to determine the scale of analysis. Measurements of the gap area between cells (using the Particle Analyze Tool) were performed on the ImageJ/Fiji[54].

Statistical analysis

Calculations of experiments were done as MEAN, standard deviation (SD) and standard error of the mean (SEM) on Microsoft Excel (Version 2016, Microsoft Office, Seattle, Washington). Different groups were compared for equality of means by using Welch's one-way among groups in orientation vector and gelatin membrane thickness analyses and two-way variance analyses (ANOVA), with Tukey's test for post-hoc analysis among groups in nuclei counting, gap area, TEER and molecule transport analyses (GraphPad Prism; version 9.0.0 for macOS, GraphPad Software, La Jolla California USA, "www.graphpad.com"). P-values were obtained and determined to be significantly different when the p-value<0.05.

Results and Discussion

Modular design and fabrication of the O-inserts with hydrogel membranes

The 3D-printed dynamic inserts (O-inserts) were designed to separate compartments with different shear profiles (Figure 1a-b-d). The inserts were intended to be functionalized in the bottom apertures using dip-casting of a hydrogel or with a hard polymeric filter[50]. The distance between the bottom of the plate and the bottom of the insert was 3 mm (Figure 1a). The two slits on the periphery of the insert were used for medium exchanges and trans-endothelial/epithelial electrical resistance (TEER) measurements using STX3/chopstick electrodes for EVOM[1,55–57]. The apical medium depth was standardized to ~2 mm depth (Figure 1b) ((I_1: 352 μL; I_2: 252 μL; I_3: 60 μL) (Figure 1d), which is a suitable depth to avoid inaccuracy in advection-driven shear stress[58]. The choice of the 'center' and 'periphery' regions (radial distances <5 mm and >5 mm from the center, respectively) was based on considerations such as (1) applicability of membrane formation by dip-casting[50], (2) sufficient wall to wall distance to ensure medium flow and (3) separating shear gradient areas for co-culturing purposes. Also, the chosen dimensions for the insert inner well dimensions were comparable to dimensions used with radially segmented well plates[44,45,47,48,59]. Previously, orbital shakers have been combined with commercialized Transwell inserts to create shear and vertical compartmentalization[41,42,49]. Here, we introduce walls to compartmentalize shear zones for both vertical and horizontal co-culture (Figure 1a-b-d). The peripheral zone (($I_{2'}$) Figure 1a and (I_2) Figure 1b-middle panel) was chosen to place endothelial cells (CI-huVECs) by aiming for the most uniform and highest shear stress. Caco-2 cells were placed in the center ($I_{3'}$) (Figure 1a) with the lower shear force. The highest shear stress values (20.7 dyn/cm^2) and the lowest shear stress (0.3 dyn/cm^2) were obtained with the speed range for the orbital shakers with orbit diameters of Ø=10 mm at 160 rpm and Ø=2 mm at 250 rpm. This is within the interesting physiological shear stress range of 10-20 dyn/cm^2 in the arteries, 1-6 in dyn/cm^2 veins[13,60–63] and 0.02-5 dyn/cm^2 for intestine[13,64,65]. The Reynolds number range of the respective compartment was I_1: 96-600, I_2: 427-504, and I_3: 96-148. The low span of the I_2 design suggested a more homogeneous flow with a little radius effect.

We mainly used endothelial cell alignment under flow [43–45,66] to assess the appropriate dimensions of the O-insert. Preliminary experiments showed that 24-well plate dimensions with an associated reduction in the wall-to-wall distance could not align cells while a 12-well plate could. Likely, walls too close together suppress flow due to surface tensions. While the design could not be scaled down from 12-well plates to 24-well plates, it could likely be scaled up to 6-well plate format [43–45,66,67] and, therefore, include more "rings" to study varying shear forces simultaneously or increase the number of co-cultures.

Other mechanical forces such as hydrostatic pressure, tensile strain, and stiffness also influence cells[68–70]. When the physiological stiffness values (5-20 kPa for vascular cells[68]; 1-40 kPa for intestine cells[71–73]) are compared with hydrated Transwell Polyethylene (PE) membranes (~180 MPa[74]), it becomes obvious that the PE membranes are not representative of the physiological ECM microenvironment conditions. Therefore, we used the previously presented dip-casting technique[50] (Figure S1) to fabricate inserts with 15% (w/v) gelatin with a mean Young's modulus of ~9.36 kPa. The gel thickness was measured in the middle of the gels (I_1, I_2 and

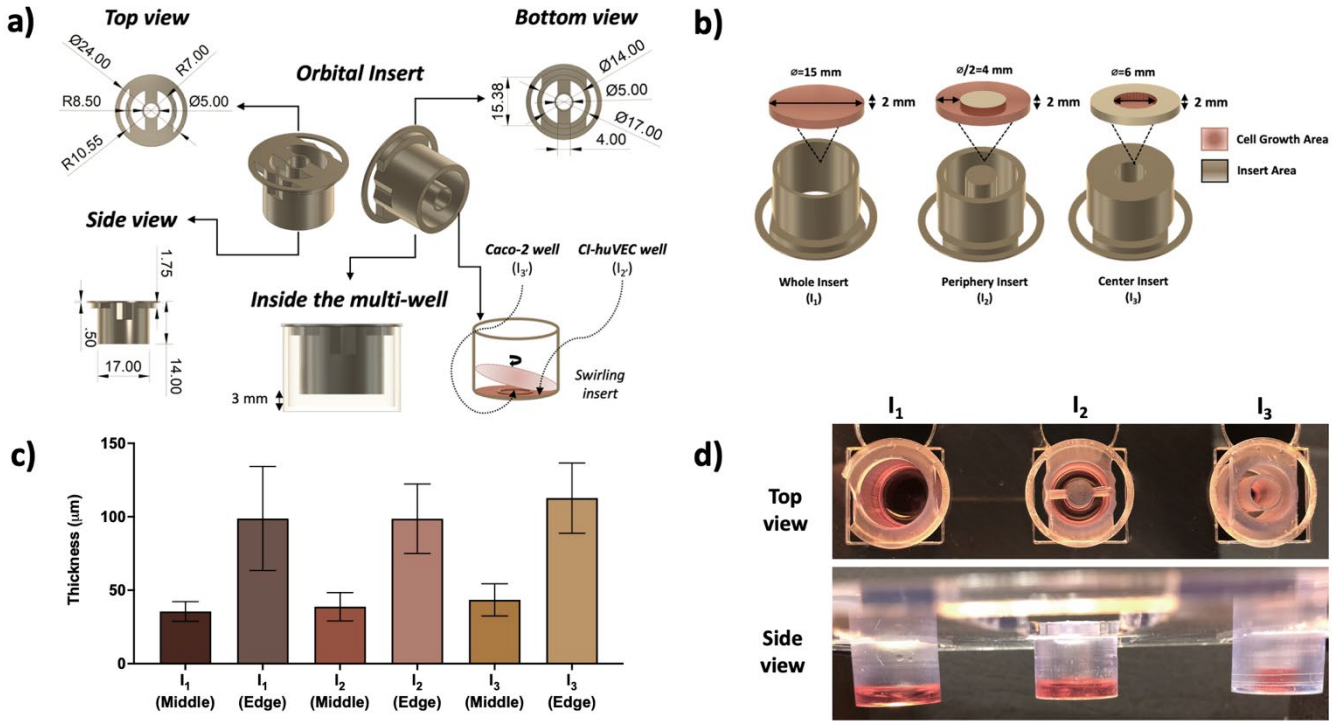

Figure 1. 3D-printed orbital inserts (O-insert) design for mono- and co-culture of cells. **a)** Dimensions of co-culture inserts with dual compartments in mm. **b)** Schematic of the compartmentalized insert bottoms whole (I_1), periphery (I_2) and center (I_3), for shear stress gradient zones. The pink illustrations indicate cell growth area and medium level (= 2 mm) to define the growth medium volume. **c)** 15% (w/v) Gelatin membrane thicknesses for the respective insert bottom zones. Measurements were taken from middle and edge of membranes in each insert (Mean±SD). **d)** top (**upper panel**) and side (**below panel**) views of gelatin membrane assembled compartmentalized inserts. Red liquid is medium (about 2 mm high in the compartment) while the membrane is not stained.

I_3) (Figure 2c) and where the gel grips the 3D printed walls. The thicknesses of gelatin membranes were around 50 µm in the middle part ("center"). Close to the edge where the gels grip the 3D printed walls, the thickness of the membranes was measured to be about 100 µm suggesting that the membranes were thinner towards the center. The gel will, however, be 1.5 times thicker when fully hydrated[50]. Similar to the dip-casting procedure of the gelatin membrane in 1 mm diameter apertures in a horizontal bottom resulted in gels in the order of 500 µm when the wall thickness was around 500 µm. The measured permeability of lucifer yellow was 300 nm/s through the 500 µm thick gel, and the PTFE filter had about 2800 nm/s [50]. Here, by contrast, we observe a permeability of about 1500 nm/s (see below for details) which is expected of a much thinner membrane as the time to diffuse will be shorter.

Zone-specific morphology and orientation of endothelium

The effects of the different zones corresponding to different shear stress profiles were tested using immortalized HUVEC cell lines (CI-huVECs). 48h exposure to shear stress resulted in clear alignment in the periphery compartment using an orbital shaker with settings that would theoretically result in 20.7 dyn/cm^2 shear. 24h exposure of shear did not show reproducible alignment (Figure S4); therefore, 48h exposure was chosen in the following experiment. Actin staining showed that CI-huVEC was aligned and elongated in the periphery regions of I_1 and the I_2 inserts (Figure 2a). By contrast, CI-huVEC at the center of the I_1 and I_3 inserts exhibited a cobblestone morphology, no alignment and, in some cases, detachment (Figure 2a). This is likely due to the multi-directional shear of the cells in the center [44,45,47,48]. The cells in the periphery region were straight and unbranched, suggesting a condition similar to *in vivo* arteries [47,48].

Periphery inserts (I_2) were chosen and further investigated in terms of the angle of alignment and uniformity of the cells by the direction of the flow (Figure 2b). The angular orientation of alignment correlated with the position in the circle the image was taken. The image taken at about 90**°** had an alignment of 8.45±0.27° (Mean ± SEM), where the calculated value by means of symmetry should be 0**°** (see Figure 2 for explanations). The polar plots (Figure 2b middle lower) show that the direction of the cells is around 0**°**. Cells would theoretically have a direction of 30° when the pictures were captured at the position of 150°, and we also observe that the majority of cells have a direction of 34.88±0.3° (Mean ± SEM). The polar plots indicate that the majority of cells had a direction of about 30° (Figure 2b left panels). The cells in corresponding positions in an insert that was not shaken had, by contrast, no signs of orientation (Figure 2b right column).

It should be noted that one image is not a single point and will, therefore, have a natural spread of flow directions which might

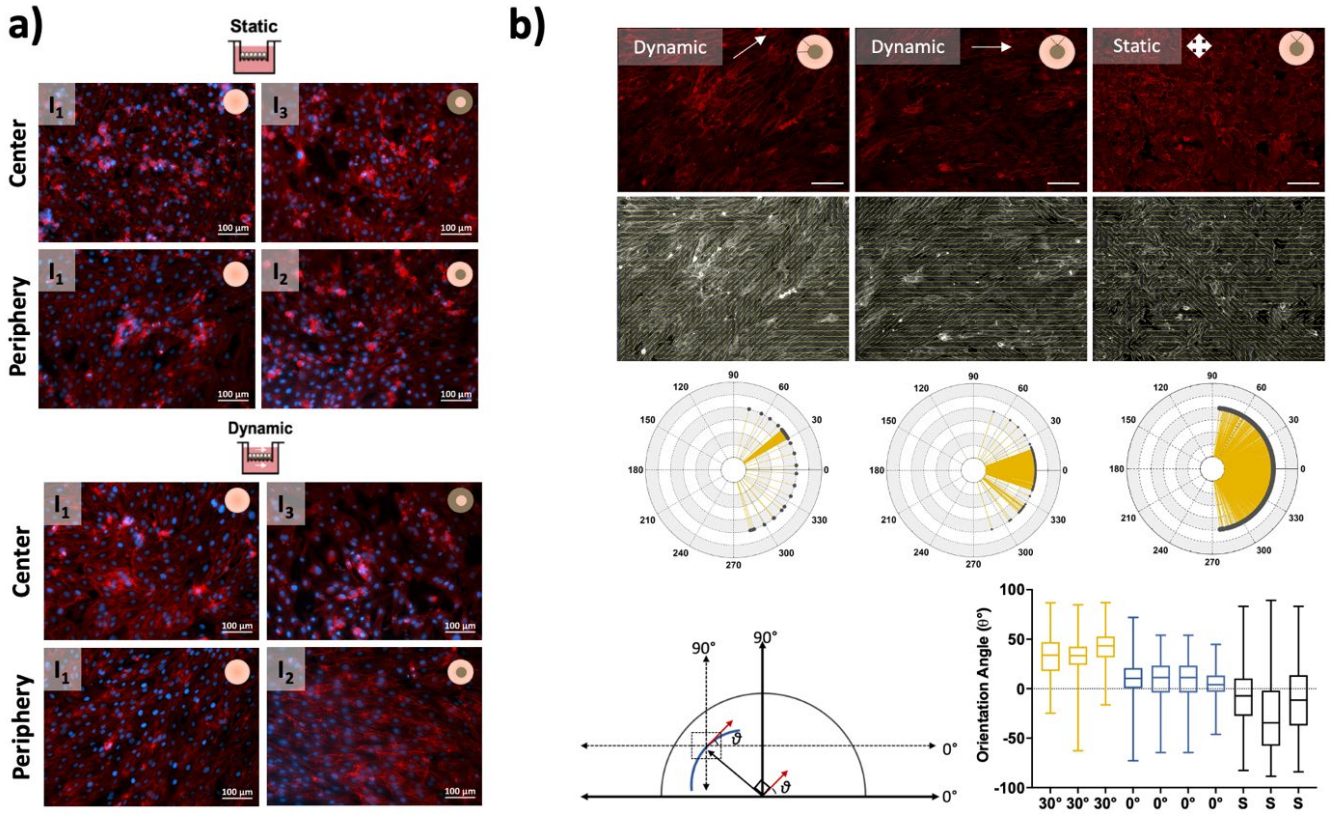

Figure 2. Morphology of CI-huVECs in compartmentalized inserts. **a)** F-actin (red) and nuclei (blue) staining of cells under static (**top panel**) and dynamic (**bottom panel**) conditions. Cells in the center zone of I_1 and I_3 inserts showed random distribution, whereas cells in the periphery zones of I_1 and I_2 inserts were more aligned. **b)** Orientation vector analysis done on obtained images (80x80 pixel^2) from approximate coordinates (150 and 90 degrees) (top and middle panels). The orientation angle (θ) was calculated from largest eigenvalue of the vector gradient structure tensor matrix by OrientationJ macro on the Fiji (-90°(270°)<θ<90°). By order or symmetry, θ° will be 30° for picture taken at angle 150° and θ° will be near 0° in picture taken near 90°. The polar diagrams illustrating the relationship between obtained polar eigenvectors and Cartesian coordinates by OriginPro software (**bottom panel**).

explain some of the spread of cell orientations. According to the example coordinates, if the images have a field of view of 1 mm wide, meaning that over a 1 mm wide picture was taken at 6 mm from the center, the flow shifts direction about 10° ($2*\sin^{-1}(0.5/6)$). Some of the variations are, therefore, due to the relatively large image taken. The observed alignments and directions agree with the literature[43,44,75].

Effect of conditioned medium on monolayers treated with TNF-α

To investigate the relationship between barrier integrity and hydrodynamic shear stress, CI-huVEC cells were treated with and without 50 ng/mL TNF-α in static and dynamic conditions. The cell layer was formed using 24h static culture followed by 48h HSS (20.7 dyn/cm^2). TNF-α treatment decreased the TEER values over time in both static and dynamic conditions (Figure 3a and Table S1). TEER was slightly but significantly higher in dynamic incubation compared with static incubation without TNF-α treatment (Figure 3a and Table S1). Cells from the 12h group were stained with F-actin and nuclei staining to assess the morphological effects of TNF-α treatment. In both static and dynamic groups without TNF-α stimulation, most actin filaments were localized around the periphery of cells and parallel with cell-cell junctions. Cells were more elongated and showed signs of alignment in the dynamic group compared to the static group.

Adding TNF-α profoundly impacted the cells in the respective group (Figure 3b). In the static group, the cell shrunk significantly, leaving significant gaps in the cell layer. TNF-α treatment of the dynamic group resulted in elongated cells, with thick actin stress fibers that traversed the cells in the direction of cell elongation/alignment, with the appearance of larger gaps at cell-cell junctions (Figure 3b). Quantifying the gap size showed a two-fold increase in gap areas in TNF-α treated group under dynamic conditions, while the gap size increased to about 10-fold in static conditions (Figure 3c and Table S2). The number of cells in the different conditions was evaluated using the nuclear count. The dynamic cultured had higher cell counts than the static cultures (Figure 3d and Table S3). In both conditions, the number of cells decreased about 3-fold after the TNF-α treatment (Figure 3d and Table S3). The loss of cells would explain the large gaps in the static cultures. In the dynamic cultures, by contrast, the cells seem to swell, which would explain why the gap area increase is relatively modest compared to the static condition culture (Figure 3c and Table S2). These data suggest a model where

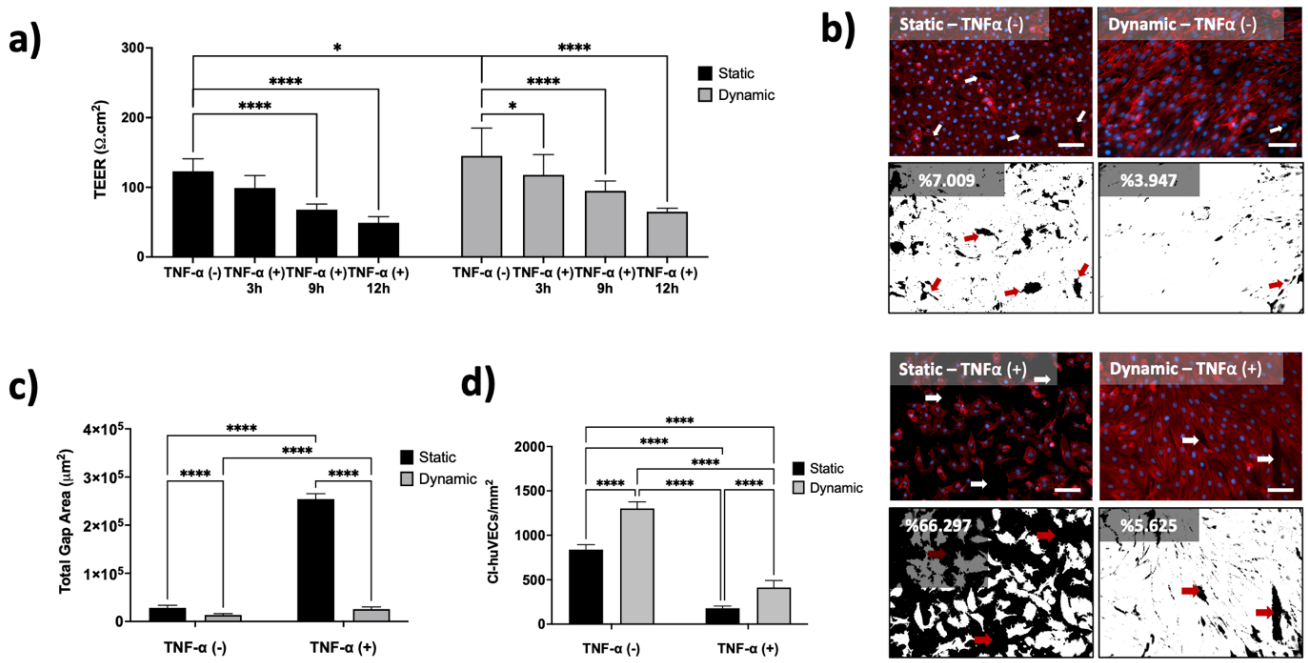

Figure 3. The effect of TNF-α treatment on barrier integrity and hydrodynamic shear stress on endothelial cells. **a)** 50 ng/mL TNF-α treatment decreased the TEER values over time (left) without a significant difference between static and dynamic groups (right) (n≥12). **b)** Gap size analysis on the F-actin-stained CI-huVECs after the TNF-α and shear exposure were done (using Particle Analyze Tool) was performed on the ImageJ/Fiji[54]. White and red arrows indicate intercellular gaps in the analyzed images (n=3). **Black spots:** intercellular gap; **white spots:** cell area. **c)** Quantified gap area. **d)** Cell density in the respective condition (n≥5). Only significant between conditions is annotated with asteroids (*p< 0.1; ****p< 0.0001); all other combinations are non-significant (ns=p>0.05).

TNF-α induced cell losses and gap formation, and while shear did not protect from cell losses, at least not using the conditions applied here, shear counteracted gap formation by swelling the cells. Counteracting gap formation induced by TNF-α would reduce, for instance, LDL uptake and therefore be one of many flow mechanisms that protect against atherosclerosis[76,77].

Molecular transport through the endothelial barrier

Next, we performed permeability experiments with tracer molecules to verify findings (Figure 3a and Table S1) on barrier integrity of CI-huVEC monolayers with and without TNF-α treatment. To explore the potential molecular size effect, 0.44 kDa LY, 4 kDa FITC-Dextran (FITC-Dex) and 70 kDa Rhodamine B-Dextran (RhB-Dex) were used as paracellular transport markers. The permeability decreased with the increase in the size of the tracer molecule (Figure 4 and Table S5-7). The empty gel dominated permeability but was generally higher than cells before TNF-α treatment (compare the different colored bars). After TNF-α treatment, the permeability increased and was similar to the empty gel indicating no barrier functions. The most significant difference between the membrane with and without cells before TNF-α treatment was observed in the dynamic system. TEER correlated with permeability (Figure 3a and 4) as only relatively minor changes are seen in TEER upon TNF-α treatment. These results correlate to some extent with the magnitude of gaps observed above (Figure 3b-c). A tight barrier would require a complete monolayer and tight junctions (see below where Caco-2 cells are used). This is not seen in any condition prior to TNF-α treatment (Figure 3a). However, the cells seem to inhibit transport as permeability was always, although not significantly, higher in empty membranes than in membranes with cells (Figure 4). Even small gaps would decrease the TEER significantly (Figure 3a). Likewise, the small gaps will work as gateways for molecules to diffuse through. In conclusion, the data showed that chronically applied physiological shear stress increased barrier integrity of the cells, which is in accordance with the literature[41,42]. The intercellular gap formation and changes in morphology and actin organization, as observed in CI-huVECs after the TNF-α treatment, correlated with increased permeability and agree with the literature[78,79] .

Coupled endothelial and epithelial barriers

Next, we wanted to connect an intestine model with a vascular model with the correct orientation of cells as *in vivo* (Figure 5a). To that end, co-culture inserts were used where Caco-2 cells were placed in the center and the CI-huVECs in the periphery. A two-step process was, however, used. In the first step, Caco-2 cells were seeded (10^5 cells/cm^2) to the center compartment of co-culture inserts, and after 3d-static culture to reach confluency, they were differentiated at LSS (0.3 dyn/cm^2) using orbital thermomixer (at 250 rpm) for 6 days. 3D villi-like intestinal microstructures were formed under dynamic conditions (Figure 5b, rightmost panel). This is in accordance with previous results that showed enhanced cytodifferentiation

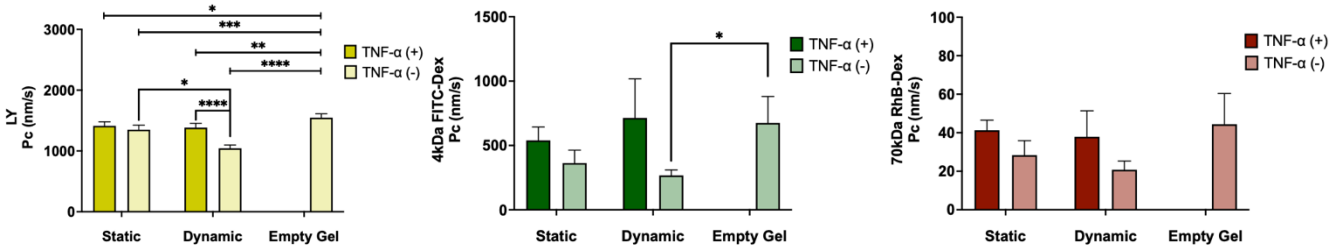

Figure 4. Permeability coefficients for lucifer yellow (LY) **(left)**, 4 kDa FITC-Dextran **(middle)** and 70 kDa Rhodamine B-Dextran **(right)** after TNF-α treatment. **Empty gel:** control without cell monolayer (n≥3). Only significant between conditions is annotated with asteroids (*p< 0.1; **p< 0.001; ***p< 0.001; ****p< 0.0001); all other combinations are non-significant (ns=p>0.05).

with 3D villi-like structure 3D epithelial layers formed in their orbital shaker platform[49]. There was more mucus in cultures under the dynamic condition as compared to the static conditions (Figure 5b, two rightmost panels), which agrees with previous observations [49]. After 6d of incubation, TEER values of mono-cultured Caco-2 cells increased 4-fold as compared with the static system (Figure 5c and Table S8). Taken together, this indicates that the Caco-2 barrier was formed with expected functionalities and ready to be connected to the endothelial layer. In the second step, insert with a high Caco-2 barrier function in the central area were seeded with CI-huVECs in the periphery and incubated for 1d at the static condition to reach confluency. High-shear conditions were applied as in the mono-culture, see above. The TEER measurement showed no difference between the mono-cultured and co-cultured intestinal cells indicating that shear stress and the presence of endothelial cells did not affect the barrier (Figure 5d and Table S9). However, co-cultured CI-huVECs showed lower TEER values compared to the mono-cultured group in the dynamic conditions, indicating crosstalk between Caco-2 cells and the endothelial layer (Figure 5d and Table S9). The mechanism is unclear, but it is unlikely medium incompatibility as the endothelial optimized medium is used in the well (1 mL) and only 60 µL epithelial medium at the apical side.

The barrier function was further investigated. LY and FITC-Dex (4 kDa) were added to the apical side of the Caco-2 layer, and samples from the well and the apical side of the endothelial layer were taken after 2h. The amount of LY molecules on top of the Caco-2 layer (donor compartment) was relatively constant for all three conditions (Figure 5e top left graph and Table S10-11). A slight but insignificant decrease in the number of molecules was observed without cells indicating a more rapid transport over the empty gel of LY. The quicker transport over empty gels was corroborated by a higher number of molecules in the well compartment as compared with culture with cells (Figure 5e, top middle graph and Table S10-11). A very low amount of LY molecules was observed in culture with Caco-2 cells as compared with the empty gel indicating a tight barrier. There was no difference between dynamic and static incubation in transport despite the latter having a higher TEER value (Figure 5c). The endothelium in the co-culture conditions did not seem to have any barrier function, as the ratio between the empty gel and cell cultures did not change between the well compartment and the Ci-huVEC apical side compartment (Figure 5e, top right graph and Table S10-11). Dynamic incubation did not change the barrier of the endothelial cell regarding LY, which correlated with TEER measurements in co-cultures (Figure 5d and Table S9).

The amount of transport of 4 kDa-FITC-Dex was slightly higher in the static culture compared to dynamic cultures and the empty gel, but the difference was minor (Figure 5e, lower left graph and Table S12-13). The amount of 4 kDa-FITC-Dex transported over the empty gel was higher than in cell cultures, indicating a Caco-2 barrier function. The lowest number of molecules was observed in the dynamic system, indicating that the barrier was tightest under shear (Figure 5e, lower middle graph and Table S12-13), which correlated with an increase in TEER value (Figure 5c and Table S8). The fraction of tracer diffusing through the gel in the middle compartment is much higher using the smaller LY (25%) compared to the larger 4 kDa-FITC-Dex (2%), which can be explained by the faster diffusion of the smaller LY molecule through the gel. The CI-huVECs seemed not to form any barrier in the static or the dynamic co-culture, which correlated with the measured TEER values (Figure 5d and Table S9).

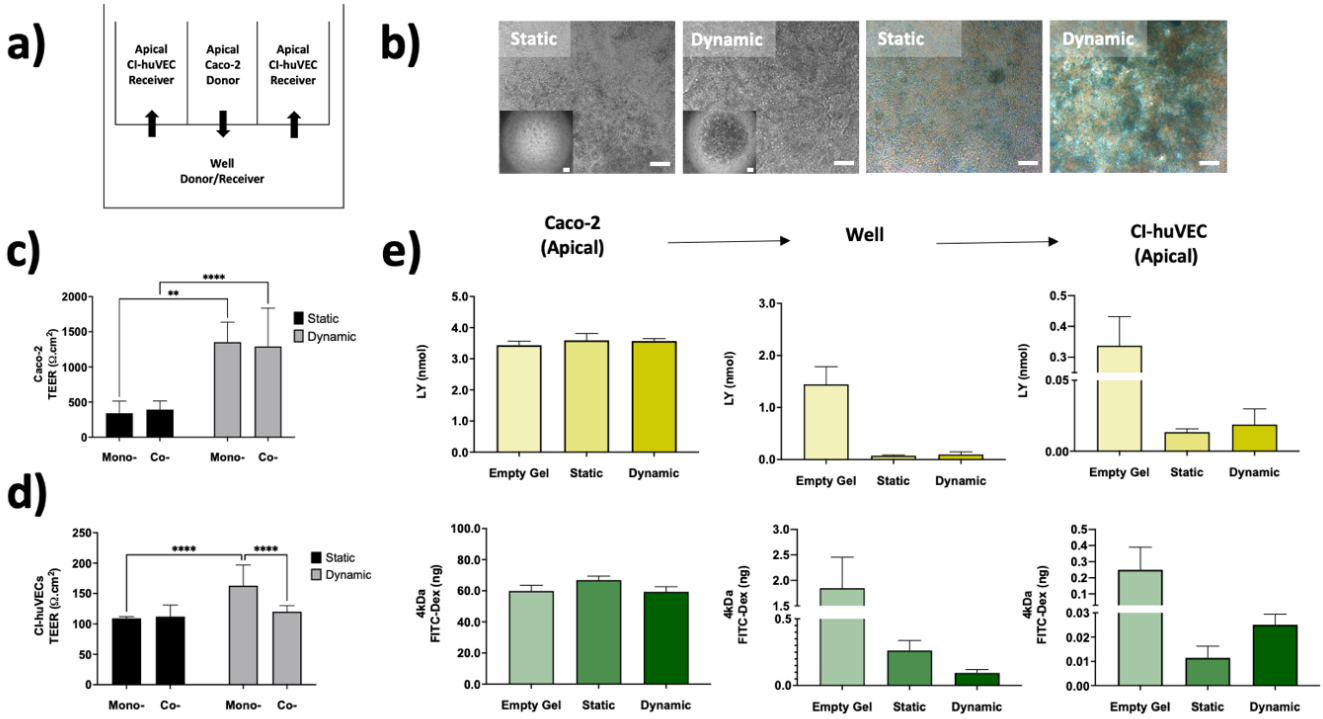

Figure 5. a) Illustration to demonstrate molecular transport route. b) Caco-2 cells cultured under LSS for 6 days. **Left:** Light microscopy micrographs of Caco-2 monolayers under static and dynamic conditions. 3D villi-like morphology was observed in the central region of the dynamic group. **Right:** Alcian blue staining was as indication of mucus secretion. TEER measurement comparison between mono- and co-cultured **c)** Caco-2 and **d)** CI-huVECs' barrier tissue integrities under static and dynamic conditions (n≥6). Only significant between conditions is annotated with asteroids (*p< 0.1); all other combinations are non-significant (ns=p>0.05). **e)** Molecular transports of lucifer yellow (LY) and 4 kDa FITC-Dextran (4 kDa FITC-Dex) from intestinal and endothelial barriers to mimic gut-vasculature diffusion and absorption route in the body. **Empty gel:** control without cell monolayer (n≥3).

Conclusions

The 3D-printed inserts displayed and validated here provide a more homogeneous flow than a completely open well such as commercial Transwells when actuated using an orbital shaker. In particular, the center region can be avoided if needed, but the peripheral regions can also be designed to minimize gradients due to radial effects. The dual lateral compartments allow for combining two barriers instead of only one in a traditional Transwell system, which would significantly extend the usability of hanging inserts. The convenient top loading of the cell to create the respective barrier is amiable to automation. Furthermore, the data showed that the insert provides sufficient shear to activate cell functions. Therefore, the reported two compartment inserts are a direct competitor of corresponding microfluidics systems but with much higher throughput and lower complexity.

Author Contributions

A.A.D.: Project administration, Conceptualization, Data curation, Formal analysis, Investigation, Methodology, Validation, Visualization, Writing—original draft, review, editing. M.D.: Project administration, Conceptualization, Resources, Supervision, Writing—review & editing.

Conflicts of interest

There are no conflicts to declare.

Acknowledgements

This project has financially supported by the European Union's Horizon 2020 research and innovation program under the Marie Skłodowska-Curie grant agreement No. 812673 and was conducted within the Organoids for Virus Research (OrganoVIR) network.

References

1. Srinivasan, B. *et al.* TEER Measurement Techniques for In Vitro Barrier Model Systems. *Journal of Laboratory Automation* vol. 20 107–126 Preprint at (2015).

2. Muzykantov, V. & Muro, S. Targeting delivery of drugs in the vascular system. *Int J Transp Phenom* **12**, 41–49 (2011).

3. Brake, K., Gumireddy, A., Tiwari, A., Chauhan, H. & Kumari, D. In vivo Studies for Drug Development via Oral Delivery: Challenges, Animal Models and Techniques. *Pharmaceutica Analytica Acta* **08**, (2017).

4. Harloff-Helleberg, S., Nielsen, L. H. & Nielsen, H. M. Animal models for evaluation of oral delivery of biopharmaceuticals. *Journal of Controlled Release* **268**, 57–71 (2017).

5. Hatton, G. B., Yadav, V., Basit, A. W. & Merchant, H. A. Animal Farm: Considerations in Animal Gastrointestinal Physiology and Relevance to Drug Delivery in Humans. *Journal of Pharmaceutical Sciences* **104**, 2747–2776 (2015).

6. Kararli, T. T. & Searle, G. D. Comparison of the gastrointestinal anatomy, physiology, and biochemistry of humans and commonly used laboratory animals. *Biopharmaceutics & Drug Disposition* **16**, 351–380 (1995).

7. Parrish, J., Lim, K., Zhang, B., Radisic, M. & Woodfield, T. B. F. New Frontiers for Biofabrication and Bioreactor Design in Microphysiological System Development. *Trends in Biotechnology* vol. 37 1327–1343 Preprint at (2019).

8. Wang, Y. I., Carmona, C., Hickman, J. J. & Shuler, M. L. Multiorgan Microphysiological Systems for Drug Development: Strategies, Advances, and Challenges. *Advanced Healthcare Materials* vol. 7 Preprint at (2018).

9. Ingber, D. E. Human organs-on-chips for disease modelling, drug development and personalized medicine. *Nature Reviews Genetics* Preprint at (2022).

10. Hasenberg, T. *et al.* Emulating human microcapillaries in a multi-organ-chip platform. *Journal of Biotechnology* **216**, 1–10 (2015).

11. Maschmeyer, I. *et al.* A four-organ-chip for interconnected long-term co-culture of human intestine, liver, skin and kidney equivalents. *Lab on a Chip* **15**, 2688–2699 (2015).

12. Sergachev, I. *et al.* Fluorescent optical fiber sensors for cell viability monitoring. *Analyst* **138**, 4066–4069 (2013).

13. Tan, H. Y. *et al.* A multi-chamber microfluidic intestinal barrier model using Caco-2 cells for drug transport studies. *PLoS ONE* **13**, (2018).

14. Kim, H. J. & Ingber, D. E. Gut-on-a-Chip microenvironment induces human intestinal cells to undergo villus differentiation. *Integrative Biology (United Kingdom)* **5**, 1130–1140 (2013).

15. Nikolaev, M. *et al.* Homeostatic mini-intestines through scaffold-guided organoid morphogenesis. *Nature* **585**, 574–578 (2020).

16. Itabashi, Y. *et al.* A new method for manufacturing cardiac cell sheets using fibrin-coated dishes and its electrophysiological studies by optical mapping. *Artificial Organs* **29**, 95–103 (2005).

17. de Graaf, M. N. S. *et al.* Scalable microphysiological system to model three-dimensional blood vessels. *APL Bioengineering* **3**, (2019).

18. Chan, C. Y. *et al.* Accelerating drug discovery via organs-on-chips. *Lab on a Chip* **13**, 4697–4710 (2013).

19. Goral, V. N., Zhou, C., Lai, F. & Yuen, P. K. A continuous perfusion microplate for cell culture. *Lab on a Chip* **13**, 1039–1043 (2013).

20. Lee, P. J., Ghorashian, N., Gaige, T. A. & Hung, P. J. Microfluidic System for Automated Cell-Based Assays. *Journal of Laboratory Automation* **12**, 363–367 (2007).

21. Kim, J. Y. *et al.* 3D spherical microtissues and microfluidic technology for multi-tissue experiments and analysis. *Journal of Biotechnology* **205**, 24–35 (2015).

22. Zhang, W. *et al.* Ex vivo maintenance of primary human multiple myeloma cells through the optimization of the osteoblastic niche. *PLoS ONE* **10**, (2015).

23. Correia Carreira, S., Taghavi, M., Pavez Loriè, E. & Rossiter, J. FleXert: A Soft, Actuatable Multiwell Plate Insert for Cell Culture under Stretch. *ACS Biomaterials Science and Engineering* **7**, 2225–2245 (2021).

24. Kim, H. J., Huh, D., Hamilton, G. & Ingber, D. E. Human gut-on-a-chip inhabited by microbial flora that experiences intestinal peristalsis-like motions and flow. *Lab on a Chip* **12**, 2165–2174 (2012).

25. Kim, J. Y., Fluri, D. A., Kelm, J. M., Hierlemann, A. & Frey, O. 96-Well Format-Based Microfluidic Platform for Parallel Interconnection of Multiple Multicellular Spheroids. *Journal of Laboratory Automation* **20**, 274–282 (2015).

26. Phan, D. T. T. *et al.* A vascularized and perfused organ-on-a-chip platform for large-scale drug screening applications. *Lab on a Chip* **17**, 511–520 (2017).

27. Trietsch, S. J., Israëls, G. D., Joore, J., Hankemeier, T. & Vulto, P. Microfluidic titer plate for stratified 3D cell culture. *Lab on a Chip* **13**, 3548–3554 (2013).

28. Sobrino, A. *et al.* 3D microtumors in vitro supported by perfused vascular networks. *Scientific Reports 2016 6:1* **6**, 1–11 (2016).

29. Lai, B. F. L. *et al.* InVADE: Integrated Vasculature for Assessing Dynamic Events. *Advanced Functional Materials* **27**, 1703524 (2017).

30. Wang, Y. I. & Shuler, M. L. UniChip enables long-term recirculating unidirectional perfusion with gravity-driven flow for microphysiological systems. *Lab on a Chip* **18**, 2563–2574 (2018).

31. Dreyer, L., Smith, C., Deane, S. M., Dicks, L. M. T. & van Staden, A. D. Migration of Bacteriocins Across Gastrointestinal Epithelial and Vascular Endothelial Cells, as Determined Using In Vitro Simulations. *Scientific Reports* **9**, (2019).

32. Bian, Y. *et al.* Protective Effect of Kaempferol on LPS-Induced Inflammation and Barrier Dysfunction in a Coculture Model of Intestinal Epithelial Cells and Intestinal Microvascular Endothelial Cells. *Journal of Agricultural and Food Chemistry* **68**, 160–167 (2020).

33. Boyden, B. S. The chemotactic effect of mixtures of antibody and antigen on polymorphonuclear leucocytes. *J Exp Med.* **115**, 453–466 (1962).

34. Wang, Y. I., Carmona, C., Hickman, J. J. & Shuler, M. L. Multiorgan Microphysiological Systems for Drug Development: Strategies, Advances, and Challenges. *Advanced Healthcare Materials* vol. 7 Preprint at (2018).

35. Leth Jepsen, M. *et al.* 3D Printed Stackable Titer Plate Inserts Supporting Three Interconnected Tissue Models for Drug Transport Studies. *Advanced Biosystems* **4**, (2020).

36. Picollet-D'hahan, N., Zuchowska, A., Lemeunier, I. & le Gac, S. Multiorgan-on-a-Chip: A Systemic Approach To Model and Decipher Inter-Organ Communication. *Trends in Biotechnology* vol. 39 788–810 Preprint at (2021).

37. Nicolas, J. *et al.* 3D Extracellular Matrix Mimics: Fundamental Concepts and Role of Materials Chemistry to Influence Stem Cell Fate. *Biomacromolecules* **21**, 1968–1994 (2020).

38. Hwang, J., Sullivan, M. O. & Kiick, K. L. Targeted Drug Delivery via the Use of ECM-Mimetic Materials. *Frontiers in Bioengineering and Biotechnology* vol. 8 Preprint at (2020).

39. Coppeta, J. R. *et al.* A portable and reconfigurable multi-organ platform for drug development with onboard microfluidic flow control. *Lab on a Chip* **17**, 134–144 (2016).

40. Xiao, S. *et al.* A microfluidic culture model of the human reproductive tract and 28-day menstrual cycle. *Nature Communications 2017 8:1* **8**, 1–13 (2017).

41. Warboys, C. M. *et al.* Acute and chronic exposure to shear stress have opposite effects on endothelial permeability to macromolecules. *Am J Physiol Heart Circ Physiol* **298**, 1850–1856 (2010).

42. Warboys, C. M., Overby, D. R. & Weinberg, P. D. Dendritic cells lower the permeability of endothelial monolayers. in *Cellular and Molecular Bioengineering* vol. 5 184–193 (2012).

43. Driessen, R. *et al.* Computational characterization of the dish-in-a-dish, a high yield culture platform for endothelial shear stress studies on the orbital shaker. *Micromachines (Basel)* **11**, (2020).

44. Dardik, A. *et al.* Differential effects of orbital and laminar shear stress on endothelial cells. *Journal of Vascular Surgery* **41**, 869–880 (2005).

45. Ghim, M., Pang, K. T., Arshad, M., Wang, X. & Weinberg, P. D. A novel method for segmenting growth of cells in sheared endothelial culture reveals the secretion of an anti-inflammatory mediator. *Journal of Biological Engineering* **12**, (2018).

46. Warboys, C. M., Ghim, M. & Weinberg, P. D. Understanding mechanobiology in cultured endothelium: A review of the orbital shaker method. *Atherosclerosis* vol. 285 170–177 Preprint at (2019).

47. Filipovic, N., Ghimire, K., Saveljic, I., Milosevic, Z. & Ruegg, C. Computational modeling of shear forces and experimental validation of endothelial cell responses in an orbital well shaker system. *Computer Methods in Biomechanics and Biomedical Engineering* **19**, 581–590 (2016).

48. Ghim, M. *et al.* Visualization of three pathways for macromolecule transport across cultured endothelium and

their modification by flow. *Am J Physiol Heart Circ Physiol* **313**, 959–973 (2017).

49. Chong, H. B., Youn, J., Shin, W., Kim, H. J. & Kim, D. S. Multiplex recreation of human intestinal morphogenesis on a multi-well insert platform by basolateral convective flow. *Lab on a Chip* **21**, 3316–3327 (2021).

50. Dogan, A. A. & Dufva, M. Customized 3D-printed stackable cell culture inserts tailored with bioactive membranes. *Scientific Reports 2022 12:1* **12**, 1–12 (2022).

51. Formlabs. *BIOMED CLEAR MATERIAL*. vol. 18 https://formlabs.com/store/materials/biomed-clear-resin/ (2020).

52. Thomas, J. M. D., Chakraborty, A., Berson, R. E., Shakeri, M. & Sharp, M. K. Validation of a CFD model of an orbiting culture dish with PIV and analytical solutions. *AIChE Journal* **63**, 4233–4242 (2017).

53. GitHub - neuroeddu/OrgM: A Fiji macro for measuring organoid area and size. https://github.com/neuroeddu/OrgM.

54. Schindelin, J. *et al.* Fiji: An open-source platform for biological-image analysis. *Nature Methods* vol. 9 676–682 Preprint at (2012).

55. Hickman, J. Transepithelial/endothelial Electrical Resistance (TEER) theory and applications for microfluidic body-on-a-chip devices. *Journal of Rare Diseases Research & Treatment* **1**, 46–52 (2016).

56. Arlk, Y. B. *et al.* Barriers-on-chips: Measurement of barrier function of tissues in organs-on-chips. *Biomicrofluidics* **12**, 42218 (2018).

57. Nicolas, A. *et al.* High throughput transepithelial electrical resistance (TEER) measurements on perfused membrane-free epithelia. *Lab on a Chip* **21**, 1676–1685 (2021).

58. Pereiro, I., Fomitcheva-Khartchenko, A. & Kaigala, G. v. Shake It or Shrink It: Mass Transport and Kinetics in Surface Bioassays Using Agitation and Microfluidics. *Analytical Chemistry* **92**, 10187–10195 (2020).

59. Arshad, M., Ghim, M., Mohamied, Y., Sherwin, S. J. & Weinberg, P. D. Endothelial cells do not align with the mean wall shear stress vector: Endothelial cells do not align with the mean wall shear stress vector. *Journal of the Royal Society Interface* **18**, (2021).

60. Roux, E., Bougaran, P., Dufourcq, P. & Couffinhal, T. Fluid Shear Stress Sensing by the Endothelial Layer. *Frontiers in Physiology* vol. 11 Preprint at (2020).

61. Davies, P. F. Flow-Mediated Endothelial Mechanotransduction. *Physiol Rev* **75**, 519 (1995).

62. Papaioannou, T. G. & Stefanadisz, C. Vascular Wall Shear Stress- Basic Principles and Methods. *Hellenic J Cardiol .* **46**, 9–15 (2005).

63. Ballermann, B. J., Dardik, A., Eng, E. & Liu, A. Shear stress and the endothelium. *Kidney International, Supplement* **54**, (1998).

64. Marzorati, M. *et al.* The HMI™ module: A new tool to study the Host-Microbiota Interaction in the human gastrointestinal tract in vitro. *BMC Microbiology* **14**, 1–14 (2014).

65. Guo, P., Weinstein, A. M. & Weinbaum, A. S. A hydrodynamic mechanosensory hypothesis for brush border microvilli. *Am J Physiol Renal Physiol* **279**, 698–712 (2000).

66. Ghim, M. *et al.* Endothelial cells exposed to atheroprotective flow secrete follistatin-like 1 protein which reduces transcytosis and inflammation. *Atherosclerosis* **333**, 56–66 (2021).

67. Holliday, C. J., Ankeny, R. F., Jo, H. & Nerem, R. M. Discovery of shear-and side-specific mRNAs and miRNAs in human aortic valvular endothelial cells. *American Journal of Physiology - Heart and Circulatory Physiology* **301**, 856–867 (2011).

68. Dessalles, C. A., Leclech, C., Castagnino, A. & Barakat, A. I. Integration of substrate- and flow-derived stresses in endothelial cell mechanobiology. *Communications Biology* vol. 4 Preprint at (2021).

69. Yu, H., Kang, D., Whang, M., Kim, T. & Kim, J. A Microfluidic Model Artery for Studying the Mechanobiology of Endothelial Cells. *Advanced Healthcare Materials* **10**, 2100508 (2021).

70. Wong, L. *et al.* Substrate stiffness directs diverging vascular fates. *Acta Biomaterialia* **96**, 321–329 (2019).

71. Johnson, L. A. *et al.* Matrix stiffness corresponding to strictured bowel induces a fibrogenic response in human colonic fibroblasts. *Inflammatory Bowel Diseases* **19**, 891–903 (2013).

72. Handorf, A. M., Zhou, Y., Halanski, M. A. & Li, W. J. Tissue stiffness dictates development, homeostasis, and disease progression. *Organogenesis* vol. 11 1–15 Preprint at (2015).

73. Costa, J. & Ahluwalia, A. Advances and Current Challenges in Intestinal in vitro Model Engineering: A Digest. *Frontiers*

in Bioengineering and Biotechnology vol. 7 Preprint at https://doi.org/10.3389/fbioe.2019.00144 (2019).

74. Mondrinos, M. J., Yi, Y. S., Wu, N. K., Ding, X. & Huh, D. Native extracellular matrix-derived semipermeable, optically transparent, and inexpensive membrane inserts for microfluidic cell culture. *Lab on a Chip* **17**, 3146–3158 (2017).

75. Salek, M. M., Sattari, P. & Martinuzzi, R. J. Analysis of fluid flow and wall shear stress patterns inside partially filled agitated culture well plates. *Annals of Biomedical Engineering* **40**, 707–728 (2012).

76. Junaid, A. *et al.* Metabolic response of blood vessels to tnfα. *Elife* **9**, 1–28 (2020).

77. Zhang, H. *et al.* Role of TNF-α in vascular dysfunction. *Clinical Science* **116**, 219–230 (2009).

78. Xu, C., Wu, X., Hack, B. K., Bao, L. & Cunningham, P. N. TNF causes changes in glomerular endothelial permeability and morphology through a Rho and myosin light chain kinase-dependent mechanism. *Physiological Reports* **3**, (2015).

79. Mckenzie, J. A. G. & Ridley, A. J. Roles of Rho/ROCK and MLCK in TNF-α-induced changes in endothelial morphology and permeability. *Journal of Cellular Physiology* **213**, 221–228 (2007).

Supplementary Information

High throughput shear stress platform to couple intestine and blood vessel models

Asli Aybike Dogan[a], Martin Dufva*[a]

a Department of Health Technology, Technical University of Denmark, 2800 Kgs. Lyngby, Denmark.

* Corresponding author. (Email: dufva@dtu.dk)

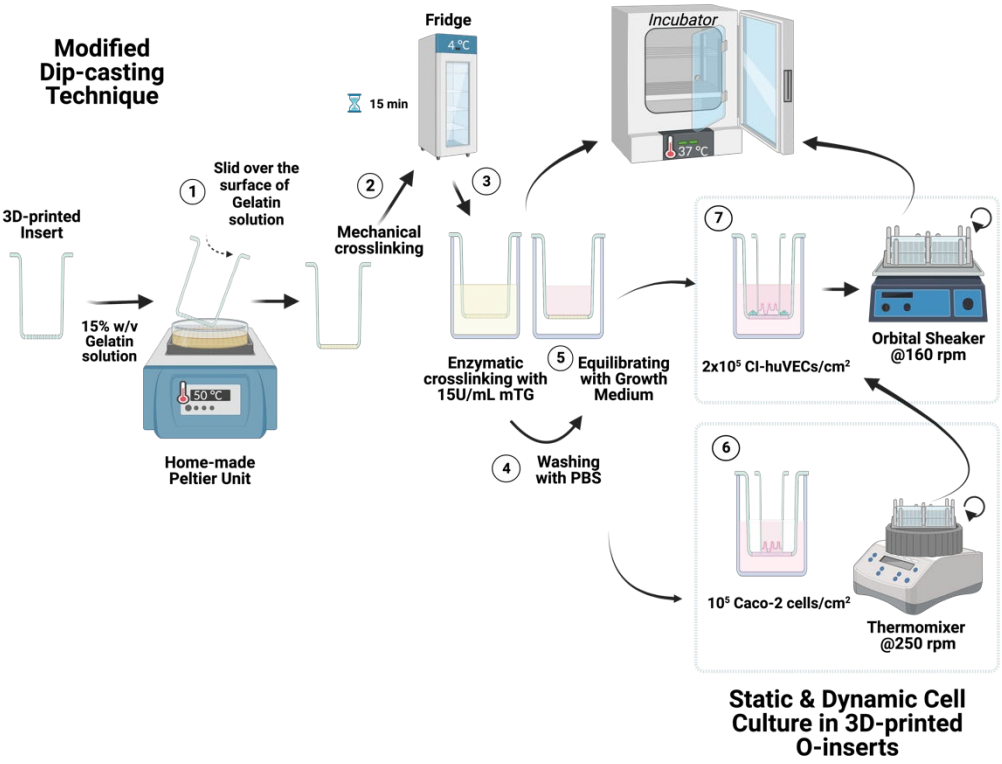

Figure S1. Illustrative outline of **1-2)** the dip-casting method for Gelatin hydrogel membrane assembling to the 3D-printed inserts platforms and summary of orbital shaker experimental procedure. Additional sliding step was added to the protocol for O-inserts with relatively big apertures. Modified from the illustration presented (**DOI:** https://doi.org/10.1038/s41598-022-07739-7). Created with BioRender.com.

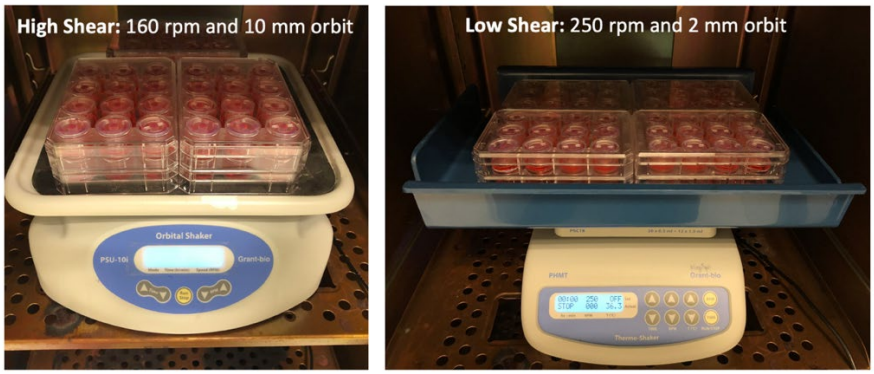

Figure S2. O-inserts on Orbital shaker (**left**) for high shear stress (HSS) and thermomixer (**right**) for low shear stress (LSS) induction on intestinal and epithelial cells.

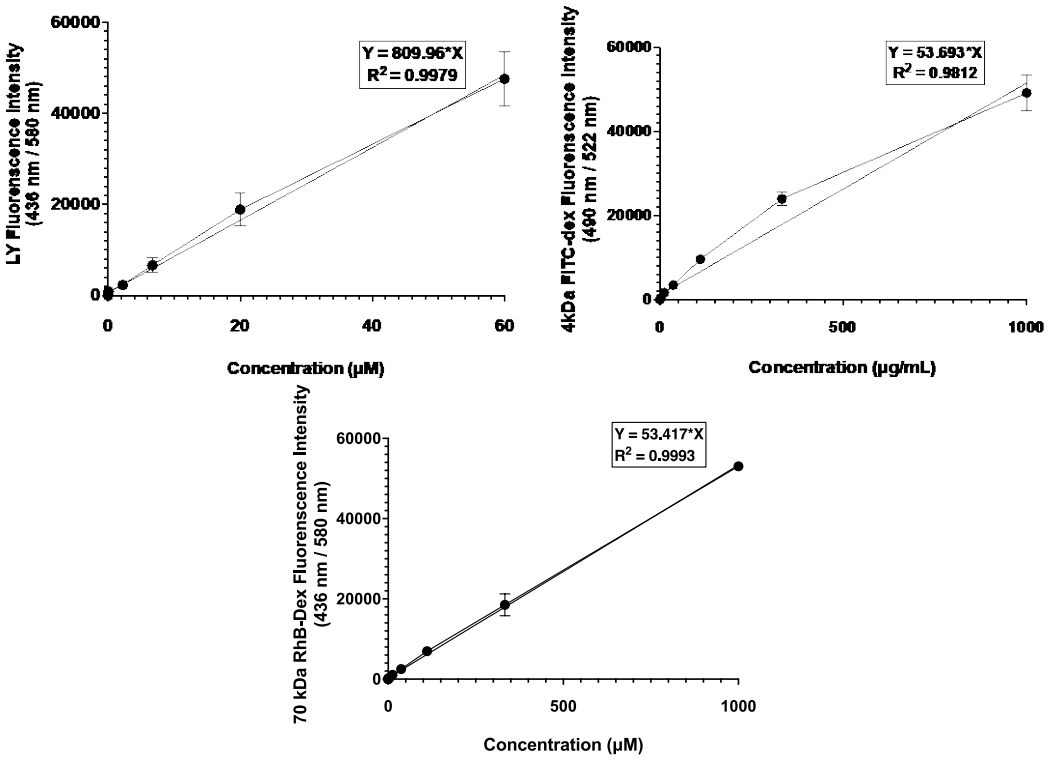

Figure S3. Standard curve of Lucifer Yellow (**leftmost panel**), 4kDa FITC-Dextran (**rightmost panel**), and 70kDa Rhodamine B-Dextran (**bottom panel**) for Gelatin membrane thickness measurement.

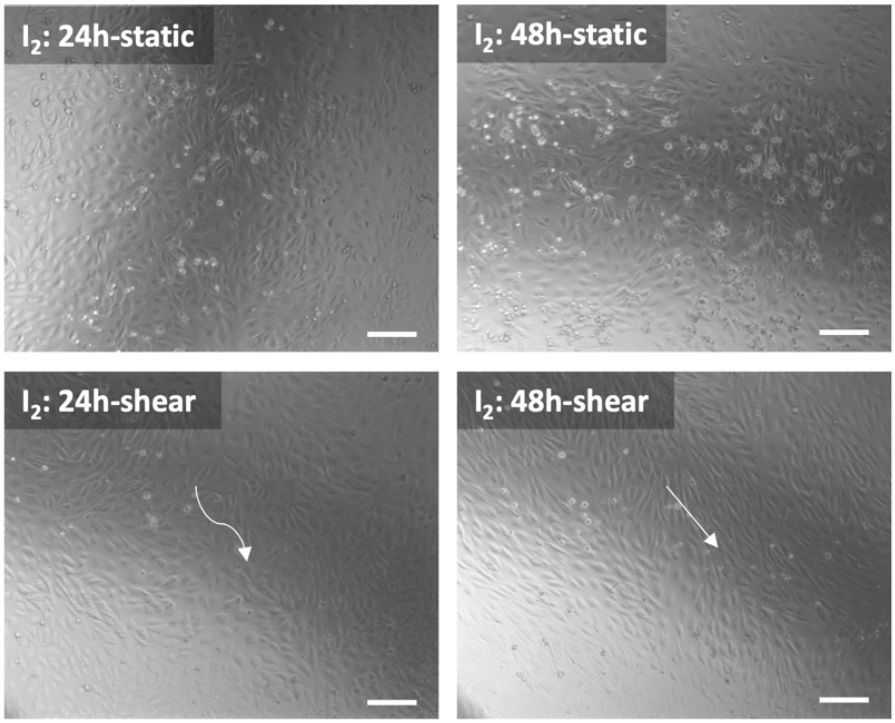

Figure S4. The effect of 20.7 dyn/cm^2 shear induction time on alignment of CI-huVECs cultured in periphery inserts (I_2). Scale bar: 200 µm, , the magnification: 10x. Upper panels: Static condition after 24h and 48h. Bottom panel: Dynamic shear conditions.

TABLES

Table S1. TEER values of CI-huVECs after TNF-α exposure for 3-12h ($\Omega \times cm^2$; n≥12)

	TNF-α (-) *(Mean±SD)*	**TNF-α (+) 3h** *(Mean±SD)*	**TNF-α (+) 9h** *(Mean±SD)*	**TNF-α (+) 12h** *(Mean±SD)*
Static	123±18	99±18	68±8	49±9
Dynamic	145±40	118±29	95±14	65±5

Table S2. Total Gap Area of CI-huVECs after 12h TNF-α exposure (μm^2; images: n=3; gaps: n≥121)

	Static *(Mean±SD)*	**Dynamic** *(Mean±SD)*
TNF-a (-)	28158.53±5200.47	13437.36±2803.6
TNF-a (+)	254043.87±11086.25	25644.52±4629.22

Table S3. Nuclei Counting Analysis of CI-huVECs after 12h TNF-α exposure (CI-huVECs/mm^2; n≥5)

	Dynamic *(Mean±SD)*	**Static** *(Mean±SD)*
TNF-α (-)	1303±74	839±56
TNF-α (+)	413±78	179±25

Table S4. Vector Orientation Angle (θ°) for alignment of endothelial cells (CI-huVECs) after 20.7 dyn/cm^2 shear induction (Images: n=3; Vectors: n≥1253)

Dynamic (30°) (Mean±SEM)	**Dynamic (0°)** (Mean±SEM)	**Static** (Mean±SEM)
34.88 ± 0.30	8.45 ± 0.28	-8.92 ± 0.56

Table S5. Permeability Coefficients (Pc; nm/s) of CI-huVECs' after 12h TNF-a exposure under static and dynamic conditions for 0.44 kDa Lucifer Yellow (LY) transport (n≥3)

LY	**TNF-α (+)** *(Mean±SD)*	**TNF-α (-)** *(Mean±SD)*	**Empty Gel** *(Mean±SD)*
Static	1414.36±66.03	1350.38±74.16	1547.63±63.22
Dynamic	1383.79±71.03	1043.69±53.36	-

Table S6. Permeability Coefficients (Pc; nm/s) of CI-huVECs after 12h TNF-a exposure under static and dynamic conditions for 4 kDa FITC-Dextran (4kDa FITC-Dex) transport (n≥3)

4kDa FITC-Dex	**TNF-α (+)**	**TNF-α (-)**	**Empty Gel**

	(Mean±SD)	*(Mean±SD)*	*(Mean±SD)*
Static	539.40±104.06	362.88±100.30	675.27±204.97
Dynamic	713.84±303.89	267.01±43.21	-

Table S7. Permeability Coefficients (Pc; nm/s) of CI-huVECs' after 12h TNF-a exposure under static and dynamic conditions for 70 kDa Rhodamine B-Dextran (70kDa RhB-Dex) transport (n≥3)

70kDa RhB-Dex	**TNF-α (+)** *(Mean±SD)*	**TNF-α (-)** *(Mean±SD)*	**Empty Gel** *(Mean±SD)*
Static	41.31±5.23	28.36±7.50	44.40±15.96
Dynamic	37.92±13.45	20.75±4.52	-

Table S8. TEER values of Caco-2 cells cultured in mono- and co-culture with CI-huVEC (**Ω**×cm^2; n≥6)

	Static *(Mean±SD)*	**Dynamic** *(Mean±SD)*
Mono-	341±171	1353±284
Co-	393±121	1291±544

Table S9. TEER values of CI-huVECs cultured in mono- and co-culture with Caco-2 cells (**Ω**×cm^2; n≥6)

	Static *(Mean±SD)*	**Dynamic** *(Mean±SD)*
Mono-	109±3	163±34
Co-	112±19	120±10

Table S10. Absolute concentrations of LY in each compartment of co-culture O-insert (LY transport direction: Caco-2 → Well → CI-huVECs) under static and dynamic conditions (n≥3; nmol)

Static *(Mean±SD)*			**Dynamic** *(Mean±SD)*			**Empty Gel** *(Mean±SD)*		
Caco-2	**Cl-huVECs**	**Well**	**Caco-2**	**Cl-huVECs**	**Well**	**Caco-2**	**Cl-huVECs**	**Well**
3.592 ±0.220	0.013 ±0.002	0.073 ±0.013	3.570 ±0.078	0.019 ±0.011	0.096 ±0.051	3.433 ±0.133	0.337 ±0.094	1.445 ±0.341

Table S11. Permeability Coefficients (Pc; nm/s) of co-cultured CI-huVECs and Caco-2 cells under static and dynamic conditions for LY transport (n≥3)

Static *(Mean±SD)*		**Dynamic** *(Mean±SD)*		**Empty Gel** *(Mean±SD)*	
Caco-2	**Cl-huVECs**	**Caco-2**	**Cl-huVECs**	**Caco-2**	**Cl-huVECs**
5.67±0.90	203.35±23.36	7.46±3.73	211.62±14.04	116.50±25.13	1547.63±63.22

Table S12. Absolute concentrations of 4 kDa FITC-Dex in each compartment of co-culture O-insert (4 kDa FITC-Dex transport direction: Caco-2 → Well → CI-huVECs) under static and dynamic conditions (n≥3; ng/mL)

Static *(Mean±SD)*			**Dynamic** *(Mean±SD)*			**Empty Gel** *(Mean±SD)*		
Caco-2	**Cl-huVECs**	**Well**	**Caco-2**	**Cl-huVECs**	**Well**	**Caco-2**	**Cl-huVECs**	**Well**
66.801 ±2.559	0.011 ±0.005	0.262 ±0.076	59.306 ±3.288	0.025 ±0.004	0.095 ±0.025	59.830 ±3.662	0.249 ±0.141	1.846 ±0.606

Table S13. Permeability Coefficients (Pc; nm/s) of co-cultured CI-huVECs and Caco-2 cells under static and dynamic conditions for 4 kDa FITC-Dex transport (n≥3)

Static *(Mean±SD)*		**Dynamic** *(Mean±SD)*		**Empty Gel** *(Mean±SD)*	
Caco-2	**Cl-huVECs**	**Caco-2**	**Cl-huVECs**	**Caco-2**	**Cl-huVECs**
1.09±0.30	214.21±64.50	0.46±0.17	297.11±53.08	8.62±2.89	414.05±63.31

Chapter 8

POSTER PRESENTATIONS

Evaluation of Biocompatibility on 3D-printed Inserts using Mouse Intestinal Organoids

Asli Aybike Dogan, Martin Dufva

EUROoCS 2020 (08 - 09 July 2020)

Evaluation of Biocompatibility on 3D-printed Inserts using Mouse Intestinal Organoids

Asli Aybike DOGAN[1*], Martin DUFVA[1]

[1] Department of Health Technology, Technical University of Denmark, 2800 Kgs. Lyngby, Denmark

***E-mail:** aado@dtu.dk

Goal

Testing customized 3D-printed inserts as an alternative to commercialized air-liquid interphase (ALI) culture systems.

Materials & Method

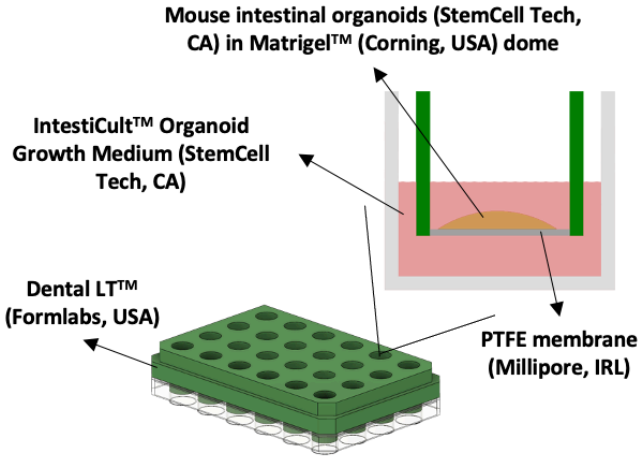

Figure 1. ALI culture of mouse intestinal organoids on 3D-printed 24-well insert plate (*Material:* Dental LT resin; *Printer:* Form 2, Formlabs, USA).

Results

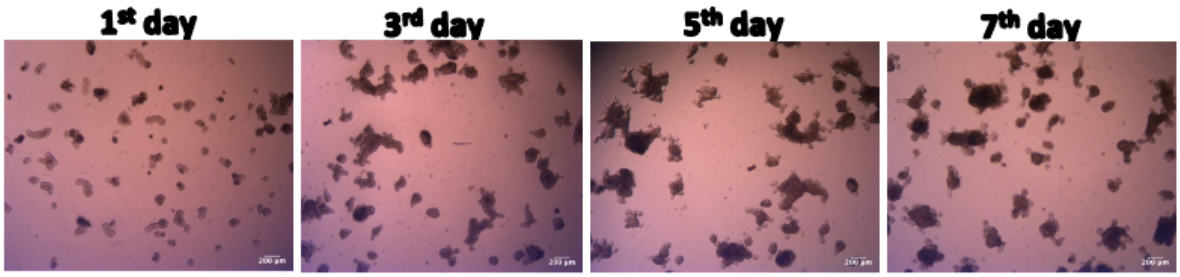

Figure 2. Light microscope images of mouse intestinal organoids on 1st, 3rd, 5th and 7th days (*Scale bar:* 200 μm; 4X magnification; Zeiss Primovert).

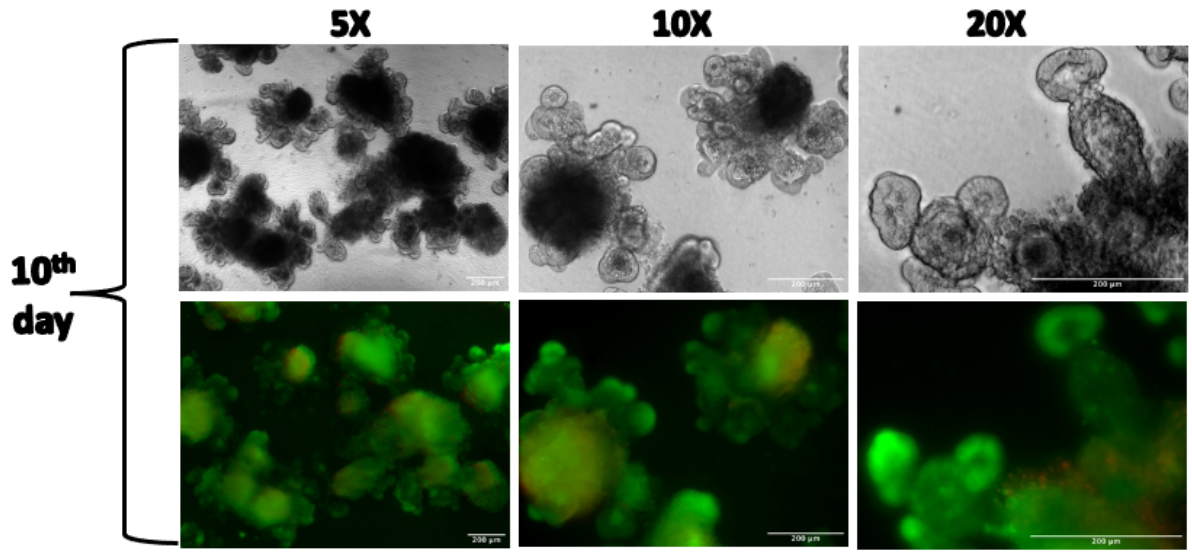

Figure 3. Bright field and Live&Dead staining images of organoids on 10th day (*Green:* Live, *Red:* Dead; *Scale bar: 200 µm* , Zeiss Axio Observer).

Conclusion

- ✓ No cytotoxic effect on mouse intestinal organoids
- ✓ Easy & broad application
  - ALI culture
  - 3D cell culture
  - High-throughput screening (HTS)
- ✓ Reusable insert
- ✓ Low-cost fabricated insert
- ✓ Customized design

Zoom Link:
https://dtudk.zoom.us/j/3076664324?pwd=WERkbzB3QkV4WC8xRHhpR05XU0ZTZz09

https://euroocs.eu/ (The European Organ-on-Chip Society (EUROoCS), 8-9 July 2020)

EUROoCS
CONFERENCE 2020

This work is supported by the MSCA-ITN OrganoVIR project.

3D-printed Bioengineered Platform for Co-culturing Caco-2/Immune Cells to Study SARS-CoV-2 Infection

Asli Aybike Dogan & Emilia Barreto Durán, Krzysztof Pyrć & Martin Dufva

ScSB 2022 (13 - 15 June 2022)

3D-printed Bioengineered Platform for Co-culturing Caco-2/Immune Cells

Asli Aybike Dogan[1], Emilia Barreto-Durán[2], Krzysztof Pyrc[2], Martin Dufva[1]
[1]Department of Health Technology, Technical University of Denmark, Kgs. Lyngby, Denmark
[2]Małopolska Center of Biotechnology, Jagiellonian University, Kraków, Poland

1. Abstract

Transwell inserts are a popular 3D cell culture platform due to their commercial availability, ease to use, and versatility. However, they are limited in terms of the number of insert layers, the height between the layers and the size and composition of the bioactive membrane. Therefore, there is a demand for customized inserts[1,2]. This project introduces a 3D-printed stackable platform (**Section 2**) or co-culturing epithelial and immune system cells in close-contact (**Section 3**) to mimic intestinal barrier tissue microenvironment[3]. Furthermore, we characterized the physical properties (**Section 4**) of the microenvironment. Finally, we tested our 3D-printed bioengineered co-culture platform to investigate the SARS-CoV-2 (COVID-19) viral infection (**Section 5**) that has first been characterized by an infection of the upper airways and the lung, but recent evidence suggests a complex disease including gastrointestinal symptoms[4].

2. Design & Fabrication Overview of 3D-printed Stackable Co-culture Inserts

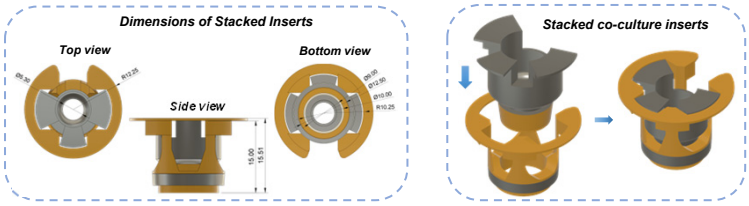

CAD modelling software: *Fusion 360 (Autodesk, USA);* ***Slicing software:*** *PreForm (Formlabs, USA);* ***Printer:*** *Form 3B (Formlabs, USA);* ***Printing resin:*** *BioMed Clear (Formlabs, USA);* ***Post-processing:*** *Isopropanol Washing Tank & Form Cure UV Machine (Formlabs, USA);* ***Scales*** *in mm.*

Polyester (PET) membrane assembling to inserts

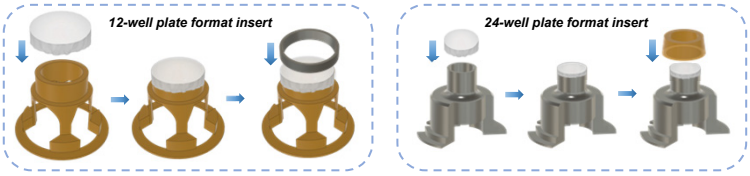

PET membrane: *8 µm, ipCELLCULTURE™ Track-Etched (It4ip, BE)*

3. Close-contact Stacking Technique

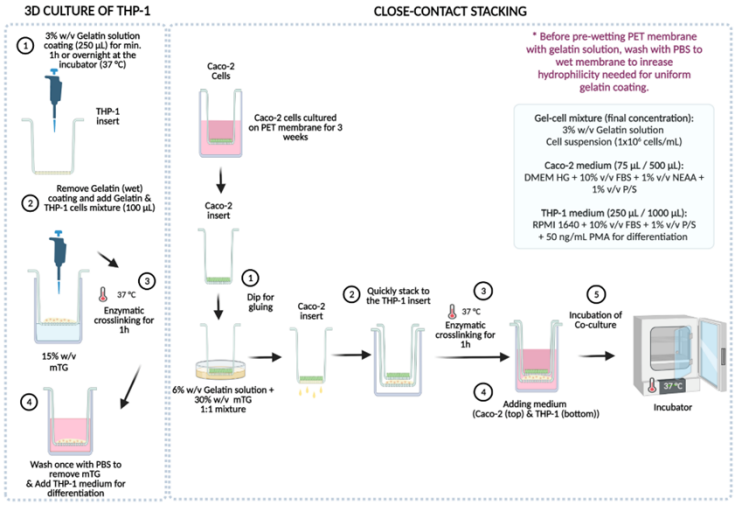

4. Physical Characterization of 3D Hydrogel Matrix

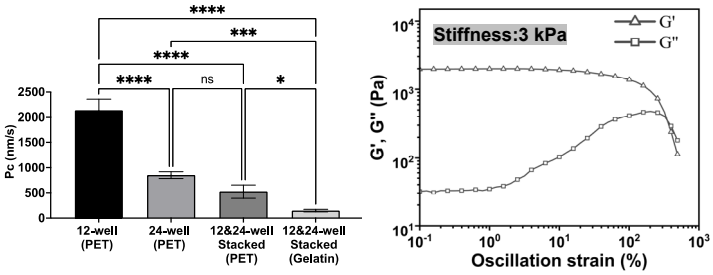

Figure 1. Left: Comparison of 60 µM Fluorescein sodium salt dye transport through each PET membrane assembled single and stacked 3D-printed inserts (n = 3). Insert well aperture surface area for transport is 0.22 cm² (24-well) and 0.785 cm² (12-well). Data were analyzed using one-way ANOVA with post hoc Tukey tests. Error bars indicate Mean ± SD. Statistical significance: ns = P > 0.05, *P < 0.1, ***P < 0.01 ****P < 0.0001. **Right:** Analysis of storage (G') and loss modulus (G'') of each membrane under applied oscillatory compression by conducting dynamic strain sweeps between 0.1 and 500 %. Young's modulus (E) was calculated as ~3 kPa.

5. 3D Interaction of Macrophages with Caco-2 Cells

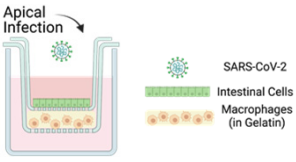

The SARS-CoV-2 virus infection was investigated in mono- and co-culture of intestinal cells in the presence or absence of macrophages after 48h post-infection.

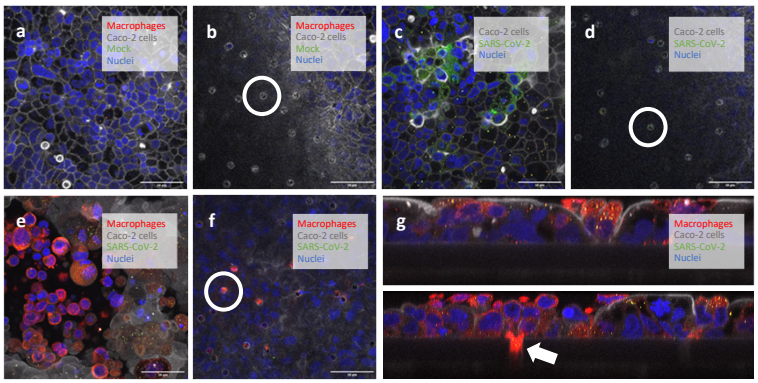

Figure 2. Immunofluorescence confocal micrographs of 3D Stacked Co-culture Platform. Micrographs showing the apical (**a, c, e**) and basolateral (**b, d, f**) sides of 3D co-cultures of the intestinal epithelium cultured for about 3 weeks on porous PET membrane and activated macrophages after SARS-CoV-2 infection. Representative immunofluorescence confocal micrographs (**g-top and bottom panels**) visualizing a cross-section of co-culture. **White** indicates phalloidin-stained intestinal apical border, **red** indicates CD68-stained macrophages, **green** indicates SARS-CoV-2 nucleocapsid proteins, and **blue** indicates DAPI-stained nuclei (scale bars, 50 µm). **White circles** indicate PET membrane pores, and the **white arrow** indicates a migrated macrophage through the membrane pore to the infected intestinal tissue.

6. Conclusion & Outlook

- BioMed Clear printing resin used to make the customized 3D-printed platform is biocompatible for co-cultured intestinal epithelial cells and macrophages.
- The 3D soft hydrogel matrix (**Figure 1-Right**) supports migrations of macrophages (**Figure 2. e-g**) and their interactions with the intestinal barrier tissue like *in vivo*; therefore, we concluded that permeability delay due to the distance between stacked membranes and gel matrix is negligible (**Figure 1-Left**).
- The close-contact stacking inserts are scalable, and the technique has the potential to be implemented in other *in vitro* barriers tissue models such as lung, skin and blood-brain-barrier.
- Future studies will investigate the technique in more complex cellular models such as stem cells and organoids.

The illustrations in Sections 3-5 were created with BioRender.com. Statistical analysis and plots in Section 4 were performed on GraphPad and Origin Pro software.

References: *(1) Dogan & Dufva, (2022), Scientific Reports, 3694; (2) Jepsen et al. (2020), Advanced Biosystems, 1900289; (3) Bain and Schridde (2018), Frontiers in Immunology, 9:2733; (4) Lehmann, et al. (2021), Society for Mucosal Immunology, 14:1381.*

This project has received funding from the European Union's Horizon 2020 research and innovation program under the Marie Skłodowska-Curie grant agreement No. 812673 and was conducted within the OrganoVIR network.

Contact: *aado@dtu.dk; emilia.duran@uj.edu.pl; k.a.pyrc@uj.edu.pl; dufva@dtu.dk*

Perfusion Device for 3D Gastrointestinal Spheroids

Asli Aybike Dogan, Daina Santapau Arbós, Alexander Jönsson, Hakan Gurbuz, Martin Dufva

TERMIS 2022 EU Chapter (28 June - 01 July 2022)

PERFUSION DEVICE FOR 3D GASTROINTESTINAL SPHEROIDS

Asli Aybike Dogan[1], Daina Santapau Arbós[1], Alexander Jönsson[1], Hakan Gurbuz[1], Martin Dufva[1]
[1] Department of Health Technology, Technical University of Denmark, Kgs. Lyngby, Denmark

1. Introduction

Caco-2 cells are one of model cell lines are used to preclinical tests of drug permeability and absorption across the intestine. These cells are commonly used as 2D (two-dimensional) monolayers on Transwell inserts to mimic intestinal barrier function *in vitro*. However, they are lacking the function of 3D (three-dimensional) physiological relevant *in vivo* microenvironment *to* simulate cell-cell and cell-extracellular matrix interactions[1–5]. Therefore, the characteristics of these Caco-2 spheroids need to be well-understood. With this motivation, we designed a simplistic, 3D-printed device to culture geometrically controlled Caco-2 spheroids. Furthermore, we developed the device (**Section 2**) to enable the perfusion of medium to overcome the limitation in cell-construct size due to mass exchange. We optimized culture conditions to provide supportive microenvironment to intestinal spheroid formations (**Section 3-4**) and finally, we conduct a comparative study to evaluate static and dynamic conditions (**Section 5**) to validate the advantage of spheroid culture with perfusion.

2. Design & Fabrication Overview of 3D-printed Device

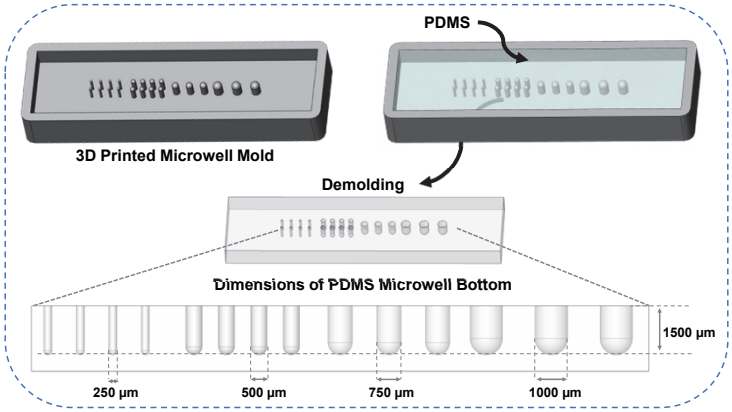

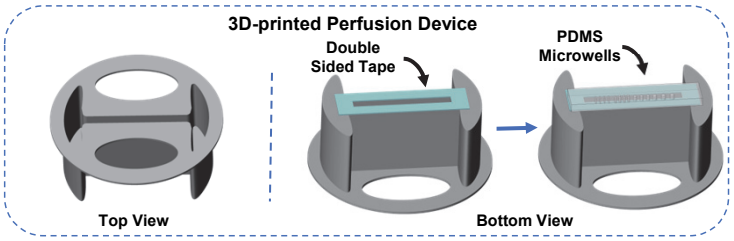

Printers: *Asiga Pico2 (Asiga, AUS) & Form 3B (Formlabs, USA);* ***Printing resin:*** *DentaForm (Asiga, AUS) & BioMed Clear (Formlabs, USA);* ***Post-processing:*** *Isopropanol Washing Tank & Form Cure UV Machine (Formlabs, USA).* ***Double Sided Tape:*** *ARcare® 90106NB (Adhesive Research, IRL)*

3. Materials & Method

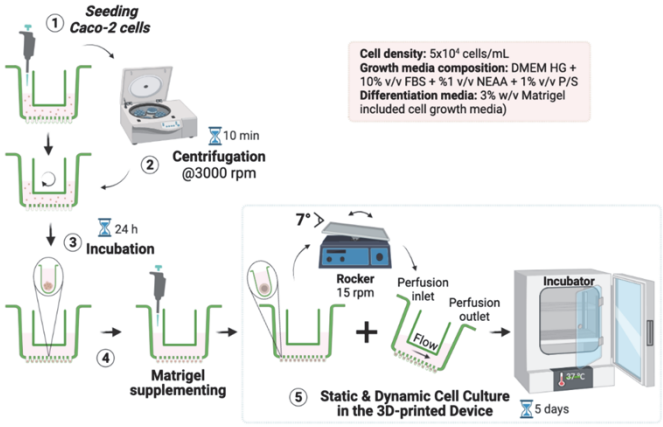

4. Spheroid Size Analysis

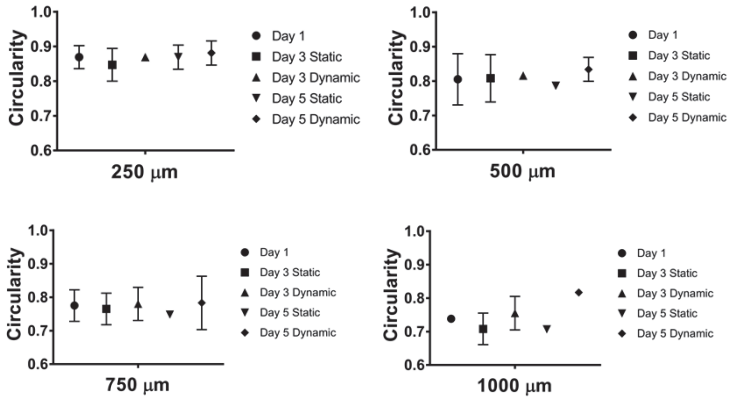

Figure 1. Comparison of circularity of spheroid formation in 1000 µm, 750 µm, 500 µm and 250 µm diameter sized hemisphere-type microwells under static and dynamic perfusion conditions. **=1.0** indicates regular spheroid shape; **<1.0** shows irregularity of spheroids. Data were analyzed using the macro; OrgM[6] on the ImageJ/Fiji7. Error bars indicate Mean ± SD.

5. Viability & Morphological Analysis of Spheroids

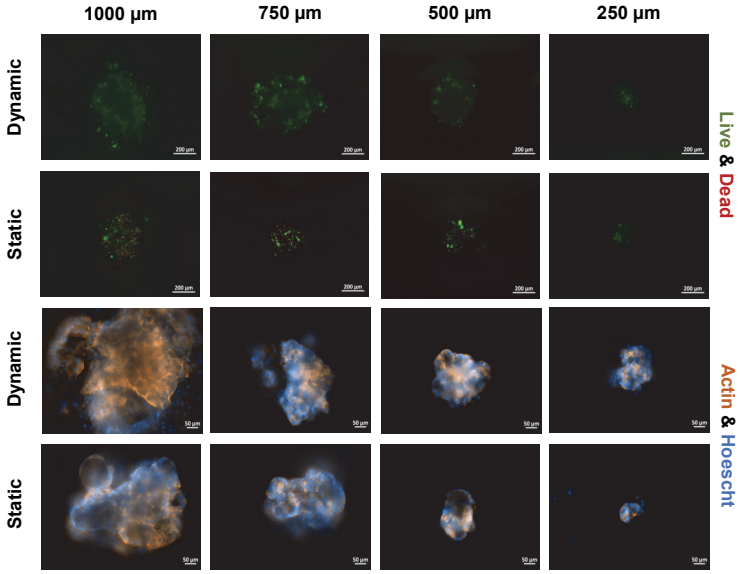

Figure 2. Representative fluorescence micrographs of intestinal spheroids in 1000 µm, 750 µm, 500 µm and 250 µm diameter sized hemisphere-type microwells under static and dynamic perfusion conditions. **Top panels:** Viability of spheroids by Live & Dead staining. ***Green:*** Calcein AM (live cells); ***Red:*** Ethidium Homodimer-1 (dead cells). **Bottom panels:** Cytoskeleton (**F-Actin; orange**) and nuclei (**Hoechst; blue**) staining. **Magnifications & Scale bars:** 10X, 200 µm (Live & Dead); 20X, 50 µm (Actin & Hoechst).

6. Conclusion & Outlook

- The 3D-printed dynamic device enables perfusion of the medium and the flow shear to overcome the limitation in cell-construct size due to mass exchange.
- The 3D-printed devices are scalable and have the potential to be customized for other 3D microtissue models such as organoids and assembloids.
- 3D in vitro intestinal model can serve as a valuable system to expedite drug screening as well as to study intestinal transporter function.

The illustrations in Sections 3-5 were created with BioRender.com. Statistical analysis and plots were performed on GraphPad software and image analysis was performed on Zeiss Zen Blue 3.4 Lite Digital Imaging Software (Carl Zeiss Microscopy GmbH, DE) and ImageJ/Fiji software.

References: ***(1)*** *Samy K (2019), PhD Thesis, University of California, Berkeley;* ***(2)*** *Miyakawa M, et al. (2020), International Journal of Molecular Sciences, 21:1–19;* ***(3)*** *Gheytanchi E, et al. (2021), Cancer Cell International. 21;* ***(4)*** *Elamin E, et al. (2012), PLoS ONE, 7;* ***(5)*** *Rainaldi G, et al. (2016), Journal of Pharmacy and Pharmacology, 4;* ***(6)*** *Cai & Thomas (2019), https://github.com/neuroeddu/OrgM;* ***(7)*** *Schindelin, et al. (2012), Nat. Methods 9, 676–682.*

This project is funded by the EU's Horizon 2020 research and innovation program under the Marie Skłodowska-Curie, OrganoVIR project (Grant AG.: 812673) and the Next Generation Organ-On-Chip Call, GUTVIBRATIONS (Grant AG.: DT-NMBP-23)

Contact: *aado@dtu.dk (Asli Aybike Dogan); hakgu@dtu.dk (Hakan Gurbuz); dufva@dtu.dk (Martin Dufva)*

3D-printed Shear Stress Platform for Endothelial Cell Mechanoinduction

Asli Aybike Dogan, Martin Dufva

TERMIS 2022 EU Chapter (28 June - 01 July 2022)

3D-PRINTED SHEAR PLATFORM FOR ENDOTHELIAL CELL MECHANOINDUCTION

Asli Aybike Dogan[1], Martin Dufva[1]
[1] Department of Health Technology, Technical University of Denmark, Kgs. Lyngby, Denmark

1. Introduction

Endothelial cells (EC) are subjected to mechanical stimuli and respond *via* mechanotransduction *in vivo*. Endothelial cells aligning along the laminar fluid flow direction is widely known to be a morphological feature of vascular function. In contrast, nonlaminar, disturbed shear stress correlates with pathological conditions such as atherosclerosis. Moreover, the effect of flow on EC pathophysiology has been primarily studied in two-dimensional (2D) *in vitro* cell culture platforms or microfluidic devices[1-3]. Previously, we introduced customized hanging inserts that could be an alternative to Transwell inserts[4]. Here, we present an implementation of the fluidic approach to customized 3D-printed inserts to provide additional physiological functionality by mimicking blood and interstitial flows. These alternative customized, 3D-printed insert platforms (**Section 2**) allow laminar flow regime (Re=101-629) and steady fluid shear from both apical and basolateral sides of human endothelial cell monolayer (huVECs) cultured on soft, porous, extracellular matrix-mimetic hydrogel membranes made by the dip-casting technique (**Section 3**). We presented our proof-of-concept experiment results on cellular morphology analyses with aligned huVECs after the 48h physiologically relevant shear stress induction (20.7 dyn/cm^2) (**Section 4**).

2. Design & Fabrication Overview of 3D-printed Shear Platform

Design Boundary Conditions

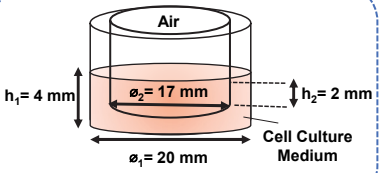

Fabrication Method

SLA Printer: *Form 3B (Formlabs, USA);* ***Printing resin:*** *BioMed Clear (Formlabs, USA);* ***Post-processing:*** *Isopropanol Washing Tank & Form Cure UV Machine (Formlabs, USA).*

12-well Plate Format Shear Inserts

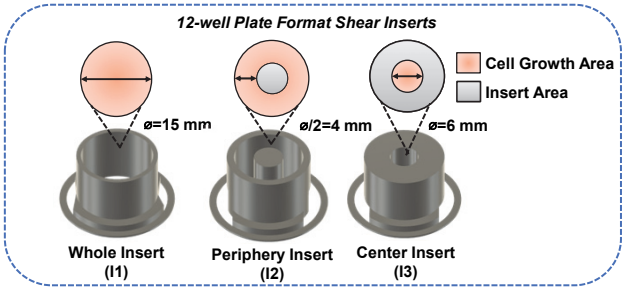

3. Materials & Method

Dip-casting Technique to form Gelatin membrane

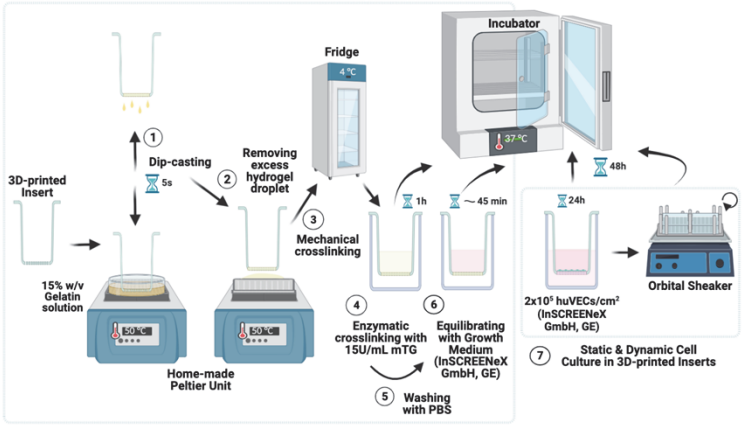

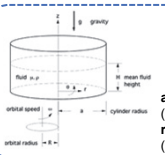

Shear stress (τ_{max}) Estimation[1]:

$$\tau_{max} = a\sqrt{\eta\rho(2\pi\omega)^3}$$

Reynolds Number[3]:

$$Re = f\rho d^2/\eta$$

a (R) is the **orbital radius** of the shaker (0.5 cm), **ρ** is the **density** of the culture medium (0.9973 g/mL), **η** is the **dynamic viscosity** of the medium (0.0101 poise), and **f** is the **rotational frequency** (rotation/sec), **w** is the **orbital speed**, **υ** is the **kinematic viscosity** (1.012 × 10^{-6} m^2/s), and **d** is the **inner diameter** of the insert.

4. Alignment Analysis of HUVECs

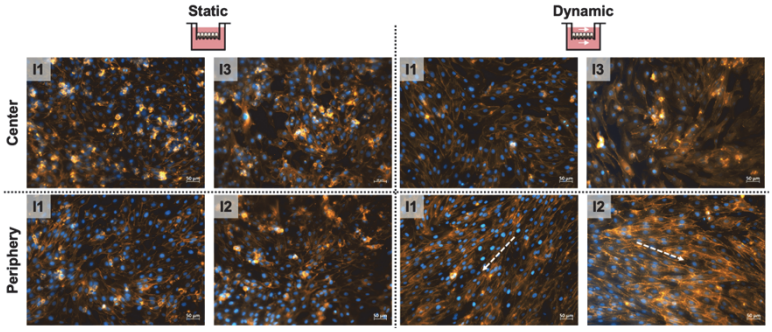

Figure 1. Morphological responses of HUVECs to shear stress on the whole (I1), periphery (I2) and center (I3) compartmentalized inserts. (a) Morphology of HUVECs after 48 h of orbital shear stress in the center of the well (up-right panel) or in the periphery of the well (down-right panel). HUVECs under static conditions are shown for comparison in the left panel. 20.7 dyn/cm^2 orbital shear stress in the periphery of the well causes HUVECs to align in the direction of flow.

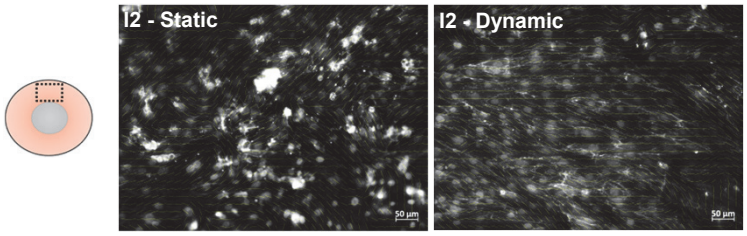

Figure 2. Representative orientation vector analysis of HUVECs on I2 inserts for the spontaneous orientation under static conditions and induced alignment of cells through the direction of flow. The yellow lines represent the average orientation of each 80 × 80 pixel^2. Analyses were done by the OrientationJ plugin[5] on Fiji image processing software[6].

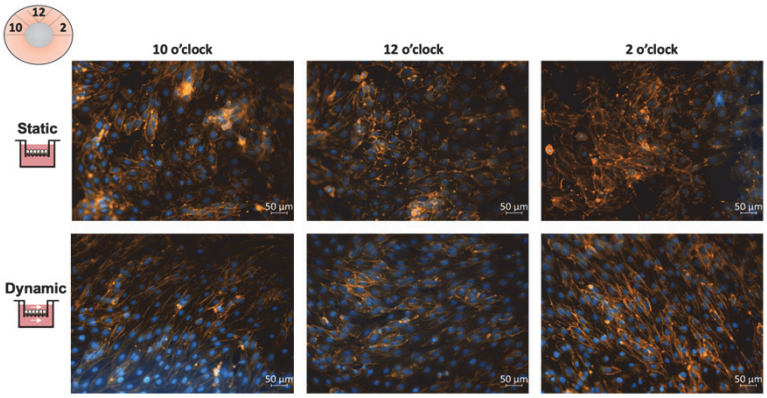

Figure 3. Morphological responses of HUVECs to shear stress at 10 o'clock, 12 o'clock and 2 o'clock locations of the periphery (I2) compartmentalized insert. HUVECs under static conditions show spontaneous orientation and cobblestone-like morphology whereas in the dynamic condition, they are aligned through the unidirectional flow and 20.7 dyn/cm^2 orbital shear.

5. Conclusion & Outlook

- Preliminary results showed that the alignment of endothelial cells through the unidirectional flow is achievable in the periphery inserts with the most uniform shear stress. In contrast, the center area of inserts (I1 & I3) groups showed similar morphology with static controls due to uneven and low shear stress.
- The 3D-printed fluidic inserts enable perfusion of the medium and controlled laminar flow areas to create complete in-plane intercellular stress fields that are important for healthy vascular tissue dynamics.
- This simple and cost-effective dynamic approach can serve as a simple, easily accessible and effective platform to identify new therapeutic targets in vascular disease and significantly increase our understanding of the mechanobiology of endothelial cells.
- Future studies will focus on biological characterization analyses to evaluate the effects of the applied shear stress on vascular tissue dynamics and endothelial barrier formation.
- The customized inserts are scalable and can be used for drug screening and more complex tissue models such as co-culturing purposes by adjustments to the insert geometry and applied shear stress.

The illustrations in Section 3 were created with BioRender.com and image analysis was performed on Zeiss Zen Blue 3.4 Lite Digital Imaging Software (Carl Zeiss Microscopy GmbH, DE) and ImageJ/Fiji software.

References: **(1)** Dardik et al. (2005), Journal of Vascular Surgery, 41:5; **(2)** Gray & Stroka (2017), Seminars in Cell and Developmental Biology, vol. 71 106–117; **(3)** Rothbauer, et al. (2021), Micromachines, vol.12; **(4)** Dogan & Dufva (2022), Scientific Reports, 3694; **(5)** Rezakhaniha, et al. (2012), Biomech Model Mechanobiol 11(3–4):461–473; (6) Schindelin, et al. (2012), Nat. Methods 9, 676–682.

* This project is funded by the EU's Horizon 2020 research and innovation program under the Marie Skłodowska-Curie, OrganoVIR project (Grant AG.: 812673).

Contact: aado@dtu.dk; dufva@dtu.dk

Patterning of Photo-crosslinkable Hydrogels to Mimic Intestine Tissue

Asli Aybike Dogan, Marina Orenga Sánchez, Martin Dufva

OrganoVIR Virtual Event 2021 (01 - 02 July 2021)

Patterning of Photo-crosslinkable Hydrogels to Mimic Intestine Tissue

Asli Aybike DOGAN[1*], Marina Orenga Sánchez[1], Martin DUFVA[1]
[1] Department of Health Technology, Technical University of Denmark, 2800 Kgs. Lyngby, Denmark
***E-mail:** aado@dtu.dk

Background

The intestinal epithelium is characterized by the presence of villi, finger-like structures projected 0.5-1 mm into the lumen at a density of 10-40 mm2 in the native tissue. Moreover, it is known that stiffness of the intestinal epithelium tissue's extracellular matrix (ECM) is 0.5-1 kPa [1] leads to the organization, adhesion, proliferation and dynamics of cells as they would do in vivo [2, 3].

Materials & Method

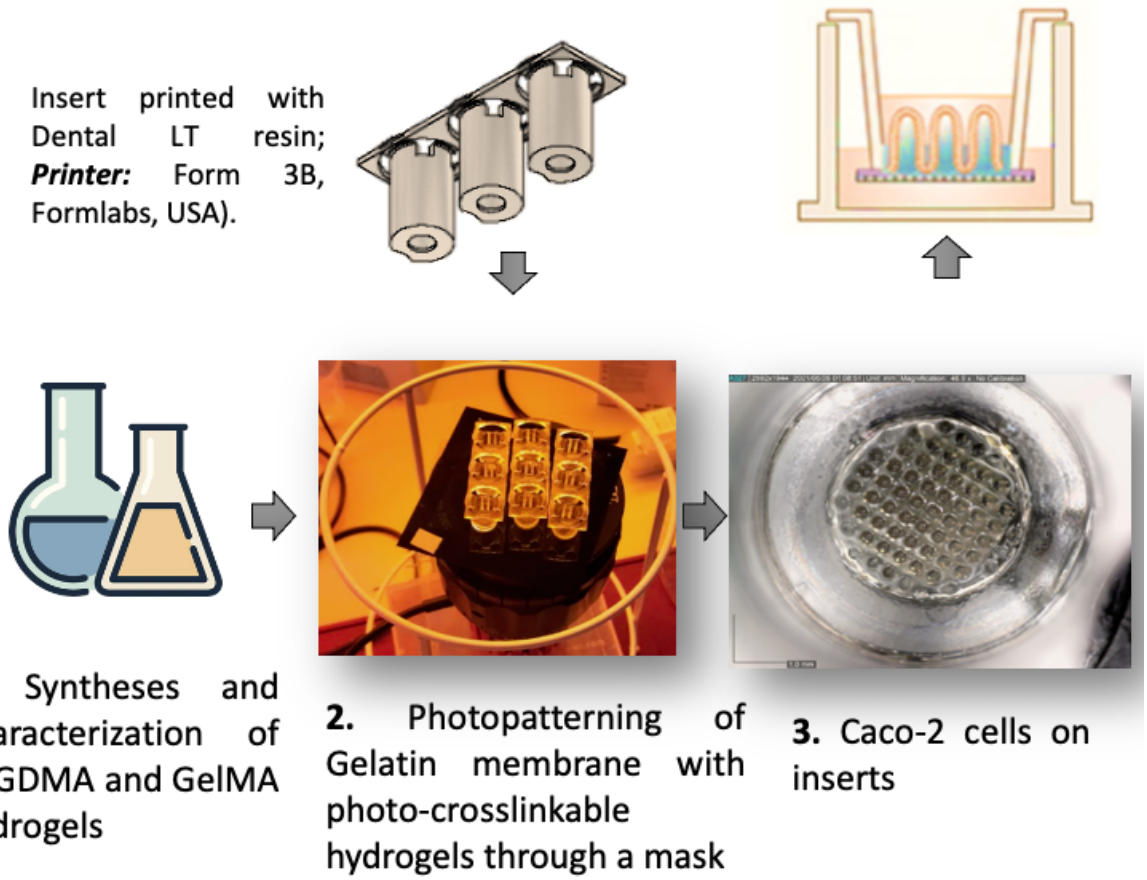

Results

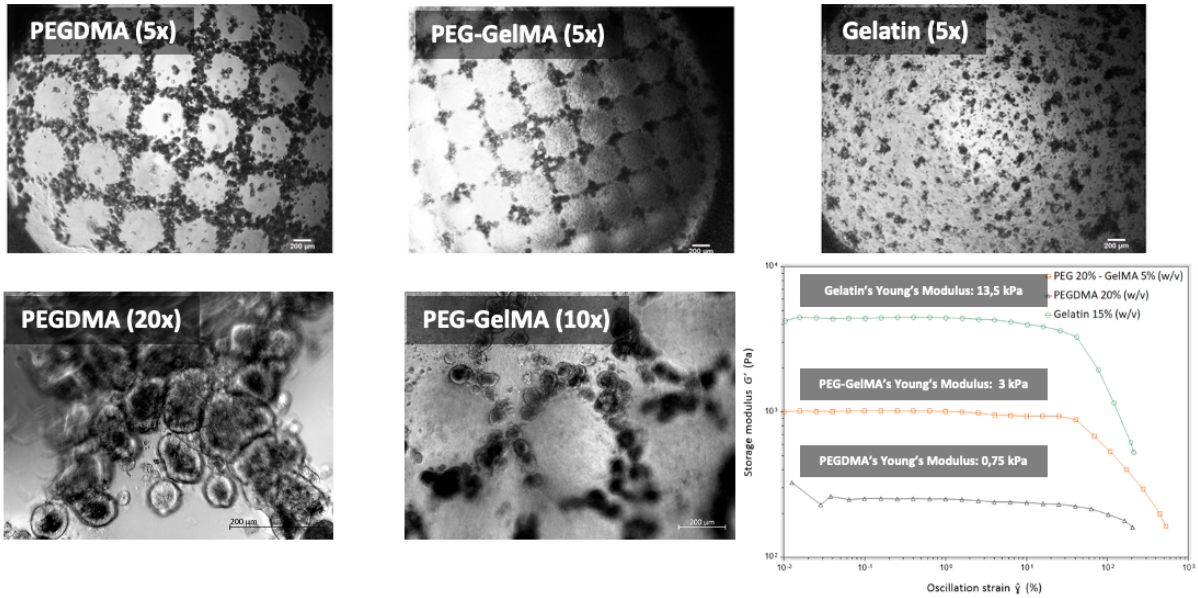

Figure 1. Brightfield microscope images of Caco-2 cells (Scale bar: 200 μm; Zeiss Axiovision) and strain sweep plot for rheological evaluation o the hydrogel stiffness.

Conclusion

- ✓ No cytotoxic effect of synthesized photo-crosslinkable hydrogels on Caco-2 cells
- ✓ Intestinal spheroid formation
- ✓ Need for modification to increase adhesion and stiffness for 2D culture of Caco-2 cells for the barrier function

References:

[1] Costa *et al*., 2019.
[2] Kleiveland *et al*., 2015.
[3] Discher *et al*., 2005.

Gathertown: https://gather.town/invite?token=jcayOKOG
OrganoVIR; For Your Science Only Event (1-2 July 2021)

This work is supported by the grant, E.U. Horizon 2020 Program (H2020-MSCA-ITN-2018) under the Grant Agreement No. 812673.

BIBLIOGRAPHY

1. Blutt, S. E. *et al.* Gastrointestinal microphysiological systems. *Experimental Biology and Medicine* vol. 242 1633 –1642 Preprint at https://doi.org/10.1177/1535370217710638 (2017).
2. Parrish, J., Lim, K., Zhang, B., Radisic, M. & Woodfield, T. B. F. New Frontiers for Biofabrication and Bioreactor Design in Microphysiological System Development. *Trends i n Biotechnology* vol. 37 1327 –1343 Preprint at https://doi.org/10.1016/j.tibtech.2019.04.009 (2019).
3. Wang, Y. I., Carmona, C., Hickman, J. J. & Shuler, M. L. Multiorgan Microphysiological Systems for Drug Development: Strategies, Advances, and Challenges . *Advanced Healthcare Materials* vol. 7 Preprint at https://doi.org/10.1002/adhm.201701000 (2018).
4. Chen, Z., Zilberberg, J. & Lee, W. Pumpless microfluidic device with open top cell culture under oscillatory shear stress. *Biomed Microdevices* **22**, (2020).
5. Wang, Y. I. & Shuler, M. L. UniChip enables long -term recirculating unidirectional perfusion with gravity -driven flow for microphysiological systems. *Lab Chip* **18**, 2563–2574 (2018).
6. Ailiani, A. C. *et al.* Quantitative analysis of peristaltic and segmental motion in vivo in the rat small intestine using dynamic MRI. *Magn Reson Med* **62**, 116–126 (2009).
7. Chen, Z., He, S., Zilberberg, J. & Lee, W. Pumpless platform for high-throughput dynamic multicellular culture and chemosensitivity evaluation. in *Transactions of the Annual Meeting of the Society for Biomaterials and the Annual International Biomaterials Symposium* vol. 40 705 (Society for Biomaterials, 2019).
8. Jung, O., Jae Song, M. & Ferrer, M. Operationalizing the Use of Biofabricated Tissue Models as Preclinical Screening Platforms for Drug Discovery and Development. (2021) doi:10.1177/24725552211030903.
9. Khalil, A. S., Jaenisch, R. & Mooney, D. J. Engineered tissues and strategies to overcome challenges in drug development. *Adv Drug Deliv Rev* **158**, 116 (2020).
10. Jepsen, M. L. *et al.* 3D Printed Stackable Titer Plate Inserts Supporting Three Interconnected Tissue Models for Drug Transport Studies. *Adv Biosyst* **4**, (2020).

11. Jepsen, M. L., Nielsen, L. H., Boisen, A., Almdal, K. & Dufva, M. Characterization of thin gelatin hydrogel membranes with balloon properties for dynamic tissue engineering. *Biopolymers* **110**, (2019).
12. Tan, H. Y. *et al.* A multi-chamber microfluidic intestinal barrier model using Caco-2 cells for drug transport studies. *PLoS One* **13**, (2018).
13. Starokozhko, V. *et al.* Differentiation of human-induced pluripotent stem cell under flow conditions to mature hepatocytes for liver tissue engineering. *J Tissue Eng Regen Med* **12**, 1273–1284 (2018).
14. Jensen, J. H. *et al.* Large-scale spontaneous self-organization and maturation of skeletal muscle tissues on ultra-compliant gelatin hydrogel substrates. *Sci Rep* **10**, (2020).
15. C., R. P. *et al.* Three-dimensional fabrication of thick and densely populated soft constructs with complex and actively perfused channel network. *Acta Biomater* **65**, 174–184 (2018).
16. Evans, N. D. & Gentleman, E. The role of material structure and mechanical properties in cell–matrix interactions. *J Mater Chem B* **2**, 2345–2356 (2014).
17. Koch, S. *et al.* Dkk-1 inhibits intestinal epithelial cell migration by attenuating directional polarization of leading edge cells. *Mol Biol Cell* **20**, 4816–4825 (2009).
18. Shin, W., Hinojosa, C. D., Ingber, D. E. & Kim, H. J. Human Intestinal Morphogenesis Controlled by Transepithelial Morphogen Gradient and Flow-Dependent Physical Cues in a Microengineered Gut-on-a-Chip. *iScience* **15**, 391–406 (2019).
19. Chong, H. B., Youn, J., Shin, W., Kim, H. J. & Kim, D. S. Multiplex recreation of human intestinal morphogenesis on a multi-well insert platform by basolateral convective flow. *Lab Chip* **21**, 3316–3327 (2021).
20. Shin, W. & Kim, H. J. 3D in vitro morphogenesis of human intestinal epithelium in a gut-on-a-chip or a hybrid chip with a cell culture insert. *Nature Protocols* vol. 17 910–939 Preprint at https://doi.org/10.1038/s41596-021-00674-3 (2022).
21. Yu, J. *et al.* Reconfigurable open microfluidics for studying the spatiotemporal dynamics of paracrine signalling. *Nature Biomedical Engineering 2019 3:10* **3**, 830–841 (2019).
22. Hatton, G. B., Yadav, V., Basit, A. W. & Merchant, H. A. Animal Farm: Considerations in Animal Gastrointestinal Physiology and Relevance to Drug Delivery in Humans. *J Pharm Sci* **104**, 2747–2776 (2015).

23. Kararli, T. T. & Searle, G. D. Comparison of the gastrointestinal anatomy, physiology, and biochemistry of humans and commonly used laboratory animals. *Biopharm Drug Dispos* **16**, 351–380 (1995).
24. Torras, N., García-Díaz, M., Fernández-Majada, V. & Martínez, E. Mimicking epithelial tissues in three -dimensional cell culture models. *Frontiers in Bioengineering and Biotechnology* vol. 6 Preprint at https://doi.org/10.3389/fbioe.2018.00197 (2018).
25. Shafran, Y. *et al.* Co-culture hydrogel micro -chamber array-based plate for anti -tumor drug development at single-element resolution. *Toxicology in Vitro* **71**, (2021).
26. Leth Jepsen, M. *et al.* 3D Printed Stackable Titer Plate Inserts Supporting Three Interconnected Tissue Models for Drug Transport Studies. *Adv Biosyst* **4**, (2020).
27. Sambuy, Y. *et al. The Caco-2 cell line as a model of the intestinal barrier: in£uence of cell and culture-related factors on Caco-2 cell functional characteristics*. *Cell Biology and Toxicology* vol. 21 (2005).
28. Hewes, S. A. *et al.* In Vitro Models of the Small Intestine: Engineering Challenges and Engineering Solutions. *Tissue Engineering - Part B: Reviews* vol. 26 313–326 Preprint at https://doi.org/10.1089/ten.teb.2019.0334 (2020).
29. Thompson, C. L., Fu, S., Knight, M. M. & Thorpe, S. D. Mechanical Stimulation: A Crucial Element of Organ-on-Chip Models. *Frontiers in Bioengineering and Biotechnology* vol. 8 Preprint at https://doi.org/10.3389/fbioe.2020.602646 (2020).
30. Gayer, C. P. & Basson, M. D. The effects of mechanical forces on intestinal physiology and pathology. *Cellular Signalling* vol. 21 1237 –1244 Preprint at https://doi.org/10.1016/j.cellsig.2009.02.011 (2009).
31. Balcells, M., Fernández Suárez, M., Vázquez, M. & Edelman, E. R. Cells in fluidic environments are sensitive to flow frequency. *J Cell Physiol* **204**, 329–335 (2005).
32. Lindner, M., Laporte, A., Block, S., Elomaa, L. & Weinhart, M. Physiological shear stress enhances differentiation, mucus -formation and structural 3d organization of intestinal epithelial cells in vitro. *Cells* **10**, (2021).
33. Srinivasan, B. *et al.* TEER Measurement Techniques for In Vitro Barrier Model Systems. *Journal of Laboratory Automation* vol. 20 107–126 Preprint at (2015).
34. Yeste, J., Illa, X., Alvarez, M. & Villa, R. Engineering and monitoring cellular barrier models. *Journal of Biological Engineering 2018 12:1* **12**, 1–19 (2018).
35. Gleeson, J. P., Fein, K. C. & Whitehead, K. A. Oral delivery of peptide therapeutics in infants: Challenges and opportunities. *Adv Drug Deliv Rev* **173**, 112–124 (2021).

36. Brunner, J., Ragupathy, S. & Borchard, G. Target specific tight junction modulators *Adv Drug Deliv Rev* **171**, 266–288 (2021).
37. Gehart, H. & Clevers, H. Tales from the crypt: new insights into intestinal stem cells *Nat Rev Gastroenterol Hepatol* **16**, 19–34 (2019).
38. Kazakoff, P. W., Mcguire, T. R., Hoie, E. B., Cano, M. & Iversen, P. L. *AN IN VITRO MODEL FOR ENDOTHELI AL PERMEABILITY: ASSESSMENT OF MONOLAYER INTEGRITY*. *In Vitro Ceil. Dev. Biol. Animal* vol. 31 (1995).
39. Schöneberg, J. *et al.* Engineering biofunctional in vitro vessel models using a multilayer bioprinting technique. *Sci Rep* **8**, 10430 (2018).
40. Holm Niel sen, S. *et al.* Exploring the role of extracellular matrix proteins to develop biomarkers of plaque vulnerability and outcome. *J Intern Med* **287**, 493–513 (2020).
41. Kim, S. H., Turnbull, J. & Guimond, S. Extracellular matrix and cell signalling: the dynamic cooperation of integrin, proteoglycan and growth factor receptor. *J Endocrinol* **209**, 139–151 (2011).
42. Costa, J. & Ahluwalia, A. Advances and Current Challenges in Intestinal in vitro Model Engineering: A Digest. *Frontiers in Bioengineering and Biotechnology* vol. 7 Preprint at https://doi.org/10.3389/fbioe.2019.00144 (2019).
43. Paluch, E. K. *et al.* Mechanotransduction: Use the force(s). *BMC Biol* **13**, 1–14 (2015).
44. Mousavi, S. J. & Hamdy Doweidar, M. Role of Mechanical Cues in Cell Differentiation and Proliferation: A 3D Numerical Model. *PLoS One* **10**, (2015).
45. Gray, K. M. & Stroka, K. M. Vascular endothelial cell mechanosensing: New insights gained from biomimetic microfluidic models. *Seminars in Cell and Developmental Biology* vol. 71 106 –117 Preprint at https://doi.org/10.1016/j.semcdb.2017.06.002 (2017).
46. Dessalles, C. A., Leclech, C., Castagnino, A. & Barakat, A. I. Integration of substrate - and flow-derived stresses in endothelial cell mechanobiology. *Communications Biology 2021 4:1* **4**, 1–15 (2021).
47. Dessalles, C. A., Leclech, C., Castagnino, A. & Baraka t, A. I. Integration of substrate - and flow-derived stresses in endothelial cell mechanobiology. *Communications Biology* vol. 4 Preprint at (2021).
48. Janmey, P. A., Fletcher, D. A. & Reinhart-King, C. A. Stiffness Sensing by Cells. *Physiol Rev* **100**, 695 (2020).

49. Wong, L. *et al.* Substrate stiffness directs diverging vascular fates. *Acta Biomater* **96**, 321–329 (2019).
50. Handorf, A. M., Zhou, Y., Halanski, M. A. & Li, W. J. Tissue stiffness dictates development, homeostasis, and disease progression. *Organogenesis* vol. 11 1 –15 Preprint at (2015).
51. Roy, N., Turner -Brannen, E. & West, A. R. DEVELOPMENT OF AN IN VITRO EXPERIMENTAL MODEL FOR INVESTIGATING THE EFFECT OF MATRIX STIFFNESS ON EPITHELIAL BARRIER PERMEABILITY Matrix stiffness and epithelial barrier. doi:10.1101/828079.
52. Guimarães, C. F., Gasperini, L., Marques, A. P. & Reis, R. L. The stiffness of living tissues and its implications for tissue engineering.*Nature Reviews Materials* vol. 5 351–370 Preprint at https://doi.org/10.1038/s41578-019-0169-1 (2020).
53. Discher, D. E., Janmey, P. & Wang, Y. L. Tissue cells feel and respond to the stiffness of their substrate. *Science* vol. 310 1139 –1143 Preprint at https://doi.org/10.1126/science.1116995 (2005).
54. Yi, B., Xu, Q. & Liu, W. An overview of substrate stiffness guided cellular response and its applications in tissue regeneration. *Bioact Mater* **15**, 82–102 (2022).
55. Jepsen, M. L., Nielsen, L. H., Boisen, A., Almdal, K. & Dufva, M. Characterization of thin gelatin hydrogel membranes with balloon properties for dynamic tissue engineering. *Biopolymers* **110**, (2019).
56. Cruz-Acuña, R.*et al.* PEG-4MAL hydrogels for human organoid generation, culture, and in vivo delivery. *Nat Protoc* **13**, 2102–2119 (2018).
57. Gustafsson, L. *et al.* Recombinant Spider Silk Forms Tough and Elastic Nanomembranes that are Protein-Permeable and Support Cell Attachment and Growth. *Adv Funct Mater* **30**, (2020).
58. Altay, G. *et al.* Self-organized intestinal epithelial monolayers in crypt and villus -like domains show effective barrier function. *Sci Rep* **9**, (2019).
59. Rozmus, E. *A novel 3D PDAC model system developed with the use of decellularized matrix scaffolds* . (2019).
60. Leth Jepsen, M. *et al.* 3D Printed Stackable Titer Plate Inserts Supporting Three Interconnected Tissue Models for Drug Transport Studies. *Adv Biosyst* **4**, (2020).
61. Jensen, J. H.*et al.* Large-scale spontaneous self-organization and maturation of skeletal muscle tissues on ultra-compliant gelatin hydrogel substrates. *Sci Rep* **10**, (2020).

62. Pimentel C., R. *et al.* Three-dimensional fabrication of thick and densely populated soft constructs with complex and actively perfused channel network. *Acta Biomater* **65**, 174–184 (2018).
63. Yung, C. W. *et al.* Transglutaminase crosslinked gelatin as a tissue engineering scaffold. *J Biomed Mater Res A* **83**, 1039–1046 (2007).
64. Rosiak, J. M. & Yoshii, F. Hydrogels and their medical applications. *Nucl Instrum Methods Phys Res B* **151**, 56–64 (1999).
65. Hennink, W. E. & van Nostrum, C. F. Novel crosslinking methods to design hydrogels. *Adv Drug Deliv Rev* **54**, 13–36 (2002).
66. Gombotz, W. R. & Wee, S. F. Protein release from alginate matrices. *Adv Drug Deliv Rev* **31**, 267–285 (1998).
67. O'Leary, L. E. R., Fallas, J. A., Bakota, E. L., Kang, M. K. & Hartgerink, J. D. Multi-hierarchical self-assembly of a collagen mimetic peptide from triple helix to nanofibre and hydrogel. *Nature Chemistry 2011 3:10* **3**, 821–828 (2011).
68. Heck, T., Faccio, G., Richter, M. & Thöny-Meyer, L. Enzyme-catalyzed protein crosslinking. *Appl Microbiol Biotechnol* **97**, 461 (2013).
69. Akther, F., Little, P., Li, Z., Nguyen, N. T. & Ta, H. T. Hydrogels as artificial matrices for cell seeding in microfluidic devices. *RSC Adv* **10**, 43682–43703 (2020).
70. Sung, J. H., Yu, J., Luo, D., Shuler, M. L. & March, J. C. Microscale 3D hydrogel scaffold for biomimetic gastrointestinal (GI) tract model. *Lab Chip* **11**, 389–392 (2011).
71. Benjamin, A. D. *et al.* Light-based 3D printing of hydrogels with high-resolution channels. *Biomed Phys Eng Express* **5**, (2019).
72. Taebnia, N. *et al.* Dual-Material 3D-Printed Intestinal Model Devices with Integrated Villi-like Scaffolds. *ACS Appl Mater Interfaces* (2021) doi:10.1021/acsami.1c22185.
73. Schrieber, R. & Gareis, H. Gelatine Handbook: Theory and Industrial Practice.
74. Lukin, I. *et al.* Progress in Gelatin as Biomaterial for Tissue Engineering. *Pharmaceutics* vol. 14 Preprint at https://doi.org/10.3390/pharmaceutics14061177 (2022).
75. Baltazar, T. *et al.* Native human collagen type I provides a viable physiologically relevant alternative to xenogeneic sources for tissue engineering applications: A comparative in vitro and in vivo study. *J Biomed Mater Res B Appl Biomater* **110**, 2323–2337 (2022).
76. Gomez-Guillen, M. C., Gimenez, B., Lopez-Caballero, M. E. & Montero, M. P. Functional and bioactive properties of collagen and gelatin from alternative sources: A review. *Food Hydrocoll* **25**, 1813–1827 (2011).

77. Wudebwe, U. N. G. *et al.* Exploiting cell-mediated contraction and adhesion to structure tissues in vitro. *Philosophical Transactions of the Royal Society B: Biol ogical Sciences* **370**, (2015).
78. Boedtker, H. & Doty, P. A study of gelatin molecules, aggregates and gels. *Journal of Physical Chemistry* **58**, 968–983 (1954).
79. Djabourov, M., Leblond, J. & Papon, P. Gelation of aqueous gelatin solutions. II. Rheology of the sol-gel transition. *Journal de Physique* **49**, 333–343 (1988).
80. Haiyan, L., Kunlong, M., Zhenghua, X., Xiaomei, R. & Gang, Y. Preparation and characteristics of gelatin sponges crosslinked by microbial transglutaminase. *PeerJ* **2017**, 3665 (2017).
81. Lerner, A. & Benzvi, C. Microbial Transglutaminase Is a Very Frequently Used Food Additive and Is a Potential Inducer of Autoimmune/Neurodegenerative Diseases. *Toxics* **9**, (2021).
82. Yung, C. W. *et al.* Transglutaminase crosslinked gelatin as a tissue engineering scaffold. *J Biomed Mater Res A* **83**, 1039–1046 (2007).
83. Vion, A. C. *et al.* Endothelial Cell Orientation and Polarity Are Controlled by Shear Stress and VEGF Through Distinct Signaling Pathways. *Front Physiol* **11**, (2021).
84. Chiu, J. J. & Chien, S. Effects of Disturbed Flow on Vascular Endothelium: Pathophysiological Basis and Clinical Perspectives. *Physiol Rev* **91**, 327–387 (2011).
85. Ballermann, B. J., Dardik, A., Eng, E. & Liu, A. Shear stress and the endothelium. *Kidney Int* **54**, S100–S108 (1998).
86. Roux, E., Bougaran, P., Dufourcq, P. & Couffinhal, T. Fluid Shear Stress Sensing by the Endothelial Layer. *Front Physiol* **11**, 861 (2020).
87. Chatzizisis, Y. S. *et al.* Role of Endothelial Shear Stress in the Natural History of Coronary Atherosclerosis and Vascular Remodeling: Molecular, Cellular, and Vascular Behavior. *J Am Coll Cardiol* **49**, 2379–2393 (2007).
88. Jacobs, C. R. *et al. Differential effect of steady versus oscillating flow on bone cells* .
89. Franzoni, M. *et al.* Design of a cone-and-plate device for controlled realistic shear stress stimulation on endothelial cell monolayers. *Cytotechnology* **68**, 1885–1896 (2016).
90. Malek, A. M., Ahlquist, R., Gibbons, G. H., Dzau, V. J. & Izumo, S. *A cone -plate apparatus for the in vitro biochemical and molecular analysis of the effect of shear stress on adherent cells* . *Methods in Cell Science* vol. 17 (1995).

91. Breen, L. T. *et al.* Development of a novel bioreactor to apply shear stress and tensile strain simultaneously to cell monolayers. in *Review of Scientific Instruments* vol. 77 (2006).
92. Deligianni, D. D. *et al.* Effect of surface roughness of the titanium alloy Ti –6Al–4V on human bone marrow cell response and on protein adsorption. *Biomaterials* **22**, 1241–1251 (2001).
93. Warboys, C. M., Ghim, M. & Weinberg, P. D. Understanding mechanobiology in cultured endothelium: A review of the orbital shaker method. *Atherosclerosis* vol. 285 170–177 Preprint at (2019).
94. Warboys, C. M., Overby, D. R. & Weinberg, P. D. Dendritic cells lower the permeability of endothelial monolayers. in *Cellular and Molecular Bioengineering* vol. 5 184 –193 (2012).
95. Warboys, C. M. *et al.* Acute and chronic exposure to shear stress have opposite effects on endothelial permeability to macromolecules. *Am J Physiol Heart Circ Physiol* **298**, 1850–1856 (2010).
96. Puwanun, S. *et al.* A simple rocker -induced mechanical stimulus upregulates mineralization by human osteoprogenitor cells in fibrous scaffolds. *J Tissue Eng Regen Med* **12**, 370–381 (2018).
97. Srinivasan, B., Hickman, J. & Shuler, M. *Simulation of Gravity -Driven Flow Through a Microfluidic Device on a Rocker Platform* .
98. Tucker, R. P. *et al.* See-saw rocking: An in vitro mo del for mechanotransduction research. *J R Soc Interface* **11**, (2014).
99. Miller, P. G. & Shuler, M. L. Design and Demonstration of a Pumpless 14 Compartment Microphysiological System. *Biotechnol. Bioeng* **113**, 2213–2227 (2016).
100. Abaci, H. E., Gledhill, K, Guo, Z., Christiano, A. M. & Shuler, M. L. Pumpless microfluidic platform for drug testing on human skin equivalents. *Lab Chip* **15**, 882–888 (2015).
101. Esch, M. B., Ueno, H., Applegate, D. R. & Shuler, M. L. Modular, pumpless body -on-a-chip platform for the co-culture of GI tract epithelium and 3D primary liver tissue. *Lab Chip* **16**, 2719–2729 (2016).
102. Chen, H. J., Miller, P. & Shuler, M. L. A pumpless body-on-a-chip model using a primary culture of human intestinal cells and a 3D culture of liver cells. *Lab Chip* **18**, 2036–2046 (2018).

103. Wang, Y. I., Carmona, C., Hickman, J. J. & Shuler, M. L. Multiorgan Microphysiological Systems for Drug Development: Strategies, Advances, and Challenges. *Advanced Healthcare Materials* vol. 7 Preprint at (2018).
104. Hasenberg, T. *et al.* Emulating human microcapillaries in a multi-organ-chip platform. *J Biotechnol* **216**, 1–10 (2015).
105. Maschmeyer, I. *et al.* A four-organ-chip for interconnected long-term co-culture of human intestine, liver, skin and kidney equivalents. *Lab Chip* **15**, 2688–2699 (2015).
106. Sergachev, I. *et al.* Fluorescent optical fiber sensors for cell viability monitoring. *Analyst* **138**, 4066–4069 (2013).
107. Tan, H. Y. *et al.* A multi-chamber microfluidic intestinal barrier model using Caco-2 cells for drug transport studies. *PLoS One* **13**, (2018).
108. Kim, H. J. & Ingber, D. E. Gut-on-a-Chip microenvironment induces human intestinal cells to undergo villus differentiation. *Integrative Biology (United Kingdom)* **5**, 1130–1140 (2013).
109. Nikolaev, M. *et al.* Homeostatic mini-intestines through scaffold-guided organoid morphogenesis. *Nature* **585**, 574–578 (2020).
110. Leung, C. M. *et al.* A guide to the organ-on-a-chip. *Nature Reviews Methods Primers* vol. 2 Preprint at https://doi.org/10.1038/s43586-022-00118-6 (2022).
111. Danku, A. E., Dulf, E. H., Braicu, C., Jurj, A. & Berindan-Neagoe, I. Organ-On-A-Chip: A Survey of Technical Results and Problems. *Frontiers in Bioengineering and Biotechnology* vol. 10 Preprint at https://doi.org/10.3389/fbioe.2022.840674 (2022).
112. Castiaux, A. D., Spence, D. M. & Martin, R. S. Review of 3D cell culture with analysis in microfluidic systems. *Analytical Methods* vol. 11 4220–4232 Preprint at https://doi.org/10.1039/c9ay01328h (2019).
113. Xing, Y. *et al.* A pumpless microfluidic device driven by surface tension for pancreatic islet analysis. *Biomed Microdevices* **18**, (2016).
114. Berthier, E., Dostie, A. M., Lee, U. N., Berthier, J. & Theberge, A. B. Open Microfluidic Capillary Systems. *Analytical Chemistry* vol. 91 8739–8750 Preprint at https://doi.org/10.1021/acs.analchem.9b01429 (2019).
115. Zhang, Q., Feng, S., Lin, L., Mao, S. & Lin, J. M. Emerging open microfluidics for cell manipulation. *Chemical Society Reviews* vol. 50 5333–5348 Preprint at https://doi.org/10.1039/d0cs01516d (2021).

116. Tan, J. N., Alan, T. & Neild, A. Stability of flowing open fluidic channels. *AIP Adv* **3**, (2013).
117. Oliveira, N. M., Vilabril, S., Oliveira, M. B., Reis, R. L. & Mano, J. F. Rece nt advances on open fluidic systems for biomedical applications: A review. *Materials Science and Engineering C* vol. 97 851 –863 Preprint at https://doi.org/10.1016/j.msec.2018.12.040 (2019).
118. Zhou, X., Liu, D., You, L. & Wang, L. Quantifying fluid shear stress in a rocking culture dish. *J Biomech* **43**, 1598–1602 (2010).
119. Hyler, A. R. *et al.* Fluid shear stress impacts ovarian cancer cell viability, subcellular organization, and promotes genomic instability. *PLoS One* **13**, (2018).
120. Gater, R. *et al.* Investigation of Conjunctival Fibrosis Response Using a 3D Glaucoma Tenon's Capsule + Conjunctival Model. *Invest Ophthalmol Vis Sci* **60**, 605–614 (2019).
121. Wittkowske, C. *The role of mechanical forces in bone formation* . (2016).
122. Wang, Y. I., Abaci, H. E. & Shuler, M. L. Microfluidic blood–brain barrier model provides in vivo-like barrier properties for drug permeability screening. *Biotechnol Bioeng* **114**, 184–194 (2017).
123. Beaurivage, C. *et al.* Development of a gut-on-a-chip model for high throughput disease modeling and drug discovery. *Int J Mol Sci* **20**, (2019).
124. Rajasekar, S. *et al.* IFlowPlate—A Customized 384 -Well Plate for the Culture of Perfusable Vascularized Colon Organoids. *Advanced Materials* **32**, (2020).
125. Beaurivage, C. *et al.* Development of a human primary gut -on-a-chip to model inflammatory processes. *Sci Rep* **10**, (2020).
126. Trietsch, S. J. *et al.* Membrane-free culture and real-time barrier integrity assessment of perfused intestinal epithelium tubes. *Nat Commun* **8**, (2017).
127. Nicolas, A. *et al.* High throughput transepithelial electrical resistance (TEER) measurements on perfused membrane-free epithelia. *Lab Chip* **21**, 1676–1685 (2021).
128. Leth Jepsen, M. *et al.* 3D Printed Stackable Titer Plate Inserts Supporting Three Interconnected Tissue Models for Drug Transport Studies. *Adv Biosyst* **4**, (2020).
129. Boyden, B. S. The c hemotactic effect of mixtures of antibody and antigen on polymorphonuclear leucocytes. *J Exp Med.* **115**, 453–466 (1962).
130. Transwell ® Permeable Supports Selection and Use Guide.

131. Mondrinos, M. J., Yi, Y. S., Wu, N. K., Ding, X. & Huh, D. Native extracellular matrix-derived semipermeable, optically transparent, and inexpensive membrane inserts for microfluidic cell culture. *Lab Chip* **17**, 3146–3158 (2017).
132. Johnson, L. A. *et al.* Matrix stiffness corresponding to strictured bowel induces a fibrogenic response in human colonic fibroblasts. *Inflamm Bowel Dis* **19**, 891–903 (2013).
133. Picollet-D'hahan, N., Zuchowska, A., Lemeunier, I. & le Gac, S. Multiorgan-on-a-Chip: A Systemic Approach To Model and Decipher Inter-Organ Communication. *Trends in Biotechnology* vol. 39 788–810 Preprint at (2021).
134. Ingber, D. E. Human organs-on-chips for disease modelling, drug development and personalized medicine. *Nature Reviews Genetics* Preprint at (2022).
135. Nicolas, J. *et al.* 3D Extracellular Matrix Mimics: Fundamental Concepts and Role of Materials Chemistry to Influence Stem Cell Fate. *Biomacromolecules* **21**, 1968–1994 (2020).
136. Hwang, J., Sullivan, M. O. & Kiick, K. L. Targeted Drug Delivery via the Use of ECM-Mimetic Materials. *Frontiers in Bioengineering and Biotechnology* vol. 8 Preprint at (2020).
137. Coppeta, J. R. *et al.* A portable and reconfigurable multi-organ platform for drug development with onboard microfluidic flow control. *Lab Chip* **17**, 134–144 (2016).
138. Xiao, S. *et al.* A microfluidic culture model of the human reproductive tract and 28-day menstrual cycle. *Nature Communications 2017 8:1* **8**, 1–13 (2017).
139. Sass, L. & Oxman, R. Materializing design: the implications of rapid prototyping in digital design. *Des Stud* **27**, 325–355 (2006).
140. Jensen, L. S., Özkil, A. G. & Mortensen, N. H. PROTOTYPES IN ENGINEERING DESIGN: DEFINITIONS AND STRATEGIES. in *DS 84: Proceedings of the DESIGN 2016 14th International Design Conference* (eds. Marjanovic Dorian, Storga Mario, Pavkovic Neven, Bojcetic Nenad & Skec Stanko) 821–830 (2016).
141. Sketches and Wireframes and Prototypes! Oh My! Creating Your Own Magical Wizard Experience :: UXmatters. https://www.uxmatters.com/mt/archives/2010/05/sketches-and-wireframes-and-prototypes-oh-my-creating-your-own-magical-wizard-experience.php.
142. Oksdath Mansilla, M. *et al.* 3D-printed microplate inserts for long term high-resolution imaging of live brain organoids. *BMC Biomedical Engineering 2021 3:1* **3**, 1–14 (2021).

143. Bauer, M. *et al.* Novel 3D-Printed Cell Culture Inserts for Air–Liquid Interface Cell Culture. *Life* **12**, 1216 (2022).
144. Pinnock, C. B., Meier, E. M., Joshi, N. N., Wu, B. & Lam, M. T. Customizable engineered blood vessels using 3D printed inserts. *Methods* **99**, 20–27 (2016).
145. Boyer, C. J. *et al.* High-throughput scaffold-free microtissues through 3D printing. *3D Print Med* **4**, 1–6 (2018).
146. Formlabs. FDM vs. SLA: Compare the Two Most Popular Types of 3D Printers. https://formlabs.com/eu/blog/fdm-vs-sla-compare-types-of-3d-printers/.
147. Currens, E. R., Armbruster, M. R., Castiaux, A. D., Edwards, J. L. & Martin, R. S. Evaluation and optimization of PolyJet 3D-printed materials for cell culture studies. *Anal Bioanal Chem* **414**, 3329–3339 (2022).
148. Chen, C. *et al.* Insert-based microfluidics for 3D cell culture with analysis. *Anal Bioanal Chem* **410**, 3025–3035 (2018).
149. Formlabs. SLA vs. PolyJet 3D Printing: In-Depth Comparison. https://formlabs.com/blog/sla-vs-polyjet-3d-printing/.
150. Skliutas, E. *et al.* A Bio-Based Resin for a Multi-Scale Optical 3D Printing. *Scientific Reports 2020 10:1* **10**, 1–9 (2020).
151. Formlabs. BioMed Clear: Biocompatible Photopolymer Resin for Formlabs SLA Printers. https://formlabs-media.formlabs.com/datasheets/2001432-TDS-ENUS-0.pdf (2020).
152. Grigaleviciute, G., Baltriukiene, D., Bukelskiene, V. & Malinauskas, M. Biocompatibility Evaluation and Enhancement of Elastomeric Coatings Made Using Table-Top Optical 3D Printer. *Coatings 2020, Vol. 10, Page 254* **10**, 254 (2020).
153. Dogan, A. A. & Dufva, M. Customized 3D-printed stackable cell culture inserts tailored with bioactive membranes. *Scientific Reports 2022 12:1* **12**, 1–12 (2022).
154. Kim, G. B. *et al.* Three-Dimensional Printing: Basic Principles and Applications in Medicine and Radiology. *Korean J Radiol* **17**, 182 (2016).
155. Stereolithography (SLA) 3D Printing Guide. https://formlabs.com/blog/ultimate-guide-to-stereolithography-sla-3d-printing/.
156. Lamers, M. M. *et al.* SARS-CoV-2 productively infects human gut enterocytes. Preprint at http://science.sciencemag.org/.
157. Lehmann, M. *et al.* Human small intestinal infection by SARS-CoV-2 is characterized by a mucosal infiltration with activated CD8+ T cells. *Mucosal Immunology 2021 14:6* **14**, 1381–1392 (2021).

158. Marzorati, M. *et al.* The HMI ™ module: A new tool to study the Host -Microbiota Interaction in the human gastrointestinal tract in vitro. *BMC Microbiol* **14**, 1–14 (2014).
159. Guo, P., Weinstein, A. M. & Weinbaum, A. S. A hydrodynamic mechanosensory hypothesis for brush border microvilli. *Am J Physiol Renal Physiol* **279**, 698–712 (2000).
160. CellCrown inserts 96 well plate inserts, 8 -well strips, sterile 3D Cell Culture. https://www.sigmaaldrich.com/DK/en/product/aldrich/z682004?gclid=Cj0KCQjw94WZBhDtARIsAKxWG--oJXk1Ni3O_yK9_ZiKNtepiHzIhqdCVBkz_rMFdwEJ-LyWrI6fsPgaAorFEALw_wcB&gclsrc=aw.ds.
161. HTS Transwell® 96 - well Permeable Support | Corning. https://ecatalog.corning.com/life-sciences/b2b/DK/en/Permeable-Supports/HTS/HTS-Transwell%C2%AE-96-well-Permeable-Support/p/hTSTranswell96WellPermeableSupports.
162. Jepsen, M. L., Nielsen, L. H., Boisen, A., Almdal, K. & Dufva, M. Characterization of thin gelatin hydrogel membranes with balloon properties for dynamic tissue engineering. *Biopolymers* **110**, (2019).
163. Zamprogno, P. *et al.* Second-generation lung -on-a-chip with an array of stretchable alveoli made with a biological membrane. *Communications Biology 2021 4:1* **4**, 1–10 (2021).
164. Natoli, M., Leoni, B. D., D'Agnano, I., Zucco, F. & Felsani, A. Good Caco -2 cell culture practices. *Toxicol In Vitro* **26**, 1243–1246 (2012).
165. Swiderek, M. S., Scientist, N. & Mannuzza, F. J. Effects of ECM Proteins on Barrier Formation in Caco-2 Cells.
166. Yamashita, S. *et al.* New and Better Protocols for a Short -Term Caco -2 Cell Culture System.
167. Cai, Y. *et al.* Development, validation, and application of a novel 7 -day Caco -2 cell culture system. *J Pharmacol Toxicol Methods* **70**, 175–181 (2014).
168. Kant Avvari, R. Biomechanics of the Small Intestinal Contractions. in *Digestive System - Recent Advances* (eds. Qi, X. & Koruth, S.) (IntechOpen, 2019). doi:10.5772/intechopen.86539.
169. de Jonge, C. S., Sprengers, A. M. J., van Rijn, K. L., Nederveen, A. J. & Stoker, J. Assessment of fasted and fed gastrointestinal contraction frequencies in healthy subjects using continuously tagged MRI. *Neurogastroenterology and Motility* **32**, (2020).

170. Wnorowski, A., Yang, H. & Wu, J. C. Progress, obstacles, and limitations in the use of stem cells in organ-on-a-chip models. *Advanced Drug Delivery Reviews* vol. 140 3–11 Preprint at https://doi.org/10.1016/j.addr.2018.06.001 (2019).
171. Ghim, M., Pang, K. T., Arshad, M., Wang, X. & Weinberg, P. D. A novel method for segmenting growth of cells in sheared endothelial culture reveals the secretion of an anti-inflammatory mediator. *J Biol Eng* **12**, (2018).
172. Ghim, M. *et al.* Endothelial cells exposed to atheroprotective flow secrete follistatin-like 1 protein which reduces transcytosis and inflammation. *Atherosclerosis* **333**, 56–66 (2021).
173. Dardik, A. *et al.* Differential effects of orbital and laminar shear stress on endothelial cells. *J Vasc Surg* **41**, 869–880 (2005).
174. Driessen, R. *et al.* Computational characterization of the dish-in-a-dish, a high yield culture platform for endothelial shear stress studies on the orbital shaker. *Micromachines (Basel)* **11**, (2020).
175. Holliday, C. J., Ankeny, R. F., Jo, H. & Nerem, R. M. Discovery of shear- and side-specific mRNAs and miRNAs in human aortic valvular endothelial cells. *Am J Physiol Heart Circ Physiol* **301**, 856–867 (2011).
176. Hickman, J. Transepithelial/endothelial Electrical Resistance (TEER) theory and applications for microfluidic body-on-a-chip devices. *J Rare Dis Res Treat* **1**, 46–52 (2016).
177. Arlk, Y. B. *et al.* Barriers-on-chips: Measurement of barrier function of tissues in organs-on-chips. *Biomicrofluidics* **12**, 42218 (2018).
178. Nicolas, A. *et al.* High throughput transepithelial electrical resistance (TEER) measurements on perfused membrane-free epithelia. *Lab Chip* **21**, 1676–1685 (2021).
179. Shin, W. *et al.* Spatiotemporal Gradient and Instability of Wnt Induce Heterogeneous Growth and Differentiation of Human Intestinal Organoids. *iScience* **23**, (2020).
180. Patient, J. D. *et al.* Nanofibrous scaffolds support a 3D in vitro permeability model of the human intestinal epithelium. *Front Pharmacol* **10**, (2019).
181. Ghaffarian, R. & Muro, S. Models and methods to evaluate transport of drug delivery systems across cellular barriers. *J Vis Exp* (2013) doi:10.3791/50638.
182. Tavelin, S., Gråsjö, J., Taipalensuu, J., Ocklind, G. & Artursson, P. *Epithelial Cell Culture Protocols*. vol. 188 (Humana Press, 2002).

183. Lea, T. Caco-2 Cell Line. in *The Impact of Food Bioactives on Health In Vitro and Ex Vivo Models* (eds. Kleiveland, C. et al.) 103–111 (Springer, 2015).
184. Natoli, M. *et al.* Cell growing density affects the structural and functional properties of Caco-2 differentiated monolayer. *J Cell Physiol* **226**, 1531–1543 (2011).
185. Nikulin, S. v., Poloznikov, A. A. & Sakharov, D. A. A method for rapid generation of model intestinal barriers in vitro. *Bulletin of Russian State Medical University* 97–103 (2020) doi:10.24075/BRSMU.2020.077.
186. Cai, Y. *et al.* Development, validation, and application of a novel 7-day Caco-2 cell culture system. *J Pharmacol Toxicol Methods* **70**, 175–181 (2014).
187. Costa, J. & Ahluwalia, A. Advances and Current Challenges in Intestinal in vitro Model Engineering: A Digest. *Frontiers in Bioengineering and Biotechnology* vol. 7 Preprint at https://doi.org/10.3389/fbioe.2019.00144 (2019).
188. Behrens, I. & Kissel, T. Do cell culture conditions influence the carrier-mediated transport of peptides in Caco-2 cell monolayers? *European Journal of Pharmaceutical Sciences* **19**, 433–442 (2003).
189. Chopra, D. P., Dombkowski, A. A., Stemmer, P. M. & Parker, G. C. Intestinal Epithelial Cells In Vitro. *Stem Cells Dev* **19**, 131 (2010).
190. Ding, Q.-M., Ko, T. C. & Evers, B. M. Caco-2 intestinal cell differentiation is associated with G_1 arrest and suppression of CDK2 and CDK4. *American Journal of Physiology - Cell Physiology* **275**, C1193–C1200 (1998).
191. Kim, H. J. & Ingber, D. E. Gut-on-a-Chip microenvironment induces human intestinal cells to undergo villus differentiation. *Integrative Biology (United Kingdom)* **5**, 1130–1140 (2013).
192. Kim, H. J., Huh, D., Hamilton, G. & Ingber, D. E. Human gut-on-a-chip inhabited by microbial flora that experiences intestinal peristalsis-like motions and flow. *Lab Chip* **12**, 2165–2174 (2012).
193. Shin, W. & Kim, H. J. Intestinal barrier dysfunction orchestrates the onset of inflammatory host-microbiome cross-talk in a human gut inflammation-on-a-chip. *Proc Natl Acad Sci U S A* **115**, E10539–E10547 (2018).
194. Rapid prototyping of a multilayer microphysiological system for primary human intestinal epithelial culture. doi:10.1101/400721.

195. Hughes, P., Marshall, D., Reid, Y., Parkes, H. & Gelber, C. The costs of using unauthenticated, over-passaged cell lines: How much more data do we need?*BioTechniques* vol. 43 575–586 Preprint at https://doi.org/10.2144/000112598 (2007).

196. Fois, C. A. M., Schindeler, A., Valtchev, P. & Dehghani, F. Dynamic flow and shear stress as key parameters for intestinal cells morphology and polarization in an organ-on-a-chip model. *Biomed Microdevices* **23**, (2021).

197. Delon, L. C. *et al.* A systematic investigation of the effect of the fluid shear stress on Caco-2 cells towards the optimization of epithelial organ-on-chip models. *Biomaterials* **225**, (2019).

198. Ghim, M. *et al.* Visualization of three pathways for macromolecule transport across cultured endothelium and their modification by flow. *Am J Physiol Heart Circ Physiol* **313**, 959–973 (2017).

199. Filipovic, N., Ghimire, K., Saveljic, I., Milosevic, Z. & Ruegg, C. Computational modeling of shear forces and experimental validation of endothelial cell responses in an orbital well shaker system. *Comput Methods Biomech Biomed Engin* **19**, 581–590 (2016).

200. Junaid, A. *et al.* Metabolic response of blood vessels to tnfα. *Elife* **9**, 1–28 (2020).

201. Zhang, H. *et al.* Role of TNF-α in vascular dysfunction. *Clin Sci* **116**, 219–230 (2009).

202. Chong, H. B., Youn, J., Shin, W., Kim, H. J. & Kim, D. S. Multiplex recreation of human intestinal morphogenes is on a multi-well insert platform by basolateral convective flow. *Lab Chip* **21**, 3316–3327 (2021).

203. Formlabs. Guide to Thermoforming. https://formlabs.com/blog/thermoforming/.

204. Formlabs. 3D Printing Applications: Injection Molding. https://formlabs.com/eu/applications/injection-molding/.

205. Wang, Y., Kankala, R. K., Ou, C., Chen, A. & Yang, Z. Advances in hydrogel-based vascularized tissues for tissue repair and drug screening. *Bioact Mater* **9**, 198–220 (2022).

206. Yang, Y. *et al.* Pumpless microfluidic devices for generating healthy and diseased endothelia. *Lab Chip* **19**, 3212–3219 (2019).

207. Kleinman, H. K. *et al.* Basement Membrane Complexes with Biological Activity. *Biochemistry* **25**, 312–318 (1986).

208. Kim, S. *et al.* Tissue extracellular matrix hydrogels as alternatives to Matrigel for culturing gastrointestinal organoids. *Nature Communications 2022 13:1* **13**, 1–21 (2022).

209. Jee, J. H. *et al.* Development of Collagen -Based 3D Matrix for Gastrointestinal Tract - Derived Organoid Culture. *Stem Cells Int* **2019**, (2019).
210. Fisher, S. A., Baker, A. E. G. & Shoichet, M. S. Designing Peptide and Protein Modified Hydrogels: Selecting the Optimal Conjugation Strategy. *J Am Chem Soc* **139**, 7416–7427 (2017).
211. Ito, A. *et al.* Transglutaminase-mediated gelatin matrices incorporating cell adhesion factors as a biomaterial for tissue engineering. *J Biosci Bioeng* **95**, 196–199 (2003).
212. Zhang, K., Xiao, X., Wang, X., Fan, Y. & Li, X. Topographical patterning: characteristics of current processing techniques, controllable effects on material properties and co - cultured cell fate, updated applications in tissue engineering, and improvement strategies. *J. Mater. Chem. B* **7090**, 7090 (2019).